Vibration energy loss mechanisms in high quality factor resonator of gyroscope for space applications

A Thesis Submitted

In Partial Fulfillment of the Requirements

for the Degree of

Doctor of Philosophy

by

Gireesh Sharma. N

(Roll no: 166103023)

(External Registration, ISRO)

to the

DEPARTMENT OF MECHANICAL ENGINEERING

INDIAN INSTITUTE OF TECHNOLOGY, GUWAHATI, ASSAM

June 2021

CERTIFICATE

It is certified that the work contained in the thesis entitled "**Vibration energy loss mechanisms in high quality factor resonator of gyroscope for space applications**", by "Mr. Gireesh Sharma N", has been carried out under our supervision and that this work has not been submitted elsewhere for a degree.

Dr. T. Sundararajan
Vikram Sarabhai Space Centre
Thiruvananthapuram

Dr. Sachin Singh Gautam
Department of Mechanical Engineering
I.I.T. Guwahati

03-06-2021

Dedicated to

My beloved late parents

and

dear brother

Synopsis

Name of the student: Gireesh Sharma N

Roll No.: 166103023 (External Registration, ISRO)

Degree for which submitted: PhD

Department: Mechanical

Thesis title: Vibration energy loss mechanisms in high quality factor resonator of gyroscope for space applications

Names of thesis supervisors: Dr. Sachin Singh Gautam
Department of Mechanical Engineering
I.I.T. Guwahati

Dr. T. Sundararajan
Vikram Sarabhai Space Centre
I.S.R.O., Thiruvananthapuram

A gyroscope is a device to sense an angular velocity of a rotating frame where the device is mounted. Gyroscopes are mainly classified as mechanical and optical types. Mechanical gyroscopes are again classified based on the working principle such as angular momentum based and Coriolis acceleration based. Coriolis vibratory gyroscopes (CVG) use the Coriolis acceleration principle for angular velocity measurement. CVG gyroscopes generally use a vibrating mechanical element as a sensing element for detecting the angular velocity. All vibratory gyroscopes are based on the transfer of energy between two vibration modes of a structure caused by Coriolis acceleration. Gyroscopes are used for measuring the orientation of launch vehicle, spacecraft, and ballistic missiles as part of inertial navigation in aerospace and space applications. The most critical parameter for aerospace and space application is reliability. Sensor with lesser number of parts provides higher reliability. Hence, “solid-state” CVG technology is the state-of-the-art choice for these applications.

Coriolis vibratory gyroscopes (CVG) are the fastest developing type of gyroscope technology in inertial navigation systems. Hemispherical resonator gyroscope (HRG), which is a kind of wine glass mode CVG, meets the high-end navigation grade performance. HRG shows its superiority in size, very fine resolution, very good accuracy, shock resistance and highly reliable operation life with a smaller number of parts (Xu *et al.* [2011]). Hence, the solid state HRG is the best suitable high end inertial class candidate for critical and high value long duration interplanetary spacecraft missions.

The mechanical resonator element is the most critical functional part of HRG. The hemispherical resonator is excited in its $N = 2$ wine glass elliptical mode at its mechanical natural frequency. When an input rate is applied to the HRG along the axis of symmetry of the hemispherical resonator under resonance, a precession of a vibrating pattern (standing wave) around the axis of rotation occurs due to the action of Coriolis force. The angular rate of the standing wave precession is different from the input rate around the resonator shell symmetry axis, i.e., the standing wave does not totally rotate as that of input rotation. The difference between both the rotations is perfectly proportional to the input rotation. Thus, this device is able to sense the rotation angular velocity of the body to which the sensor is mounted.

Signal to noise ratio (SNR) is one of the key parameters for designing a low-resolution gyroscope. Therefore, it is desired to design gyroscopes more sensitive to input rotation and have a lower noise floor. The resolution of a gyroscope is the minimum input angular velocity that can be distinguished from the noise floor of the sensor per square root of the bandwidth of measurement. The overall resolution of the gyroscope total noise equivalent rotation (TNER) is determined by two uncorrelated components: the mechanical (or Brownian) noise equivalent rotation (MNER) and the electronic noise equivalent rotation (ENER). MNER can be reduced by increasing angular gain, input drive axis amplitude, increasing frequency of operation, increasing quality factor (Q factor) and increasing effective mass and lowering operating temperature. Increasing the mass results against the miniaturisation and also lowers the frequency. Also, lowering the operating temperature puts limitations on sensor applications. Hence, the performance of a CVG resonator is measured by the critical parameter quality factor. The Q factor is the ratio of the amount of energy stored in the vibrating resonator to the amount of energy dissipated by the resonator in one cycle. The Q factor of the CVG resonator determines the sensor's resolution and scale factor. Hence, the primary choice is to maximise the Q factor of the resonator followed by effective mass and angular gain to improve sensor performance.

Whenever a high sensitivity sensor is being designed, an analysis of sources of mechanical-thermal noise should be included in the early stage to avoid issues with an unacceptably high noise floor at the testing stage. Thus, ultra-high Q factor is required to achieve a very low mechanical noise equivalent rate for a gyroscope to achieve the smallest possible resolution limit. Hence, studying the different energy loss mechanisms in HRG resonator is very critical for achieving ultra-high Q factor for realizing a high-end performance sensor. In order to achieve ultra-high Q factor, the energy loss from the vibrating resonator structure should be kept as minimum as possible. The general damping mechanisms are thermoelastic damping (TED), anchor loss, surface loss, material internal friction, fluid damping, and electronics damping (Joshi *et al.* [2014]). The Q factor is defined for each individual energy loss mechanisms such as thermoelastic damping (Q_{TED}), anchor loss (Q_{Anchor}), surface loss ($Q_{Surface}$), fluid damping (Q_{Fluid}), material internal friction (Q_{MIF}) and electronics damping (Q_{Ele}). Since these different kinds of damping mechanisms are simultaneously present in the sensor, the effective Q factor (Q_{Eff}) is defined. It is very difficult to separate individual contributions during the hardware realization and evaluation.

Hence, it is mandatory that the design of the sensor resonator should be done to minimize all possible kinds of dissipation mechanisms. Also, it is to be ensured that the design requirements are met during realization.

Literature available indicates that analytical models for TED are available for simple resonator structures like beams, rings, and plates (Zener [1937], Lifshitz and Roukes [2000]). Closed-form analytical solution is available for simple beam resonator structures for anchor loss estimation (Hao *et al*. [2003]). Analytical estimation of anchor loss for disk resonator with center support could be validated with experimental results only with an error coefficient to take care of interactions between disk and support structure, and for non-ideal support conditions (Hao and Ayazi [2007]). Complex resonator geometries could be solved only with numerical methods (Frangi *et al.* [2013]).

Theoretical and experimental studies are available mainly for MEMS resonators of relatively simple structures (Duwel *et al.* [2003]). Quite a reasonable comparison of theoretical predictions could be obtained with appropriate best fit correction factors obtained from experimental results. Numerical models for energy loss prediction and experimental studies are available for hemispherical shells mainly birdbath geometries which are fabricated through MEMS and micro-glass blowing methods (Darvishian *et al.* [2014]). TED studies could not be found for hybrid resonator configuration with a combination of hemispherical and cylindrical resonator geometry with inside mounting stem in all millimeter size dimensions. The effect of thin film coating was studied on micron thickness hemispherical shells with a volume fraction of 0.1%. However, the sensitivity study of ultra-thin coating (volume fraction as low as 0.01%), coating configurations and effect of partial coating does not seem to have been attempted on hybrid configuration resonator.

Even though there are many studies on anchor loss of MEMS class resonators (Darvishian *et al.* [2017]), extensive anchor loss simulations on the effect of possible imperfections are very limited on millimeter size hemispherical-cylindrical hybrid resonators. To the best of the author's knowledge, experimental evaluation on hybrid configuration of resonator is not available. The effect of different combinations of mass unbalance and its effect on frequency split and *Q* factor mismatch on such configuration are not available in the open literature domain. Many surface characterization studies are based on profile measurements and microscopy methods. Surface and subsurface mechanical property evaluation at nanometer depth is not generally used as a tool for evaluating the surface damage to access the surface loss. Significant attempts are limited for studying of multiple energy loss mechanisms present simultaneously in the resonator in its functional configuration from design to demonstration.

Meeting the required ultra-high *Q* factor and long decay time constant for very low mechanical noise and good bias stability is still a challenge in the MEMS technology-based resonators compared to macro scale high precision resonators. MEMS technology is still not widely accepted in space application gyroscope resonators which demand low frequency split of degenerate modes for high rate sensitivity and whole-angle mode of operation.

In view of the above, the objectives of the present work are studying different vibration energy loss mechanisms related to mechanical resonator for gyroscopes, design of resonator well away from the TED driven Debye peak to achieve ultra-high *Q* factor, study of hybrid resonator configuration with increased effective mass and angular gain compared to general hemispherical configuration to achieve low resolution, effect of ultra-thin film conductive coating, different coating configurations and coating variations on TED, anchor loss estimation and detailed parametric study of dimensions and imperfections, realization and comprehensive experimental evaluation, study of significance of other loss mechanisms such as surface loss, material internal friction, fluid damping and demonstration of ultra-high quality factor precision macro scale gyroscope resonator for high end inertial applications in space sector. To achieve the above objectives of the present work, comprehensive simulation studies of different damping mechanisms and experiments on realized precision resonators are carried out, and the details are as follows.

In the present work, the quantitative requirement of Q_{Eff} is arrived for the mechanical resonator of HRG. The Q_{Eff} requirement is estimated based on MNER for the very fine resolution. The primary choice to improve MNER is to maximise the Q_{Eff} of the resonator followed by improving the effective mass and the angular gain. Minimum Q_{Eff} of 10^6 (one million) is required to achieve MNER of 10^{-3} $^\circ$/hr. Hence, it is proposed to design a macro scale resonator as it is very difficult to establish the required Q_{Eff} in micron scale resonators in its final functional form with all dissipative mechanisms. Different damping mechanisms such as thermoelastic damping (TED), anchor loss, surface loss, material internal friction, fluid damping, and electronics damping are addressed. The study of damping mechanisms is done using finite element simulations.

To start with, a simple ring resonator structure is considered to arrive at HRG resonator size. Q_{TED} of fused silica ring resonator of mm scale is 10^8 without any conductive coating. Since the mechanical frequency is much larger compared to the relaxation rate, the oscillations are adiabatic in nature. As this range of size is sufficiently away from the Debye peak of highest dissipation, the thermoelastic dissipation is very less. As the operating frequency is in the range of a few kHz in the present macro size resonators, the frequency-dependent Young's modulus change is very small and it is very close to isothermal relaxed Young's modulus. Thus, the design of the resonator is done well away from the TED driven Debye peak to achieve ultra-high *Q* factor in the design phase.

Initially, a simple hemispherical geometry is considered for the design of the HRG resonator. The basic size of the resonator is arrived at based on a sensitivity study done in ring resonator for achieving high Q_{TED}. Parametric study of different materials and dimensions is done. The sensor operating frequency is decided by this sensitivity study. The functional $N = 2$ elliptical mode eigenfrequency of HRG resonator, which operates nearly in the adiabatic region, is kept well above 2000 Hz to avoid launch induced resonance vibration loading and well separated from other nearby modes to reduce energy loss. As the thermal relaxation time becomes smaller, the resonator works away from the adiabatic region and close to the Debye peak which results in more dissipation. Also, the radial thickness direction temperature gradient contributes more to the thermoelastic dissipation. The polar and the

circumferential thermal relaxation time have less influence on the Q_{TED} of this resonator size. A decrease in thermal conductivity causes a longer thermal transport time and increases the Q_{TED}. Young's modulus and coefficient of thermal expansion do not have the same effect. An increase in Young's modulus causes more thermo-mechanical coupling and reduces the Q_{TED}. Also, an increase in Young's modulus increases the frequency and shifts the operating region to more adiabatic and hence improves the Q_{TED}. But, a more predominant effect is to reduce the Q_{TED} with an increase of Young's modulus. When operating temperature increases, the coupling between the structural and the thermal domains increases and reduces Q_{TED}. When the shell mean radius reduces, the frequency increases, and the behaviour become more adiabatic which results in higher Q_{TED}. The influence of shell thickness increase on Q_{TED} increase is more compared to that of shell mean radius.

The specific advantages of hemispherical-cylindrical hybrid resonator configuration are brought out in terms of improved effective mass and angular gain for lower MNER. The effective mass and the angular gain of a hybrid resonator configuration is 15% more than that of a hemispherical alone configuration. The selection of the $N = 2$ mode as the functional mode is also justified considering the angular gain. $N = 2$ mode is considered for functional mode as it gives 75% more angular gain compared to $N = 3$ mode. The configuration design of the hybrid resonator is shown in Figure 1. The final functional hybrid resonator configuration has a hemispherical region, a cylindrical region, an inside long bottom stem for resonator mounting and an outside short top stem.

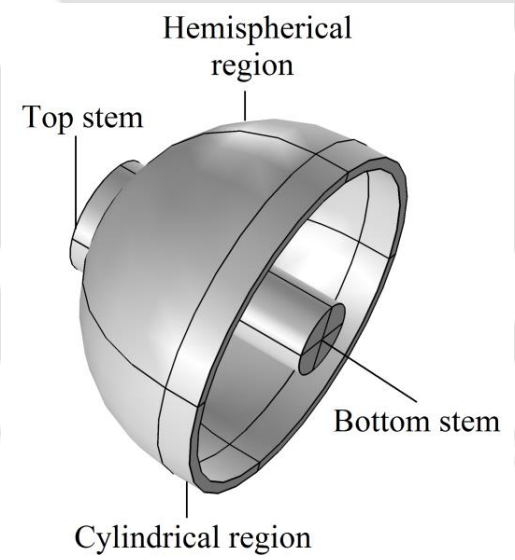

Figure 1: Functional hemispherical-cylindrical hybrid resonator configuration

Then, a detailed study of TED with thin-film electrically conductive coating, effect of coating variations and coating configurations is carried out for the hybrid resonator configuration. This is done to arrive at the coating configuration to meet the Q factor requirement for the functional resonator for electrostatic excitation and sensing. Q_{TED} decreases significantly by an order of three even with thin-film coating of 1000 A^o (coating thickness is 0.01% of 1 mm shell thickness). As the coating thickness increases, the

thermoelastic damping increases due to higher entropy generation. However, the initial reduction in Q_{TED} is more. This is due to the high strain rate at the boundary between the bulk material and the coating. The natural frequency comes down by few Hz only with 1000 A^o due to the mass effect of the gold film compared to the stiffness effect. The most significant coating material properties are Young's modulus and coefficient of thermal expansion with respect to Q_{TED}. The effect of coating thickness variations depends on the overlap between the circumferential direction thickness variation and the N = 2 elliptical mode shape. Q_{TED} increases as the coating area reduces with a reduced latitude angle of the coating. Q_{TED} reduction is more for the outside coating case compared to the inside coating case. It is found that the eigenfrequency increases by few milliHz in 1000 A^o coated resonator from the isothermal Young's modulus based eigenvalue. It is can be inferred that the change (increase) of frequency dependent Young's modulus increases as the dissipation increases.

Q_{Anchor} is high for an ideal symmetrical hemispherical resonator with inside stem of sufficient length. A sensitivity study of the effect of different dimensional parameters such as shell mean radius, shell thickness, stem radius and stem height on the Q_{Anchor} is carried out. Q_{Anchor} decreases with an increase in the shell radial thickness and decreases with the shell radius. The effect of mode interactions is also included in the present study. When the N = 2 mode frequency is closer to the stem tilt mode frequency, the anchor loss increases by a few orders of magnitude. The ratio of Young's modulus value of the resonator to that of the supporting substrate is found to have an effect on the Q_{Anchor}.

Q_{Anchor} is not significant for a designed perfect resonator structure. However, it approaches Q_{TED} even with minor geometric imperfections in the hardware realisation. Anchor loss sensitivity to the possible imperfections during fabrication is done to arrive at the critical fabrication tolerances. Effect of geometric imperfections due to fabrication such as shell offset, shell tilt, shell thickness variation, mass unbalance is studied in detail and arrived at the fabrication tolerances. It is found that the shell-stem offset value of less than 50 microns, the tilt value of less than 0.25° and the radial thickness variation of less than 20 microns should be achieved during the fabrication.

The effect of different combinations of mass unbalance and its effect on the frequency split and Q_{Anchor} mismatch are analyzed as they are very critical for the sensor performance. As the unbalanced mass increases, the frequency split increases with the sensitivity of 0.29×10^{-6} kg/Hz. The effect of unbalanced mass profile on the frequency, overall reduction and variation of the Q_{Anchor} depends on the overlap of N = 2 mode shape over the unbalance pattern in the circumferential direction.

The fabrication procedure of fused silica brittle material and its effect on $Q_{Surface}$ is discussed next. The birefringence measurement shows that higher diameter blank material has $(1/5)^{th}$ internal stress compared to lower blank diameter. The hemispherical resonator, as shown in Figure 2, is realized using high precision machines. A total of eight numbers of resonators are made. Then, detailed metrology measurements of the realized resonators are done for assessing the precision of fabrication. The precision levels achieved during fabrication are different for different resonators. Characterization facilities for frequency, Q

factor, and surface defects have been established. N = 2 mode resonance frequency measurement is carried out for the resonators and compared with the simulation results. The effect of the measured dimensional and geometric deviations on frequency and frequency split is analyzed. The frequency increases as the radial thickness increases and the frequency split increases as the geometric error increases. Shell offset is achieved well within 50 microns and shell tilt is achieved well within 0.25° in one high precision resonator and achieved frequency split less than 0.5 Hz for nominal frequency of around 5550 Hz. Thus, a highly symmetrical precision resonator is realized as per the dimensional and geometric tolerance requirement from the anchor loss sensitivity analysis.

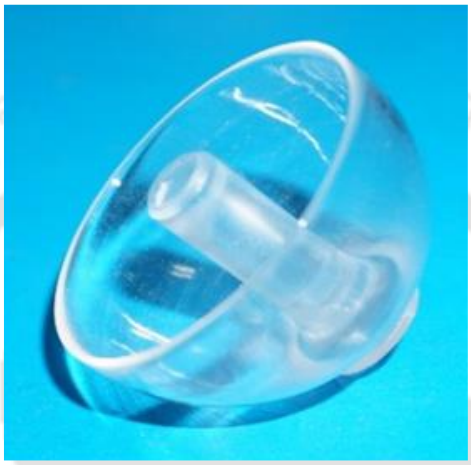

Figure 2: High precision fused silica resonator after precision machining

Specific surface characterization methods are adopted for the realized high precision resonators. Surface characterization has been carried out after machining and after chemical etching using the nanoindentation technique. A comprehensive experimental evaluation for frequency, Q factor and its variations are carried out under ambient and high vacuum. Unbalance sensitivity verification is done with the fabrication deviations and balancing scheme is established. Coarse and fine methods of balancing are arrived. These balancing procedures have been established for correcting the frequency split of realized resonators. It is found from the numerical simulation that four-point mass correction of equal amount at 90° apart in the circumferential direction results in lower frequency split. Low precision resonator is balanced by mass removal method from frequency split of 5.95 Hz to less than 0.5 Hz.

Vibration response measurements are done using non-contact Laser Doppler Vibrometry (LDV) instrument. Response measurement is carried out over 90° circumferential direction. Figure 3 shows the two different N = 2 frequencies (ω_1 and ω_2) due to frequency split and the corresponding axes locations around the circumferential direction. At the antinodal location of one of the N = 2 mode axes, there is one response peak. Two responses are seen when the monitoring location is between the antinodal points of the two degenerate modes. The anti-nodal location of low-frequency mode 1 is at a reference circumferential location 0° and the anti-nodal location of high-frequency mode 2 is at circumferential location 45°. Thus, the low and the high-frequency axes are found out for balancing purpose.

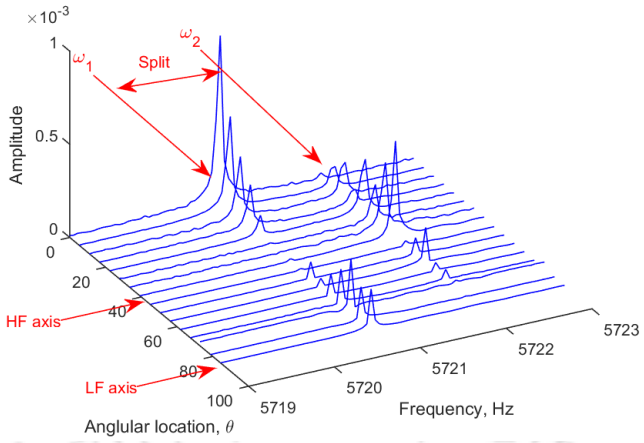

Figure 3: Responses of the two $N = 2$ modes (ω_1 and ω_2) showing the frequencies and the corresponding axes locations around circumferential direction

Q factor estimation from internal friction and surface loss is also studied. It is seen from the nanoindentation test that the hardness and the reduced Young's modulus is very less compared to the bulk material nominal hardness of 11 GPa and Young's modulus of 73 GPa because of the formation of damaged surface layer after USM. These values improved after each stage of chemical etching due to the removal of a major part of the damaged surface layer. Q factor measurement is carried out from 'ring-down' response measurement using LDV for the uncoated resonator. Very low Q_{Eff} only is obtained after ultrasonic machining. The Q_{Eff} is improved by order of three to the range of millions after chemical etching. Some resonators needed more etching trials because wet chemical etching method is not a precisely controlled process. Q_{Eff} is evaluated in the circumferential direction as shown in Figure 4 and 15% variation is found.

Experiments are carried out to estimate the effect of fluid damping and arrived at the sensor operating pressure level for the present resonator design. No significant Q_{Eff} improvement is found for pressure less than 1 N/m^2 (10^{-2} millibar). The sensor operation is proposed to be done much lower than 1 N/m^2 to eliminate contribution of Q_{Fluid} in Q_{Eff}.

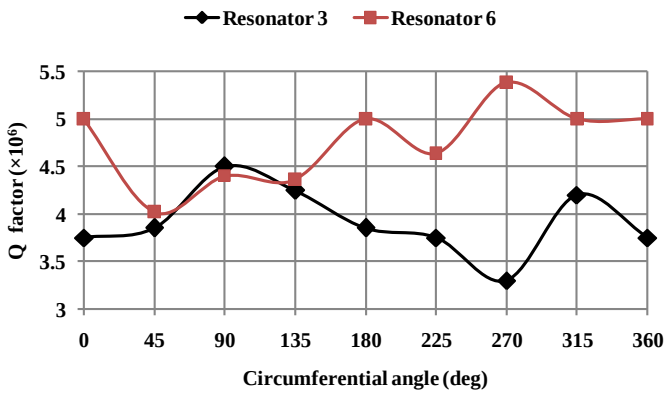

Figure 4: Q_{Eff} variation in the circumferential direction

Q factor measurement of thin film coated resonator is carried out along with the detailed coating film characterization. The resonator, which has a frequency split of 0.39 Hz and Q_{Eff} of 4.5×10^6 before coating, is balanced using the precise mass addition technique and one order reduction is achieved in the frequency split. The achieved frequency split is 0.05 Hz which meets the fine balancing specification. The achieved Q_{Eff} after coating is 2.4×10^6 which also meets the specification of more than one million *Q* factor. Q_{Eff} of uncoated resonator is limited by the surface loss. Q_{Eff} of coated resonator is limited by the effective *Q* factor of Q_{TED} (with coating) and $Q_{Surface}$ because both these losses are in the same order (10^6). The frequency split and Q_{Eff} meets the specification requirement for the final functional hybrid resonator. The atomic force microscopy (AFM) measurement ensures the surface profile requirement for thin film coating. The scratch test results show the thin film gold coating integrity with the base silica material. Scratch depth and width increases as the normal load increases. Friction coefficient variation is less than 10% under different normal load tests. Thus, the demonstration of high *Q* factor in the final functional high precision macro scale resonator configuration is done.

Now, the salient achievements are summarized. The quantitative requirement of the effective quality factor of the order of few millions is arrived for the mechanical resonator from the sensor resolution requirement. Then, the size of the hemispherical resonator is arrived based on achieving high Q_{TED}. The specific advantages of hybrid resonator configuration are brought out in terms of improved effective mass and angular gain and hybrid resonator is proposed as final configuration. Detailed study of TED with thin film electrically conductive coating, effect of coating variations and configurations is done and found that coating reduces the quality factor significantly. Effect of geometric imperfections due to fabrication is studied and arrived at the fabrication tolerances. Hemispherical resonators are fabricated and detailed metrology measurements showed that different precision class resonators are realized. $N = 2$ mode resonance frequency measurements are carried out and good comparison obtained with simulation result. Surface characterization using nanoindentation technique showed that the surface loss is limiting the effective quality factor. Chemical etching, which is used for removing post-fabrication surface damage, improved the quality factor by few orders. Experiment is also carried out to estimate the effect of fluid damping and arrived at the sensor operating pressure level. Thin film coating and its characterization have been carried out and ensured coating adhesion. It can be inferred that the effective quality factor of uncoated high precision resonator of millimetre size is limited by resonator material internal friction and fabrication induced surface loss while that of coated resonator is limited by the effective *Q* factor of Q_{TED} (with coating), $Q_{Surface}$ and coating material internal friction. *Q* factor of few millions is demonstrated in the final functional hybrid configuration of the critical mechanical resonator of HRG for high end inertial applications in space sector. Thus, the objectives of the present research work are met.

References

W. Xu, W.Wenqi, L. Bing, and L. Yun. The modelling of hemispherical gyro and its space applications. *Proceedings of 7thInternational Symposium on Precision Engineering Measurements and Instrumentation*, 8321(1);4-9, 2011.

S. Joshi, S. Hung, and S. Vengallatore. Design strategies for controlling damping in micromechanical and nanomechanical resonators. *EPJ Techniques and Instrumentation*, 1(5);1-14, 2014.

C. Zener. Internal friction in solids. I. Theory of internal friction in reeds.*Physical Review*, 52(3);230-235, 1937.

R. Lifshitz and M. L. Roukes. Thermoelastic damping in micro and nano mechanical systems. *Physical Review B*, 61(8);5600-5609, 2000.

Z. Hao, A. Erbil, and F. Ayazi. An analytical model for support loss in micromachined beam resonators with in plane flexural vibrations. *Sensors and Actuators A: Physical*, 109(1);156-164, 2003.

Z. Hao and F. Ayazi. Support loss in the radial bulk-mode vibrations of center-supported micromechanical disk resonators. *Sensors and Actuators A: Physical*, 134(2);582-593, 2007.

A. Frangi, A. Bugada, M. Martello, P. T. Savadkoohi. Validation of PML based models for the evaluation of anchor dissipation in MEMS resonators. *European Journal of Mechanics A/Solids*, 37;256-265, 2013.

A. Duwel, J. Gorman, M. Weinstein, J. Borenstein, and P. Ward. Experimental study of thermoelastic damping in MEMS gyros. *Sensors and Actuators A: Physical*, 103(1-2);70-75, 2003.

A. Darvishian, B. Shiari, J.Y. Cho, T. Nagourney, and K. Najafi. Investigation of thermoelastic loss mechanism in shell resonators. *Proceedings of ASME International Mechanical Engineering Congress and Exposition*, 39331-39336, Montreal, Canada, 2014.

A. Darvishian, B. Shiari, J. Y. Cho, T. Nagourney, and K. Najafi. Anchor loss in hemispherical shell resonators. *Journal of Microelectromechanical Systems*, 26(1);51-66, 2017.

Acknowledgement

“Great discoveries and improvements invariably involve cooperation of many minds”

This work is not a great discovery but gives an improvement in understanding design and development of high performance inertial gyroscope resonator for space application. Even the work of this stature has to have contributions of many people. During the course of this work, I have been supported, emotionally and technically, by many people. I feel honoured at being having this opportunity to express my gratitude for all of them. This is a challenging task, given the many people that have helped, I am going to try anyway, and if your name is not listed, rest assured that my gratitude is not less than from those listed below.

I am extremely satisfied to express my deepest gratitude and heartfelt thanks to my thesis supervisors Dr. Sachin Singh Gautam and Dr. T. Sundararajan. During these years I have known Dr. Gautam as a sympathetic person with high level of honesty, integrity and work ethics. His enthusiasm and systematic approach on research work have made a deep impression on me. His way of making and maintaining friendship with all kinds and classes of persons attracted me very much. Dr. Gautam’s invaluable guidance on the technical areas, encouragement and inspiring advices enabled me to approach the research work in an efficient and innovative way. Dr. Sundararajan is a very composed and generous person with exceptional human values. His advice of maintaining regular and focussed working attitude till the end of the research helped me to complete this work in time. I would like to once again thank my dear supervisors for their support and invaluable suggestions during the entire course of this work as my well-wishers. The technical and personal lessons that I learned by working under them are considered as very precious for the rest of my life.

I extend my sincere gratitude to Dr. D. Sam Dayala Dev and Shri. S. Paul Pandian of I.S.R.O. Inertial Systems Unit (I.I.S.U.) for granted permission to pursue this dream of doing doctoral research work and extended all supports as well wishers of my professional growth.

I am extremely thankful to Shri. Arun George, Dr. Allen Anilkumar, Shri. R. Sivakumaran, Shri. S. R. Unnikrishna, Shri. Gaurav Behrani and Shri. Tony Thomas of I.I.S.U. for imparting me knowledge in different areas and immense support during experimental studies. I express my thanks to Shri. Joji J. Chaman, Shri. K. Vijayan and fabrication team of I.I.S.U. for supporting this work by realizing hardwares and metrology. I express my sincere gratitude to Shri. Abhilash M., Shri. Ajay P. Roy and Shri. Karthik R. for

the support extended to me in various capabilities. I am thankful to all my colleagues in I.I.S.U. who have directly and indirectly helped me to complete this work.

I extend my gratitude to Prof. D. Chakraborty, Prof. S. K. Dwivedy, (Late) Dr. A. N. Reddy, Dr. Arup Nandy, Dr. Atanu Banerjee, Dr. Manas Das and other faculty members of Department of Mechanical Engineering and Prof. S. Talukdar (Department of Civil Engineering) for technically guiding and personally supporting me throughout the research work.

I am also thankful to Prof. Padma K. Padmanabhan (Department of Physics), Shri. Vishal Agrawal, Shri. G. Saipraneeth, Shri. Prabhat Kumar, Shri. Utpal Kiran and Shri. Bhabesh Das for their affection and care during my stay in I. I. T., Guwahati and made it enjoyable and memorable. I am also thankful to Shri. S. Dattatraya Kulkarni of N. A. L. and Shri. Enni Krishna of I.I.S.U. for guiding me in the administrative procedures as co-research scholars.

I am grateful to my beloved late parents Dr. N. N. Sharma and Smt. K. N. Radhamany, who left me to heavenly world during my research period, for providing me invaluable support and constant encouragement at every step of my life. I am also so much thankful to my dear brother Mr. Rajesh Sharma N who stands with me as a companion over all these years. I am extremely thankful to my loving wife Mrs. Sripriya V. for taking care of all the family affairs and allowing me to concentrate on my research work. Once again, I express my deepest gratitude to my better-half for her co-operation, inspiration and support during all ups and downs. My special thanks to sweet daughters Kum. Theerthasree Sharma and Kum. Mythili Sharma who filled my tense and busy times with moments of pleasure. My family sacrificed their many personal needs and stood side by side to me for during my work peacefully and patiently. I also express my gratitude to Shri. M. N. G. Elayath and Dr. P. Veeramuthuvel for the inspiration to do the research work. I express my sincere thanks to all relatives and friends.

Finally, I express my thanks to all those who have helped me directly or indirectly for successful completion of this work.

Gireesh Sharma N

I.I.S.U., I.S.R.O.

June 2021

List of publications

Journal papers (published / under review)

Sharma G. N., Sundararajan T., and Gautam S. S., *Effect of geometric imperfections on anchor loss and characterisation of a coriolis vibratory gyroscope resonator with high quality factor,* Journal of Gyroscopy and Navigation, 11(3);206-213, 2020.

Sharma G. N., T. Sundararajan, Sachin Singh Gautam, *Thermoelastic damping based design, sensitivity study, and demonstration of a functional hybrid gyroscope resonator for high quality factor,* Journal of Gyroscopy and Navigation, 12(1);69-85, 2021.

Sharma G. N., T. Sundararajan, Sachin Singh Gautam, *Design to operational parameters dependency on quality factor of sensor mechanical resonators,* Journal of Gyroscopy and Navigation, 12(2), 2021.

Sharma G. N., T. Sundararajan, Sachin Singh Gautam, *Design, sensitivity study of damping mechanisms and quality factor evaluation of a hybrid gyroscope resonator,* Advances in Space Research - Under review.

Book chapter

Gireesh Sharma N., George A., Pandian S. P., Sundararajan S., Gautam S. S., *Design of inertial class gyroscope resonator with ultra-high quality factor for interplanetary space missions,* Lecture notes in Mechanical Engineering - Springer book series: Advances in Mechanical Engineering, 1071-1084, 2020.

International conference papers

Gireesh Sharma N., George A., Pandian S. P., Sundararajan S., Gautam S. S., *Anchor loss estimation of a mechanical resonator with low energy loss for satellite application,* 2nd International Conference on Future Learning Aspects of Mechanical Engineering (FLAME 2020), Amity University, Noida, August 5th- 7th, 2020 - Best paper award received.

Gireesh Sharma N., George A., Pandian S. P., Sundararajan S., Gautam S. S., *A multiphysics simulation of thermo elastic dynamic damping of a vibratory gyroscope resonator for space application,* 7th International Congress on Computational Mechanics and Simulation (ICCMS 2019), IIT Mandi, December 11th-13th, 2019**.**

Gireesh Sharma N., George A., Pandian S. P., Sundararajan S., Gautam S. S., *Design of inertial class gyroscope resonator with ultra-high quality factor for interplanetary space missions,* International Conference on Recent Innovations and Developments in Mechanical Engineering, NIT Meghalaya, November 8th- 10th, 2018**.**

Contents

List of Figures

List of tables

Nomenclature

Latin Symbols

A	Projected contact area
A_g	Angular gain
b	Width of beam resonator
c_x	Damping coefficient in primary direction
c_y	Damping coefficient in secondary direction
c_{ij}	Components of elastic stiffness
C_L	Longitudinal wave propagation velocity
C_P	Specific heat capacity
C_T	Transverse wave propagation velocity
ΔC_{min}	Minimum detectable capacitance of sense electronics
d	Beam thickness
d_c	Thickness of coating
D	Thermal diffusivity
E	Young's modulus
E_c	Young's modulus of coating
E_i	Young's modulus of indenter
E_s	Young's modulusof sample
E_{ds}	Surface complex Young's modulus
E_R	Relaxed isothermal Young's modulus
E_U	Unrelaxed adiabatic Young's modulus
$E(\omega)$	Frequency dependent complex Young's modulus
E^*	Composite reduced Young's modulus
Δ_E	Relaxation strength
f	Resonant eigen frequency
Δf	Frequency split
F_c	Coriolis force in resonator element
F_x	Additional externally applied force in primary direction
F_y	Additional externally applied force in secondary direction

f_{BW}	Frequency bandwidth at half power point
h	Indenter penetration depth
h_c	Contact depth
H	Hardness
I	Moment of inertia of beam resonator
k	Thermal conductivity
k_d	Boltzmann constant
k_x	Stiffness coefficient in primary direction
k_y	Stiffness coefficient in secondary direction
L	Length of beam resonator
m	Mass of resonator element
m_u	Unbalanced mass
m_{eff}	Effective mass participating in N^{th} mode
N	Vibration mode number of HRG resonator
N_r	Vibration mode number of ring resonator
P	Force applied to indenter
P_f	Fluid pressure
Q	Quality factor
Q_n	Quality factor of n^{th} mode of beam resonator
Q_{Anchor}	Quality factor limited by anchor loss
Q_{Eff}	Effective quality factor
$Q_{Electronics}$	Quality factor limited by electronics damping
Q_{freq}	Quality factor limited by operating frequency
Q_{Fluid}	Quality factor limited by fluid damping
Q_{mat}	Quality factor limited by material properties
Q_{MIF}	Quality factor limited by material internal friction
$Q_{MIF\ coating}$	Quality factor limited by coating material internal friction
$Q_{Surface}$	Quality factor limited by surface loss
Q_{TED}	Quality factor limited by thermoelastic damping
r	Mean radius of ring resonator
R_a	Surface roughness

S	Cross-section area of beam resonator
t	Radial thickness of ring resonator
T	Operating temperature
T_0	Absolute equilibrium temperature
ΔT	Temperature deviation from absolute equillibrium temperature
u	General displacement
u_x	In-plane displacement of support structure in x direction
u_y	In-plane displacement of support structure in y direction
U_n	Vibration displacement of n^{th} mode of beam resonator
v	Linear velocity of resonator element
W_n	Stored vibration energy for n^{th} resonant mode
W_{PML}	Perfectly matched layer (PML) size
ΔW_n	Energy loss per cycle for n^{th} resonant mode
x	Displacement in primary direction
x_d	Amplitude of vibration along resonator drive axis
y	Displacement in secondary direction (Chapter 1)
y	Transverse displacement of beam resonator

Greek Symbols

α	Semi angle of indenter (Chapter 7)
α_{ij}	Components of coefficient of thermal expansion
β_n	Mode constant of n^{th} mode of beam resonator
Γ_n	Shear force at attachment area due to n^{th} mode of beam resonator
δ	Characterized thickness of surface layer
δ_c	Intrinsic viscoelasticity of coating
ε_{ij}	Components of strain
ζ	Damping ratio
ζ_L	Longitudinal wavelength
ζ_T	Transverse wavelength
ζ_x	Damping ratio in primary direction
ζ_y	Damping ratio in secondary direction
ϑ	Poisson's ratio

ϑ_i	Poisson's ratio of indenter
ϑ_s	Poisson's ratio of sample
λ	Lame's parameter
μ	Lame's parameter
ρ	Density
σ_{ij}	Components of stress
τ_r	Decay time constant from ring-down test
τ_ε	Relaxation time for stress to relax exponentially at constant strain
τ_σ	Relaxation time for strain to relax exponentially at constant stress
τ_{th}	Thermal relaxation time
$\tau_{th\text{-}c}$	Thermal relaxation time in circumferential direction of ring resonator
$\tau_{th\text{-}r}$	Thermal relaxation time in radial direction of ring resonator
υ	Wave number
χ_n	Mode shape factor n^{th} mode of beam resonator
ω	Resonant angular eigen frequency
ω_0	Relaxed isothermal resonant angular eigen frequency
ω_n	Resonant angular eigen frequency of n^{th} mode of beam resonator
ω_x	Resonant angular eigen frequency in primary direction
ω_y	Resonant angular eigen frequency in secondary direction
ω_{mech}	Mechanical resonant angular eigen frequency
Ω	Input angular velocity to gyroscope sensing axis

Mathematical Symbols

∇^2	Laplacian operator
∇	Gradient operator
$d(.)$	Differential of a quantity
$\partial(.)$	Partial derivative of a quantity
.	Differentiation with respect to time; for example, $\dot{u} = \frac{du}{dt}$

Chapter 1

Introduction and Literature review

Gyroscope is a device to sense an angular velocity of a rotating frame where the device is mounted (Bose *et al.* [2002]). The invention of conventional gyroscope was inspired by a spinning top. When a top rotates, it preserves its vertical orientation even if the base is tilted. This mechanism was invented in 1852 by physicist Leon Foucault. He used a fast spinning rotor inside gimbals to demonstrate Earth's rotation (Apostolyuk [2016]).

1.1 Types of gyroscopes

Gyroscopes are mainly classified as mechanical and optical types (Passaro *et al.* [2017]). Mechanical gyroscopes are again classified based on working principle such as angular momentum based and Coriolis acceleration based. Angular momentum based gyroscopes are electro-mechanical gyroscopes which use inertial properties of a rotating flywheel. They are further classified as dynamically tuned gyroscope and rate gyroscope. Coriolis vibratory gyroscopes (CVG) use Coriolis acceleration principle for angular velocity measurement (Passaro *et al.* [2017]). Generally, CVG comes in two configurations based on sensing element mass distribution such as tuning fork and vibrating shell. Optical gyroscopes such as ring laser gyroscope (RLG) and fibre optic gyroscope (FOG) are based on Sagnac effect (Bose *et al.* [2002]). Figure 1.1 shows classification of the different types of gyroscopes.

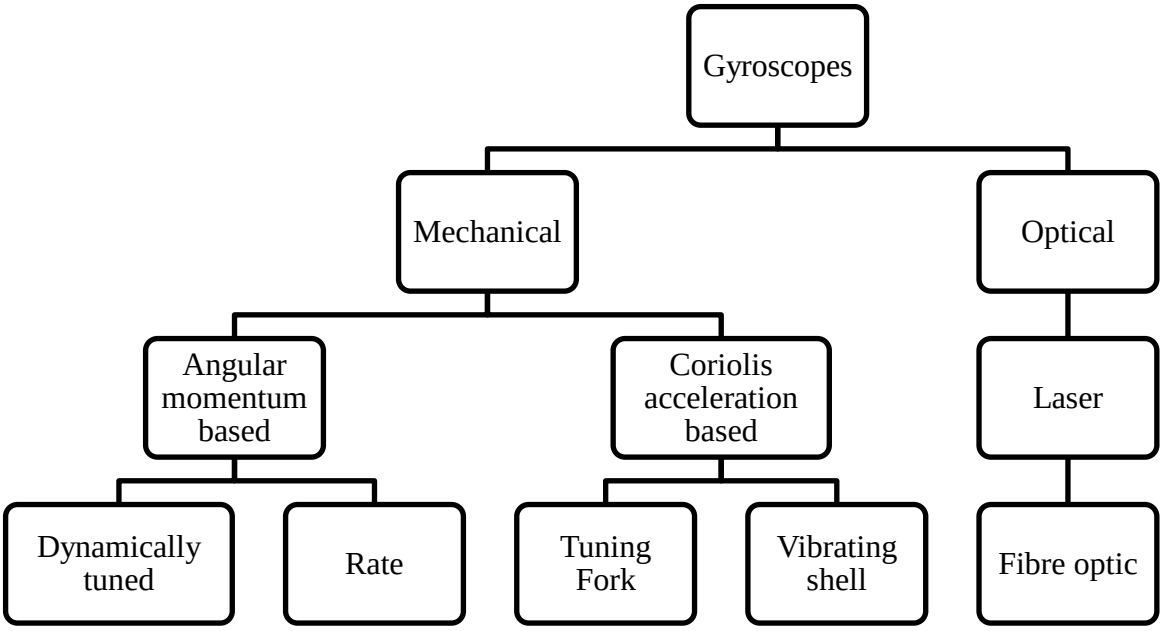

Figure 1.1: Classification of different types of gyroscopes

1.1.1 Optical Gyroscopes

Optical gyroscopes operate by sensing the difference in propagation time between counter propagating beams in a closed or open optical path. A rotation induced change in the path lengths generates a phase difference between the counter propagating light beams. This rotation induced phase difference, which physically consists in the Sagnac effect, is the basic operating principle of all optical gyroscopes. Ring laser gyroscopes and fibre optic gyroscopes, whose features differ in terms of size, mass, power requirements, performance and cost, are the classifications under optical gyroscope technology (Passaro *et al.* [2017]).

1.1.2 Mechanical Gyroscopes

1.1.2.1 Angular momentum based gyroscopes

Angular momentum based mechanical gyroscope essentially consists of a spinning mass that rotates in its axis of rotation. When the mass is rotating on its axis, it tends to remain parallel to itself and oppose any attempt to change its orientation. The spinning mass is mounted on a gimbaled frame which allows rotation along two perpendicular axes. The gimbaled frame of the gyroscope is attached to the vehicle and it is free to rotate. The rotation axis of the spinning mass keeps its angular position during the motion of the vehicle. The basic effect upon which a gyroscope relies is that an isolated spinning mass tends to keep its angular position with respect to an inertial reference frame. When a constant angular velocity is applied to the mass, its rotation axis undergoes a precession motion with a constant output torque, in a direction that is normal to the direction of the constant angular velocity. This is called gyroscopic effect and is used in the measurement of the angular position of a moving vehicle (Passaro *et al.* [2017]). The variation of the absolute angle of the vehicle can be associated to the relative variation of the angle between the rotation axis of the mass and a fixed direction on the frame of the gyroscope. Dynamically tuned rate integrating gyroscopes and rate gyroscopes are the major classifications based on functionality and related construction (Ragan [1984]).

1.1.2.2 Coriolis Vibratory Gyroscope (CVG)

Coriolis vibratory gyroscopes generally use a vibrating mechanical element as a sensing element for detecting the angular velocity. Undesired complexities, which are associated with gimbal bearings in conventional gyroscopes, are avoided in oscillatory motion based CVGs. It also significantly simplifies design of the sensitive element since there are no electrical motors. This allows miniaturization, mass production and cost effective (Jeanroy *et al.* [2014]).

All vibratory gyroscopes are based on transfer of energy between two vibration modes of a structure caused by Coriolis acceleration (Apostolyuk [2016]). Principle of CVG operation is shown in Figure 1.2. A discrete element with mass m is driven to oscillate at one of its resonance vibration mode. This motion is called primary motion and its linear velocity is v. When this mass is rotated about a fixed body axis (out of plane axis in Figure 1.2) with an angular velocity Ω, a Coriolis force is developed which is perpendicular to both v and Ω .

Coriolis force in resonator element F_C for discrete mass CVG is given by:

$$F_C = 2 \times m \times v \times \Omega \tag{1.1}$$

where m is the mass of the resonator element, v is the linear velocity of the resonator element, Ω is the input angular velocity to the gyroscope sensing axis. This Coriolis force causes secondary motion. Two motions are dynamically coupled through the Coriolis effect.

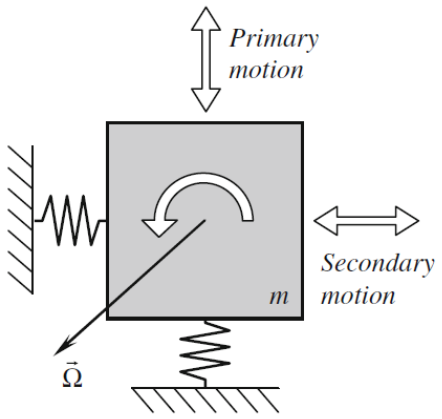

Figure 1.2: Principle of CVG operation (Reproduced with permission from Apostolyuk [2016])

Now, the equations of motion of a point mass broad class of CVGs is discussed. Simplified dynamic equation of motion can be described in non-inertial coordinate frame as (Shkel [2006]):

$$m\ddot{x} = -c_x\dot{x} - k_x x + m\,(\Omega^2 x + 2\Omega\dot{y} + \dot{\Omega}y) + F_x \tag{1.2}$$

$$m\ddot{y} = -c_y\dot{y} - k_y y + m\,(\Omega^2 y - 2\Omega\dot{x} - \dot{\Omega}x) + F_y \tag{1.3}$$

where x is the displacement in primary (drive) direction, y is the displacement in the secondary (sense) direction, c_x and c_y are damping coefficients, k_x and k_y are stiffness coefficients, F_x and F_y are additional externally applied forces to the mass with respect to the reference coordinate system. Gyroscopes are typically designed for detection of small angular velocities and often for the constant rate conditions ($\dot{\Omega} = 0$). Typically, the natural frequencies of gyroscopes are much higher than the measured rotation rates, $\omega_x^2 \gg \Omega^2$ and $\omega_y^2 \gg \Omega^2$. These assumptions allow to ignore the terms with Ω^2 and $\dot{\Omega}$ in the equations of motion. The CVG gyroscope sensitivity can be improved by matching the resonant frequencies of primary and secondary motions. Hence, most gyroscopes are designed for mode matched operation with high sense direction displacement. Thus, the natural frequency of primary motion and the natural frequency of secondary motion are ideally identical ($\omega_x = \omega_y = \omega$). CVGs are also designed to match the damping ratios ($\zeta_x = \zeta_y = \zeta$). Based on these typical considerations, the governing equations of motion can be simplified as:

$$\ddot{x} + \frac{\omega}{Q}\dot{x} + \omega^2 x - 2\Omega\dot{y} = \frac{F_x}{m} \tag{1.4}$$

$$\ddot{y} + \frac{\omega}{Q}\dot{y} + \omega^2 y + 2\Omega\dot{x} = \frac{F_y}{m} \tag{1.5}$$

where Q is called the quality factor ($Q = \frac{1}{2\zeta}$) of the resonator. In reality, there are different types of energy dissipations from the resonator. Quality factor represents the total energy dissipation. Also, there is difference in the two natural frequencies of primary and secondary motions due to realization imperfections. This difference is called frequency split. Hence, Q factor and frequency split are two critical parameters with respect to the sensitivity of the CVG.

An actuation and a sensing mechanism are required for structure to vibrate at its resonance and sense the Coriolis response. The response is proportional to the angular velocity of the frame where the sensor is mounted. CVGs are classified based on the sensing element mass distribution and the number of sensing mass elements as shown in Figure 1.3.

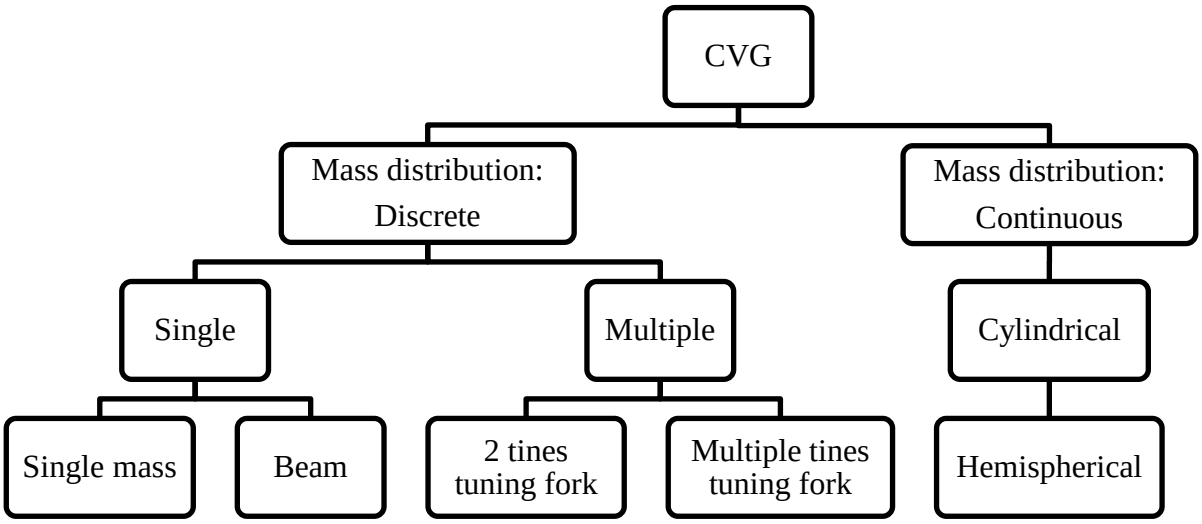

Figure 1.3: Classification of CVGs

1.2 Gyroscope for aerospace and space applications

Gyroscopes are used for measuring orientation of launch vehicle, spacecraft and ballistic missiles as part of inertial navigation in aerospace and space applications (Greenspan [1995]). Inertial navigation is a navigation method that uses a computer, motion sensors (accelerometers) and rotation sensors (gyroscopes) to continuously calculate the position, the orientation and the velocity of a moving object without the need for external references. The most critical parameter for the aerospace and the space application is reliability. The driving parameter for reliability is lesser number of parts necessary to build the sensor. Hence, solid state CVG technology is the state-of-the-art choice for these applications. It can be realized with very few parts compared to other types of mechanical and optical gyroscopes (Rosellini *et al.* [2007]). Typical number of parts required to build different types of gyroscopes is given in Table 1.1

Table 1.1: Typical number of parts of different types of gyroscopes (Xu *et al.* [2011])

Gyro family	Mechanical (Tuned gyroscopes)	Optical (Laser gyroscope)	Optical (Fibre optic gyroscope)	CVG
Number of parts	90-100	50-60	30-40	approx. 5

The major sensor performance parameters are resolution, bias, bias stability, scale factor, scale factor stability, temperature sensitivity, vibration sensitivity and shock sensitivity. Among these, one of the most critical performance parameters is the bias stability since it is difficult to calibrate and compensate. Bias stability is the change of bias over a certain specified period of time. The rate (velocity) output is constantly mathematically integrated to get the orientation (angle). The error is cumulative during mission time. This is very critical for long duration space missions with highly accurate navigation requirements. So, bias stability is the most critical factor in the gyroscope selection process in such applications. Different grades exist mainly based on this performance parameter for different kinds of application as given in Table 1.2.

Table 1.2: Different performance grades (Passaro *et al.* [2017])

Performance parameter	Tactical	Navigation	Strategic
Bias stability (^{o}/hr)	0.1 - 30	0.01-0.10	0.0001-0.01

1.2.1 Hemispherical resonator gyroscope (HRG)

Coriolis vibratory gyroscopes (CVG) are the fastest developing type of gyroscope in inertial navigation systems. Wine glass mode gyroscope is a kind of high performance gyroscope among CVGs. The principle of the wine glass mode gyroscope was first found by Bryan [1890]. The hemispherical resonator gyroscope (HRG), which is a kind of wine glass mode CVG, meets the high end navigation grade performance (Lynch [1984]). HRG shows its superiority in size, very fine resolution, very good accuracy, shock resistance and highly reliable operation life with a smaller number of parts (Xu *et al.* [2011]). Hence, the solid state HRG is the best suitable high end inertial class candidate for critical and high value long duration interplanetary spacecraft missions. Despite its remarkable advantages, HRG demands high precision manufacturing process and is extremely costly (Pan *et al.* [2016]). A typical hemispherical configuration with its two elliptical vibration modes (represented as 1 and 2) is shown in Figure 1.4. This configuration is able to sense the input rate Ω along the symmetrical axis of hemisphere.

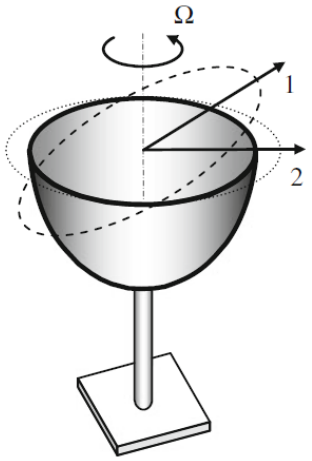

Figure 1.4**:** Typical HRG resonator (Reproduced with permission from Apostolyuk [2016])

1.2.1.1 HRG configuration

The main parts of HRG are hemispherical resonator shell, actuator (drive element) and pickoff (sense element). Typical HRG configuration is shown in Figure 1.5. Resonator is

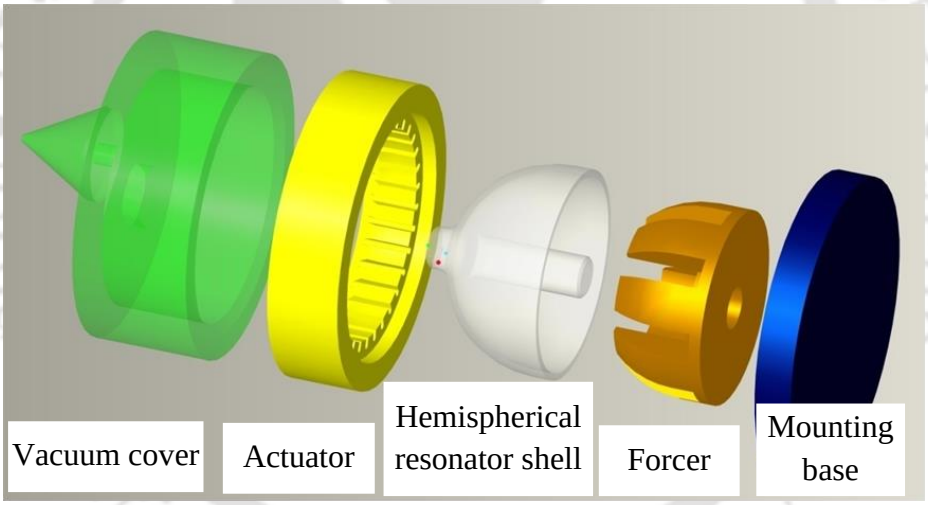

Figure 1.5: Typical HRG configuration

positioned between the actuator and the pickoff, and is driven to flexural resonance by electrostatic forces. Pick off senses the vibration pattern of the resonator and gives sensor output as rotation angle or as angular rate depends on whole-angle or force-to-rebalance mode of operation. It also has a mounting base and a vaccum sealing cover.

1.2.1.2 Working principle

Hemispherical resonator is excited in its $N = 2$ wine glass elliptical mode at its mechanical natural frequency where N is the operating vibration mode number. When an input rate is applied to the HRG along the axis of symmetry of the hemispherical resonator under resonance, a precession of a vibrating pattern (standing wave) around the axis of

rotation occurs due to the action of Coriolis force. The angular rate of the standing wave precession is different from the input rate around the resonator shell symmetry axis, i.e., the standing wave does not totally rotate with the same value as that of input rotation. The difference between both the rotations is perfectly proportional to the input rotation. Thus, this device is able to sense the rotation. Also, a perfect resonator is completely unaffected by input rates applied around any other axis (Fox [1988]).

Now the Coriolis force generation in the operation of HRG is discussed in detail. Figure 1.6 shows the elliptical mode shape, velocity vectors, and input rate induced Coriolis force vectors. The velocity vectors are oriented radially at the antinodes and tangentially at the nodes. When the shell experiences an inertial input angular velocity Ω, which is perpendicular to the plane of pattern along its sensitive axis, Coriolis forces are generated. Coriolis forces are proportional to $v \times \Omega$ along a direction perpendicular to both v and Ω. The resultant of these forces excites another standing wave whose antinode points becomes the node points of the original wave and vice versa. The second standing wave is the degenerate mode of the first elliptical mode.

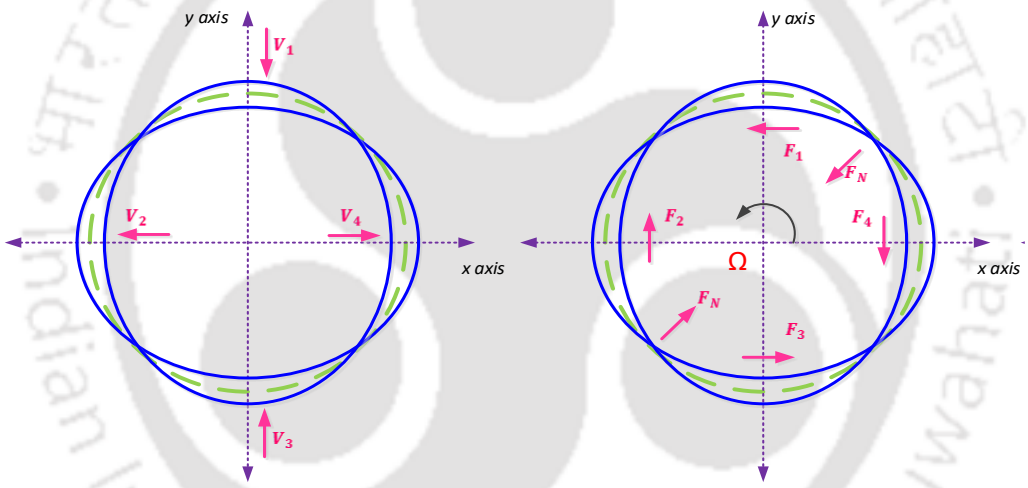

Figure 1.6: Coriolis forces in HRG resonator

The superposition of these two standing waves forms another resultant wave. The effective amount of coupling between two degenerate modes is defined by a parameter called angular gain A_g. The angular rate of the resultant standing wave precession is different from the input rate. In the presence of rotation, standing wave precesses against the inertial angle by this angular gain. Angular gain is a proportionality constant by which the precession of the standing wave is proportional to the inertial rotation and in reverse direction as shown in Figure 1.7. Thus, A_g is also called as the scale factor of a rate integrating gyroscope (Cho and Najafi [2015]). The angular gain depends only on geometry and mode shape but not on the absolute size. The value of A_g of hemisphere is 0.27 and is a stable value (Fan *et al.* [1992]).

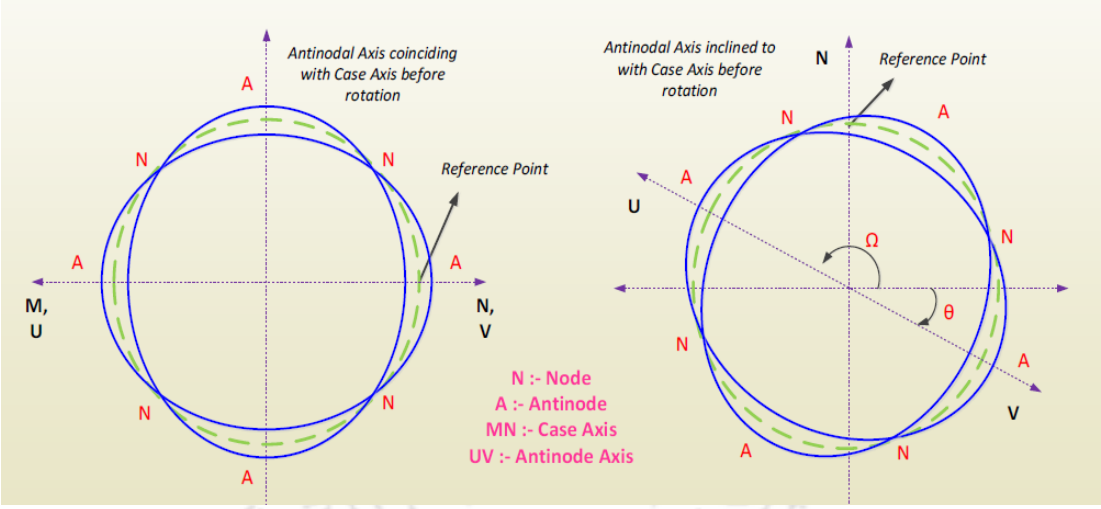

Figure 1.7: Schematic of precession in HRG

The Coriolis force given in equation (1.1) is for single discrete mass resonator configurations. However, this equation is modified for continuous mass resonator configurations which are working in a particular mode number.

Coriolis force in resonator element F_C for continuous mass HRG type CVG is given by:

$$F_C = 2 \times N \times A_g \times m_{eff} \times v \times \Omega \tag{1.6}$$

where N is the operating vibration mode number of HRG resonator, A_g is the angular gain, m_{eff} is the effective mass participating in the N^{th} mode of vibration. Unlike in lumped single mass discrete resonator, the whole mass of the resonator will not participate in the vibration mode displacement in continuous mass resonator configuration. Hence, the effective mass is a portion of the total mass of the resonator. Equation (1.6) is applicable for continuous mass configuration HRG which works in $N = 2$ elliptical mode. For lumped single mass discrete resonator, effective mass is equal to the total mass of the resonator element. Since there is full coupling between the primary drive motion and the Coriolis force induced secondary motion in lumped mass configuration, angular gain is equal to one.

1.2.2 Quality factor (*Q* factor)

The performance of a CVG resonator is measured by the critical parameter, the Quality factor (*Q* factor), as mentioned in section 1.1.2.2. *Q* factor is the ratio of the amount of energy stored in the vibrating resonator to the amount of energy dissipated by the resonator in one cycle (Tilmans *et al.* [1992]). The energy dissipation is through different damping mechanisms in different proportions to the total damping. The *Q* factor of the CVG resonator determines the sensor's resolution and scale factor as discussed below.

1.2.2.1 Resolution

Miniature small-signal high performance sensors are attractive for many space-limited applications. However, proof mass or resonator in these sensors are susceptible to mechanical

noise resulting from molecular agitation. This mechanical-thermal noise is not a new concept but its effects are frequently rediscovered when a sensor technology is pushed to the limit of its sensitivity. This mechanical-thermal noise is often one of the limiting noise components for the high performnce sensors designed for small-signal applications (Gabrielson [1993]). Signal to noise ratio (SNR) is one of the key parameters for designing high resolution sensors. For many MEMS grade performance gyroscopes today, mechanical noise is not dominant compared to the electrical noise. However, the mechanical and the electrical noise should be equally considered for gyroscopes which are intended for high end inertial grade performance. The overall noise floor of the gyroscope is determined by the mechanical noise floor and the electronic noise floor. Therefore, it is desired to design gyroscopes more sensitive to input rotation and have lower noise floor.

The resonating gyroscopes, including wine glass mode gyroscopes, are based on the energy transfer by a rotation based Coriolis force as explained earlier. Since the Coriolis force acting on a resonator is generally very small, the output signal generated by the Coriolis force is so weak that it is always overwhelmed by the noise. One of the important performance parameters of CVG is its resolution. The resolution of a gyroscope is the minimum input angular velocity that can be distinguished from the noise floor of the sensor per square root of bandwidth of measurement. It is expressed in units of ^{o}/h/√Hz. The overall resolution of the gyroscope (total noise equivalent rotation (TNER) is determined by two uncorrelated components: the mechanical noise equivalent rotation (MNER) and the electronic noise equivalent rotation (ENER) and is given by (Zhou *et al.* [2017], Ayazi and Najafi [2001]):

$$\text{TNER} = \sqrt{\text{MNER}^2 + \text{ENER}^2} \tag{1.7}$$

The mechanism of the mechanical noise is the Brownian motion which is caused by the molecular collisions. Random thermal agitation from the environment affects the oscillator's motion. This is the essence of the fluctuation-dissipation theorem (Gabrielson [1993]). By equating the displacement caused by Brownian motion to the displacement induced by Coriolis force, the mechanical resolution of a CVG is derived and is given by (Choudhary and Iniewski [2013], Wang *et al.* [2014]):

$$\text{MNER} = \frac{1}{N A_g x_d} \sqrt{\frac{k_b T}{\omega m_{eff} Q_{Eff}}} \sqrt{\text{BW}} \tag{1.8}$$

where x_d is the amplitude of vibration along the resonator drive axis, k_b is the Boltzmann constant, T is the operating temperature, ω is the resonant angular eigen frequency, m_{eff} is the effective mass participating in the N^{th} mode of vibration, Q_{Eff} is the effective quality factor of different damping mechanisms applicable to the resonator and BW is the bandwidth of measurement.

From the equation (1.8), it is clear that MNER can be reduced by increasing the angular gain, input drive axis amplitude, increasing the frequency, increasing the Q factor and increasing the effective mass and lowering the operating temperature. Increasing the mass

results against the miniaturisation and also lowers the frequency. Also, lowering operating temperature puts limitation on sensor applications. Hence, the primary choice is to maximise the Q_{Eff} of the resonator followed by effective mass and angular gain. Whenever a high sensitivity sensor is being designed, an analysis of sources of mechanical-thermal noise should be included in the early stage to avoid issues with an unacceptably high noise floor at testing stage. Thus, ultra-high Q_{Eff} is required to achieve a very low mechanical noise equivalent rate for a gyroscope to achieve the smallest possible resolution limit. The ENER of the CVG is given by (Choudhary and Iniewski [2013]):

$$\text{ENER} = \frac{\Delta C_{min}}{\text{Capacitance sensitivity}} \tag{1.9}$$

where ΔC_{min} is the minimum detectable capacitance of the sense electronics.

Since the resolution of sensor depends on mechanical and electronics noise contributions, system level device noise estimation of TNER and characterization are essential before deployment in application. The present work discusses the MNER part of TNER for the mechanical resonator of HRG.

1.2.2.2 Scale factor

The scale factor of a CVG is the ratio of a change in output (generally read out in electrical unit - volts) to a change in input angular velocity (deg/sec). In a CVG, the sense mode deflections are proportional to both the effective quality factor and drive amplitude. Increasing sense mode deflections, while maintaining a high aspect ratio for the sensing capacitive gaps, results in large changes in the sense capacitance. This generates a larger electrical pick-off signal for a given input angular velocity. Therefore, high effective quality factor, large drive amplitude and a high sense capacitance contribute to a high scale factor.

From the above discussions, it is understood that Q_{Eff} is the critical parameter for improving the performance of the sensor in terms of its resolution and scale factor. Hence, ultra-high Q_{Eff} is required for the hemispherical resonator in HRG. Q_{Eff} of the HRG can be achieved in the order of millions, which is one of the reasons why HRG is the only kind of CVG that has achieved high end navigation grade performance (Izmailov *et al.* [1999]). Northrop Grumman Corporation, USA has developed space proven HRG with millions of quality factor mechanical resonator (Rozelle [2009]). However, specific design details for low damping and individual contributions of different damping mechanisms associated with the resonator are not available in open domain except the final senor performance parameters. Hence, studying the different energy loss mechanisms in HRG resonator is very critical for achieving ultra-high Q_{Eff} for realizing a high end performance sensor. The following section covers different damping mechanisms which affect the effective quality factor of the mechanical resonator.

1.3 Damping mechanisms

In order to achieve ultra high Q_{Eff}, the energy loss from the vibrating resonator structure should be kept as minimum as possible. The general damping mechanisms are thermoelastic damping (TED), anchor (support) loss, surface loss, material internal friction, fluid damping and electronics damping (Joshi *et al.* [2014], Imboden and Mohanty [2014]). The effects of these damping mechanisms can be reduced by proper design, material selection, precise fabrication and post fabrication treatments and operating conditions.

Q factor is defined for each individual energy loss mechanisms such as TED, anchor loss, surface loss, material internal friction, fluid damping and electronics damping. Since these different kinds of damping mechanisms are simultaneously present in the sensor, the effective *Q* factor (Q_{Eff}) can be expressed as (Imboden and Mohanty [2014]):

$$\frac{1}{Q_{Eff}} = \frac{1}{Q_{TED}} + \frac{1}{Q_{Anchor}} + \frac{1}{Q_{Surface}} + \frac{1}{Q_{MIF}} + \frac{1}{Q_{Fluid}} + \frac{1}{Q_{Electronics}} \tag{1.10}$$

It is very difficult to separate individual contributions during the hardware evaluation. Hence, it is mandatory that the design of the sensor resonator should be done to minimize all possible kinds of dissipation mechanisms. Also, it is to be ensured that the design requirements are met during realization. Next, individual damping mechanisms are discussed in detail.

1.3.1 Thermo elastic damping (TED)

In accordance with the Thomson effect (Thomson [1853]), when a thermoelastic solid is subjected to a tensile stress, it cools. Similarly, when a homogeneous material is subjected to an inhomogeneous stress field or when a heterogeneous material is subjected to any stress field (homogeneous or inhomogeneous), different parts of the material undergo different temperature changes. As a result, irreversible heat conduction occurs and entropy is produced. The entropy produced is a measure of the amount of work converted into heat i.e., mechanical damping. The theory is quite general and can be used to predict damping either due to the application of an inhomogeneous stress field to a homogeneous body or due to the application of a homogeneous (or inhomogeneous) stress field to a heterogeneous material.

Now the physics of the vibration induced thermal currents and the energy dissipation is explained in more detail. Consider the flow of heat to and from an idealized region (uniform temperature with infinite thermal conductivity) in a specimen which is undergoing vibration. Heat is generated due to mechanical strain rate during vibration. If the region is thermally insulated, its temperature would undergo periodic fluctuations. Since there is no flow of heat, the entropy remains unaltered. On the other hand, if it were connected by a perfect thermal conductor (infinite conductivity) to a heat reservoir, vibration would be accompanied by a flow of heat back and forth between the region and the reservoir. Again,

the entropy remains unaltered, since the flow of heat is between regions with the same temperature due to perfect thermal conductor.

Now consider that the region is connected to the heat reservoir by a wall with a finite thermal conductivity. Such a wall introduces a finite time of relaxation for the establishment of temperature equilibrium. Any temperature difference between the idealized region and the heat reservoir would decay. This thermoelastic coupling is operative only when the stresses in the vibrating solid are inhomogeneous. Periodic changes in stresses during vibration causes periodic changes in temperature. If the stresses are not uniform, the temperature will likewise not be uniform. Hence, the thermal and the mechanical strains are not in phase. Gradients in temperature give rise to heat currents. But this irreversible heat current across the temperature gradient of the wall is necessarily associated with an increase in the entropy of the system. If the entropy of a freely vibrating solid is increasing, its internal energy must be increasing at the expense of its mechanical energy. This causes energy dissipation. As this energy dissipation mechanism involves the interaction of thermal and elastic domains, it is called thermo elastic damping (TED). But, Bishop and Kinra [1997] used elastothermodynamic damping terminology for this damping mechanism. However, it is more popularly known as thermoelastic damping (TED).

Zener [1937] studied various causes of thermoelastic induced internal friction in solids for the first time. This study is considered as the fundamental study in thermoelastic damping. He used the term ‘internal friction’ which refers to the capacity of a solid to convert its mechanical energy of vibration into internal energy. The theory developed was based on extension of Hooke’s law involving stress, strain as well as their first time derivatives. This model is also called ‘standard anelastic solid’ model. He calculated thermal relaxation time associated with different transverse modes for a thin beam flexure. It was found that approximately 98.6% of relaxation occurs through the first vibration mode for rectangular beams. Approximation of having single relaxation time for geometry of a rectangular beam is fairly good. It was found that the damping due to this thermoelastic effect is of a larger order of magnitude than that due to all other causes over a wide frequency band in mechanical resonators.

Zener [1937] also arrived at the general guideline for minimising this thermoelastic loss and found that it exhibits a Lorentzian behavior as a function of $\omega\tau$ with maximum dissipation occurs when $\omega\tau = 1$ where ω is the angular resonant frequency and τ is the thermal time constant related to relaxation rate. Dissipation peak is called Debye peak. When frequency is much smaller compared to relaxation rate i.e., $\omega\tau << 1$, dissipation is less and oscillations are isothermal. When frequency is much larger compared to relaxation rate i.e., $\omega\tau >> 1$, dissipation is less and oscillations are adiabatic. He demonstrated the presence of TED through experimental work and calculated relaxation strengths for different materials using isothermal and adiabatic Young’s modulus.

In an extension of the earlier work, Zener *et al.* [1938] provided more generalized analysis for transverse vibrations. Explicit formulae were obtained for reeds and wires. Microscopic stress inhomogeneities arise from imperfections such as cavities, elastic

anisotropy of individual crystallites mixture of phases and random crystal orientations was considered. Two experimental methods, which are used to measure such dissipation mechanism, were also mentioned. In the first method, the ring-down time, which is the time taken for the vibration amplitude to reach $(1/e)^{th}$ of the original amplitude, is determined. This is called logarithmic decrement method. In the second method, dissipation is measured using full width at half maximum (FWHM) of a response plot.

Transverse vibration of metal rods was again used by Berry [1955] for his dissipation investigations. Measurements were made at room temperature and estimation was done by free decay logarithmic decrement method. Mechanical and thermal properties like Young's modulus, thermal expansion coefficient, density, heat capacity and thermal conductivity were measured. The frequency dependence of damping mechanism in four brass reeds was measured. By using specimans of different thickness, frequencies differing from the frequency of peak damping (Debye peak) to nearly a factor of 20 were obtained. He very well established the Zener's theory of thermoelastic damping. Now the thermoelastic damping in mechanical resonators of different geometries are discussed.

1.3.1.1 TED in beam resonators

Extensive research activities started in the area of micro mechanical resonators towards the end of 19^{th} century to meet the emerging applications. Micromechanical cantilevers are commonly used for detection of small forces in microelectromechanical sensors such as micro accelerometers and gyroscopes and in high end scientific instruments such as atomic force microscopes. A fundamental limit to the detection of small forces is imposed by thermomechanical noise as explained earlier. Hence, it is very critical to understand the dissipation mechanism in cantilever structures when they are used as resonators in their application domain.

Single crystal silicon resonators in the form of flexural beams are very common in many micro mechanical applications. Roszhart [1990] did theoretical analysis of thermoelastic damping of flexural beams and compared with the experimental measurements. It was found that the thermoelastic damping is the fundamental damping mechanism that can determine the quality of high Q resonators over a range of operating conditions. Single crystal silicon beams were tested under vacuum condition over a range of frequencies from 80 kHz to 1.6 MHz and temperatures from 300 K to 400 K. Measured values of Q factor varied from 10^4 to more than 7×10^4. The damping dependence on material and geometry was studied by Yasumura *et al.* [2000] using measurements on micro-cantilevers made out of silicon and silicon nitride. It was proved that the TED is not critical for submicron level, but significant in micron level sizes. A monotonic reduction in Q factor was seen with decreasing thickness for both silicon nitride and single crystal silicon cantilevers which showed the dominance of other damping mechanism like surface loss in submicron level.

Micrometer and nanometer scale electro-mechanical systems (MEMS and NEMS) of 20^{th} century demand even higher Q factor mechanical resonators. In the light of this, detailed studies of thermoelastic damping were carried out by many researchers for small scale

mechanical resonators. Lifshitz and Roukes [2000] work is one among the most referred detailed study for mechanical resonators. They derived exact expression for thin rectangular beams where transverse temperature profile is more accurately modelled. The Zener theory was improved by using beam theory. Zener [1938] approximated transverse tempertaure profile as sinusoidal. However, the temperature profile is derived in Lifshitz and Roukes model (LR model). Coupled thermo-elastic equations were generated and solved for the case of harmonic vibrations. The temperature profile in the beam was computed explicitly without expanding it in terms of the thermal eigenmodes. The major conclusion was that the peak value of thermoelastic damping is independent of the dimensions of the beam. It only depends on temperature through the thermodynamic properties like Young's modulus, coefficient of thermal expansion and thermal capacity of the material. They calculated frequency shift due to TED in the entire range from isothermal to adiabatic. De and Aluru [2006] compared Zener and LR model and found that Zener's well known approximation with single thermal relaxation time slightly deviates from the exact expression. As a result, the LR model is shown to be more accurate than the Zener model for predicting the quality factor in rectangular beams undergoing simple harmonic vibrations in the flexural mode. However, both models can be used only for isotropic flexural beams.

The maximum damping values of gallium arsenide (GaAs) and silicon, which are typical materials used in the fabrication of MEMS and NEMS, were arrived as a function of resonator size and temperature by Lifshitz and Roukes [2000]. They showed that TED is a significant source of dissipation at temperatures around 100 K and above. The reason is that as the beam becomes smaller its eigenfrequency increases and thermal relaxation time decreases. The product of the two remain near unity which results in high dissipation.

The effect of different support and thermal boundary conditions on the *Q* factor was studied by Sun *et al.* [2006]. As explained earlier, their study also has seen that the TED increases as the resonator size decreases from macro to micro. Beams in smaller size experience larger volume change and higher temperature gradient for the same initial displacement which leads to more energy dissipation. Thermoelastic coupling generally shifts the vibration frequency and this effect increases as the size of the beam decreases. The vibration frequency is analyzed for three boundary conditions i.e., clamped and isothermal, simply supported and isothermal, and simply supported and adiabatic. Guo and Rogerson [2003] also studied the thermoelastic coupling in a doubly clamped beam and examined its size dependence. Houston *et al.* [2004] indicated that the internal friction arising from TED mechanism is strong and persists down to 500 A^o size structures from the studies on silicon based MEMS structures. Candler *et al.* [2003] carried out investigation of energy loss on doubly clamped tuning forks. It was found that support loss was seen to limit when the length to width ratio was less than approximately 10. However, TED was the limiting loss mechanism for the functionaly useable resonator configuration.

Different approaches were studied for modelling the thermal profile by researchers. One such different approach was that of using a finite element formulation by Yi and Matin [2007]. In their approach, a perturbation of the temperature field was explicitly applied to the governing equations associated with heat transfer, thermoelasticity and structural vibration.

The finite element method was then applied to obtain an approximate solution to the eigenvalue equation. The finite element formulation presented in this work has advantages over the analytical approaches because the method can be easily extended to general geometries and boundary conditions without extensive computations associated with the numerical iterations. Parametric studies on a variety of geometries and material properties demonstrated their effects on the frequency and the quality factor. The same formulation can also be extended to 3D geometries and nonuniform boundary conditions where analytical solutions are extremely difficult to obtain.

As the fully coupled TED equations are difficult to solve for 2D and 3D, Rajagopalan and Saif [2007] presented a single degree of freedom (SDOF) model that explores the possibility of estimating thermoelastic damping in a vibrating body by the use its geometry and material properties without solving the heat equation. The model incorporated the notion of 'modal temperatures' similar to modal displacements and modal frequencies. However, the characteristic length, which is a parameter that determines the heat transfer, shall be experimentally generated for complex geometries. Since the strain field and its rate of change can be captured using a modal displacement and the corresponding modal frequency, it might be possible to find a modal temperature that describes the temperature field in the body. The procedure was implemented for the specific case of a rectangular cantilever beam vibrating in its first mode. Good qualitative agreement between the predictions and Zener's approximation suggests that their modelling approach captures the essence of thermoelastic damping in vibrating bodies.

Prabhakar and Vengallatore [2008] mentioned that Zener model is not able to capture the effects of beam geometry, mode shapes or the boundary conditions. The differences between the 2D and 1D theories are governed by two primary and counteracting factors. The first is the additional damping due to axial heat conduction which leads the 2D model to predict a higher value of TED compared with the 1D model. The second factor is the difference in the temperature fields. A Green's function method was used to solve the 2D heat conduction equation and an expression for TED was derived in the form of an infinite series. The effects of beam geometry, aspect ratio, natural frequency, flexural mode shapes and structural boundary conditions were investigated for single crystal silicon microbeam resonators. The errors in the exact 1D theory range from 2% to 80% depending upon the aspect ratio and the mode shape. In contrast, the 2D model accounts for all these factors but also requires significant effort to compute the infinite series. Therefore, there is a tradeoff between the accuracy and the computational cost during different stages of MEMS design. This suggests that the Zener and LR models can be used in preliminary design to evaluate multiple structural options rapidly and the 2D model can be used for the accurate computation of TED in a few structures during the final stages of design. The effect of structural boundary conditions was also studied by Prabhakar *et al.* [2009].

Entropy generation based estimation of thermoelastic damping was also attempted by many researchers for accurate prediction especially in more complex 3D geometries. Kinra and Milligan [1994] took the second law of thermodynamics as a starting point and developed a general theory for calculating the thermoelastic damping in composite Bernoulli-

Euler beam under flexural vibrations from the entropy produced. Chandorkar *et al.* [2009] did TED formulation based on entropy generation that accounts for 3D heat transfer which is essential for less aspect ratio. It was emphasised that the length direction heat transfer needs to be considered for aspect ratio less than 20. Considering the fact that multiple thermal modes (decay time constant) add to the damping of a single mechanical resonance (strain), spatial overlap of thermal modes with the strain profile in the mechanical mode of interest was used for damping estimation. The *Q* factor is expressed as a weighted sum of Zener's formula. Multimode entropy generation approach was also used by Ghaffari and Kenny [2012]. Duwel *et al.* [2006] used eigenvalues and eigenvectors of the uncoupled thermal and mechanical dynamic equations to calculate damping. In addition, the frequency separation between relevant thermal modes and the mechanical resonance frequency was considered. The method was numerically implemented using finite element tool [COMSOL].

Effort was taken to reduce the TED of resonator using machined slots into flexural beams by Candler *et al.* [2006]. Novel slot geometries at specific regions of high strain were utilized to improve *Q* factor by reducing the thermo-mechanical coupling. This enabled tuning of the quality factor by structure design without the need to scale up its size keeping the miniaturization aspect intact. Similar trimming approach is reported in Darvishian *et al.* [2017] to improve the *Q* factor using slots along the rim.

The nonlinear nature of the electrostatic force can give rise to complex nonlinear oscillations in the MEMS device which can significantly alter the nature of thermoelastic damping from the prediction by the classical theories of TED. The electrostatic force is generated by applying a potential difference which is a combination of a DC and an AC voltage between the beam microstructure and the ground plane in the MEMS device. De and Aluru [2006] modified the classical theory of thermoelastic damping under arbitrary electrostatic actuation. The nonlinearity due to the drive voltage of the electrostatic force is found to affect the thermoelastic *Q* factor even at small voltages far from pull-in voltage. At larger voltages, which are closer to the pull-in voltage, the nonlinearity due to the sensing electrostatic force is found to affect *Q* factor. Microplate resonator configurations are used in various MEMS devices such as micro pumps and pressure sensors. Nayfeh and Younis [2004] presented a model and derived analytical expression for the quality factors of micro plates of general shapes for different modes and boundary conditions.

1.3.1.2 TED in ring resonators

The in-plane vibration of the circular ring is very relevant to the CVG type gyroscope resonator sensing element. It uses in-plane vibration modes to generate the Coriolis force. The use of silicon ring resonators are common in such devices. Zener's theory can be applied to the thin circular rings for arriving a simple expression for the *Q* factor associated with in-plane flexural modes of vibration.

Wong *et al.* [2004] approached the problem of ring resonators by considering the beam depth as radial thickness of the ring. It is mentioned that LR model is more accurate than the Zener model when the ring is thicker. They proved that a high *Q* factor is possible

with two design configurations viz. large radius with small width and small radius with large width. In the first case, the natural frequency of the ring is well below the frequency at which maximum dissipation occurs. Conversely, in the second case, the natural frequency of the ring is relatively high and is well above the frequency at which maximum dissipation occurs. Thus, the dimensions shall be chosen to achieve high *Q* factor. The effect of temperature on the *Q* factor was also studied as the sensors are often required to be operated over a wide temperature range. The theoretical predictions were shown to be in good agreement with the experimental measurements in a practically relevant range of ring sizes. In the extended work in this topic, Wong *et al.* [2006] made comparison between LR model and Zener model for higher modes other than the elliptical degenerate N = 2 mode. Sensitivity study of dimensions was also carried out for higher modes.

1.3.1.3 TED in coated resonators

Microresonators are typically coated with a metal to act as an electrode for electrostatic actuation and sensing. The design choices are the choice of metal (typically Al, Cu, Ag and Au) and the thickness of metallic coating. Such structures are widely employed in MEMS such as gold coated silicon microcantilevers of scanning force microscopy, aluminum coated electrostatically actuated SiC microresonators.

Prabhakar and Vengallatore [2007] presented an exact theory to compute the frequency dependence of thermoelastic damping in asymmetric, bilayered, micromechanical beam resonators. They computed thermoelastic damping in multilayer Al-SiC, Cu-SiC, Ag-SiC and Au-SiC resonators and made comparison with previously measured damping of gold coated microcantilevers reported in Sandberg *et al.* [2005]. Trilayered symmetric circular plate was studied by Sun *et al.* [2014] for the out of plane vibration. Based on the classical laminated plate theory assumptions, the governing equations of the coupled thermoelastic problem were established. The analytical expression was obtained and the accuracy was verified through comparison with finite element analysis using multiphysics software tool [COMSOL]. In this study, the ratio of base to layer thickness was approximately 20. Two cases of Au-Si-Au and Ag-Si-Ag coatings were studied.

Proper selection of coating material in multilayer coating can be used to inhibit the TED. An important characteristic of micromechanical resonators is the linear temperature coefficient of frequency (TCF) that needs to be minimized for frequency stability over temperature. The temperature dependence of the Young's modulus is the main cause of the linear TCF in MEMS. One technique for temperature compensation of MEMS resonators is through the addition of thin films of other materials. Typically, the base resonator is coated with a layer of a material with opposing temperature coefficient of Young's modulus (TCE). A convenient compensator for Si resonators is SiO_2 because SiO_2 features a positive TCE. Ghaffari and Kenny [2012] computed TED in 2D composite SiO_2 coated silicon flexural resonators. It was reported that the TED also got reduced in the presence of a thin silicon dioxide film.

Bishop and Kinra [1997] suggested that TED mechanism can be used for response control in composite structures during vibration. As the damping is due to thermal currents within the structure, there is no loss of stiffness or strength of the structure. Moreover, damping is linear, i.e., it is independent of the stress amplitude. Also, it can be tailored in a manner analogous to that used currently for tailoring stiffness, strength and coefficient of thermal expansion. Analytical and numerical results were presented for a symmetric three-layer plate in biaxial bending.

1.3.1.4 TED in gyroscope resonators

Now TED in gyroscope resonators of different configurations are discussed including the planar and the 3D configurations. Duwel *et al.* [2003] measured *Q* factor of tuning fork MEMS gyroscope resonators made out of different semiconductor materials and established the operation away from the Debye peak by altering materials and structural geometries. The effect of the material properties on TED was studied using SiGe alloy as the base material. It was found that percentage of Ge changes the *Q* factor. Best fit values of other damping mechanisms were used to match the predictions with the measured *Q* values. This planar structure resonator could reach a *Q* factor of the order of 10^4. The topology of a 3D axisymmetric shell mounted on a stem minimizes unwanted coupling to the base substrate and improves *Q* factor. With the use of high purity fused silica material, reasonably higher *Q* factor operation is possible to meet medium class micro scale gyroscopes. These characteristics have spurred recent interest in the development of microscale HRGs that can be mass manufactured in a wafer scale level and to achieve low-cost sensors with a small volume and reasonably high dynamic range.

The study of hemispherical configuration for gyroscope resonator application was started by Hwang [1966] with vibration experiments to excite axisymmetrical and asymmetrical modes. Finite element equation for the hemispherical shell and prediction of resonant frequencies under different boundary conditions is reported in Fan *et al.* [1991]. Thermoelastic damping effect on the silicon hemispherical shells was investigated using Rayleigh energy method by Choi *et al.* [2009] under the assumptions of inextensional bending and thermal expansion in circumferential direction. Effects of mode numbers, radii and radial thicknesses on the natural frequencies and *Q* factor were analyzed. The regions for larger *Q* factor were similar to that obtained by Wong *et al.* [2006]. *Q* factor of hemispherical shell is larger for most of the size regions when compare to circular ring.

Chan *et al.* [2011] used 1 mm diameter thin diamond axisymmetric hemispherical shell resonator for study. Resonators were fabricated through a combination of electro discharge machining and silicon micromachining techniques. By using piezoelectric actuation and Laser Doppler Vibrometer (LDV) optical characterization, two degenerate elliptical wineglass modes were observed with frequency split of 2% of nominal N = 2 frequency. The experimental results were compared with the numerical result obtained using finite element tool [COMSOL].

Darvishian *et al.* [2014] simulated thermoelastic loss in the wineglass mode of birdbath configuration shell resonators of MEMS class gyro. It was shown that resonator material properties and conductive thin film have a remarkable effect on the *Q* factor. Even a thin gold film reduces thermal resistance between hot and cold regions of the resonator and increases coupling between the thermal and the mechanical domains. It was also shown that as temperature increases, the *Q* factor reduces. As an extension of this work, Darvishian *et al.* [2017] studied the effects of shell geometry, edge chipping around the shell rim and thin film coatings. Edge chipping and most of the shell geometrical parameters other than rim thickness do not have large impact. In addition to bulk material TED, Sorenson *et al.* [2015] investigated surface TED due to asperities of a micro hemispherical shell resonator. They relaxed Rayleigh's inextensional assumption to evaluate bulk TED by undulating deviations of the neutral surface away from the shell's mid surface. An analytical model was developed to evaluate surface TED from the surface asperities and the resulting volumetric strain concentrations.

1.3.2 Anchor (support) loss

The resonators need to be physically anchored to the mounting substrate. Unlike free-free beam vibrating in space, this anchor can also provide a pathway for energy loss from the resonator to the support. All loss mechanisms that refer to energy propagation through the anchor are classified as anchor loss. This is another major source of energy loss in resonators. When the resonator is operating in its functional mode of vibration, it applies harmonic forces and moments at the attachment point of the resonator to its support substrate and generates elastic waves in the substrate. This radiation of elastic (stress) waves in the substrate causes mechanical energy dissipation from the resonator and this dissipation mechanism is called anchor (support) loss (Jimbo and Itao [1968]). Anchor loss can be reduced by proper selection of sensitive design parameters such as highly symmetric structure configuration, proper anchoring, dimensions, modes and frequencies. In order to reduce anchor loss, resonators should be designed with their anchors at the nodal points of the vibration modes where the displacement of a certain mode is zero.

1.3.2.1 Closed form solutions in beam and disk structures

One of the first models for anchor loss was developed by Jimbo and Itao in 1968 for an isotropic, homogeneous, linear elastic cantilever which is attached to a semi-infinite elastic medium. They derived an expression for the energy loss from a cantilever resonator into a semi-infinite elastic medium by comparing the vibration energy of the cantilever with the elastic energy generated in the elastic medium. However, detailed anchor loss estimation procedure for a beam structure was provided by Hao *et al*. [2003]. In this model, the flexural vibration of a beam resonator is described using the beam theory. An elastic wave is excited in the support structure from the beam resonator. The decoupling between the resonant modes of a beam resonator and the elastic wave modes in its support is done with the assumption that the beam thickness is much smaller than the transverse elastic wavelength. Hence, the energy transmission from the beam to the support is treated as perturbation. The support loss due to the vibrating moment has been theoretically proved to be negligible compared to that

incurred by the vibrating shear force. Anchor loss due to moment is negligible compared to shear as the radiation efficiency of the normal force is reduced since two halves of radiation source cancel each other. Thus, only the anchor loss is formulated as the integral of the product of the shear force and its corresponding displacement in the support over one period. The shear force at the beam anchor point is evaluated based on the beam equation of resonant motion. This acts as the source of elastic waves in the support structure and the wave propagating in the support is described through the 2D elastic wave theory. It is generally assumed that all the vibration energy of a beam resonator that enters its support propagates away to large distances so that no energy is returned to the beam resonator. Thus, closed form solution for anchor loss for beam structure is obtained.

Yang *et al*. [2000] carried out experiments to understand the mechanical behavior of ultrathin cantilever for different sensing functions which requires high sensitivity. It was concluded that shorter cantilevers have lower *Q* factor than longer ones due to more anchor loss. Cross and Lifshitz [2001] considered the elastic wave transmission across the junction between two plates of same thickness with different widths and calculated the associated energy loss. Photiadis and Judge [2004] extended the highly idealized scenarios in the estimation of anchor loss like the cases where the width of the cantilever is small relative to a wavelength to general scenarios. These extensions result in significant improvement in the estimates of anchor loss by obtaining simple formulas covering most of the geometrical parameter range.

Closed form solution for anchor loss of beams under flexural vibration for two boundary conditions like clamped-clamped and clamped-free was obtained by Hao *et al*. [2003]. It was found that the quality factor is proportional to the cubic power of the ratio of the beam length to the beam width. The quality factor is independent of the Young's modulus of the resonator material but it depends on ratio of Young's modulus of the resonator and the support substrate. The model suggested lower support quality factor for higher order resonant modes compared to the fundamental mode of a beam resonator. TED and surface loss were also discussed and quantified in their study. Since it was very difficult to characterize the values of thickness and Young's modulus of dissipative surface layer, the best-fit values were chosen to minimize the error between the model and the experimental data. An experimental verification of this analytical methodology was attempted in Hao and Ayazi [2005].

Hao and Ayazi [2007] presented a comprehensive closed form solution of the support loss in center-supported micromechanical disk resonators which operate in radial bulk modes. Strong dependence on the material properties suggests high strength materials for the disk and the substrate while low strength materials for the support beam (anchor stem) for low anchor loss. It also depends strongly on the ratio of the support beam radius to the disk radius. Support loss increases with the mode orders because the support beam of the same radius has more interference with the higher-order modes. A coefficient was introduced in the closed form solution to take into account for the errors caused by neglecting the interactions of individual elements of the resonator like disk, support beam and support structure in the analytical solution, and for the non-ideal support structure. Best fit value was determined for

this coefficient from the experiments to match the model prediction with the experimental result.

1.3.2.2 Perfectly matched layer (PML)

As the resonator configurations are becoming complex from the functional and performance point of view, closed form solutions are not possible for anchor loss estimation. Numerical solutions are required to address this issue. To predict the mechanical energy that is transmitted to the substrate, the substrate of a resonator can be considered as an elastic half-space. Only outgoing waves are allowed in this infinite domain problem. It is not possible to model an infinite substrate using FEM. Therefore, the substrate is considered as a finite domain structure surrounded by an artificial boundary that mimics the infinite substrate. The main property of the infinite substrate is that waves entering the substrate will not reflect back from the boundaries. One method to achieve this condition is using a non-reflecting boundary for a finite substrate. However, this boundary has a significant limitation that it only works if the incident waves are exactly normal to the boundary. Therefore, a better method is required to prevent the reflection of all the waves reaching the boundary. From the numerical standpoint, different options are available for the simulation of wave dissipation, among which higher order absorbing boundary conditions (ABC) and perfectly matched layer (PML) techniques are the most commonly employed (Rabinovich *et al.* [2010]). The layers rapidly attenuate waves and also perfectly match the rest of the domain. No spurious reflections are induced at the interface due to perfect impedance matching. A PML is a refinement of absorbing boundary conditions (Bindel *et al.* [2005]). Now the property and implementation of PML is discussed in detail.

A non-physical absorbing layer can be added along the exterior boundary of the substrate to absorb all outgoing waves before they reach the absorbing layer's finite boundary. The substrate and absorbing layer do not need to be modelled to reflect the geometry of the whole device's substrate, but only to ensure that waves do not reflect back from the absorbing layer's fixed boundary into the vibrating resonator. A PML can be used as an absorbing layer. As a wave enters the PML, it is attenuated exponentially and damped by this layer. In fact, a PML works as a complex valued modulus material that adds damping to the waves. To be modelled mathematically, waves are transformed from a real coordinate solution to a complex coordinate solution inside the PML region. Therefore, the amplitude of wave solution inside the PML has an exponentially decaying coefficient. Since the transformation is continuously differentiable, there are no impedance mismatches. If the size of the PML region is large enough, using an exponentially decaying coefficient ensures that waves are attenuated to a very small amount.

Basu and Chopra [2003] developed PML concept for time-harmonic motion of a 1D rod on elastic foundation in Cartesian coordinates. They compared analytical model with PML model and demonstrated high accuracy of PML model even for small bounded domains. Frangi *et al.* [2013] discussed theoretical framework and implementation guidelines of PML approach for robust applications. 2D and 3D implementations were described in their study and tested against the analytical estimates. It is always a good practice to select PML

size (W_{PML}) as a function of wave number (υ) such that $\upsilon W_{PML} > 0.1$ to optimize the global size of the problem. In order to avoid spurious reflections and allow for a smooth dissipation of waves, the decay over one single element should be limited by setting an upper bound on the typical dimension of elements. Larger value of W_{PML} ensures better Q factor convergence. It was shown that the commonly accepted decoupling assumption in analytical solutions leads to errors up to 20% of the predicted quality factor in 2D. Deviations might occur in 3D especially if higher resonant modes are targeted. Hence, the PML approach is the most flexible and applicable to general boundary conditions and geometries.

1.3.2.3 Effect of anchor geometry

The anchoring design is very critical as this is the link for the energy transfer from the resonator to the substrate. Studies have been done for different geometries and dimensions for improving the Q factor of well separated functional mode and eliminating functional mode interaction with other nearby modes. Bindel [2005] used PML for modelling anchor loss on the radial mode of the poly SiGe disk resonator. The disk radial motion is coupled to anchor axial motion due to bending at the attachment point and the coupling has a large influence on the quality factor of the functional radial mode. Thakar and Rais-Zadeh [2013] reported that anchor loss is the most significant when flexural mode of tether (anchor) is in synchronization with Lame mode due to the additional energy loss. The material parameters for the substrate and PML are same as that of resonator beam. It was showed that low anchor losses can be achieved by carefully optimizing the resonator tether geometry such that the flexural mode of the tether is far from the fundamental Lame mode frequency.

Effect of two anchor geometries, namely a straight anchor spring and a T-shaped spring, for extensional and wine glass resonant modes was studied by Lee *et al.* [2008]. Numerical study was carried out by analyzing the relative elastic energy distribution of the resonator and the anchor. It was shown that anchor related loss is not very dominant in wine glass mode for the nominal Q factor requirements. Good trend correlation was obtained with measured values reported in Lee *et al.* [2011]. The anchor loss was very much minimised using a torsional support, which is attached at node points, by Wang *et al.* [2000]. One order higher Q factor was achieved in the free-free beam resonator compared to the clamped-clamped beam versions with comparable stiffness. The size of the substrate is critical in the MEMS class sensors from miniaturization and fabrication point of view. In this consideration, Darvishian *et al.* [2015] numerically analyzed the effect of the substrate thickness on the anchor loss and shown that the out-of-plane modes are more sensitive. Steeneken *et al.* [2007] used matched layers (ML) in COMSOL instead of PML but the results were obtained within few percentages of accuracy. ML is not as effective as PML because they only match perfectly for normal incident waves.

1.3.2.4 Resonators with imperfections

Imperfections are inevitable in real devices due to material anisotropy and fabrication errors. These imperfections cause frequency split of the functional degenerate mode as well as Q factor asymmetry. This results in two sets of principle axes, the frequency axes and the

damping axes. These two sets of principle axes often do not coincide with each other. This results in diminishing accuracy and vibratory performance of the resonator. The imperfections can be handled by electrical means to some extent. This is normally done electrically by dynamic balancing of the resonators to maximize the *Q* factor. Non-symmetric tuning of stiffness in a coupled 2 DOF resonator was done through the use of negative electrostatic spring effect by Zotov *et al.* [2014]. This variable stiffness was shown to be able to adjust the reaction forces of the structure at the anchors. The approach was experimentally demonstrated using a vacuum packaged microelectromechanical tuning fork resonator. Generally, MEMS fabrication processes are not precise. The effect of variations in the thickness of the resonating disks was analyzed by Bindel and Govindjee [2005].

The performance of a resonating gyro is affected by the frequency mismatch in the degenerate functional resonator mode. Mode matching is particularly important because it cannot be distinguished from an input rotation rate and is required for low sensor bias error. Heidari *et al.* [2013] did loss measurements on 3D shell from polycrystalline diamond. Electrostatic excitation and ring down test were used for Q factor measurement. Frequency split was studied with respect to the fourth harmonic radius variation using Fourier analysis. In-plane free vibration of rings with a nominally elliptical centreline was analysed by Hwang *et al.* [1999] for frequency split due to fabrication variations. Results were presented for rings of rectangular cross-section with constant and varying radial thickness.

The vibration of imperfect resonator was investigated by Choi and Kim [2011] with point mass element which represents the imperfections on the structures. Explicit functions were derived for the split of the natural frequency as high frequency mode (H mode) and low frequency mode (L mode) and the shifting angle of mode orientation. The frequencies of high and low modes are both lower than the corresponding frequency of perfect resonator. The equivalent model for a specific mode number cannot represent for the other mode numbers. In this regard, one can only expect trimming process for one pre-determined mode number by single mass equivalent model.

1.3.2.5 Anchor loss in hemispherical and cylindrical resonators

Micro HRGs and similar axisymmetric 3D MEMS structures have the potential for whole angle (WA) mode of operation of gyroscope (Jeanroy *et al.* [2014]). If one of these degenerate $N = 2$ eigen modes has a smaller coefficient of damping, the standing wave pattern will tend to align itself with this eigen mode as the other decays faster in amplitude and results in an apparent drift relative to the sensor body without input rate. This drift must be minimized or compensated for accurate WA operation. Keeping this as the objective, Sorenson and Ayazi [2014] investigated the impact of structural anisotropy on anchor loss mismatch in micro hemispherical resonator gyroscopes. They found that the functional $N = 2$ elliptical mode is more affected by fourth harmonic anisotropy. Structural anisotropy corresponding to variations in the shell radius in the circumferential direction was included in the finite element model by modulating the Young's modulus.

Cho and Najafi [2015] analysed different resonator configurations such as hollow anchor for birdbath shell, solid anchor for birdbath shell, boundary anchor hemispherical shell, solid short outside stem, long solid inside stem for wineglass mode operation. The solid stem resonator offers low anchor loss due to the large stem length to stiffness compared to hollow stem. The specific advantages of long inside stem anchoring are low anchor loss and good shock resitivity. Key parameters like effective mass (m_{eff}) and angular gain (A_g), which affects the gyroscope performance, were also discussed. Here, m_{eff} is the mass of the resonator when it is modeled as a lumped mass resonator. Angular gain increases with the height to radius ratio because the shell moves increasingly perpendicularly to the yaw axis due to increased vertical stiffness. *Q* factor was calculated from the ring-down time.

Darvishian *et al.* [2017] did anchor loss simulation studies on birdbath wine glass hemispherical configuration resonator with outside stem. Depending on the resonator configuration and its boundaries, Cartesian, cylindrical or spherical PMLs can be used for absorbing waves. Spherical PML is highly effective in absorbing waves in the radial direction and was selected for simulation in their study. Even if these attenuated waves reflect from the PML's boundary, the returning waves reaching the resonator after one round trip through the PML are extremely small and their effect becomes negligible. The effects of geometry and shell material property were investigated. Then the relationships between the anchor loss and properties of the stem and the stem-shell misalignments were studied.

Cylindrical resonator gyroscope (CRG) is considered as a lower cost and easier manufacturing variant while preserving medium accuracy and performance. It also shares HRG advantages of instant start up capability, considerable vibration and shock resistance and long lifespan. Therefore, it is highly competitive in medium accuracy market when size, mass, power consumption and cost are comprehensively considered. Pan *et al.* [2017] presented the analysis of the *Q* factor variation behaviour around the cylindrical resonator's axis of symmetry due to imperfections. They showed that the nature of this *Q* variation is due to the misalignment between the excitation direction and principle axis. During characterization, the resonator was excited in one direction and responses were measured in different directions. The vibration response is the superposition of two eigen modes for each detection point. The vibration has a tendency to drift towards the principle axes and results in misalignment between the excitation and the principle axes. This causes instability in both *Q* factor and frequency which results in sensor drift and measurement error. It is of great importance to align the excitation with principle axes when characterizing and assembling high accuracy gyroscope resonators.

1.3.3 Surface loss

Surface loss is another critical energy loss mechanism while aiming for high *Q* factor resonators. Several researchers have reported that quality factor drops as the micromechanical structures are miniaturized. At the atomistic level, the free surface of a resonator structure experiences an excess energy called the surface free energy. In classical continuum mechanics, the influence of surface energy on the dynamics of resonators is usually ignored because the ratio of the surface area to bulk volume is very small. However, in micro/nano

scale devices, the ratio of atoms on the surface to total atoms becomes gradually significant. As resonators are miniaturized, the surface to volume ratio increases and the effect of the surface loss become significant (Gretarsson and Harry [1999]). Therefore, the surface energy effect has to be taken into account in the dynamics of micro resonators. Resonator surfaces may have lattice defects, contamination or other imperfections which serve to dissipate energy (Picard *et al.* [2011], Doremus [1995], Lunin *et al.* [2001]). Since quantitative models for this loss mechanism are complex, it has been experimentally demonstrated that surface treatments such as annealing can minimize these surface imperfections to some extent so that quality factor dramatically increases (Kim *et al.* [2008]). Another main cause of surface loss is the surface damage during fabrication.

Mihailovich and MacDonald [1995] measured *Q* factors of vaccum operated single crystal silicon micro resonators. It was found that the surface loss was predominant compared to support related losses and was improved by thermal oxidation technique. A monotonic reduction in *Q* factor was seen with decreasing the thickness for both silicon nitride and single crystal silicon cantilevers by Yasumura *et al.* [2000]. They defined a loss parameter, which includes size and material properties of beams, for quantitative comparison in place of *Q* factor. They brought out the effect of a thin surface layer which exhibits enhanced dissipation. It is attributed that the dissipation enhancement can be due to the disruption of the atomic lattice at the surface or due to a thin layer of surface contamination. The surface layer will not substantially change the stored energy in the cantilever but it can significantly enhance the dissipated energy. They proposed the method of characterizing the surface layer by the product of the defective characteristic skin depth and complex surface Young's modulus, which differs from the bulk property. Similar surface loss estimation approach was used by Imboden and Mohanty [2014]. It was pointed out that the surface contains a large number of defects due to the abrupt lattice termination as well as surface impurities. The surface area increases with increase in surface roughness which also results in more dissipation. The surface effects were quantified experimentally by changing the resonator geometry. High temperature annealing was suggested to improve the quality factor.

Grinding is the most widely used process for machining hard and brittle materials like glass. Ultra sonic machining (USM) is a popular machining technique for such materials with high hardness (Guzzo *et al.* [2004]). In USM, mechanical vibrations of greater than 15 kHz are used. A tool with diamond grit is hammered on the work piece surface by the tool vibration and thus removes the material by microchipping. Ultrasonic vibration not only reduces the tool wear rate, but also minimizes brittle fracturing in glass cutting zone. Brittle mode machining of glass can cause micro cracks which results in substantial amount of surface damage. Surface damage indicates damages on the surface of the material such as surface roughness (SR). Sub surface damage (SSD) indicates the damaged layer beneath the surface like subsurface cracks, dislocations, residual stress. Both SR and SSD increases surface loss and reduce overall *Q* factor (Palasantzas [2008]). When brittle failure is the dominant mechanism in material removal process, lateral cracks lead to chips removal and create the surface roughness, and medial cracks cause subsurface damages (Lucca *et al.*

[1998], Miller *et al.* [2005]). In order to minimize the surface damage due to cracks, appropriate machining parameters shall be chosen as discussed below.

Ductile mode of machining is possible in brittle materials because all materials have some extent of ductility no matter how brittle they are. Material will undergo plastic deformation only when the penetration depth is kept below a critical value which is insufficient for cracks to form. There is a critical value of feed rate and depth of cut for every material for ductile mode machining. Very low depth of cut can avoid the situation of brittle mode cutting even for silica glass. This described mechanism is referred as ductile regime grinding. Criticality is the machining of brittle material without crack in ductile mode. High precision machine tools ensure the suppression of these cracks by using appropriate machining parameters to a great extent (Ravindra and Patten [2011], Brinksmeier *et al.* [2010]).

Post fabrication treatments are important for achieving higher *Q* factors by removing the surface damages (Matveev *et al.* [2013]). In order to remove the micro cracks created by grinding, an etching process is required. The surface loss can be reduced by chemical treatment of damaged surface layer (Wong *et al.* [2009]). Dry etching by chemical action is also possible in plasma which has slow etching rate. Raman Spectroscopy is useful for qualitative measurement of surface damage in terms of Raman shift (Gogots *et al.* [1999]). The position of the Raman shift peaks of each phase is very sensitive to the tensile or compression stress. The feed rate has the most significant effect on the SR followed by depth of cut and cutting speed. Surface roughness and subsurface damage increases with the increase in the feed rate and the depth of cut. Surface damage is characterized using scanning electron micrographs (Esmaeilzare *et al.* [2014]). Cutting speed, which has the minimal effect on SR and SSD, shows an inverse behavior such that increasing the cutting speed results in a reduction in SR and SSD (Chen and Jiang [2015]). The variation of SR with respect to depth of cut and cutting speed is approximately linear in experimental data. *Q* factor was studied as a function of the Poisson's ratio and the nature of the surface roughness profile by Shiari and Najafi [2013]. Different surface films on a silica substrate were used in their study. Surface stress and roughness change effective bending rigidity of resonator which affects the *Q* factor. As roughness inclination angle increases, *Q* factor decreases.

Ahamed *et al.* [2014] studied the effect of annealing on quartz resonator. The annealing dependence was investigated by varying the temperature from 500 ^{o}C to 800 ^{o}C. Change in *Q* factor was observed to be minimal (< 10%), when annealed at 500 ^{o}C. *Q* factor improvement of 40 % was reported from 666×10^3 to 932×10^3 when annealed at 800 ^{0}C with very slow cooling. Annealing improved surface condition like removal of hydration, fabrication residue and hydroxyl content. Nagourney *et al.* [2015] studied the effect of metal annealing on the *Q* factor of 100 A^{o} metal coated fused silica micro birdbath shell resonators. The resonator showed much lower *Q* factor than the simulation. Annealing showed improvement for some devices and reduction in others which could not be explained. Saito *et al.* [2016] demonstrated *Q* factor of 5×10^5 in 1.5 mm diameter batch-fabricated microcrystalline diamond cylindrical resonators (CR). The *Q* factor was achieved through the

annealing process at 700 ^{o}C in a nitrogen atmosphere. However, ring-down time achieved was only 8.9 s at 19 kHz for elliptical wineglass modes.

Experimental and numerical energy loss studies were done on cantilevers to examine various energy loss mechanisms by Bernstein *et al.* [2015]. Many cantilevers of varying lengths were tested. The surface damping parameters were varied in order to minimize the error between the model and the measured quality factors in a least squares sense. Annealing at temperatures above 350 °C increased the *Q* factor substantially. However, similar improvement could not be demonstrated in a diamond hemispherical resonator of 1.4 mm diameter. Post fabrication chemical and thermal treatments were done to improve the *Q* factor of cylindrical fused silica resonator by Pan *et al.* [2016] where a *Q* factor of the order of 10^5 was achieved.

1.3.4 Material internal friction

A perfect crystal loses mechanical energy through mechanisms such as thermoelastic damping as it is a fundamental intrinsic damping mechanism in vibrating body. Measured quality factors of the real structures have quality factors much below the limit from thermoelastic damping. This can be explained by the dissipation due to crystal defects such as substitutional impurities, interstitial motion, grain boundary sliding and this dissipation is called material internal friction (Imboden and Mohanty [2014]). Damping occurs due to the irreversible motion of these crystal defects. This can be minimized by selection of high purity material with lowest internal stress for ultra high *Q* resonator.

The critical sensing elements, working in the limit of thermal noise, must be made from materials with low material internal friction to extract the full potential of the sensor. Fused silica, an extremely pure form of silicate glass, has been found to have very low internal friction at room temperature. Various studies were done to measure internal friction of fused silica keeping other losses away. Startin *et al.* [1998] reported that *Q* factor of the order of 10^6 can be achieved for the bulk high purity synthetic fused silica material. Penn *et al.* [2001] measured the dissipation in a Heraeus make Suprasil 2 brand fused silica sample in the form of a rod. The sample was excited at the resonant frequency using a comb capacitor exciter. The quality factor was measured for several modes and obtained maximum value as high as 5.7×10^7 at 726 Hz at specimen level. However, it was difficult to achieve the sensor level design value of 10^7 for the polished and coated wave detector sensing element.

Numata *et al.* [2004] adopted a nodal support technique where the support loss was effectively eliminated during internal friction measurement. The resonance quality factors of the samples were measured in vacuum at room temperature with the ring-down method. The quality factors of all of the samples were improved by the annealing process which was done at 950 ^{o}C. The improvement of the intrinsic loss by annealing might be derived from the release of residual strain and/or neutralizing several imperfections in the SiO_2 network. It is to be ensured that the annealing does not degrade other properties. The *Q* factors were observed to vary between different kinds of fused silica. The values ranged from 7×10^5 to 8.1×10^7, one of the highest reported among fused silica bulk samples.

Alexandr *et al.* [2004] measured *Q* factor of transverse vibrations of fused silica rods with diameters up to 12 mm. They studied the effect of an annealing treatment which was performed in an argon atmosphere. Long annealing period and cooling period were chosen to decrease the internal density fluctuations that could be responsible for additional dissipation. The *Q* factor improved from 3.3×10^7 to 4.3×10^7 due to annealing at frequency of about 33 kHz. Suprasil 312 showed frequency dependent *Q* factor. There was a trend to higher *Q* factor with increase in rod diameter because the losses were dominated by surface losses.

Micro glass blown silica hemispherical resonators have been reported recently with *Q* factors of up to 10^6 (Senkal *et al.* [2015], Cho *et al.* [2014]). The unique glass blowing techniques were adopted to obtain reasonably good precision micro resonators. However, these resonators have higher functional mode frequency and relatively shorter ring-down time constants compared to macro scale silica resonators. But these works are very promising as it is good performing and bulk producible with lower cost.

Other materials were also used to fabricate resonators. Bulk metallic glass (PtCuNiP) material has unique combination of amorphous, smooth, and symmetric 3D structure. Michael *et al.* [2015] realised 3 mm size hemispherical resonator and carried out experiments. It was found that surface roughness and geometry variation created frequency split. However, the achieved *Q* factor was less than 10^4. Mehanathan *et al.* [2014] reported fabrication and operational characterization of electroplated invar material made micro hemispherical shell resonators. Invar has low coefficient of thermal expansion which is near to that of fused quartz. Still achieved *Q* factor was only 7500 in vacuum. Resonators made of metallic alloys typically have *Q* factors in the range of 10^4 only (Chikovani *et al.* [2009], Xi *et al.* [2014]). This is because of higher material internal damping of metallic materials with respect to that of ceramic materials like fused silica.

1.3.5 Internal friction in coated resonators

Ceramic micro resonators coated with relatively thin metallic films are widely used for sophisticated precision instruments like scanning probe microscopy. These instruments require nanometer level or better deflection sensitivity which calls for high *Q* factor in coated resonators. The metallization improves optical reflectivity and electrical conductivity, but invariably degrades the *Q* factor. Hence, it is important to study the material internal friction in the thin film coating for proper selection of coating material and thickness.

Traditionally, internal friction is considered as a bulk (volume) effect, but surface effects can dominate for submicron thick cantilever resonators. This was established by White and Pohl [1995] using a low temperature (few Kelvin) measurement of internal friction of thin SiO_2 coated film with thickness up to 10000 A^o. The internal friction of film was found to be identical to that of bulk material. Li and Bellon [2011] characterized the internal viscoelastic damping of coated micro cantilevers using different thicknesses of gold coatings. The viscoelasticity of Si, Pt and Au cantilevers as a function of the thickness of gold coating was measured. Walther [1935] found that the internal friction in gold coating is much higher than that of SiO_2 base material.

Sandberg *et al.* [2005] presented the experimental results of the effect of the gold film on the performance and sensitivity of the cantilevers when used as mass sensors. They characterized the resonance frequency and the *Q* factor of the fundamental and higher order flexural modes of silicon dioxide micro cantilevers at different pressures and for different thicknesses of gold coating. The characterization was done in vacuum at a temperature of 300 K. Experiments were done using 1000 A^o, 2000 A^o, 4000 A^o gold coated resonators with 100 A^o Ti undercoat. They found that even a thin gold coating (1000 A^o) reduces *Q* factors by few orders of magnitude. It is understood that a significant amount of damping occurs at the surface boundary between the SiO_2 and gold. Further increase of coating thickness leads only to a small additional reduction. Higher order modes are more affected by gold coating than the lower order modes. This observation was also supported by the study on layered structures by Prabhakar and Vengallatore [2007].

Sosale *et al.* [2011] presented an approach for accurate measurement of internal friction in sputter deposited thin films of aluminum, gold, and silver on single crystal silicon cantilevers which were operated at the fundamental limit of dissipation established by TED. They measured friction with thickness ranging from 500 A^o to 5000 A^o at frequencies ranging from 100 Hz to 1 kHz and found that the friction in aluminum is consistently higher than that exhibited by gold. The strategy of controlling the thin film induced damping is reported in Sosale *et al.* [2011] by selective thin film application in the regions of low strain. A simple analytical model was developed to quantify the change in damping as a function of metallization length. Serra *et al.* [2012] characterized the mechanical quality factor of micro oscillators covered by a highly reflective coating. The contributions of thermoelastic dissipation and coating losses were separately evaluated. The resonant frequencies evaluated by finite element models were in good agreement with the experimental data and enabled the estimation of the Young's modulus of the coating.

1.3.6 Fluid damping

Fluid-structure interactions limit the quality factor of mechanical resonators (Newell [1968]). The most effective way to reduce the fluid damping is to operate the resonator at ultra high vacuum (Pandey *et al.* [2007]). As the pressure is reduced, fluid flow enters into different regimes such as slip, transition and molecular regimes from continuum regime based on Knudsen number. The fluid flow enters free molecular regime for Knudsen number > 10 (Joshi *et al.* [2014], Newell [1968]). *Q* factor is proportional to $P_f^{-1/2}$ in the slip and the transition regimes, and is proportional to P_f^{-1} in the molecular regime where P_f is the fluid pressure. High *Q* factor resonators need to be operated in molecular regime or better vacuum level. When the pressure is further reduced from molecular regime, fluid damping becomes negligible at a critical value which is a function of the size, shape, and mode of vibration of the resonator (Zhang *et al.* [2003]). The typical values of this critical pressure for miniaturized mechanical resonators were measured and reported as in the range from 0.1 N/m^2 to 10^3 N/m^2 (Blom *et al.* [1992], Khine and Palaniapan [2009]). Fluid damping can be eliminated to a great extent by adequate operating vacuum level for a particular configuration.

The temperature dependence of fluid damping and TED mechanism, and their contribution to the total quality factor was investigated by Kim *et al.* [2008]. They defined temperature coefficient of quality factor (TCQ). Quality factor due to fluid damping and TED are inversely proportional to the operating temperature. It was found that the TED is the prominent energy loss mechanism at lower temperature. On the other hand, the energy dissipation is dominated by fluid damping at higher temperature. Therefore, both the temperature dependence has to be evaluated at the same time. The dependence of temperature on *Q* factor was also analysed by Ghaffari *et al.* [2013] on double ended tuning fork.

1.3.7 Electronics damping

Electronics damping is due to the excitation (drive) and sense electronics. Duwel *et al.* [2003] carried out a detailed experimental study of the MEMS gyroscopes and measured quality factor of resonators made out of different semiconductor materials. The resonator was excited by an AC voltage. Another voltage bias is needed for sensing which also produces an electrostatic force. Expression for electronics damping was established. It was concluded that designing for larger readout gains reduce the *Q* factor. However, higher amplifier gain can compensate this effect. *Q* factor was studied with respect to electrical parameters by Zotov *et al.* [2014] also. *Q* factor was estimated for different feedback resistors and carrier voltages. Their experimental results demonstrated that *Q* factor is reduced as carrier voltage is increased. Thus, the electronics damping can be minimized by the proper selection of the electrical parameters.

1.4 Objective of present work

Based on the literature review, the following observations can be made on the state of art of the different vibration energy loss mechanisms in mechanical resonators.

- Analytical models for TED are available for simple resonator structures like beams, rings and plates. Closed form analytical solution is available for simple beam resonator structures for anchor loss estimation. Analytical estimation of anchor loss for disk resonator with centre support could be validated with experimental results only with an error coefficient to take care of interactions between disk and support structure, and for non-ideal support conditions. Complex resonator geometries could be solved only with numerical methods.

- Theoretical and experimental studies are available mainly for MEMS resonators of relatively simple structures. Quite reasonable comparision of theoretical predictions could be obtained with appropriate best fit correction factors obtained from experimental results. Numerical models for energy loss prediction and experimental studies are available for hemispherical shell mainly birdbath geometries which are fabricated through MEMS and micro-glass blowing methods.

- TED studies could not be found for resonator configuration with combination of hemispherical and cylindrical resonator geometry with inside mounting stem in all

millimeter size dimensions. Effect of thin film coating was studied on micron thickness hemispherical shells with volume fraction of 0.1%. However, the sensitivity study of ultra thin coating (volume fraction as low as 0.01%), coating configurations and effect of partial coating does not seem to have been attempted on hybrid configuration resonator.

- Even though there are many studies on anchor loss of MEMS class resonators, extensive anchor loss simulations on the effect of possible imperfections are limited for millimeter size hemispherical-cylindrical hybrid resonators. To the best of author's knowledge, experimental evaluation on hybrid configuration of resonator is not available. Effect of different combinations of mass unbalance and its effect on frequency split and *Q* factor mismatch on such configuration are not available in open literature domain.

- Many surface characterization studies are based on profile measurements and microscopy methods. Surface and subsurface mechanical property evaluation at nanometer depth is not generally used as a tool for evaluating the surface damage to access the surface loss.

- Significant attempts are limited for studying of multiple energy loss mechanisms present simultaneously in the resonator in its functional configuration from design to demonstration.

- Meeting the required ultra high *Q* factor and long decay time constant for very low mechanical noise and good bias stability is still a challenge in the MEMS technology based resonators compared to macro scale precision resonators. MEMS technology is still not widely accepted in space application gyroscope resonators which demand low frequency split of degenerate modes for high rate sensitivity and whole-angle mode of operation.

In view of the above, the objective of the present work is to study different vibration energy loss mechanisms, design, manufacture and demonstration of ultra high quality factor precision macro scale gyroscope resonator for high end inertial applications in space sector. Also, a hybrid resonator configuration is proposed with increased effective mass and angular gain compared to general hemispherical configuration to achieve low resolution. The details of comprehensive simulation studies of different damping mechanisms and experimental demonstration of high *Q* factor on realized precision resonators are as follows.

- Design of the resonator is done well away from the TED driven Debye peak to achieve ultra high *Q* factor in the configuration phase. Parametric study of different materials and dimensions is done.

- The effective mass and angular gain are improved with a hemispherical-cylindrical hybrid resonator configuration compared to general hemispherical configuration.

- The effect of ultra-thin film conductive coating, different coating configurations, and coating variations on TED is done for the hybrid resonator configuration. This is done to arrive at the coating configuration to meet the *Q* factor requirement for the functional resonator for electrostatic excitation and sensing.
- Anchor loss estimation and detailed parametric study of dimensions of shell and mounting stem are done. Effect of mode interactions is also included in the study.
- Anchor loss sensitivity to the possible imperfections during fabrication is done to arrive at the critical fabrication tolerances. Effect of different combinations of mass unbalance and its effect on frequency split and *Q* factor mismatch are included which are very critical for sensor performance.
- In-house manufacturing of high precision macro scale mechanical resonator is done using appropriate and conventional machining techniques.
- Specific surface characterization methods are adopted for the realized high precision resonators. A comprehensive experimental evaluation for frequency, *Q* factor and its variations are carried out under ambient and high vaccum.
- Unbalance sensitivity verification is done with the fabrication deviations and balancing scheme is established.
- *Q* factor measurement of thin film coated resonator is carried out along with detailed coating film characterization. Thus, the demonstration of high *Q* factor in the final functional high precision macro scale resonator configuration is done.

1.5 Structure of the Thesis

The thesis is organized into 9 chapters which are followed by the list of references**.**

Chapter 1 introduces different types and grades of gyroscopes mainly the mechanical and the optical gyroscopes for navigation applications. Further, the mechanical gyroscopes are classified based on its working principle. The working principle of Coriolis based HRG is explained in detail. The critical performance parameters for high end inertial navigation are discussed and arrived at the gyroscope resonator performance parameter requirement. Finally, literature on analytical, numerical, and experimental study of different energy loss mechanism related to mechanical resonators is reviewed. First, the application based critical loss mechanisms like TED, anchor loss, surface loss is presented followed by material internal friction, fluid damping and electronics damping. Literature review covers fundamental studies on simple structures followed by numerical and experimental studies of more complex gyroscope resonator structures.

Chapter 2 discusses the basic theory of TED and anchor loss, and analytical formulations to evaluate losses for simple structures. It also covers the significance

and applicability of these losses to HRG configuration and operation. Validation of numerical solution with analytical solution is presented with details of the boundary conditions, element selection, mesh sensitivity, and error estimation.

Chapter 3 describes the requirement of high *Q* factor and other specifications for the resonator of high end inertial navigation gyroscope. It covers preliminary configuration design with respect to minimum TED loss. Detailed parametric study is carried out to understand the dependency of the *Q* factor on the resonator configuration, geometric parameters, material, operating conditions, and functional feature requirement as a sensor. The functional hemispherical-cylindrical hybrid configuration of the HRG is arrived based on the above parametric study. The effective mass and angular gain are improved with the hybrid resonator configuration compared to general hemispherical configuration. It also discusses the effect of thin conductive coating, different coating configurations and coating variations on TED.

Chapter 4 deals with detailed study on anchor loss. It covers anchor loss estimation, dimensional and geometric parametric study, and effect of possible fabrication imperfections. The effects of mode interactions and mass unbalance pattern on frequency split, *Q* factor and *Q* factor mismatch are also explained in this chapter.

Chapter 5 presents material selection, fabrication procedure, description of precision machines used, realisation of fused silica shell resonator and its metrology measurements of dimension and geometrical parameters.

Chapter 6 discusses resonator characterization set-up, equipments used for characterization, measurement procedures, natural frequency measurement and its variation with dimensional deviations in fabrication. The effect of geometric deviations on frequency split and balancing scheme are also discussed.

Chapter 7 is devoted to studies on material internal friction, details of surface characterization equipment, surface characterization using nanoindentation, *Q* factor estimation methods, *Q* factor measurement, effect of etching on *Q* factor and evaluation of fluid damping.

Chapter 8 deals with the details of the coating machine, thin film coating procedures, surface profile measurements, coating characterization and evaluation of the *Q* factor in the coated resonator.

Chapter 9 concludes the work on the study of different damping mechanisms, design and simulations, experimental evaluations, and demonstration of *Q* factor along with other specifications in the final functional configuration. It also covers scope of further future work on this topic.

Chapter 2

Thermoelastic damping and Anchor loss: Theory and validation

This chapter discusses the basic theory of thermoelastic damping and anchor loss, and analytical formulations to evaluate these losses for simple structures. Closed form analytical expressions are available for relatively simple beam and ring resonator structures. However, such expressions are not available for more complex 3D structures. Numerical based finite element method should be used for TED and anchor loss simulation of complex configurations.

Validation of numerical solution with analytical solution is presented with details of boundary conditions, element selection and mesh sensitivity. The reason for the deviation of the numerical solution with respect to the analytical solution is also discussed. It also covers the significance and applicability of these losses to HRG configuration and operation.

2.1 Thermoelastic damping (TED)

TED is due to the coupling of mechanical and thermal material domains under dynamic vibrating condition. In a resonator, a strain gradient is produced i.e., some regions of the structure experience tension while some other region experience compression when vibrated in its flexural modes. This strain gradient results in a periodic temperature gradient. The thermal strain generated is not in phase with the elastic strain and the energy is dissipated through irreversible heat flow due to thermal gradient. Thus, entropy generation happens in the system in order to achieve equilibrium of resonator. This process of energy loss is called thermoelastic damping.

If the thermal transport time constant of resonator is close to the deflection period of elastic deformation, Q_{TED} of the resonator is reduced and the resonator suffers significant energy loss. As long as the material's thermal expansion coefficient, which acts as coupling constant, is non-zero, TED presents in vibrating elements as intrinsic material damping. TED can limit the Q_{Eff} of even the most perfectly designed and constructed resonator. Study of TED is a highly coupled field problem which involves thermodynamics, solid mechanics, heat transfer, and vibration domains as shown in Figure 2.1.

In the present work, the general transient heat conduction equation with the heat generation due to the vibration induced mechanical strain and the general equation of motion with thermal strain due to the thermoelastic coupling is considered to estimate the thermoelastic damping of a mechanical resonator.

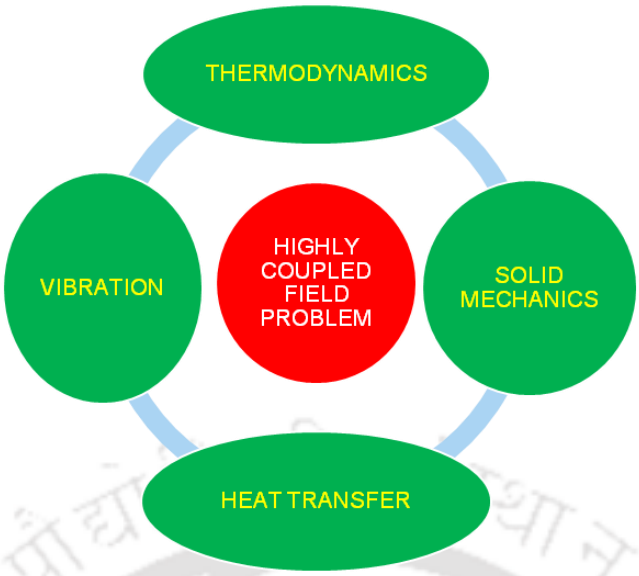

Figure 2.1: Highly coupled four mechanical domains under thermoelastic damping study

2.1.1 Theory and problem formulation

Stress-strain relation in linear solids, when there is a temperature deviation of ΔT from the absolute equilibrium temperature, is given by (Darvishian *et al.* [2017]):

$$\begin{bmatrix}\sigma_{11}\\ \sigma_{22}\\ \sigma_{33}\\ \sigma_{23}\\ \sigma_{13}\\ \sigma_{12}\end{bmatrix} = \begin{bmatrix} c_{11} & c_{12} & c_{13} & c_{14} & c_{15} & c_{16}\\ c_{12} & c_{22} & c_{23} & c_{24} & c_{25} & c_{26}\\ c_{13} & c_{23} & c_{33} & c_{34} & c_{35} & c_{36}\\ c_{14} & c_{24} & c_{34} & c_{44} & c_{45} & c_{46}\\ c_{15} & c_{25} & c_{35} & c_{45} & c_{55} & c_{56}\\ c_{16} & c_{26} & c_{36} & c_{46} & c_{56} & c_{66}\end{bmatrix} \times \left(\begin{bmatrix}\varepsilon_{11}\\ \varepsilon_{22}\\ \varepsilon_{33}\\ 2\varepsilon_{23}\\ 2\varepsilon_{13}\\ 2\varepsilon_{12}\end{bmatrix} - \Delta T \begin{bmatrix}\alpha_{11}\\ \alpha_{22}\\ \alpha_{33}\\ 2\alpha_{23}\\ 2\alpha_{13}\\ 2\alpha_{12}\end{bmatrix} \right) \tag{2.1}$$

where σ_{ij}, c_{KL}, ε_{ij}, and α_{ij} (i = 1,2,3) (j = 1,2,3) (K,L = 1,...,6) are components of stress, elastic stiffness, strain and coefficient of thermal expansion respectively. ΔT is the temperature deviation from absolute equillibrium temperature.

For a linearly elastic isotropic homogeneous material, the stress-strain relation is given by (Darvishian *et al.* [2017]):

$$\begin{bmatrix}\sigma_{11}\\ \sigma_{22}\\ \sigma_{33}\\ \sigma_{23}\\ \sigma_{13}\\ \sigma_{12}\end{bmatrix} = \frac{E}{(1+\vartheta)(1-2\vartheta)} \times \begin{bmatrix} 1-\vartheta & \vartheta & \vartheta & 0 & 0 & 0\\ \vartheta & 1-\vartheta & \vartheta & 0 & 0 & 0\\ \vartheta & \vartheta & 1-\vartheta & 0 & 0 & 0\\ 0 & 0 & 0 & \frac{1-2\vartheta}{2} & 0 & 0\\ 0 & 0 & 0 & 0 & \frac{1-2\vartheta}{2} & 0\\ 0 & 0 & 0 & 0 & 0 & \frac{1-2\vartheta}{2}\end{bmatrix} \times \left(\begin{bmatrix}\varepsilon_{11}\\ \varepsilon_{22}\\ \varepsilon_{33}\\ 2\varepsilon_{23}\\ 2\varepsilon_{13}\\ 2\varepsilon_{12}\end{bmatrix} - \frac{E\alpha\Delta T}{1-2\vartheta} \begin{bmatrix}1\\ 1\\ 1\\ 0\\ 0\\ 0\end{bmatrix} \right) \tag{2.2}$$

where E is the Young's modulus, ϑ is the Poisson's ratio.

The general equation of motion is given by (Abdolvand *et al.* [2006]):

$$\rho \frac{\partial^2 u}{\partial t^2} = \mu \nabla^2 u + (\mu+\lambda)\nabla(\nabla.u) \tag{2.3}$$

where ρ is the density, u is the general displacement, μ and λ are the Lame's parameters, $\nabla^2$is the Laplacian operator and ∇ is the gradient operator.

The heat conduction equation with heat generation is given by (Abdolvand *et al.* [2006]):

$$k\nabla^2 T = \rho C_P \frac{\partial T}{\partial t} - \frac{E\alpha T_0}{3(1-2\vartheta)} \nabla. \frac{\partial u}{\partial t} \tag{2.4}$$

where k is the thermal conductivity, T is the operating temperature, C_P is the specific heat capacity, α is the coefficient of thermal expansion, T_0 is the absolute equilibrium temperature. An additional heat source term is present as last term in the equation (2.4) when compared to the standard heat transfer equations in solids. This term couples the structural problem with the heat transfer problem. In turn, the heat transfer equation couples back into the structural problem through the constitutive relationship. The change in temperature from the absolute equilibrium temperature (T_0) is very small. Hence, the equation (2.4) can be linearized by considering $T = T_0$ (De and Aluru [2006]).

The equation of motion with additional thermal strain due to thermoelastic coupling is given by (Abdolvand *et al.* [2006]):

$$\rho \frac{\partial^2 u}{\partial t^2} = \mu \nabla^2 u + (\mu+\lambda)\nabla(\nabla.u) - \frac{E\alpha}{3(1-2\vartheta)} \nabla T \tag{2.5}$$

The equations (2.4) and (2.5) represent the thermoelastic behavior of an isotropic solid material. These coupled equations are solved for the eigenvalue which will represents the dissipation due to the thermoelastic phenomenon. This is explained next in detail using an analytical solution for a simple beam structure under flexural vibration.

2.1.2 Analytical solution for beam resonator

Zener's [1937] theory was based on the extension of Hooke's law involving stress σ, strain ε as well as their first derivatives. This model is also called 'standard anelastic solid' model and is given by (Lifshitz and Roukes [2000]):

$$\sigma + \tau_\varepsilon \dot{\sigma} = E_R (\varepsilon + \tau_\sigma \dot{\varepsilon}) \tag{2.6}$$

where σ is the stress, τ_ε is the relaxation time for stress to relax exponentially at constant strain, $\dot{\sigma}$ is the stress rate, E_R is the relaxed isothermal Young's modulus, ε is the strain, τ_σ is the relaxation time for strain to relax exponentially at constant stress and $\dot{\varepsilon}$ is the strain rate.

Zener [1937] calculated the relaxation time associated with different transverse modes for a thin beam flexure under resonance. For rectangular cross section beam resonators, a major part of the relaxation occurs through the first flexural mode. Approximation of having simple relaxation with single relaxation time for geometry of a rectangular beam is fairly

good. For a harmonic vibration with $\sigma = \sigma_0 \exp(i\omega t)$ and $\varepsilon = \varepsilon_0 \exp(i\omega t)$, the stress and the strain amplitudes are related by frequency (ω) dependent complex Young's modulus $E_{(\omega)}$. $E_{(\omega)}$ is given by (Lifshitz and Roukes [2000]):

$$E_{(\omega)} = E_R \left[\frac{1 + \omega^2 \tau_\varepsilon \tau_\sigma + i\omega(\tau_\sigma - \tau_\varepsilon)}{1 + \omega^2 \tau_\varepsilon^2}\right] \tag{2.7}$$

This can be written as a function of relaxation strength, Δ_E, and a function of resonant angular eigen frequency, f (ω), as (Lifshitz and Roukes [2000]):

$$E_{(\omega)} = E_R [1 + \Delta_E (1 + f(\omega)] \tag{2.8}$$

The relaxation strength is defined by Lifshitz and Roukes [2000] as:

$$\Delta_E = \frac{E_U - E_R}{\sqrt{E_U E_R}} \tag{2.9}$$

where E_U is the unrelaxed adiabatic Young's modulus. The unrelaxed adiabatic Young's modulus is given by:

$$E_U = E_R \left(\frac{\tau_\sigma}{\tau_\varepsilon}\right) \tag{2.10}$$

When ω is very large, f(ω) → 0 and Young's modulus tends to its adiabatic or unrelaxed value. Then, the equation (2.8) becomes

$$E_U = E_R (1 + \Delta_E) \tag{2.11}$$

The unrelaxed adiabatic value of the angular eigen frequency (ω_{ad}) is given by:

$$\omega_{ad} = \omega_0 \sqrt{1 + \Delta_E} \tag{2.12}$$

where ω_0 is the relaxed isothermal resonant angular eigen frequency.

When ω is very small, f(ω) → −1, and Young's modulus recovers its relaxed isothermal value E_R. For intermediate frequencies, $E_{(\omega)}$ is complex. Hence, the mechanical resonant angular frequencies are complex and is given by:

$$\omega = \omega_0 \sqrt{1 + \Delta_E (1 + f(\omega)} \tag{2.13}$$

The real part of frequency ω, Re(ω), gives the new eigenfrequencies of the beam resonator in the presence of thermoelastic coupling and its imaginary part, Im(ω), gives the attenuation of the vibration. The amount of thermoelastic damping, expressed in terms of the inverse of the quality factor, is obtained by the ratio of the imaginary part of the eigen frequency to the real part of the eigen frequency as (Lifshitz and Roukes [2000]):

$$Q_{TED}^{-1} = 2 \left|\frac{\text{Im}(\omega)}{\text{Re}(\omega)}\right| \tag{2.14}$$

The following closed form expression is obtained by Lifshitz and Roukes [2000] for a beam resonator under transverse vibration:

$$Q_{TED}^{-1} = \Delta_E \frac{\omega_{mech}\tau_{th}}{1+(\omega_{mech}\tau_{th})^2} = \frac{E\alpha^2 T_0}{\rho C_P}\frac{\omega_{mech}\tau_{th}}{1+(\omega_{mech}\tau_{th})^2} \quad (2.15)$$

where

$$\tau_{th} = \frac{b^2}{\pi^2 D} \quad (2.16)$$

$$Q_{mat} = \frac{\rho C_P}{E\alpha^2 T_0} \quad (2.17)$$

$$Q_{freq} = \frac{1+(\omega_{mech}\tau_{th})^2}{\omega_{mech}\tau_{th}} \quad (2.18)$$

$$Q_{TED} = Q_{mat} \times Q_{freq} \quad (2.19)$$

where ω_{mech} is the mechanical resonant angular eigen frequency, τ_{th} is the thermal relaxation time, b is the width of beam across which thermal relaxation happens, D is the thermal diffusivity, Q_{mat} is the quality factor limited by the material properties, Q_{freq} is the quality factor limited by the operating frequency. Q_{mat} depends only on the temperature and the material properties and is independent of resonator geometry. Q_{freq} is a function of ω_{mech} and τ_{th}. Equation (2.15) is extensively used for preliminary configuration design for beam resonators and for ring resonators with appropriate modifications (Wong *et al.* [2004]).

Zener [1937] arrived at the general guidelines for minimising the TED based on the resonator operating frequency region as shown in Figure 2.2. The dissipation exhibits a Lorentzian behavior as a functionof $\omega_{mech}\tau_{th}$ with a maximum value of $\Delta_E/2$ when $\omega_{mech}\tau_{th} = 1$. The dissipation peak is called the Debye peak. When the mechanical frequency is smaller compared to the relaxation rate i.e., $\omega_{mech}\tau_{th} << 1$, the oscillations are isothermal and the dissipation is less. When the frequency is larger compared to the relaxation rate i.e., $\omega_{mech}\tau_{th} >> 1$, the oscillations are adiabatic and the dissipation is less. Hence, the resonator operating region should be selected well away from the Debye peak point where $\omega_{mech}\tau_{th} = 1$. Resonator can be operated in isothermal region or in adiabatic region for low TED.

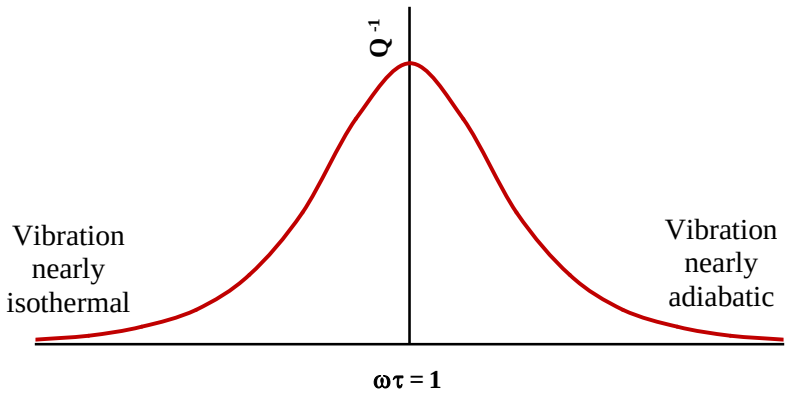

Figure 2.2: Design guideline for resonator operating region for high Q_{TED} where maximum Q^{-1} (maximum dissipation) at $\omega\tau = 1$

2.1.3 HRG configuration and TED

The basic resonator configuration is shown in Figure 2.3. It consists of a hemispherical region and a stem for mounting the resonator to the supporting structure in the gyroscope sensor. The hemispherical region is the resonator's functional vibrating region. The hemispherical region can be attached to the mounting substrate through three different ways such as inside stem, outside stem (wine glass configuration) and rim mounting. The inside mounting configuration is selected due to specific advantages in terms of low anchor loss and good shock resistance (Cho and Najafi [2015]). The inside stem is an integral part of the hemispherical region and the resonator is a single piece configuration in the present study. Even though the single piece configuration has difficulties with respect to precision fabrication and assembly, it is good option for eliminating energy loss at hemisphere-stem attachment interface. Now the functional vibrating mode shape corresponds to natural frequency and applicability of TED for this mode of operation is discussed.

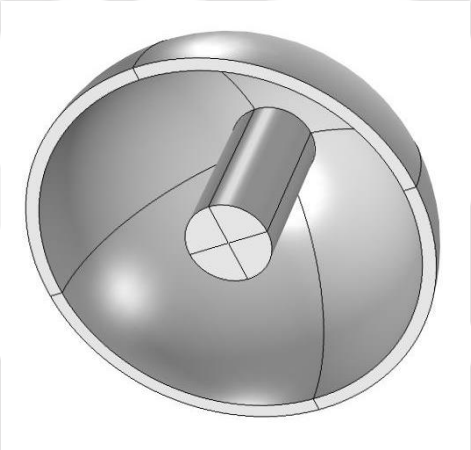

Figure 2.3: Integral hemispherical resonator configuration with inside stem

COMSOL verion 5.2 multiphysics FE tool is used for numerical simulations in the present study. In this section, the applicability of TED for HRG configuration only is discussed in terms of its functional vibration mode shape. Details of hemispherical resonator finite element modelling and its sensitivity is covered in the susequent Chapter 3 when quantitative damping estimation is done. Normalized displacement plot of the functional elliptical mode (N = 2) of HRG resonator is shown in Figure 2.4. There are two N = 2 modes which are circumferentially separated by 45 deg for an ideal structure as shown in Figures (2.5) and (2.6). These two N = 2 modes have the same frequency for an ideal resonator. There are four nodal and four antinodal points for each of the modes. In a resonating HRG hemispherical shell, a strain gradient is produced i.e., some region of the structure experiences tension while the other region experiences compression when vibrated in its functional elliptical modes. This strain gradient results in periodic temperature change. COMSOL normalizes the solution for temperature from eigen frequency solver. The normalized temperature deviation from equilibrium temperature is shown in Figure 2.7. Temperature increases from the equilibrium temperature when there is compressive strain and positive temperature deviation (red color in Figure 2.7) is seen. Temperature decreases

from equilibrium temperature when there is tensile strain and negative temperature deviation (blue color in Figure 2.7) is seen. The thermal strain generated is not in phase with the elastic strain and the energy is dissipated through irreversible heat flow due to this strain induced temperature gradient. From the Figure 2.7, it is clear that there are different temperature gradients in this functional vibration mode. This results in an entropy generation in the system in order to relax back to the equilibrium position of the resonator. This causes thermoelastic dissipation. If the thermal transport time constant of the resonator is close to the deflection period of the elastic deformation of the mode of vibration, Q_{TED} of the resonator is reduced and the resonator suffers significant energy loss. As long as the material's thermal expansion coefficient is non-zero, TED can limit the Q_{Eff}. Hence, it is very essential to understand, design and do a sensitivity study of the resonator configuration to achieve ultra-low TED resonator for a high performance inertial class gyroscope.

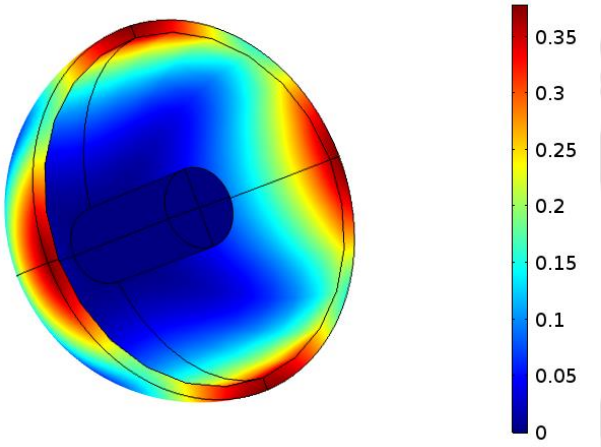

Figure 2.4: Functional elliptical mode (N = 2) normalized displacement

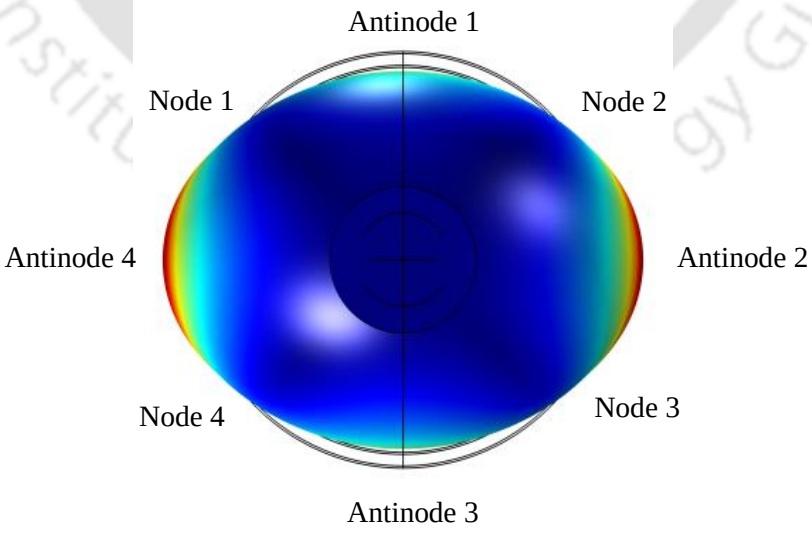

Figure 2.5: N = 2 elliptical degenerate mode 1 showing nodal and antinodal locations

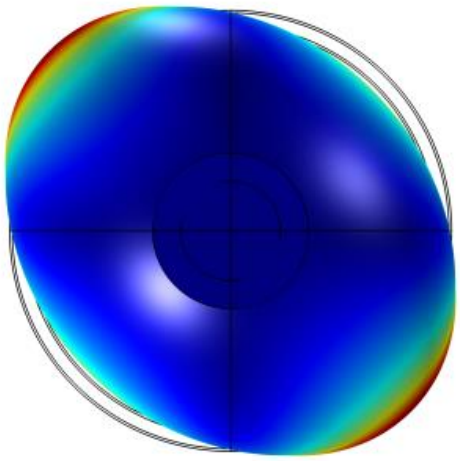

Figure 2.6: $N = 2$ elliptical degenerate mode 2 at circumferential angle 45 deg to mode 1

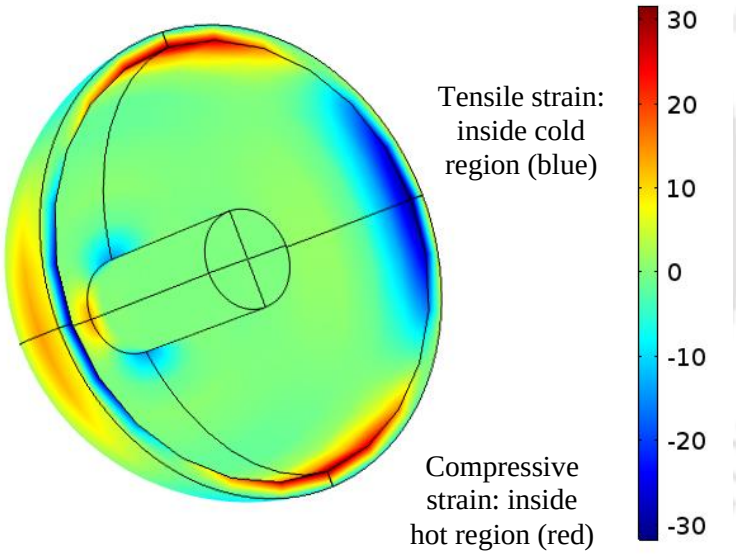

Figure 2.7: A typical plot of strain induced normalised temperature deviation from absolute equillibium temperature

2.2 Anchor loss

Elastic waves are generated when the resonator applies harmonic forces and moments at the point of attachment to support substrate. Anchor loss is caused by elastic waves propagating in the substrate that carry energy away from the resonator. This phenomenon is effectively a source of damping because mechanical energy of the resonator is transferred to substrate in the form of stress waves and dissipated in substrate. By assuming that the radiated energy does not reflect back into resonator, damping can be estimated by performing

calculations solely in the elastic domain without specifying the detailed mechanisms by which energy is dissipated in the substrate.

2.2.1 Theory and problem formulation

Hao *et al*. [2003] generated closed form expressions for the anchor loss estimation of the beam resonator. The schematic of the beam resonator, which vibrates in x-y plane, is shown in Figure 2.8. The beam resonator and support structure are made of same material and the dimensions of the support in the x-y plane are much larger than those of beam resonator. When the beam thickness (d) is much smaller than the wavelength of propagating wave, the coupling between the resonant modes of beam and the elastic wave motion is very weak. Hence, the energy transmission from resonator to the support can be treated as perturbation. Vibration behaviour of a beam resonator can be calculated using beam theory. Anchor loss due to moment is negligible compared to shear as the radiation efficiency of the normal force is reduced since two halves of radiation source cancel each other (Cross and Lifshitz [2001]). The shear force at the beam anchor point is evaluated based on the beam equation of resonant motion. This acts as the source of elastic waves in the support structure. Then, 2D elastic wave equation is used for estimating the behaviour of the support due to the shear force. The energy loss to the support is formulated using the shear force from the resonator and the corresponding displacement in the support. Thus, closed form solution of Q_{Anchor} is obtained for clamped-free beam.

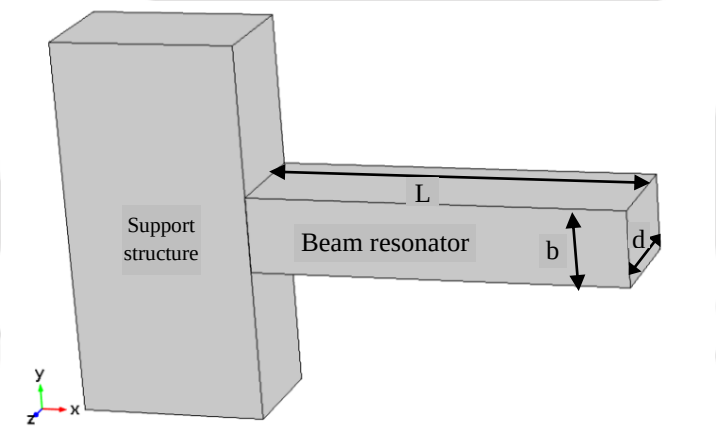

Figure 2.8: Schematic of beam resonator

The equation of motion of the in-plane (x-y plane) flexural vibration of the beam resonator is given by (Hao *et al*. [2003], Morse [1936]):

$$\frac{\partial^4 y}{\partial x^4} + \frac{\rho S}{EI}\frac{\partial^2 y}{\partial t^2} = 0 \qquad (2.20)$$

where I is the moment of inertia of the beam resonator, S is the cross-section area of the beam resonator and y is the transverse displacement of the beam resonator.

The vibrating shear force Γ_n exerted by the resonator at attachment area due to n^{th} mode vibration is given by (Hao *et al*. [2003]):

$$\Gamma_n = EIU_n \left[\frac{\pi\beta_n}{L}\right]^3 \chi_n \tag{2.21}$$

where U_n is the n^{th} mode vibration amplitude of the beam resonator, L is the length of the beam resonator, β_n is n^{th} mode constant and χ_n is n^{th} mode shape factor.

This shear force excites elastic waves and the elastic waves propagate into the support. The elastic wave generates in-plane displacements in the support. When the beam thickness is much less than the elastic wavelength, the wave can be treated as 2D. The wave equation is given by (Hao *et al*. [2003], Landau and Lifshitz [1959]):

$$\frac{\partial^2 u_x}{\partial t^2} = C_L^2 \frac{\partial^2 u_x}{\partial x^2} + C_T^2 \frac{\partial^2 u_x}{\partial y^2} + \left(C_L^2 - C_T^2\right) \frac{\partial^2 u_y}{\partial x \partial y} \tag{2.22}$$

$$\frac{\partial^2 u_y}{\partial t^2} = C_L^2 \frac{\partial^2 u_y}{\partial y^2} + C_T^2 \frac{\partial^2 u_y}{\partial x^2} + \left(C_L^2 - C_T^2\right) \frac{\partial^2 u_x}{\partial x \partial y} \tag{2.23}$$

where u_x and u_y are the in-plane displacements of support structure in x direction and y direction respectively, C_L and C_T are the longitudinal and the transverse wave propagation velocities in the support structure.

2.2.2 Analytical solution for beam resonator

By assuming $u_x = u\, e^{i\omega t}$ and $u_y = v\, e^{i\omega t}$, the in-plane displacements u and v at the support point can be found out. The anchor loss is related to the displacement v along the direction of shear.

Amount of energy loss per cycle ΔW of a beam resonator is given by (Hao *et al*. [2003]):

$$\Delta W = \pi \Gamma_n v \tag{2.24}$$

The stored vibration energy Wn for n^{th} resonant mode of beam resonator is given by (Hao *et al*. [2003]):

$$W_n = \frac{1}{8} \rho S L \omega_n^2 U_n^2 \tag{2.25}$$

where ω_n is the angular resonant eigen frequency of n^{th} mode of the beam resonator. The Q factor of the n^{th} mode of the beam resonator is defined by (Hao *et al*. [2003]):

$$Q_n = 2\pi \frac{W_n}{\Delta W} \tag{2.26}$$

The analytical expression of Q_n for clamped-free beam resonator is given by (Hao *et al*. [2003]):

$$Q_n = \left[\frac{0.24(1-\vartheta)}{(1+\vartheta)\psi}\right] \frac{1}{(\beta_n \chi_n)^2} \left[\frac{L}{b}\right]^3 \tag{2.27}$$

where ψ is a function of resonator natural frequency and wave propagation velocity and b is the width of the beam resonator.

Many critical inferences were generated by the fundamental study of Hao *et al.* [2003]. The quality factor is proportional to the cubic power of the ratio of the beam length to the beam width. The support quality factor of a beam resonator is independent of the Young's modulus of the resonator's material. However, it depends on the ratio of the Young's modulus of the resonator and to that of the support. It is also dependent on the Poisson's ratio of the resonator's material. The quality factor has no dependency on the vibration amplitude. The quality factor of a beam resonator decreases as its mode order increases.

2.2.3 Anchor loss in HRG

During HRG operation, the resonating hemispherical region applies resultant harmonic forces and moments to the support structure through the inside stem when vibrated in its functional elliptical mode. The resultant forces and moments generate elastic waves in the support structure at the point of attachment of stem. The elastic waves carry energy away from the resonator and results in Q_{Anchor} reduction. Since the analytical expressions are available only for very simple structures, numerical simulation is used for the anchor loss studies in 3D structures. COMSOL is used for numerical simulation of anchor loss in the present study. In this section, the applicability of anchor loss for HRG configuration only is discussed in terms of its functional vibration mode shape. Details of finite element modelling and its sensitivity is covered in Chapter 3 when quantitative damping estimation is done. Perfectly matched layer (PML) concept is used by COMSOL to generate a perfectly absorbing medium for the elastic waves in the support structure. The PML approach is the most flexible and applicable to complex resonator geometries. The construction of the PML is done in such a way that the wave energy is fully attenuated in the PML so that there will not be any reflected energy coming back to the resonator. The normalised deformation inside the substrate, when the resonator vibrates in one of the elliptical modes, is shown in Figure 2.9.

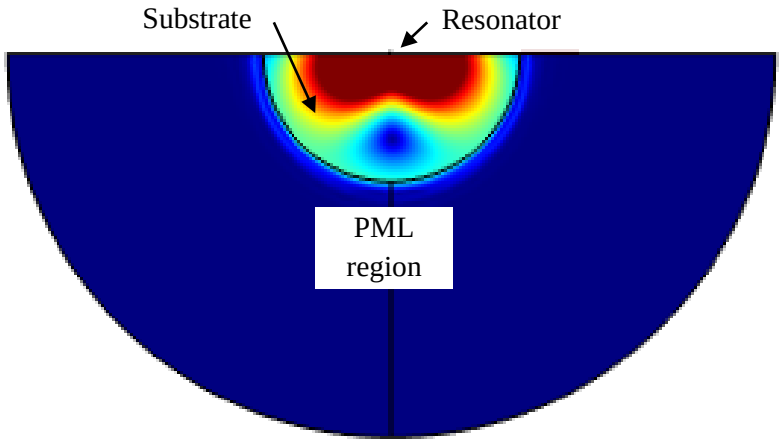

Figure 2.9: The normalised deformation inside the substrate and the PML when the resonator vibrates in one of the elliptical modes.

Resonator is located at the top centre of Figure 2.9 and the relative size of resonator is very small compared to the PML region for simulation. The deformation is at the end of time period of vibration. Maximum deformation is below the resonator and decays as it passes through the substrate and the PML region. It is very essential to understand, design and do a sensitive study of the resonator configuration to have minimum anchor loss resonator for a high performance inertial class gyroscope.

2.3 Numerical solution validation

As discussed earlier, numerical methods need to be used for simulating TED and anchor loss in more complex real resonator 3D structures. COMSOL multiphysics finite element based numerical tool is used for simulations. Hence, validation of this tool is done for TED and anchor loss using simple structures where the analytical solutions are available.

2.3.1 Validation for TED

A silicon beam resonator with 12 micron thickness, 24 micron width and 400 micron length is considered for the validation problem. Both ends of the beam are with fixed boundary condition. Two cases of extreme thermal boundary conditions are considered i.e., all faces insulated (Case 1), and zero temperature deviation from equilibrium temperature at the ends and remaining faces insulated (Case 2). COMSOL is used to solve the fully coupled thermo-mechanical finite element eigen value problem to obtain the frequency and the Q_{TED} numerically. It solves the linearized form of the thermoelasticity equation and equation of motion (equations (2.4) and (2.5)).

A mapped quadrilateral mesh is generated in the 2D plane of one end of the beam. Then, the 2D mesh is extruded along the length of the beam to generate 3D hexahedral mesh. Quadratic shape function is used for displacement field and linear shape function is used for temperature field. Material properties are taken from COMSOL material library. Table 2.1 gives the material properties of silicon used for study. Mesh sensitivity study also is carried out. The results are tabulated in Table 2.2.

Table 2.1: Material properties of silicon [COMSOL]

Property	Value
Thermal conductivity	90 W/mK
Density	2330 kg/m^3
Specific heat capacity	700 J/kgK
Young's modulus	157×10^9 N/m^2
Coefficient of thermal expansion	2.6×10^{-6} 1/K
Poisson's ratio	0.3

Table 2.2: Validation of FE simulation with analytical results for TED of beam resonator

Model details	Q_{TED}	Deviation (%)
Zener model (analytical) (Zener [1937])	10269	Reference model
LR model (analytical) (Lifshitz and Roukes [2000])	10362	1.0
COMSOL FE results		
Case 1: 5×5×20 elements	9172	10.6
Case 2: 5×5×20 elements	11714	14.1
Case 1: 5×5×40 elements	9578	6.7
Case 2: 5×5×40 elements	10939	6.5
Case 1: 10×10×20 elements	9176	10.6
Case 2: 10×10×20 elements	11715	14.1
Case 1: 10×10×40 elements	9582	6.7
Case 2: 10×10×40 elements	10936	6.5

Figure 2.10 shows normalized temperature deviation (increase and decrease from absolute equilibrium temperature) and heat transfer path due to thermoelasticity in first bending mode. There is a decrease in temperature (blue region) from absolute equilibrium temperature when the material gets elongated and increase in temperature (red region) from absolute equilibrium temperature when the material gets compressed due to the bending mode. There are seven thermal heat transfer paths in the beam resonator due to thermoelasticity during the transverse vibration. Thermal relaxation occurs through these thermal paths during vibration. Since the thermal relaxation and mechanical vibration are not in phase, TED occurs in 3D beam geometry. 3D finite element model captures all the thermal paths and corresponding dissipations for a given vibration mode.

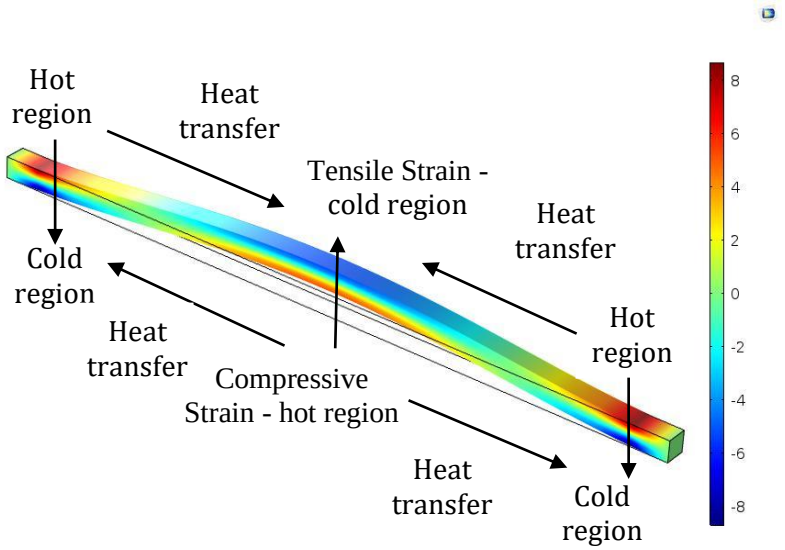

Figure 2.10: Normalized temperature deviation (increase and decrease from absolute equilibrium temperature) and heat transfer path due to thermoelasticity in first bending mode

In order to understand the resonator operation region with respect to peak thermoelastic dissipation, the mechanical resonance frequency and the frequenecy corresponds to the thermal relaxation time are evaluated. The mechanical resonance frequency is 0.63 MHz while the frequenecy corresponds to the thermal relaxation time is 0.60 MHz for this beam resonator configuration. Since these two frequecies are very close, the resonator works very close to the Debye peak and suffers high thermoelastic dissipation. The analytical and COMSOL results of frequency and the Q_{TED} are matching as shown in Table 2.2. The average value of natural frequency of the two cases for fine mesh is 10259 Hz which is very close to the Zener model. There is reasonably good match is seen for Q_{TED} between the analytical and the numerical solutions. There is 12% difference in Q_{TED} between the two extreme thermal boundary conditions for the finer mesh. Some of the thermal gradients are removed with isothermal boundary condition at the end and this condition (Case 2) gives higher Q_{TED} than Case 1. Analytical Q_{TED} falls between the numerically evaluated Q_{TED} of extreme thermal boundary conditions. The actual thermal boundary condition at the ends will be between the two extreme cases. Analytical models calculate Q_{TED} based on the heat transfer only at the middle of the beam for its first flexural mode which is also the major contributor for dissipation. Mesh density in the length direction is more sensitive than cross-section mesh density for TED estimation of beam resonator.

2.3.2 Validation for anchor loss

A silicon cantilever beam resonator of 500 micron length, 4 micron width and 20 micron thickness is considered for the validation problem. Closed form solution by Hao *et al.* [2003] is used for the analytical estimation. For the first cantilever mode in-plane vibration, mode constant β_1 is 0.597, mode shape factor χ_1 is −0.734 and the coefficient $\left[\frac{0.24(1-\vartheta)}{(1+\vartheta)\psi}\right]\frac{1}{(\beta_1\chi_1)^2}$ is 2.081 (Hao *et al.* [2003]). Q_{Anchor} of first cantilever mode is found as the ratio of real part to

imaginary part of angular resonant frequency. COMSOL is used to solve the eigen value problem numerically. PML concept is used to generate a perfectly absorbing medium for the elastic waves to estimate anchor loss. Table 2.3 gives the propogating wave properties for PML region parameter estimation.

In Table 2.3, C_L and C_T are the longitudinal and the transverse wave propagation velocities and are given by (Hao *et al*. [2003]):

$$C_L^2 = \frac{E}{\rho\left(1-\vartheta^2\right)} \tag{2.28}$$

$$C_T^2 = \frac{E}{2\rho\,(1+\vartheta)} \tag{2.29}$$

Also, ζ_L and ζ_T are the longitudinal and the transverse direction wavelengths and are given by (Hao *et al*. [2003]):

$$\zeta_{L,T} = \frac{C_{L,T}}{f} \tag{2.30}$$

where f is the resonant eigen frequency.

The wave number υ is given by:

$$\upsilon^2 = f^2 \frac{\rho}{(\lambda+2\mu)} \tag{2.31}$$

Table 2.3: Propogating wave properties for calculation of PML parameter

Resonant eigen frequency, f (kHz)	Speed of sound (longitudinal), C_L (m/sec)	Speed of sound (transverse), C_T (m/sec)	Wavelength (longitudinal), ζ_L (m)	Wavelength (transverse), ζ_T (m)	Wave number, υ (1/m)
19.3	7780	4668	0.403	0.242	2.4

The value of ζ_T/d is calculated as 12095 where d is beam thickness. As $\zeta_T/d \gg 1$, 2D analysis is valid. PML is modelled beyond the mounting substrate structure as shown in Figure 2.11 where the resonator is located at the top side and centre of substrate. Figure 2.12 shows zoomed view of FE model showing cantilever beam resonator with substrate as the size of resonator is very small compared to PML size. Anchor loss prediction using FE is sensitive to parameters such as PML thickness and mesh size. Modelling parameters of PML are arrived based on the guidelines in Frangi *et al.* [2013]. It is always a good practice to select PML size, $W_{PML,}$ as a function of wave number (υ) such that $\upsilon W_{PML} > 0.1$ to optimize the global size of the problem and better convergence. The minimum value of PML size is selected based on this criterion. The effect of PML size on Q_{Anchor} is given in Table 2.4. Larger value of W_{PML} ensures better Q_{Anchor} convergence. When PML size is equal to one

wavelength, Q_{Anchor} converges to 5×10^6. This ensures that the waves entering to the PML are totally absorbed within the PML. In order to avoid spurious reflections and allow for a smooth dissipation of waves, the decay over one single element should be limited by setting an upper bound on the typical dimension of elements. Fixed constrain is applied at PML outer surface. The resonant eigen frequency of cantilever mode obtained from numerical simulation is 20.5 kHz which is matching with analytical solution of 19.3 kHz. The comparison of the analytical and the numerical results are shown in Table 2.5 for three cases of PML size.

Table 2.4: Effect of PML size on Q_{Anchor} convergence

PML size (m)	Q_{Anchor}
0.04	3.32×10^6
0.06	3.55×10^6
0.08	3.85×10^6
0.10	4.09×10^6
0.15	4.86×10^6
0.22	5.19×10^6
0.24	5.03×10^6
0.26	5.11×10^6
0.30	5.10×10^6
0.40	4.92×10^6

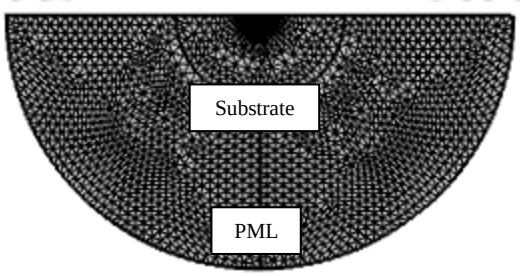

Figure 2.11: FE model of substrate and PML region with fine mesh

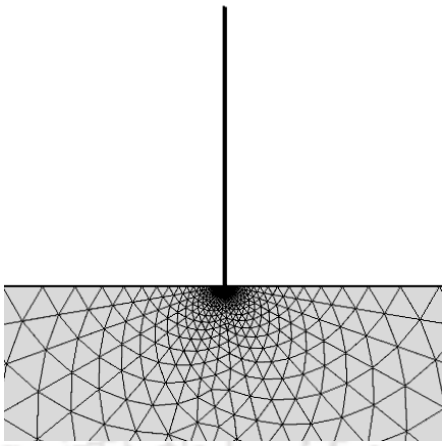

Figure 2.12: Zoomed view of FE model showing thin cantilever beam resonator with mounting substrate

Table 2.5: Validation of FE simulation with analytical results for anchor loss of beam resonator

Model details	Q_{Anchor}	Deviation (%)
Hao model (analytical) Hao *et al*. [2003]	4.06×10^6	Reference model
Frangi model (analytical) Frangi *et al.* [2013]	4.23×10^6	4
COMSOL FE results		
W_{PML} = 0.04 m	3.32×10^6	18
W_{PML} = 0.10 m	4.09×10^6	< 1
W_{PML}= 0.40 m	4.92×10^6	20

From the Table 2.5, it is clear that numerical simulation results for Q_{Anchor} are in good agreement with the analytical result with proper selection of modelling parameters. Hence, PML size should be selected such that it results in Q_{Anchor} convergence by ensuring the effectiveness of PML region.

2.4 Summary

Basic theory of thermoelastic damping and anchor loss, and analytical formulations to evaluate these losses for simple structures are discussed. Since closed form analytical expressions are not available for complex 3D structures, numerical based finite element method should be used. Simulation results of thermoelastic damping and anchor loss are matching with the analytical results by following the suitable FE modelling guidelines, selection of elements, mesh density and boundary conditions. Based on the validation studies, the numerical simulation using COMSOL is found suitable for TED and anchor loss simulations of mechanical resonators with complex geometries.

Chapter 3

Design for low thermoelastic damping and sensitivity study

The requirement of high Q_{Eff} is discussed in the Chapter 1. It is mentioned that mechanical noise equivalent rotation (MNER) should be reduced to the maximum possible for the best HRG sensor performance. It is well known that the primary choice to improve MNER is to maximise the Q_{Eff} of the resonator followed by improving the effective mass and the angular gain. From the earlier discussions, it is found that Q_{Eff} is the critical parameter for improving the performance of the sensor in terms of its resolution and scale factor. Hence, ultra high Q_{Eff} is required for the hemispherical resonator in HRG.

This chapter describes the quantitative requirement of Q_{Eff} for the resonator of high end inertial navigation gyroscope based on the nominal operating parameters. It covers preliminary configuration design with respect to minimum TED. TED is contributed by the material of the resonator and the size of the resonator. The size of the resonator decides the optimum operating region where there is sufficient separation between the thermal and the mechanical domains. Detailed parametric study is carried out to understand the dependency of the Q_{Eff} on the resonator configuration, dimensions, material, operating conditions and functional feature requirements as a sensor. The functional configuration of the HRG is arrived based on the above parametric study. It also discusses the effect of thin conductive coating, different coating configurations and coating variations on TED.

3.1 Estimation of Q_{Eff} requirement

Typical design and operational input parameters are considered to arrive at the Q_{Eff} requirement. The selection of these input values is based on design calculations and operational requirements which will be discussed subsequently. For design values of drive amplitude of 10 micron, nominal operating temperature of 293 K, resonance frequency of 5550 Hz, angular gain of 0.31, effective mass of 0.54×10^{-3} kg and sensor bandwidth of 10 Hz, MNER is calculated for different Q_{Eff} as shown in Figure 3.1. From the Figure 3.1, minimum Q_{Eff} of 10^6 (one million) is required to achieve MNER of 10^{-3} deg/hr. This range of MNER is demanded for high performance inertial navigation sensor resonator. Hence, the design target for the present study is more than a million Q_{Eff} resonator in the final functional form.

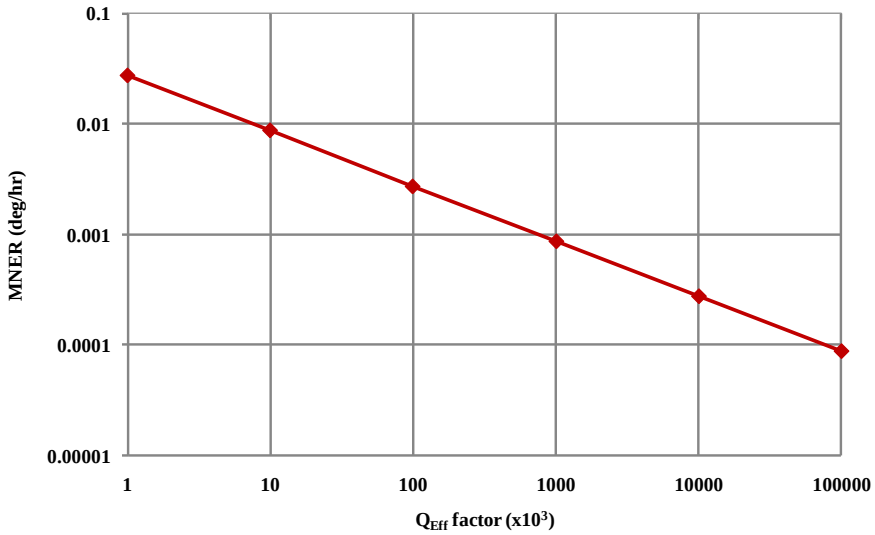

Figure 3.1: Relationship between MNER and Q_{Eff} for a given design and operating parameters

Once the Q_{Eff} requirement of mechanical resonator is arrived, the target specification of the macro size HRG can be framed based on other functional requirements and design constraints. The operating resonant frequency should be well away from the Debye peak of highest TED. Also, the operating frequency should be kept well away from launch induced excitation frequencies to avoid undesired performance deviations caused by resonance. Frequency split between the drive mode frequency and the sense mode frequency is also critical with respect to sensor output. Sensor output is maximum with matching of these two frequencies as mentioned in section 1.1.2.2. However, it is not possible in real gyroscopes. Hence, the frequency split is inevitable. Similarly, frequency separation of the functional resonant mode with respect to nearby modes is also critical for anchor loss. The overall resonator size should be limited to achieve reasonable compactness of sensor. Considering all these aspects, specifications of the mechanical resonator is arrived as given in Table 3.1.

Table 3.1: Specifications of mechanical resonator

Parameter	Value
Effective quality factor	$> 10^6$
Functional operating frequency	>> 2000 Hz
Frequency split	≤ 0.05 Hz
Frequency separation	> 500 Hz
Maximum size	< 0.04 m

Now, it is to be ensured by design that the individual Q factors should be more than 10^6. The loss mechanism considered for the resonator sizing is TED as it has got dependency through the operating region of resonance. Parametric study is carried out to understand the dependency of the Q_{TED} on the resonator configuration, different resonator dimensions,

material thermo-mechanical properties, operating conditions and functional features requirement as a sensor. Thus, the functional configuration of the HRG is arrived.

3.2 Ring resonator parametric study

The priliminary resonator size design is done primarily focussing on the natural frequency of the operating functional mode and its Q_{TED}. To start with, a simple ring structure is considered for which the analytical expressions are available for the elliptical mode eigen value and the corresponding TED (Wong *et al.* [2004]). As explained earlier, the inertial class CVGs should have a Q_{TED} of few millions. Based on the earlier studies, it is very difficult to establish the required Q_{TED} in micron scale resonators in its final functional form with all the dissipative mechanisms. Hence, it is proposed to design a macro scale resonator with a Q_{TED} of more than a million where all the resonator dimensions are in mm scale.

Both the analytical and the numerical methods are used to estimate frequency and Q_{TED} of the ring resonator configuration. Fused silica material, which has very low material internal friction and low coefficient of thermal expansion, is selected based on earlier studies. The material properties are taken from the material library of COMSOL FE multiphysics tool (version 5.2) and is given in Table 3.2. The resonator surface area requirement for electrostatic capacitive forcing and capacitive sensing is considered while configuring the resonator dimensions. A parameteric study is carried out by varying the mean ring radius and the radial thickness to evaluate the elliptical mode natural frequency and the dissipation. The ring thickness is varied from 0.6 mm to 1.4 mm and ring mean radius is varied from 10 mm to 18 mm keeping the ring height as 3 mm. Ring height is insensitive to natural frequency of the ring configuration.

Table 3.2: Material properties of fused silica [COMSOL]

Property	Value
Thermal conductivity	1.3 W/mK
Density	2203 kg/m^3
Specific heat capacity	703 J/kgK
Young's modulus	73×10^9 N/m^2
Coefficient of thermal expansion	0.55×10^{-6} 1/K
Poisson's ratio	0.17

3.2.1 Analytical solution for ring resonator

As discussed in Zener [1937], the Q_{TED} is composed of two parts. The first part, Q_{mat}, is due to the resonator material properties alone. The second part , Q_{freq}, is due to the material properties and the geometry of the resonator. The Q factors due to the material property contribution and the geometry are separately evaluated and arrived at Q_{TED}. A typical

analytical estimation of frequency and Q_{TED} of fused silica ring resonator is carried out for 14.6 mm mean radius and 1 mm radial thickness. The Q factor due to material contribution is estimated as given below.

$$Q_{mat} = \frac{\rho C_P}{E\alpha^2 T_0} = 239361 \tag{3.1}$$

Q_{freq} is decided by the separation between the mechanical resonanat eigenfrequency of operation and the frequency corresponding to thermal time constant. Mechanical resonanat angular eigen frequency ω_{mech} is given by Wong *et al.* [2006]:

$$\omega_{mech} = \frac{N_r\left(N_r^2-1\right)}{\sqrt{N_r^2-1}} \frac{t}{r^2}\sqrt{\frac{E}{12\rho}} = 20918 \tag{3.2}$$

where N_r is the vibration mode number, t is the radial thickness and r is the mean radius of the ring resonator. The elliptical mode (N_r = 2) is considered for ring resonator similar to HRG functional mode and the corresponding f_{mech} is calculated as 3331 Hz. Then, thermal relaxation time is evaluated both in the radial and in the circumferential directions to obtain the separation between the mechanical and the thermal modes.

Thermal relaxation time in radial direction, $\tau_{th\text{-}r} = \frac{t^2}{\pi^2 D} = 0.12$ sec (3.3)

Thermal relaxation time in circumferential direction, $\tau_{th\text{-}c} = \frac{r^2}{4D} = 63.5$ sec (3.4)

Frequency corresponding to thermal relaxation time in the radial direction is 1.3 Hz which is much smaller than the mechanical frequency. Frequency corresponding to thermal relaxation time in circumferential direction is 2.5 milliHz which is much smaller than that in the radial direction. Hence, thermal relaxation time in the radial direction is considered for further calculations to get worst case dissipation. Since the mechanical frequency is larger compared to the relaxation rate i.e., $\omega_{mech}\tau_{th} >> 1$, the oscillations are adiabatic in nature. It can be seen that the mechanical resonance frequency of the operating elliptical mode and the frequency corresponding to thermal time constant are well seperated for this size of resonator. The Q_{freq} and the Q_{TED} are obtained as given below.

$$Q_{freq} = \frac{1+(\omega_{mech}\tau_{th})^2}{\omega_{mech}\tau_{th}} = 2510 \tag{3.5}$$

$$Q_{TED} = Q_{mat} \times Q_{freq} = 6\times10^8 \tag{3.6}$$

As this range of size is sufficiently away from the Debye peak of highest dissipation, the thermoelastic dissipation is very less.

3.2.2 Numerical solution for ring resonator

Now, numerical solution is done using COMSOL ver 5.2. Figure 3.2 shows the finite element model of the ring resonator in COMSOL. COMSOL solves the fully coupled thermo-

mechanical finite element eigen value problem to obtain the frequency and the Q_{TED} numerically. It solves the linearized form of the thermoelasticity equation and equation of motion (equations (2.4) and (2.5)). Quadratic shape function is used for displacement field and linear shape function is used for temperature field. A mapped mesh using quadrilateral elements are generated in the cross section of the ring in a 2D plane. Initially, 4 elements are used in radial thickness and height directions of ring cross section. Then, the 2D mesh of 16 elements is revolved around the axis of the resonator to generate the 3D hexahedral mesh of ring resonator with a total of 640 elements. Further, number of elements are increased for mesh sensitivity study. Thermally insulated boundary condition is used on the outer surfaces of the ring. Figures 3.3 (a), (b) and (c) show different views of undeformed and normalised deformation plot for the two elliptical modes. There are four nodal points and four antinodal points. The blue region represents the nodal and the red regions represents the antinodal locations in Figures 3.3. Normalized temperature deviation (increase and decrease from absolute equilibrium temperature) and heat transfer path due to thermoelasticity in elliptical modes are shown in Figures 3.4 (a) and (b). There is a temperature decrease (blue) in the region of elongation and a temperature increase (red) in the region of compression corresponding to the mode shape. Temperature deviation is from the absolute equilibrium temperature of 293 K. Radial and circumferential thermal gradient induced heat trasfer is present in both the elliptical modes in a similar way. Figure 3.5 shows the normalized temperature deviation in cross-section of the ring resonator and heat transfer path from the hot region to the cold region. There is an uniform thermal gradient in the bulk fused silica material across the cross section. The relative contibution of different heat transfer paths to the overall thermoelastic dissipation depends on the dimensions of the resonator and the operating resonant mechanical frequency mode.

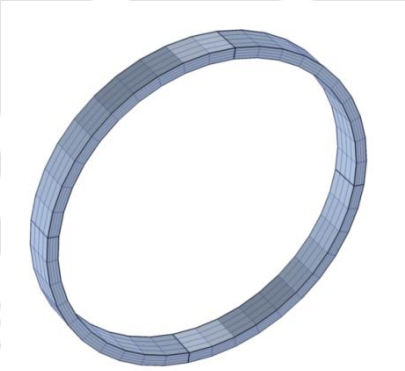

Figure 3.2: 3D Finite element model of ring resonator in COMSOL

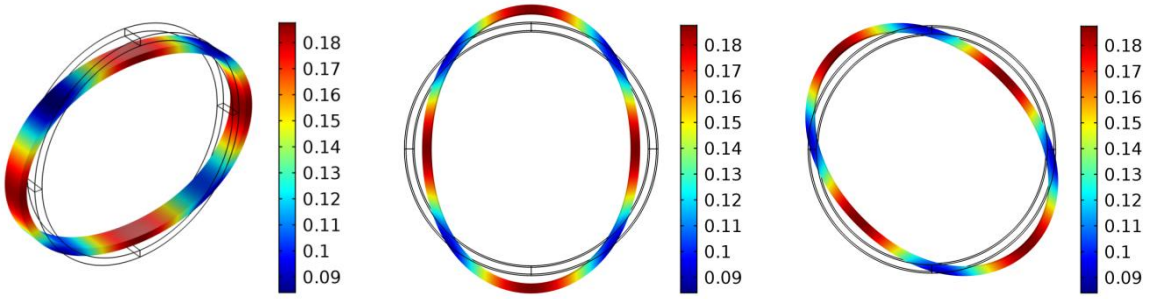

(a) 3D view of N_r = 2 mode (b) View of N_r = 2 mode 1 (c) View of N_r =2 mode 2

Figure 3.3: Different views of overplot of undeformed and normalised deformation plot for the two elliptical modes of ring resonator

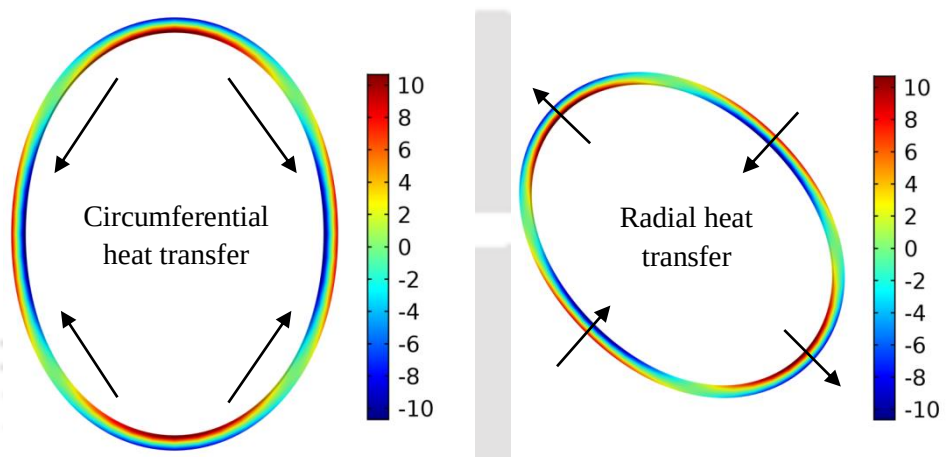

(a) View 1 (b) View 2

Figure 3.4: Normalized temperature deviation (increase and decrease from absolute equilibrium temperature) and heat transfer path due to thermoelasticity

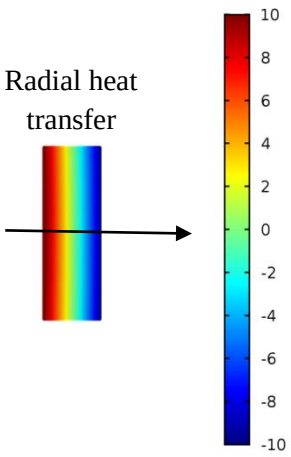

Figure 3.5: Normalized temperature deviation (increase and decrease from absolute equilibrium temperature) in cross-section of ring resonator and heat transfer path

Mesh sensitivity study has been carried out for the ring configuration with dimensions used in analytical solution, given in section 3.2.1, for comparison. In numerical simulation, mesh density is varied in the circumferential, radial and height directions. Initially, the mesh density in the circumferential direction is varied till the frequency and the Q_{TED} are converged. Thus, the number of elements required in the circumferential direction is obtained. Then, the number of elements in the other directions are varied one after the other by keeping the converged number of elements unaltered in the previous iteration. Thus, the mesh density in all the three directions are arrived for a converged result. Tables (3.3), (3.4) and (3.5) give the effect of mesh density in circumferential direction, radial direction and height direction on the frequency and the Q_{TED} respectively.

Table 3.3: Effect of circumferential direction mesh density on frequency and Q_{TED}

Number of elements			Frequency (Hz)	Q_{TED} ($\times 10^8$)
Radial direction	Height direction	Circumferential direction		
4	4	40	3339.9	5.0
4	4	50	3328.1	5.0
4	4	60	3325.4	4.9
4	4	70	3324.2	4.9

Table 3.4: Effect of radial direction mesh density on frequency and Q_{TED}

Number of elements			Frequency (Hz)	Q_{TED} ($\times 10^8$)
Radial direction	Height direction	Circumferential direction		
4	4	50	3328.1	5.0
6	4	50	3329.6	5.0
8	4	50	3331.1	5.0
10	4	50	3332.7	5.0

Table 3.5: Effect of height direction mesh density on frequency and Q_{TED}

Number of elements			Frequency (Hz)	Q_{TED} ($\times 10^8$)
Radial direction	Height direction	Circumferential direction		
8	4	50	3331.1	5.0
8	6	50	3331.1	5.0
8	8	50	3331.1	5.0

Circumferential direction mesh density has major effect on the frequency only and negligible effect on Q_{TED} while radial direction mesh density has minor effect on the frequency. Height direction mesh density has no effect on the frequency and Q_{TED} because there is no thermal gradient in the height direction.

Next, modal analysis is carried out without considering TED to understand the effect of theroelastic damping on eigen frequency. The frequency shift is due to the frequency depenedent Young's modulus under thermoelastic damping. There is an increase of Young's modulus from the relaxed isothermal value of Young's modulus in the presence of TED. The analytical frequency is compared with the numerical result in Table 3.6 along with the effect of TED on frequency shift.

Table 3.6: Comparision of analytical frequency with the numerical result and the effect of TED on frequency shift.

Frequency (Hz) (Analytical)	Frequency (Hz) (Numerical) (Normal mode analysis without TED)	Frequency (Hz) (Numerical) (Normal mode analysis with TED)
3330.9	3331.137	3331.144

For the Table 3.6, it is clear that the analytical frequency is almost exactly matching with numerical analysis result. It is found that there is only 7 milliHz change in eigen frequency with the presence of TED of present silica resonator. The increase of Young's modulus from relaxed isothermal condition to unrelaxed adiabatic condition depends mainly on the operating frequency and material's relaxation strength. The relaxation strength depends on the thermo-mechanical properties of the material. As the operating frequency is in the range of few kiloHz in the present macro size resonators, the frequency dependent Young's modulus change is very small and it is very close to isothermal relaxed Young's modulus. Hence, the frequency increase with TED is also very small. The adiabatic Young's

modulus for the silica material, which is calculated using the equation (2.11), is 73.67 GPa against the isothermal Young's modulus of 73 GPa. Hence, the corresponding maximum frequency increase for silica material is 15 Hz when the opearing frequency is very high. Table 3.7 gives the comparison of analytical Q_{TED} with the numerical result for the ring resonator for the size of 14.6 mm mean ring radius and 1 mm radial thickness.

Table 3.7: Comparision of analytical Q_{TED} with the numerical result for the ring resonator

Thermal relaxation time in radial direction (sec)	Thermal relaxation time in circumferential direction (sec)	Q_{mat}	Q_{freq}	Q_{TED} (Analytical)	Q_{TED} (Numerical)
0.12	63.5	239361	2510	6.0×10^{8}	5.0×10^{8}

For the Table 3.7, it is clear that there is a reasonable match (15%) for the Q_{TED}. For the mode considered (N_r = 2), the circumferential direction distance between the high and the low temperature regions is much more than the radial thickness for heat transfer. Thermal relaxation time in the circumferential direction is much higher than that in the radial direction. Since $\omega_{mech}\tau_{th} >> 1$, the resonator of this size works in adiabatic region and is sufficiently away from Debye peak. Hence, smaller value of τ_{th} makes the resonator to work away from adiabatic region and results in more dissipation. So the radial temperature gradient contributes more to the dissipation.

Now a parametric study of the ring resonator is done by varying the mean ring radius and the radial thickness to evaluate the N_r = 2 mode eigen frequency and the corresponding Q_{TED}. The frequency and Q_{TED} and variations with mean ring radius and radial thickness are shown in the Figures (3.6) and (3.7) respectively.

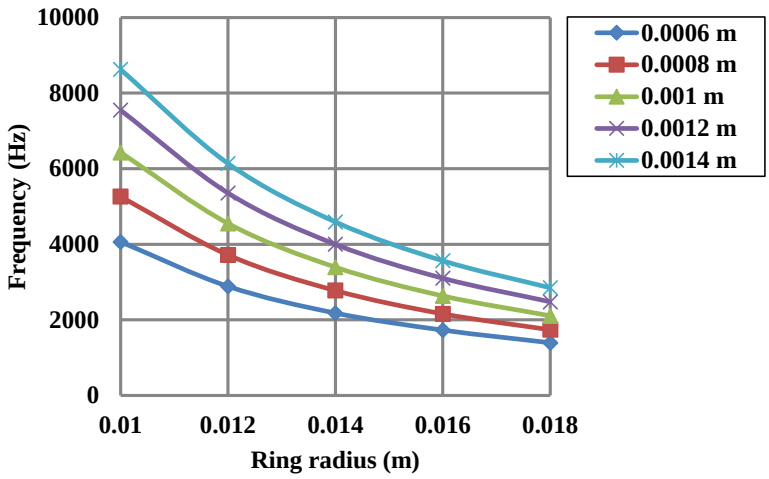

Figure 3.6: Variation of frequency with respect to mean ring radius for different ring thickness

It can be seen that the frequency increases as the shell thickness increases. Increasing the shell thickness results in increase in thermal resistance and thus increases the radial thermal time constant. Since the resonator operates in the adiabatic region, increase in frequency and thermal time constant move the operating region away from Debye peak. Hence, high Q_{TED} can be achieved with higher radial thickness as shown in Figure 3.7. Since the frequency is more, other operating considerations also should be considered before finalising the thickness. When the mean ring radius reduces, the frequency increases and the behavior becomes more adiabatic which results in higher Q_{TED} as shown in Figure 3.7.

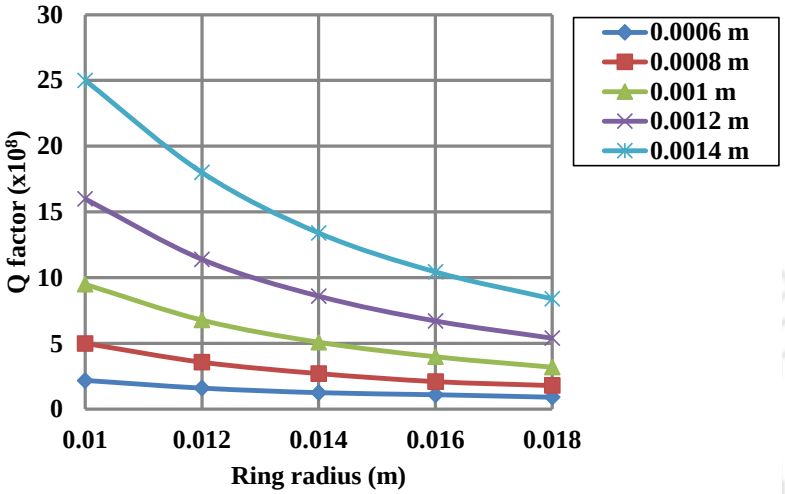

Figure 3.7: Variation of the Q_{TED} factor with respect to mean ring radius for different ring thickness

It can also be seen that the rate of increase of Q_{TED} is more in the case of higher radial thickness. When the thickness is kept same, radial direction thermal time constant remains same. The circumferential thermal time constant has lesser infuence on the Q_{TED} of this resonator size range. When the ring radius reduces to much lesser dimensions, heat transfer in the circumferential direction becomes significant.

3.2.3 Ring configuration for lowest TED

For the ring geometry considered, two cases of lowest Q_{TED} (Debye peak of highest dissipation) can be obtained as shown in Table 3.8 for a given mean ring radius and ring thickness separately. For 1 mm radial thickness of a fused silica ring, the lowest Q_{TED} is attained when the mean ring radius is 734 mm (Case 1 in Table 3.8). For 14.6 mm mean ring radius of a fused silica ring, the lowest Q_{TED} is attained when the ring radial thickness is 0.073 mm (Case 2 in Table 3.8). Hence, the combination of mean ring mean radius of 14.6 mm and ring radial thickness of 1 mm gives higher Q_{TED}.

Table 3.8: Combinations of ring geometric dimensions for lowest Q_{TED}

Cases	Radial thickness ($\times 10^{-3}$ m)	Mean ring radius ($\times 10^{-3}$ m)	Mechanical frequency (Hz)
Case 1	b = 1.000	a = 734	1.30
Case 2	b = 0.073	a = 14.6	246

The configuration and dimensions of hemispherical resonator is arrived based on this study. The range of dimensions considered in this parametric study ensure that the operating region is well away from the Debye peak. Other factors such as fabrication feasibility using conventional methods, electrostatic area requirements, constraints on overall sensor size are also considered.

3.3 Hemispherical resonator parametric study

Hemispherical configuration has the highest Q_{TED} among the different 3D configurations and 2D planar configurations. The configuration of the hemispherical resonator gyroscope structure is discussed in this section. Then, the effect of the resonator material properties and various dimensions on the Q_{TED} is studied.

3.3.1 Configuration

Based on the literature studies, it is very difficult to establish the required Q_{Eff} in micron scale resonators in its final functional form with all the dissipative mechanisms. The resonator, which is mentioned in Rozelle [2009], is in millimeter (mm) scale with resonator outside diameter as 30 mm. More than ten million quality factor could be achieved in this size range. The ring resonator TED studies, discussed in section 3.2.2, also confirm this. Hence, it is proposed to design a macro scale resonator where all the resonator dimensions are in mm scale. The initial resonator configuration in the present study consists of an axisymmetric hemispherical alone resonating structure with a central supporting region called the stem. The supporting stem is configured as inside mounting stem, which is similar to Rozelle [2009], due to low anchor loss and good shock resistance (Cho and Najafi [2015]). The present configuration considered is a shell of uniform thickness and stem of uniform diameter as it simplifies the shell fabrication using a convensional technique. The cross section view is shown in Figure 3.8. The nomenclature and nominal dimensions are provided in the Table 3.9. Later, a hybrid configuration is proposed for improved MNER in section 3.5.

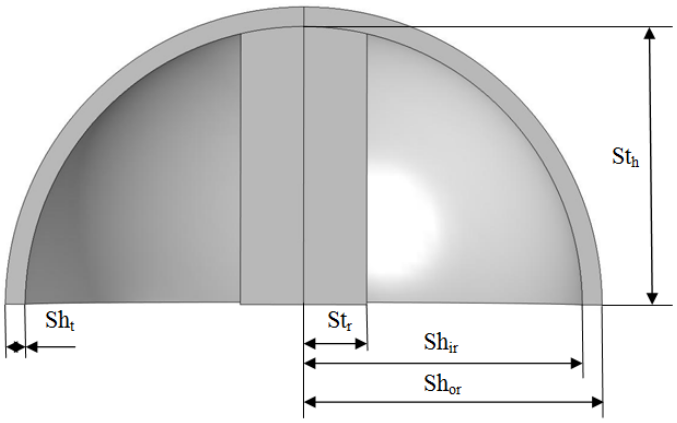

Figure 3.8: Cross section view of hemispherical shell and central supporting stem

Table 3.9: Nomenclature, description and nominal dimensions of the hemispherical shell configuration with stem

Nomenclature	Description	Dimensions ($\times 10^{-3}$ m)
Sh_{ir}	Shell inner radius	14.1
Sh_{or}	Shell outer radius	15.1
Sh_t	Shell thickness	1.0
St_r	Stem radius	3.2
St_h	Stem height	14

3.3.2 Mesh sesitivity study

Since analytical solutions are not available for the hemispherical configuration with central stem, numerical method using COMSOL is used for further study. A mapped mesh using quadrilateral elements are generated in the cross section of the resonator in a 2D plane. Then, the 2D mesh is revolved around the axis of resonator to generate 3D hexahedral finite element model as shown in Figure 3.9. Thermally insulated boundary condition is used on all the surfaces of the resonator except at the stem bottom mounting interface as the resonator operates in vaccum and nominal temperatures. Fixed boundary condition is applied at the base of the central mounting stem. Mesh sensitivity analysis has been carried out by changing the mesh density in circumferential, polar and thickness directions similar to the procedure discussed in section 3.2.2. Thermoelastic eigen frequency analysis has been carried out to obtain the $N = 2$ frequency and the Q_{TED} for the fused silica resonator with nominal dimensions. Tables (3.10), (3.11) and (3.12) give the effect of mesh density in the

circumferential direction, the polar direction and the radial thickness direction on frequency and Q_{TED} respectively.

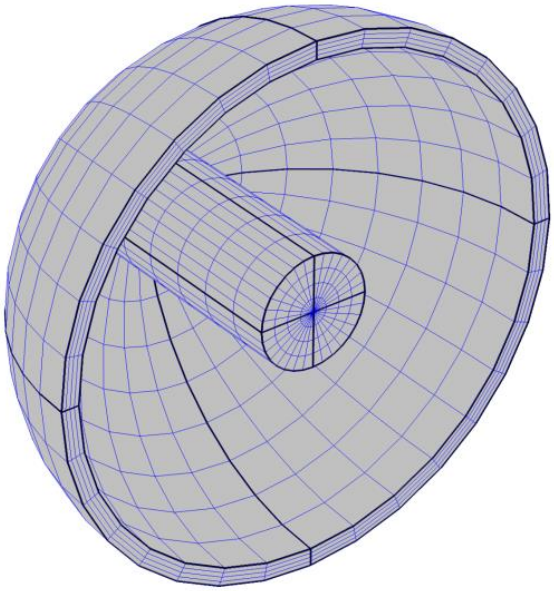

Figure 3.9: Finite element model of resonator structure

Table 3.10: Effect of the circumferential direction mesh density on frequency and Q_{TED}

Number of elements			Frequency (Hz)	Q_{TED} ($\times 10^9$)
Radial thickness direction	Polar direction	Circumferential direction		
4	12	44	5492.1	3.6
4	12	52	5487.1	3.6
4	12	60	5485.1	3.6
4	12	68	5484.2	3.6
4	12	80	5483.6	3.6

Table 3.11: Effect of the polar direction mesh density on frequency and Q_{TED}

Number of elements			Frequency (Hz)	Q_{TED} ($\times 10^9$)
Radial thickness direction	Polar direction	Circumferential direction		
4	12	60	5485.1	3.6
4	13	60	5465.0	3.7
4	14	60	5457.2	3.8
4	15	60	5452.1	3.8

Table 3.12: Effect of the radial thickness direction mesh density on frequency and Q_{TED}

Number of elements			Frequency (Hz)	Q_{TED} ($\times 10^9$)
Radial thickness direction	Polar direction	Circumferential direction		
4	14	60	5457.2	3.8
6	14	60	5458.1	3.7
8	14	60	5459.0	3.7

It can be seen that the circumferential direction mesh density is not affecting the Q_{TED}, and the polar and the radial thickness direction mesh densities affect the Q_{TED} marginally. The polar direction mesh density affects the frequency much more compared to the circumferential direction and the thickness direction mesh density.

Now, the thermoelastic induced different heat transfer paths during $N = 2$ mode of vibration operation in hemispherical configuration are identified from the temperature deviation profiles. Figures 3.10 (a) and (b) show two views of the thermoelastic strain induced normalized temperature deviation plot for $N = 2$ mode where the circumferential direction, the polar direction and the radial thickness direction heat transfer paths are marked. Thermoelastic strain regions are seen at the rim and root of the hemisphere which contribute to the thermoelastic dissipation.

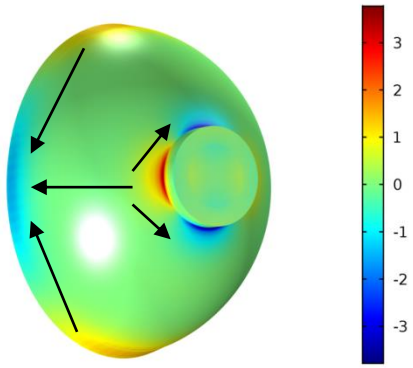

(a) The polar direction and the circumferential direction heat transfer paths

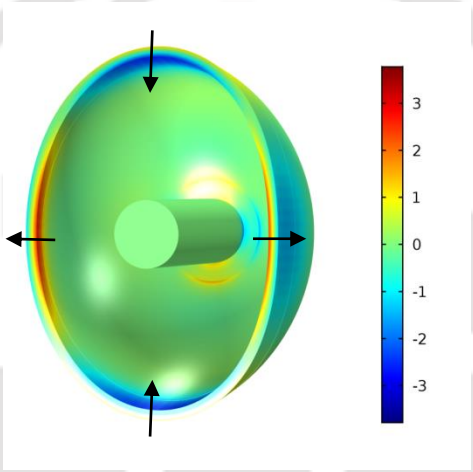

(b) The radial thickness direction heat transfer path

Figure 3.10: Thermoelastic strain induced normalized temperature deviation plot for $N = 2$ mode and heat transfer paths

3.3.3 Modal analysis

Rocket launch induced sine vibration base excitations are predominant upto 100 Hz. However, random vibration base excitations are high upto 700 Hz. The random levels are very less beyond 2000 Hz. Hence, all the launch vehicle and satellite systems are tested upto 2000 Hz for random inputs while that for sine inputs are done upto 100 Hz. So the first mode of the mechanical resonator should be kept well above 2000 Hz to avoid the launch induced excitations.

Certain other general design guidelines are also followed. This precision sensor is assembled to launch vehicle or satellite through a shock absorbing elastic rubber vibration isolator to reduce the levels at the base of the sensor. Moreover, these sensor packages are assembled sufficiently away from the shock source points of launch vehicle. The present

configuration of HRG with inside stem is a good shock resistant configuration compared to the outside stem wine glass configuration as mentioned in section 2.1.3.

In order to avoid the energy loss from the functional $N = 2$ mode, this eigenvalue need to be kept well separated from other nearby modes (Zeyuan *et al.* [2016]). Hence, normal modal analysis is carried out to identify first few natural frequencies of the resonator. The first mode is called the shell tilting mode in which the hemispherical region undergoes a tilting motion with respect to the stem-hemisphere interface. The second mode is called the breathing mode in which the majority of hemispherical region undergoes an axial and a radial motion with respect to stem-hemisphere interface. The third mode is the $N = 2$ elliptical mode which is generally the functional mode of vibratory gyroscopes because of the high angular gain which results in better performance. The quantitative comparision of angular gains for $N = 2$ and $N = 3$ mode is covered susequently. The undeformed original circular cross section shape of hemisphere shape takes the elliptical shape in this vibration mode. Only the hemispherical region is mainly participating in the first three modes. The fourth mode is the stem tilting mode where the top portion of the stem is also participating along with hemispherical region. Figures 3.11(a), (b), (c) and (d) show the mode shapes of first four natural frequencies. The first, the third and the fourth modes are degenerate modes which have a pair with same eigen frequency for an ideal resonator. The eigen frequencies for the resonator made of fused silica material with 14.6 mm mean radius and 1 mm thickness are given in the Table 3.13.

Table 3.13: First four eigen frequencies and eigen mode shapes of hemispherical resonator

Mode no	Frequency (Hz)	Mode shape
1	3855	Shell tilting
2	4474	Shell breathing
3	5459	$N = 2$ elliptical
4	8353	Stem tilting

It can be seen that the first mode is kept well above 2000 Hz which eliminates launch vibration excitation and the subsequent resoanance induced effects. The functional $N = 2$ elliptical mode eigen frequency is 5459 Hz. This mode is kept well above 2000 Hz and well separated from other nearby modes to reduce energy loss by mode interactions.

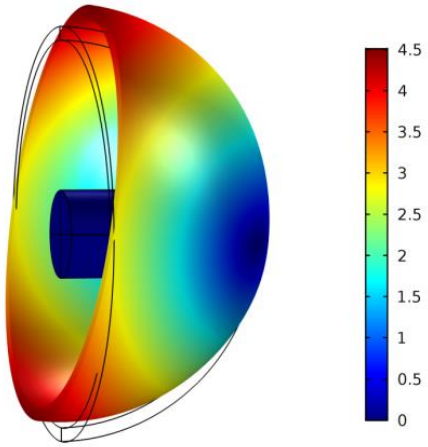

(a) Shell tilting mode with respect to shell-stem interface

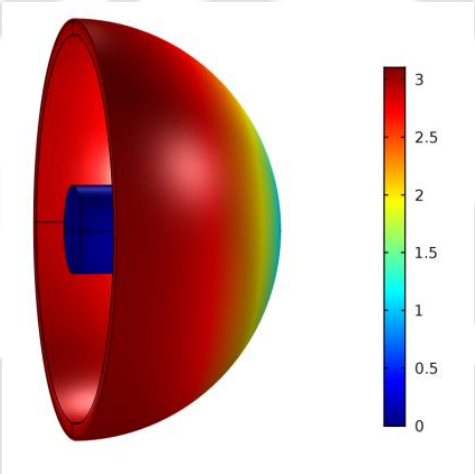

(b) Shell breathing mode with respect to shell-stem interface

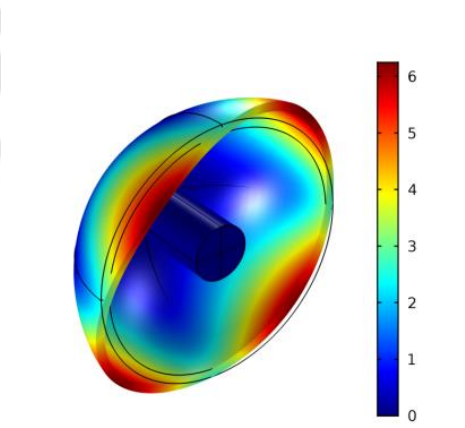

(c) $N = 2$ elliptical mode

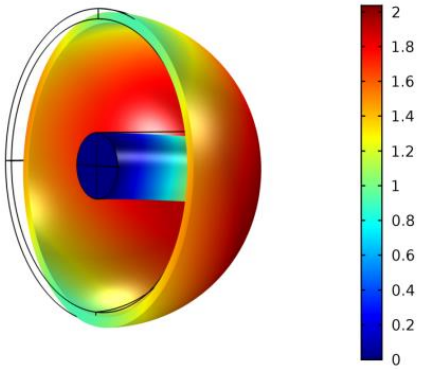

(d) Stem tilting mode

Figure 3.11: The mode shapes of first four natural frequencies of hemispherical resonator

Now, the N = 2 mode eigenfrequency is precisely compared between the modal analysis with TED and the normal modal analysis without considering TED to understand the effect of theroelastic damping on eigenfrequency. The frequencies are 5459.867 Hz and 5459.864 Hz for the cases of with and without TED respectively. There is an increase of Young's modulus from the relaxed isothermal value of Young's modulus in the presence of TED. Then, the increase of eigen frequency with TED due to the frequency dependent Young's modulus is 3 milliHz. As the operating frequency is in the range of few kiloHz in the present macro size hemispherical resonator, the frequency dependent Young's modulus change is very small and it is very close to isothermal relaxed Young's modulus. Hence, the frequency increase with TED is also very small similar to the ring resonator configuration discussed earlier.

3.3.4 Effect of resonator material property

It is clear from the original Zener model that the material property has got significant effect on the Q_{TED}. Table 3.14 gives the thermo-mechanical properties of the various ceramic and metallic materials used for the simulation. Table 3.15 gives the N = 2 mode eigen frequencies and the Q_{TED} for different ceramic and metallic materials. Fused silica shows the highest Q_{TED} (3.7×10^9) mainly because of the low coefficient of thermal expansion (more than one order less than the metals).

Table 3.14: Material properties of different ceramic and metallic materials [COMSOL]

Material	E (GPa)	α (x10^{-6} 1/K)	C_P (J/kgK)	ϑ	k (W/mK)	ρ (kg/m^3)
Silica	73	0.55	703	0.17	1.3	2203
Borosilicate	63	3.30	754	0.20	1.1	2230

Aluminum	70	23.0	904	0.35	237	2700
Ni Span C	180	7.60	500	0.25	12	8050

Table 3.15: Frequencies and Q_{TED} of hemispherical resonator for different ceramic and metallic materials

Material	Fused silica	Borosilicate	Aluminium	Ni Span C
Frequency (Hz)	5459.0	5252.8	4866.0	4609.0
Q_{TED}	3.7×10^{9}	1.5×10^{8}	2.2×10^{4}	3.3×10^{6}

Fused silica is a good choice from the low TED point of view. Hence, it is taken as the reference material to study the effect of each material property. Only one property is changed at a time keeping other properties constant. The material properties are varied as a ratio of that for the fused silica. Some material proprties have very significant effect as shown in Figure 3.12. The most significant parameter is α as it couples the thermal and the mechanical domains. Therefore, material with low α should be selected.

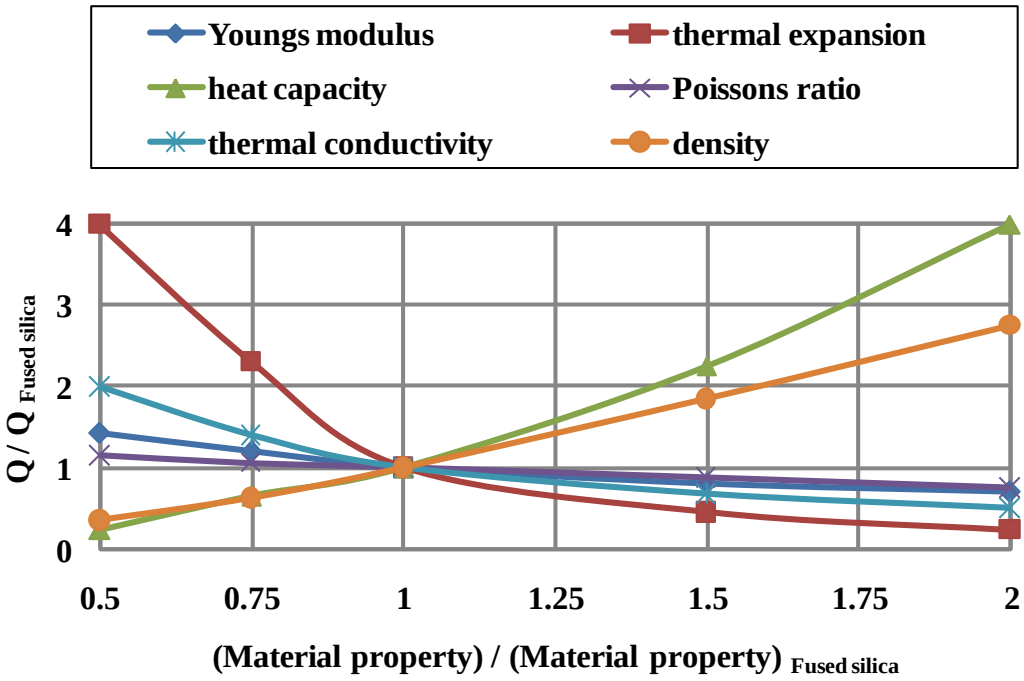

Figure 3.12: Effect of different material properties on the Q_{TED} keeping fused silica as reference material

As in the case of ring resonator, the hemispherical resonator also works nearly in the adiabatic region because the resonator frequency is much higher than the thermal relaxation

rate. A decrease in k causes a longer thermal transport time. Thus, it reduces irreversible heat transfer and increases the Q_{TED}. On the other hand, E and α do not have the same effect. An increase in E causes more thermo-mechanical coupling and reduces the Q_{TED}. Also an increase in E increases the frequency and shifts the operating region to more adiabatic and hence improves the Q_{TED}. But, a more predominant effect is the reduction of the Q_{TED} with increase of E as seen in the simuation. Increase of ρC_P helps to reduce the irreversible heat transfer. However, the increase of ρ reduces the frequency and causes the resonator to operate away from adiabatic region. C_P has sightly more influence than ρ. The effect of ϑ is not significant as compared to the other material properties.

Now, the minimum Q_{TED} possible from a fused silica material resonator is calculated. For a given material, the Q_{TED} achieves its minimum (Debye peak) when the mechanical eigen frequency equals to the relaxation thermal rate ($\omega_{mech}\tau_{th} = 1$) as discussed in section 2.1.2. Q_{freq} is equal to 2 at Debye peak as per equation (2.18). Q_{mat} of fused silica is calculated using equation (2.17) and is 2.4×10^5. Q_{TED} is the product of Q_{mat} and Q_{freq} as per equation (2.19). Thus, the minimum Q_{TED} possible for fused silica resonator is 4.8×10^5 at Debye peak while considering TED as the only loss mechanism.

3.3.5 Effect of operating temperature

The effect of the operating temperatute on the Q_{TED} is shown in Figure 3.13. When T increases, the coupling between the structural and the thermal domains increases because of the increased heat generation as per equation (2.4). This increases the temperature deviation from the absolute equilibrium temperature and reduces Q_{TED} due to the increased heat transfer. Temperature sensitivity of Q_{TED} is –0.36%/°C without considering the material property change with temperature which is close to the reported value in Darvishian *et al.* [2017].

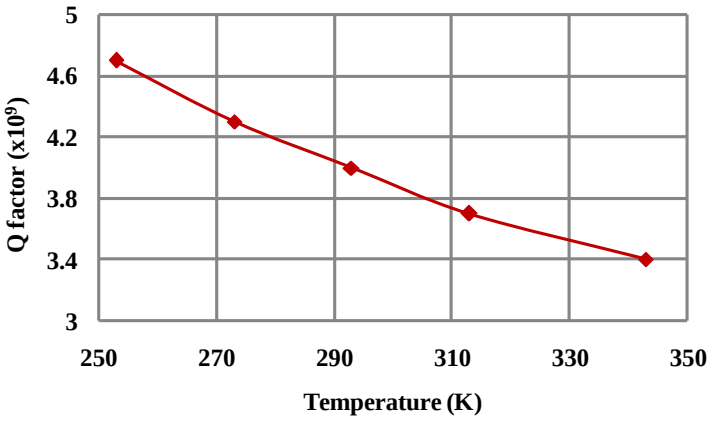

Figure 3.13: Effect of operating temperature on the Q_{TED}

Now, the effect of change in material properties with temperature on Q_{TED} is studied. The change in material property is expressed in parts per million (ppm) for a unit temperature change. The change in E, ρ, ϑ, α, C_P and k of fused silica are 141.4 ppm/°C, 0 ppm/°C, 588.1

ppm/^{o}C, 8800 ppm/^{o}C, 2130 ppm/^{o}C and 1570 ppm/^{o}C respectively (Darvishian *et al.* [2017]). The change of α with temperature is more as compared to the other material properties. Figure 3.14 shows the effect of operating temperature on the Q_{TED} with temperature dependent material properties.

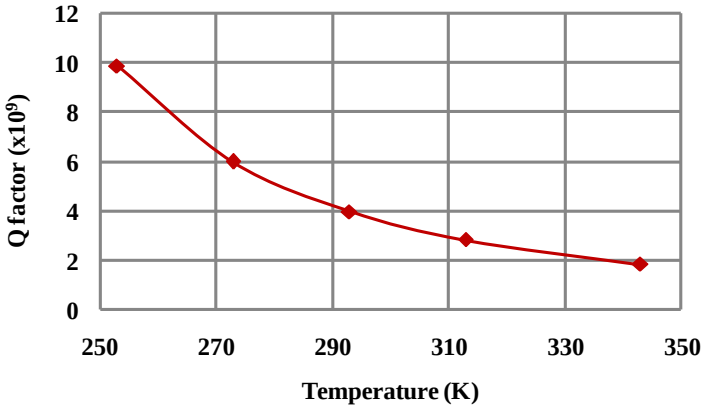

Figure 3.14: Effect of operating temperature on the Q_{TED} with temperature dependent material properties

Temperature sensitivity of Q_{TED} is as high as −3.6%/^{o}C at low temperature region when the material property change with temperature is considered. At higher temperature region, the sensitivity is −1.1%/^{o}C. The main reason for this high sensitivity with temperature is due to the strong dependence of α with temperature. Hence, lower temperature is preferred for sensor operation from thermoelastic dissipation point of view.

3.3.6 Effect of resonator geometry

Parametric study of resonator geometries such as shell mean radius, shell thickness, stem length and stem radius is done and results are shown in Figures (3.15), (3.16), (3. 17) and (3.18).

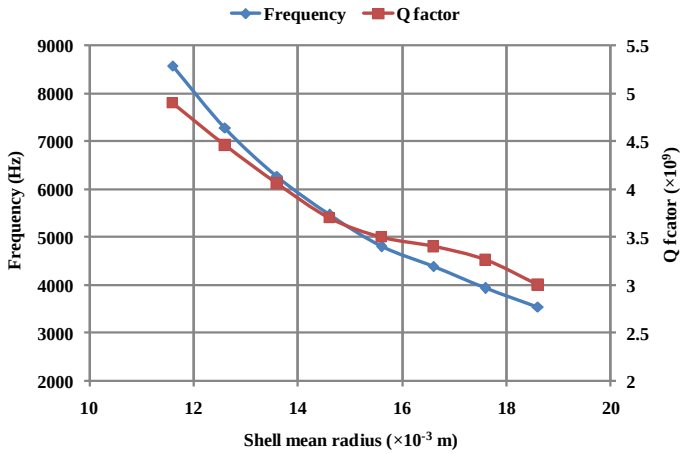

Figure 3.15: Effect of the shell mean radius on Q_{TED} and frequency

When the shell mean radius reduces, the frequency increases and the behaviour becomes more adiabatic which results in higher Q_{TED}. When the thickness is kept same, the radial direction thermal time constant remains same. Also, as discussed earlier, the polar and the circumferential thermal time constant have less influence on the Q_{TED} of this resonator size. However, heat transfer from the shell rim in the circumferential or in the polar directions influence Q_{TED} when the shell size decreases.

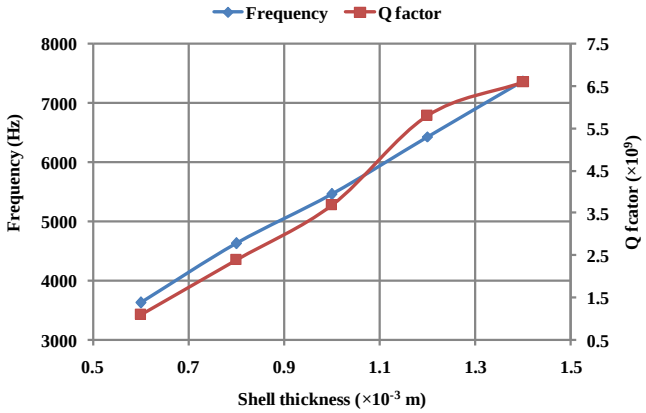

Figure 3.16: Effect of the shell thickness on Q_{TED} and frequency

When the shell thickness increases, the frequency and the radial thermal time constant increases. The shell operating region becomes more adiabatic. Both the effects result in higher Q_{TED}. The influence of shell thickness increase on Q_{TED} increase is more compared to that of the shell mean radius. For a resonator working in the region of isothermal condition, the increase in shell thickness results lower Q_{TED}. Minimum value of Q_{TED} occurs at lower frequencies as the thickness increases. This is because of the increase of thermal transport time with the shell thickness.

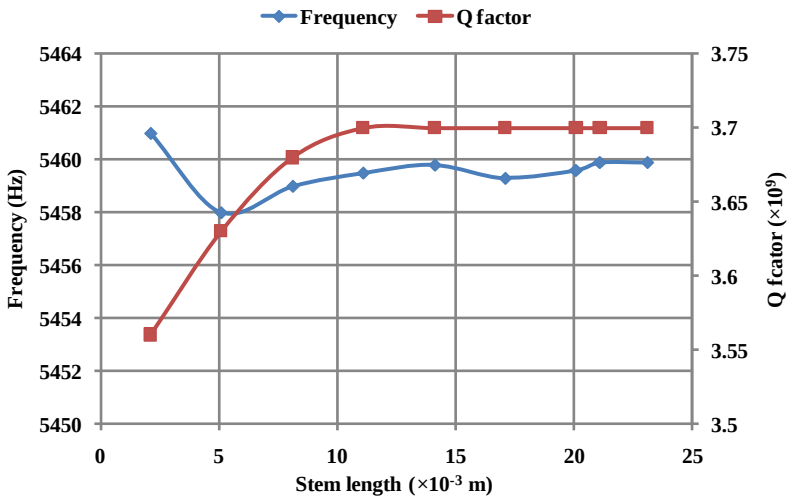

Figure 3.17: Effect of the stem length on the Q_{TED} and frequency

The effect of stem length is seen only for very short stems (stem length less than 2 mm for a shell radius of 15 mm). However, there should be sufficient length of stem for resonator mounting. Shorter stem length increases anchor loss also. Hence, the effect of very short stem is not significant for consideration.

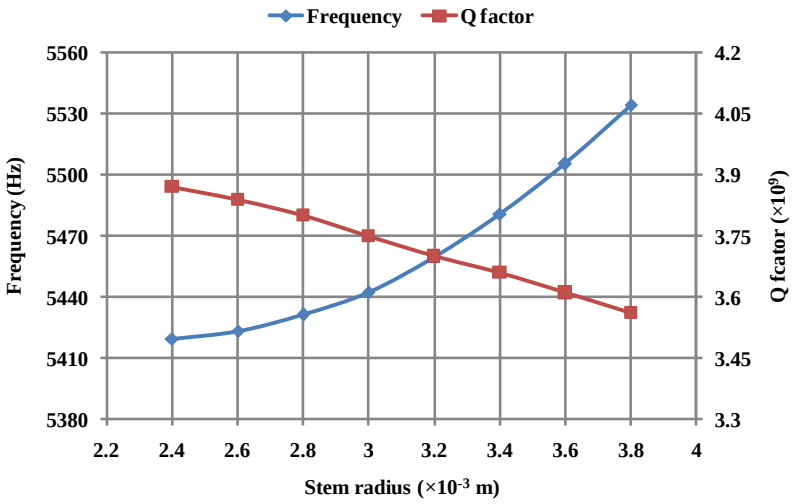

Figure 3.18: Effect of the stem radius on Q_{TED} and frequency

Smaller stem radius has higher Q_{TED} even though the Q_{TED} variation with respect to the stem radius is less.

3.4 Sensitivity study of thin film coating on TED

The resonators made from non-metallic materials are good for very low thermoelastic loss. However, the resonators need to be made electrically conductive for electrostatic excitation of its functional resonator mode and sensing of its precession for using the structure as a gyroscope. Hence, a thin layer of metallic coating need to be applied over the structure. But, most of the highly electrically conductive materials have large coefficient of thermal expansion and low TED. The primary choice of coating material is gold because of the high electrical conductivity. Hence, the effect of coating thickness, coating configurations and coating variations on TED is studied using the properties of gold which is given in Table 3.16.

Table 3.16: Material properties of gold [COMSOL]

Property	Value
Thermal conductivity	317 W/mK
Density	19300 kg/m^3
Specific heat capacity	129 J/kgK

Young's modulus	70×10^{9} N/m^2
Coefficient of thermal expansion	14.2×10^{-6} 1/K
Poisson's ratio	0.44

3.4.1 Coating studies on ring resonator

Initially, coating studies have been carried out on the ring resonator structure. Coating is done on inside and outside surfaces of ring resonator. It has been shown earlier that the Q_{TED} of ring resonator without coating is 5×10^{8}. As it is proposed to do thin film coating on ring resonator in the range of few thousands of angstrom thickness, a mesh sensitivity study has been carried out. It was seen in the section 3.2.2 that Q_{TED} is marginally sensitive to circumferential direction mesh density. Hence, coating mesh sensitivity study is carried out by varying mesh density in the radial thickness direction and in the circumferential direction. Effect of ultra low volume fraction coating is studied. The lowest coating thickness is considered (10^3 A^o) which is 0.01% of the basic shell thickness. The Young's modulus of gold is close to that of silica while the density is nearly an order higher. Modal analysis shows that the natural frequency comes down by 3 Hz only with 10^3 A^o thin film coating with respect to the uncoated ring resonator frequency mentioned in section 3.2.2. This is because the mass effect of the thin gold film is more compared to the stiffness effect in the natural frequency. Thus, the frequency change is not significant with the additional thin film coating on resonator with respect to the functional requirements. So, further studies are focussed on the effect of thin film coating on Q_{TED}. Tables (3.17) and (3.18) give the effect of mesh density in the circumferential direction and in the radial thickness direction on Q_{TED} respectively.

Table 3.17: Effect of the circumferential direction mesh density on Q_{TED}

Number of elements		Q_{TED}
Circumferential direction	Radial thickness direction	
60	6	7.3×10^{5}
80	6	1.7×10^{6}
90	6	2.5×10^{6}
100	6	3.5×10^{6}
110	6	4.2×10^{6}

Table 3.18: Effect of the radial thickness direction mesh density on Q_{TED}

Number of elements		Q_{TED}
Circumferential direction	Radial thickness direction	
100	4	3.6×10^{6}
100	6	3.5×10^{6}
100	8	3.7×10^{6}
100	10	3.6×10^{6}

It can be seen that a very thin film (very small volume fraction of coating material) metallic gold coating reduces the Q_{TED} significantly (order of two from uncoated value of 5.0×10^{8}) near the perfect adiabatic region of resonator design. Since the coefficient of thermal expansion of gold is much more compared to the fused silica, the thermo-mechanical coupling is more and leads to more heat generation. Hence, the Q_{mat} of gold is significantly less compared to that of silica. Also, the heat conduction increases due to the higher thermal conductivity of gold and the sensor operates away from the adiabatic region. Both the effects lead to a lower Q_{TED}. It can also be seen from the mesh sensitivity study that the circumferential direction mesh density has more effect on Q_{TED} compared to that in the radial thickness direction. Minimum of 100 elements are selected in the circumferential direction for further studies with thin film coating.

Simulations have been carried out by varying the coating thickness as shown in Figure 3.19. Coating thickness is varied from 10^{3} A^{o} to 10^{5} A^{o}. As the coating thickness increases, the thermoelastic damping increases due to higher entropy generation. However, the initial reduction in Q_{TED} is more even with lesser coating thickness. This is due to high strain rate at the boundary between the bulk material and the coating.

Figure 3.20 shows normalized temperature deviation (increase and decrease from absolute equilibrium temperature) in cross section of coated ring resonator and heat transfer path. Regions near to the inside and the outside surfaces show major thermal gradient as compared to the bulk fused silica material. This is because of the conductive coating on surfaces where major heat generation occurs due to vibration induced strain rate. Metal coating results in entropy generation. There is no major thermal gradient in the bulk silica material when the coating is present.

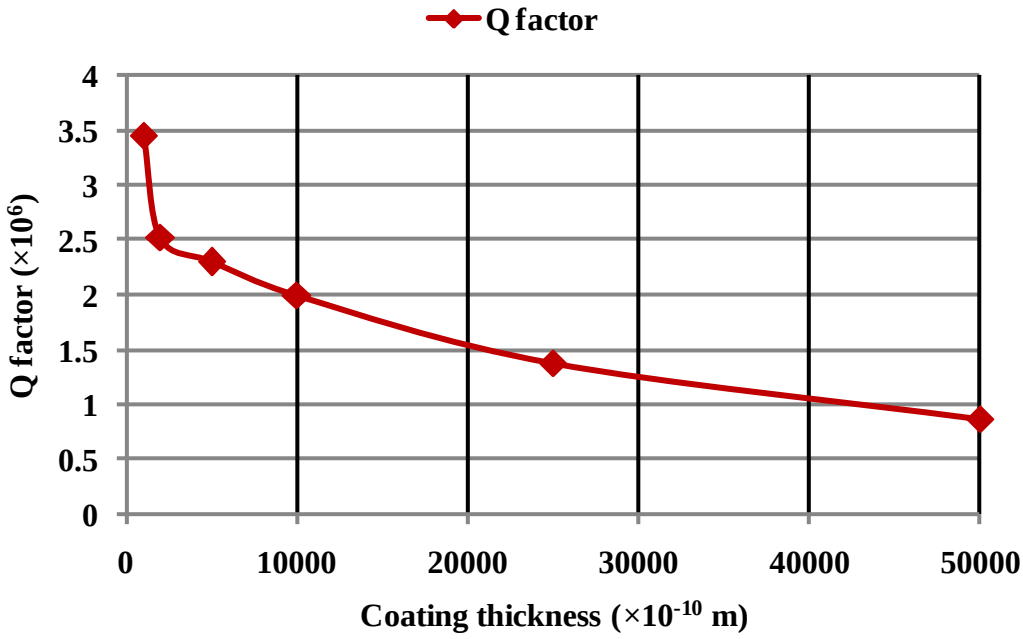

Figure 3.19: Effect of conductive thin film coating thickness on Q_{TED} of ring resonator

Generally a very thin layer of chromiun undercoat is given between the base material silica and the functional gold material for better adhesion of gold (Guzman *et al.* [2002], Darque-Ceretti *et al.* [2002]). So the effect of gold coating with a chromium undercoat is studied using the properties of chromium as given in Table 3.19. The gold coating thickness is varied keeping the chromium thickness at 500 A^{o}. The result is shown in Figure 3.21.

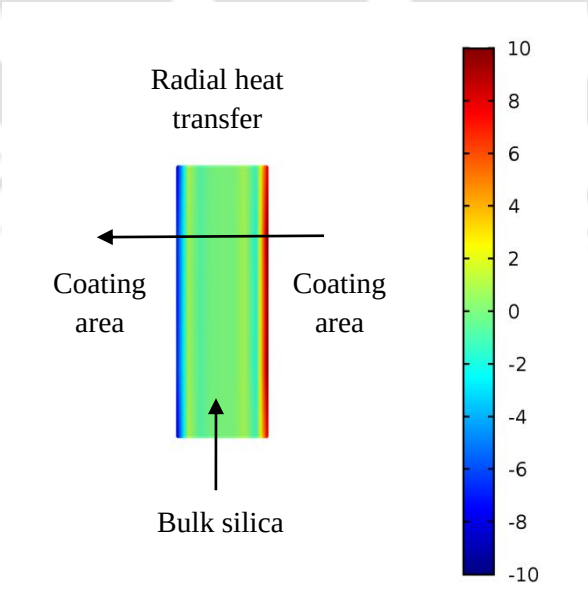

Figure 3.20: Normalized temperature deviation (increase and decrease from absolute equilibrium temperature) in cross section of coated ring resonator and heat transfer path

Table 3.19: Material properties of chromium [COMSOL]

Property	Value
Thermal conductivity	93.7 W/mK
Density	7150 kg/m^3
Specific heat capacity	448 J/kgK
Young's modulus	279×10^9 N/m^2
Coefficient of thermal expansion	4.9×10^{-6} 1/K
Poisson's ratio	0.21

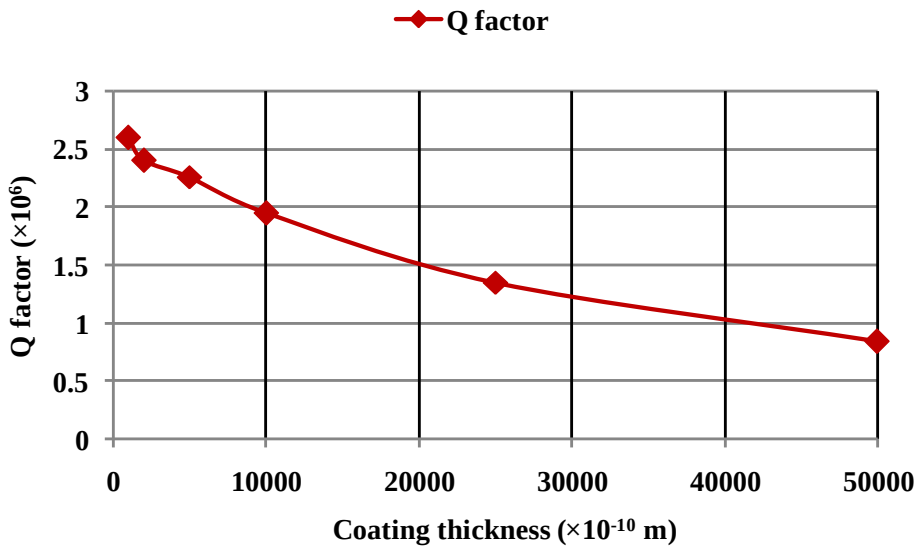

Figure 3.21: Effect of gold coating thickness on Q_{TED} of ring resonator with chromium undercoat

It can be seen that Q_{TED} further reduces because of the product of thermo-mechanical coupling parameters E and α is higher for chromium as compared to gold. The reduction is more at lower gold coating thickness and there is no significant reduction at higher coating thickness. However, Q_{TED} reduction with very thin layer of undercoat is not very significant compared to the order of magnitude reduction seen with gold coating of bare resonators.

The change of eigen frequency due to the frequency dependent Young's modulus in this coated resonator is also studied similar to the procedure discussed in section 3.2.2. The N

= 2 mode eigenfrequency of the coated resnator is compared between the modal analysis with TED and the normal modal analysis without considering TED. It is found that the eigen frequency increases by 40 milliHz in 1000 A^o coated resonator from the isothermal Young's modulus based eigen value. However, there is an increase of 7 milliHz only in the case of uncoated ring resonator as given in section 3.2.2. It shows that the change (increase) of frequency dependent Young's modulus from isothermal Young's modulus increases as the dissipation increases. The coated resonator has more TED and works more away from the adiabatic condition as compared to the uncoated resonator.

3.4.2 Effect of coating on basic hemispherical resonator configuration

Now, the effect of coating on hemispherical geometry is studied. First, the basic resonator configuration of hemispherical and inside stem is considered. The outer surface of the hemispherical area is coated with a thin gold layer. The range of coating thickness considered for the present study is based on the electrical requirement. However, thin film coating is preferred for minimum TED. Now, the effect of coating thickness on Q_{TED} is studied in detail and the result is tabulated in Table 3.20.

Table 3.20: Effect of coating thickness on basic hemispherical structure

Coating thickness (A^o)	Q_{TED}
1000	3.75×10^6
2000	3.67×10^6
5000	3.47×10^6
10000	3.18×10^6

Q_{TED} decreases significantly (order of three) even with thin film coating of 1000 A^o (coating thickness is 0.01% of 1 mm shell thickness). Further increase of coating thickness by an order results in 16% reduction in Q_{TED}. The HRG configuration is also in the adiabatic region similar to the ring resonator. Hence, high thermal conductivity coating makes the resonator operate far away from the adiabatic condition. Hence, a nominal coating thickness of 1000 A^o is preferred for low TED.

3.4.3 Effect of coating variation on hemispherical resonator configuration

There will be coating thickness variation in the polar direction and in the circumferential direction in real coating process because of the 3D configuration of the resonator. Hence, a sensitivity study is done to obtain the effect of variation of coating thickness on Q_{TED}. The results are shown in Table 3.21. No significant effect on Q_{TED} is seen for the coating thickness variation in the polar direction from 1000 A^o coating thickness at equator to 500 A^o coating thickness at pole. This is because of the fact that polar direction coating thickness variation is symmetric in the circumferential direction as far as N = 2 mode

is concerned. Then, the effect of the coating variation in circumferential direction is studied from the sensor functional requirement point of view.

Table 3.21: Effect of thin film coating thickness variation in the circumferential direction

Coating thickness (A^o)	Q_{TED} for two $N = 2$ modes	Coating variation configuration
1000	3.75×10^6 3.75×10^6	1000 A^o of 360 deg span
1000	1.0×10^7 1.1×10^7	1000 A^o of 180 deg span
1000	9.7×10^6 1.0×10^7	1000 A^o alternate sectors of 90 deg span
1000	7.0×10^6 1.9×10^7	1000 A^o alternate sectors of 45 deg span

It can be seen that the coating thickness variations has an effect on Q_{TED} variation around the circumferential direction. Effect depends on the overlap between the circumferential direction thickness variation and the $N = 2$ elliptical mode shape. There is Q_{TED} difference between the two $N = 2$ degenerate modes. The maximum difference is for 45 deg alternate coating case because degenerate modes are separated by 45 deg. Hence, it is essential to have minimum coating thickness variation over the circumferential direction to meet the functional requirement of uniform Q_{TED} in the circumferential direction which is a sensor functional requirement for minimum bias drift.

3.4.4 Effect of coating material property on Q_{TED}

Gold is a good choice from electrical property point of view. However, a study is carried out to understand the effect of thin film coating material properties on Q_{TED}. Gold is taken as the reference material to study the effect of each material property. One property is only changed at a time keeping other properties constant. The material properties are varied as a ratio of that for the gold. Some material proprties have very significant effect as shown in Figure 3.22. The most significant parameters are E and α while k and C_p are not critical parameters. The effect is same for the thermo-mechanical domain coupling properties E and α. The contribution of increased heat generation in coating material is predominant than the heat transfer resistance. Hence, the effect of thermal conductivity of coating material is not very significant.

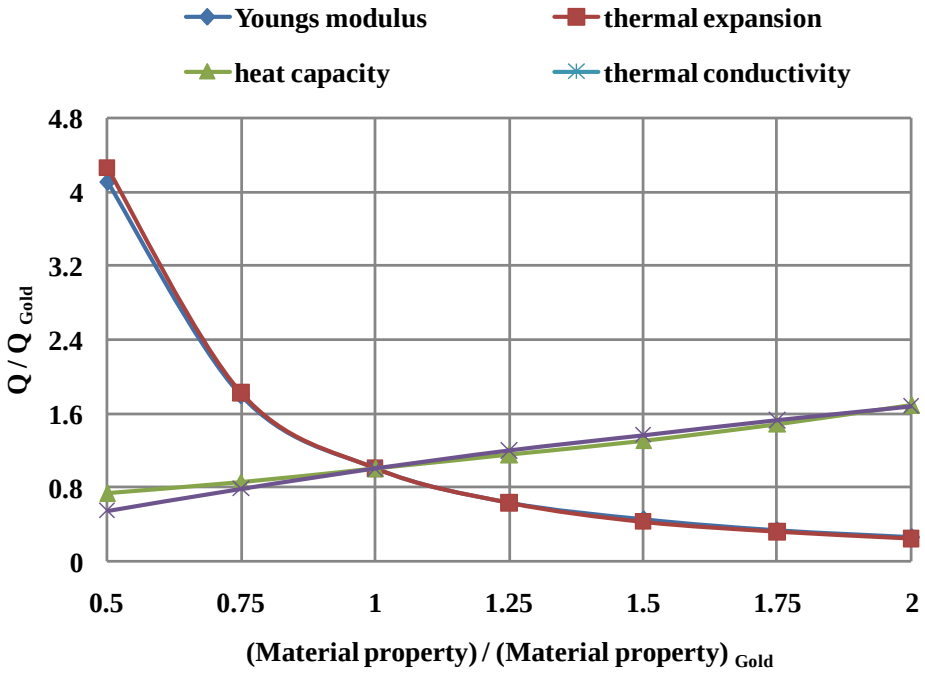

Figure 3.22: Effect of different properties of coating material on the Q_{TED} with gold as reference material

3.5 Hybrid functional resonator configuration

As explained in section 1.2.2 of Chapter 1, higher effective mass and angular gain also improves the sensor performance by reducing the mechanical noise equivalent rate (MNER). Lower MNER means lower sensor resolution. Addition of a cylindrical region below the hemispherical region increases the effective mass and the angular gain. Higher the angular gain means higher scale factor for the sensor operation. Aspect ratio of resonator is the ratio of the height of the resonator in axis of symmetry direction to the diameter of the resonator. As the aspect ratio is more for this hybrid configuration, the angular gain is more as compared to a hemispherical alone configuration. Cylindrical region also increases the effective mass participating in the $N = 2$ mode of vibration. Hence, resonator configuration in the final functional form includes hemispherical and cylindrical regions as shown in Figure 3.23.

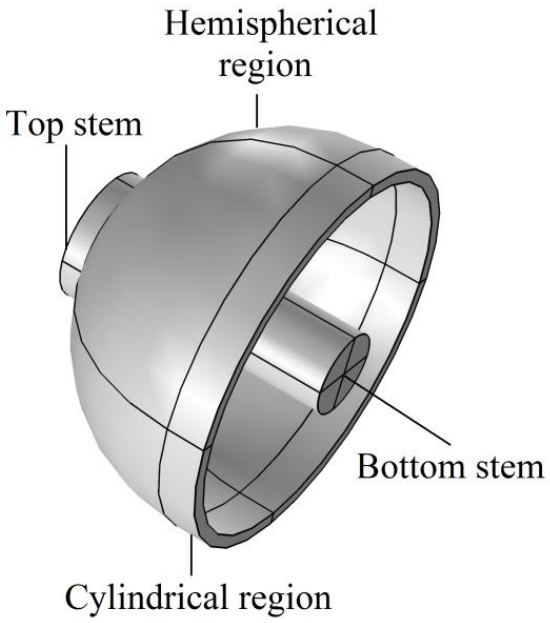

Figure 3.23: Functional hemispherical-cylindrical hybrid resonator configuration

Hemispherical region is extended with a cylindrical ring region below its equator to arrive at the hybrid configuration. The cylindrical region serves as additional increased surface area for the electrostatic forcing and sensing. This additional area increases the capacitive excitation force and generates more drive displacement and drive velocity x_d. This also increases the MNER. Increased area also increases sense capacitance which also improves the sensor SNR (signal to noise ratio) performance. Cylindrical region of the resonator can be manufactured with more precision than the hemispherical region. Hence, the cylindrical region can be used for high precision assembly of resonator between pick-off and forcer elements in order to have uniform capacitive gap for good sensor performance. The maximum displacement happens in the cylindrical ring region during resonance. This also results in more electrical output and improved signal to noise ratio. A fused silica resonator of 14.6 mm shell mean radius, 1 mm shell radial thickness with an inside stem of 3.2 mm radius and stem length projecting below the ring structure is selected for further studies. Cylindrical region has 1 mm radial thickness and 3 mm height. The final functional form also includes outside stem and filleting. The outside short stem is added for ensuring stable holding to minimize jittering during fabrication to achieve high precision. Appropriate filleting is also included in the final resonator configuration from the fabrication requirement.

3.5.1 Modal analysis for the hybrid resonator configuration

The hybrid resonator configuration consists of hemispherical region, inside and outside stem, and cylindrical region. A mapped mesh using quadrilateral elements is generated in the cross section of the resonator in a 2D plane. Then, the 2D mesh is revolved around the axis of resonator to generate 3D finite element model with hexahedral elements. Fixed boundary condition is applied at the base of the inside stem. Figure 3.24 shows finite element model of functional hybrid resonator configuration.

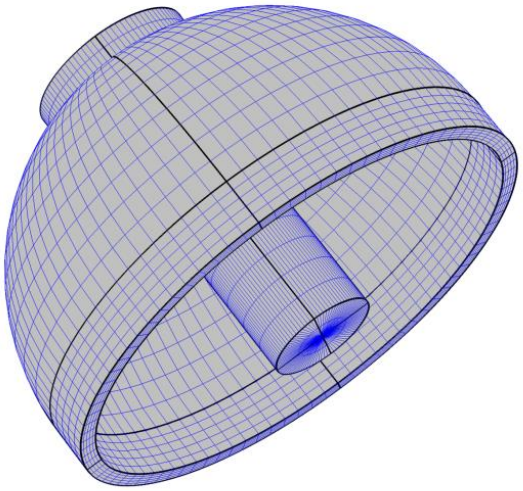

Figure 3.24: Finite element model of functional hybrid resonator configuration

In order to understand the contribution of cylindrical region and filleting to the basic resonator hemispherical configuration on first four natural frequencies, modal analysis of different configurations is carried out and results are tabulated in Tables (3.22), (3.23), (3.24) and (3.25). The frequencies are studied with respect to the separation of $N = 2$ functional mode from other nearby modes. Two cases of with and without cylindrical region and another two cases of with and without fillet are studied. Table 3.22 gives the modal analysis result of the hemispherical configuration with the inside and the outside stem without cylinderical region and fillet.

Table 3.22: First four eigen frequencies and mode shapes for the configuration without cylinderical region and without fillet

Mode no.	Frequency (Hz)	Mode shape
1	3890.2	Shell breathing
2	4354.9	Shell tilting
3	5641.5	$N = 2$ elliptical
4	5661.4	Stem tilting

It can be seen that all frequencies are well above 2000 Hz. The first mode is called the shell breathing mode. The second mode is the shell tilting mode. The third mode is the $N = 2$

elliptical mode which is the functional mode. The fourth mode is the stem tilting mode. However, the functional mode and the stem tilting mode are very close.

Table 3.23: First four eigen frequencies and mode shapes for the configuration with cylinderical region and without fillet

Mode no.	Frequency (Hz)	Mode shape
1	3404.7	Shell breathing
2	3669.0	Shell tilting
3	5196.2	$N = 2$ elliptical
4	5206.8	Stem tilting

It can be seen that the addition of the cylindrical region decreases all the frequencies due to the additional mass of cylindrical region. Also, the functional mode and the stem tilting mode are very close.

Table 3.24: First four eigen frequencies and mode shapes for the configuration without cylinderical region and with fillet

Mode no.	Frequency (Hz)	Mode shape
1	4216.9	Shell breathing
2	4477.7	Shell tilting
3	6366.7	$N = 2$ elliptical
4	7473.8	Stem tilting

It can be seen that the filleting increases the hemispherical root stiffness and increases all the frequencies. There is sufficient separation between the functional mode and the nearby modes. Now, the final functional configuration with all the features is considered.

Table 3.25: First four eigen frequencies and mode shapes for the final functional hybrid configuration resonator with cylindrical region and with fillet

Mode no.	Frequency (Hz)	Mode shape
1	3696	Shell breathing
2	4097	Shell tilting
3	5567	N = 2 elliptical
4	6364	Stem tilting

It can be seen that the natural frequency requirements of all the modes are met from launch operational load and low energy loss requirement point of view. The first mode is kept well above 2000 Hz to avoid the rocket launch induced mechanical undesired loading on the resonator and its performance deviations. In order to avoid the energy loss from the functional mode due to energy coupling from nearby modes, N = 2 mode eigen value is kept separated from the nearby modes by more than 500 Hz.

In this final functional hybrid configuration, Q_{TED} of N = 2 mode is 2.9×10^{9}. Advantages of this hybrid configuration in terms of performance parameters such as effective mass and angular gain, is further studied quantitatively and compared with the hemispherical alone configuration.

3.5.2 Performance parameters

The Coriolis force expression mentioned in equation (1.1) is valid for single mass discrete type vibratory gyroscopes where the entire mass element experiences Coriolis acceleration during the input rotation. In order to make Coriolis force expression applicable to all resonant gyroscopes, two terms such as the effective mass and the angular gain are defined. Thus, the general Coriolis force equation (1.2) is defined which includes the effective mass and the angular gain. This is applicable for continuous mass distribution vibrating shell type gyroscopes such as HRG where the kinetic energy of total structural mass does not contribute to the Coriolis force. The value of these parameters depends on the gyroscope material, resonator configuration and resonant mode shapes.

3.5.2.1 Effective mass

It is defined as the amount of the mass that has the exact same kinetic energy as the real gyroscope when the mass is resonating with an amplitude equal to the largest deflection

of the real gyroscope structure (Darvishian [2018]). The total kinetic energy corresponding to the N = 2 mode frequency is obtained from the modal analysis. The velocity of the antinodal point at the rim of the resonator, where there is largest deflection at the N = 2 mode frequency, is also obtained from the modal analysis. Then, the effective mass is calculated using the kinetic energy of the mode of vibration and velocity of the antinode. The expression for the effective mass is given by:

$$m_{eff} = \frac{2 \times \text{Kinetic energy}}{(\text{Velocity of } N = 2 \text{ antinode})^2} \tag{3.7}$$

Then, the effect of cylindrical region height on effective mass is studied and result is shown in Figure 3.25.

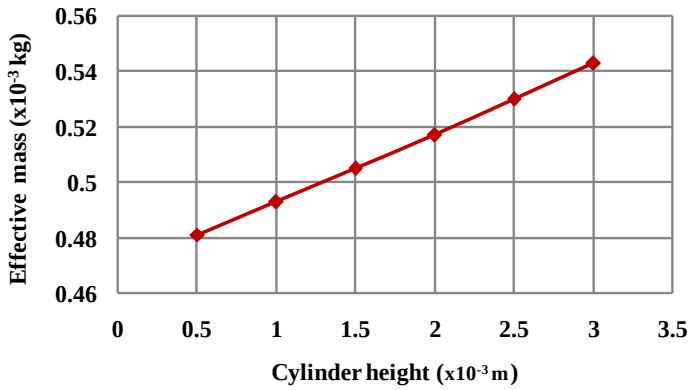

Figure 3.25: Variation of effective mass of hybrid resonator with cylindrical region height

It can be seen that effective mass increases linearly with increase in height of the cylindrical region. However, increase in the cylindrical region height also increases the size of the resonator and the sensor. Hence, the cylindrical region height is limited to 3 mm. Table 3.26 gives the effective mass for hemispherical alone configuration and hemispherical-cylindrical hybrid configuration.

Table 3.26: Comparison of the effective mass of hemispherical and hybrid configuration

Configuration	Kinetic energy of N = 2 mode (J)	Velocity of antinode of N = 2 mode (m/sec)	Effective mass, m_{eff} ($\times 10^{-3}$ kg)
Hemispherical alone configuration	8.26×10^{6}	1.88×10^{5}	0.467
Hemispherical - cylindrical hybrid configuration	4.57×10^{6}	1.30×10^{5}	0.543

It can be seen that the effective mass of hybrid resonator configuration is 16% more than that of a hemispherical alone configuration due to the additional cylindrical region. This improves the sensor resolution by reducing the MNER.

3.5.2.2 Angular gain

Angular gain (A_g) is defined as the ratio of Coriolis force generated in the resonating structure to a single mass gyroscope with the same effective mass. Angular gain is a parameter that shows ability of a gyroscope to transfer motion from the driving direction to the sensing direction using Coriolis acceleration. This parameter is one for single mass discrete type gyroscope. However, this parameter decreases to lower values for gyroscopes with continuous mass such as shell gyroscopes and its value is calculated numerically. For a given geometry, A_g gives the portion of the effective mass that actually contributes to generate the Coriolis force. Thus, A_g becomes the scale factor in the rate-integrating gyro (RIG) (Cho [2012]). As discussed in Chapter 1, A_g directly affects the resolution of the gyroscope. Hence, the higher angular gain gives better sensor performance.

Now, the effect of the hybrid configuration on angular gain is discussed quantitatively. The Coriolis force induced by the input angular velocity (Ω) of the shell will cause the $N = 2$ natural frequency of the vibration mode of the non-rotating shell to bifurcate into two frequencies (Hwang *et al.* [1997]). It causes the vibration mode to be split into two travelling waves such as the forward travelling wave with higher frequency than the nominal frequency (with no Coriolis force) and backward travelling wave with lower frequency than the nominal frequency (with no Coriolis force). The forward travelling wave has an angular frequency of ($\omega+2A_g\Omega$) and the backward travelling wave has an angular frequency of ($\omega-2A_g\Omega$). The angular gain can be obtained by normal mode analysis with input angular velocity (Ω) to produce Coriolis force and observing the frequency bifurcation of $N = 2$ mode. A_g can be obtained from the following relationship using the frequency split and the input angular velocity for a given mode number.

$$A_g = \frac{\pi \Delta f}{N \Omega} \tag{3.8}$$

where Δf is the frequency split due to input angular velocity, N is the vibration mode number, Ω is the input angular velocity. Now, the effect of the cylindrical region height on the angular gain is studied and result is shown in Figure 3.26. It can be seen that angular gain increases linearly with increase in height of cylindrical region.

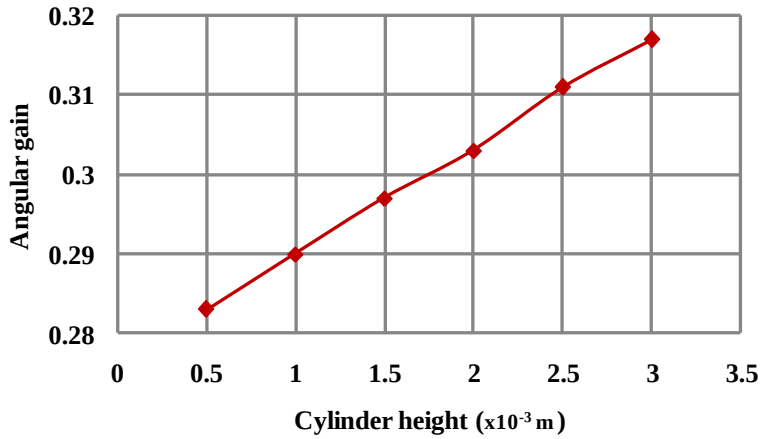

Figure 3.26: Variation of angular gain of the hybrid resonator with cylindrical region height

The angular gains (A_g) are compared for the hemisphere alone configuration and the hybrid configuration with cylindrical region of 3 mm height, and tabulated in Table 3.27.

Table 3.27: Comparison of angular gain of hemispherical and hybrid configuration for N = 2 mode

Configuration	Input angular velocity, Ω (rad/sec)	Frequency split, Δf (Hz)	Angular gain, A_g
Hemispherical alone configuration	0.5	0.088	0.276
	1.0	0.175	0.275
	5.0	0.877	0.275
Hemispherical - cylindrical hybrid configuration	0.5	0.101	0.317
	1.0	0.202	0.317
	5.0	1.00	0.315

It can be seen that there is a 15% increase in angular gain for the case of hybrid configuration. Hence, the hybrid configuration is better than the hemispherical alone configuration for better sensor performance.

Now angular gain is calculated for N = 3 mode of operation also. The N = 3 frequency for the hemispherical alone configuration is 13892.88 Hz while that of hybrid configuration is 13173.13 Hz. The angular gain calculation is done for hemispherical alone configuration and hybrid configuration, and the comparison is given in Table 3.28.

Table 3.28: Comparison of the angular gain of hemispherical and hybrid configuration for N = 3 mode

Configuration	Input angular velocity, Ω (rad/sec)	Frequency split, Δf (Hz)	Angular gain, A_g
Hemispherical alone configuration	0.5	0.077	0.161
	1.0	0.150	0.157
	5.0	0.770	0.161
Hemispherical - cylindrical hybrid configuration	0.5	0.090	0.190
	1.0	0.170	0.178
	5.0	0.870	0.180

It can be seen that N = 2 mode has 75% more angular gain for both the configurations. Hence, N = 2 mode is considered for the functional mode as it gives lower MNER and good sensor resolution. From the performance parameters study, the hybrid configuration with N = 2 as functional mode is selected. Hence, thin coating studies are carried on hybrid configuration also.

3.5.3 Coating studies on hybrid configuration resonator

The effect of 1000 A^o coating thickness on individual regions such as cylindrical region and hemispherical region is analyzed first. Then, the effect of partial area coating is studied. Finally, coating thickness parametric study on the hybrid configuration resonator is also carried out.

3.5.3.1 Effect of coating on individual regions of resonator

The effect of coating on individual regions such as the cylindrical region and the hemispherical region is analyzed with two cases of inside surface coating and outside surface coating. The result is tabulated in Table 3.29.

Table 3.29: Q_{TED} for different thin film coating configurations

Coating configuration	Q_{TED}
Cylindrical region alone outside surface	8.3×10^7

Hemispherical region alone outside surface	4.5×10^{6}
Cylindrical region and hemispherical region outside surfaces	4.4×10^{6}
Cylindrical region alone inside surface	7.3×10^{7}
Hemispherical region alone inside surface	4.8×10^{7}
Cylindrical region and hemispherical region inside surfaces	3.1×10^{7}
Cylindrical region and hemispherical region, inside and outside surfaces	4.0×10^{6}

It can be seen from the Table 3.29 that the Q_{TED} comes down by two orders from the order of 10^{9} even with coating only on the cylindrical region. Q_{TED} further comes down with both regions coating and reaches of the order of 10^{6}. Now, the effect of different coating configurations on TED is discussed with respect to the thermoelastic strain patterns and the resulting temperature deviation patterns from equilibrium temperature. Figures (3.27) and (3.28) are the normalized displacement profile and the temperature deviation plot for outside coating case. Figures (3.29) and (3.30) are the normalized displacement profile and the normalized temperature deviation plot for inside coating case.

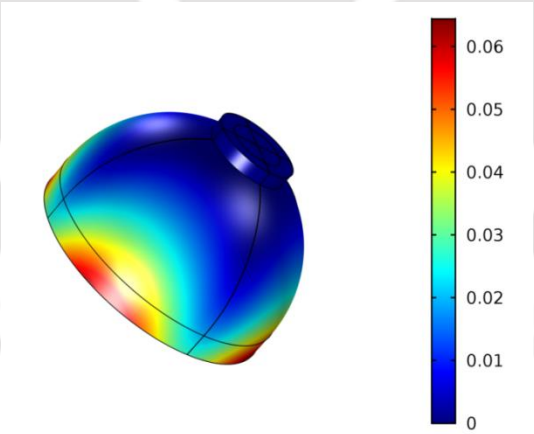

Figure 3.27: Normalized displacement profile for outside coating

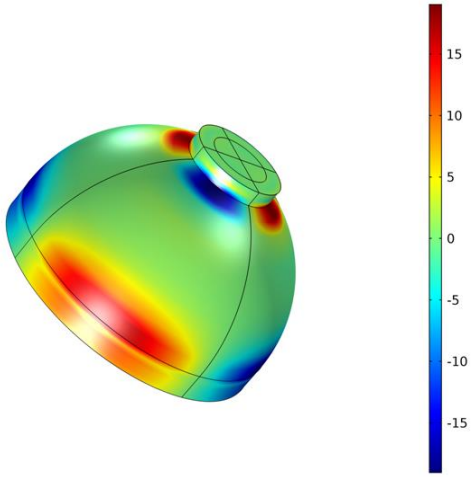

Figure 3.28: Normalized temperature deviation profile for outside coating

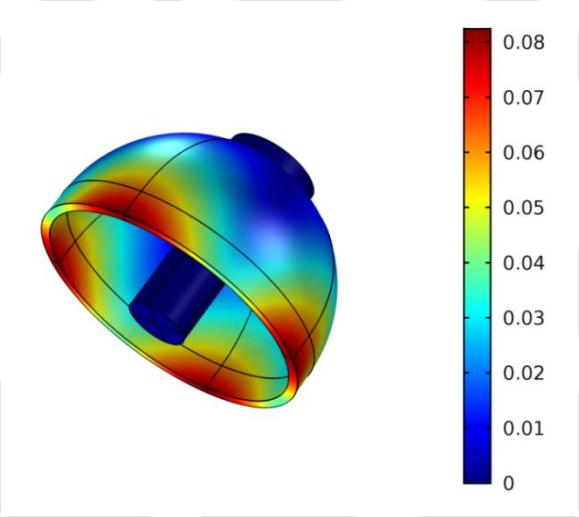

Figure 3.29: Normalized displacement profile for inside coating

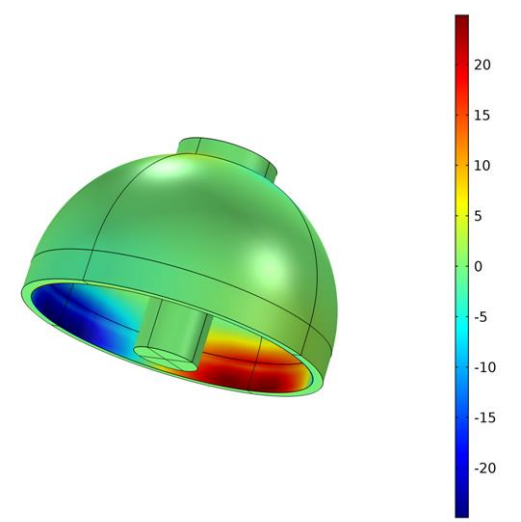

Figure 3.30: Normalized temperature deviation profile for inside coating

Temperature deviation pattern, which is the representation of strain, is different for inside and outside coating cases. Outside coating configuration has additional strain at the polar region of the hemisphere. The thermal relaxation time is further reduced at the polar region in the circumferential direction. The resonator with outside coating deviates more from the adiabatic condition due to the additional heat transfer. Hence, Q_{TED} reduction is more for the outside coated case. It can be concluded that Q_{TED} is sensitive to the coating configuration. Now, the effect of gold coating on the bottom face (1 mm radial thickness face) of cylindrical region is studied for different coating thickness and the result is tabulated in Table 3.30.

Table 3.30: Effect of the thin film coating thickness on bottom face of cylindrical region

Coating thickness (A^o)	Q_{TED}
No coating	2.90×10^9
1000	2.83×10^9
10000	2.47×10^9
25000	1.21×10^9
50000	0.29×10^9

It can be seen that the coating on this face has negligible effect for the proposed lower coating thickness range compared to other cylindrical and spherical surface coatings. Only orders of higher coating thickness have effect on Q_{TED}. Hence, the requirement of the coating on this surface can be decided based on other functional aspects than Q_{TED}.

3.5.3.2 Effect of partial coating configuration of resonator

Now the effect of partial coating is studied for different latitude coating angles from the equator. The results are shown in Tables (3.31) and (3.32).

Table 3.31: Effect of the partial outside thin film coating configuration in polar direction

Latitude coating angle from the equator (deg)	Q_{TED}
90	4.40×10^6
60	6.16×10^6
45	1.04×10^7
30	8.81×10^6
15	1.43×10^7
10	1.65×10^7

Table 3.32: Effect of the partial inside thin film coating configuration in polar direction

Latitude coating angle from the equator (deg)	Q_{TED}
55	3.17×10^{7}
45	3.66×10^{7}
30	3.44×10^{7}
15	4.26×10^{7}
10	4.13×10^{7}

This is simulated for inside and outside coating cases with 1000 A^{o} thickness. It can be seen that the effect of the coating latitude angles from the equatorial plane has got a significant effect on the Q_{TED}. Q_{TED} increases as the coating area reduces with reduced latitude angle of coating. Inside coating is done only upto the latitude coating angle of 55 deg due to the inside stem and the fillet area.

3.5.3.3 Effect of coating thickness on Q_{TED}

Coating thickness is varied from 1000 A^{o} to 10000 A^{o} and the results are tabulated in Table 3.33 for outside and inside coating cases. Q_{TED} reduces as the coating thickness increases in both cases. Q_{TED} reduces by 17% for the outside coating case while it reduces by 25% for the inside coating case.

Table 3.33: Effect of the thin film thickness for outside and inside coating

Coating thickness (A^{o})	Q_{TED}	
	Outside coating	Inside coating
1000	4.40×10^{6}	3.17×10^{7}
3000	4.27×10^{6}	2.99×10^{7}
5000	4.07×10^{6}	2.76×10^{7}
10000	3.62×10^{6}	2.35×10^{7}

3.6 Summary

In this chapter, the quantitative requirement of Q factor is arrived for the mechanical resonator for a high performance HRG. Hemispherical geometry is considered for the design of the resonator. The basic size of the resonator is arrived to achieve high Q_{TED}. The specific advantages of hybrid resonator configuration are brought out in terms of improved effective mass and angular gain. The selection of the $N = 2$ mode as the functional mode is also justified considering the performance parameter. A sensitivity study of the resonator material, dimensions and temperature on TED is carried out. TED is sensitive to the resonator material property and the hemisphere shell thickness and the mean radius. It is found that TED is not the limiting damping mechanism for an uncoated fused silica macro scale resonator of few millimetres size with respect to a quality factor requirement of few millions. Then, detailed TED simulations have been carried out with thin film electrically conductive coating. The effect of coating variations and configurations on TED is also carried out. It is seen that the thin film coating reduces the TED by few orders and limits the Q factor to few millions for a macro scale fused silica hemispherical resonator.

Chapter 4

Anchor loss and sensitivity study

In a resonating HRG hemispherical shell, elastic waves are generated when the resonator applies harmonic forces and moments at the point of attachment to the support. The elastic waves carry away energy from the resonator and results in Q_{Anchor} reduction. Since the analytical expressions are available only for very simple structures, numerical simulation is therefore used for the estimation of Q_{Anchor}. COMSOL is used for numerical simulations in the present study. Perfectly matched layer (PML) concept is used in COMSOL to generate a perfectly absorbing medium for the elastic waves in the support structure. The construction of the PML is done in such a way that the wave energy is fully attenuated in the PML so that there will not be any reflected energy back to the resonator.

This chapter deals with the detailed study on anchor loss and the critical factors which affect the Q_{Anchor}. It covers anchor loss estimation, dimensional and geometric parametric study, and impact of possible fabrication imperfections. The effects of mode interactions and unbalance mass pattern on frequency split, Q_{Anchor} and Q_{Anchor} mismatch are also discussed.

4.1 Numerical modeling of anchor loss in hemispherical resonator

For the fused silica material HRG, propagating wave properties are estimated using equations (2.28), (2.29), (2.30) and (2.31) as given in Chapter 2. Table 4.1 gives the propagating wave properties evaluated for PML region parameter estimation.

Table 4.1: Propogating wave properties for hemispherical resonator

N = 2 mode eigen frequency, f (Hz)	Speed of sound (longitudinal), C_L (m/sec)	Speed of sound (transverse), C_T (m/sec)	Wavelength (longitudinal), ζ_L (m)	Wavelength (transverse), ζ_T (m)	Wave number, υ (1/m)
5459	5968	3763	1.07	0.67	1

The finite element model of resonator with substrate and PML region is shown in Figure 4.1. Quadratic shape function is used for the displacement field. A mapped mesh using the quadrilateral elements are generated in the cross section of the resonator, the substrate and the PML in a 2D plane. Then, the 720 elements in the 2D mesh are revolved around the axis of the resonator to generate the 3D mesh with a total of 23040 hexahedral elements. Figure 4.2 shows zoomed view of the finite element model of resonator for anchor loss simulation.

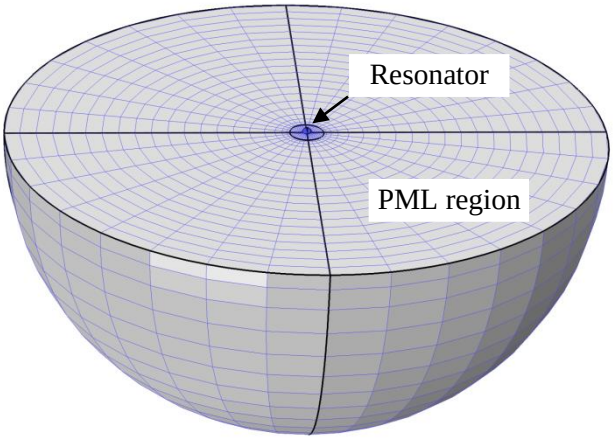

Figure 4.1: Finite element model of resonator with substrate and PML region

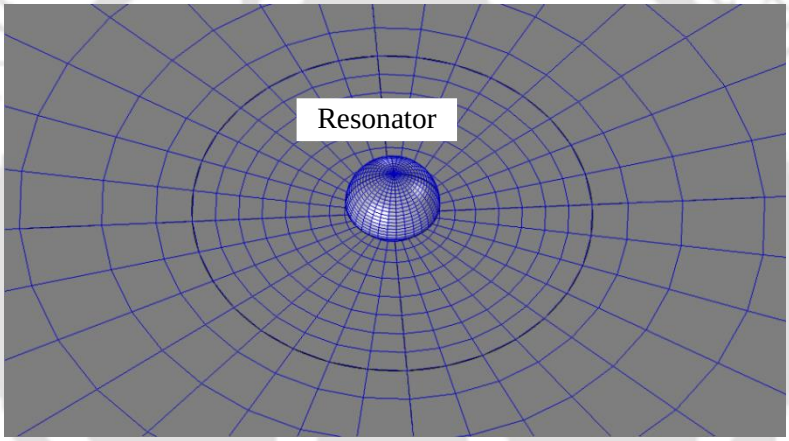

Figure 4.2: Zoomed view of finite element model of resonator for anchor loss simulation

Figure 4.3 shows half cross section view of finite element model of resonator with substrate and PML region where PML is modelled beyond the mounting substrate structure. The resonator is located at the top left corner of Figure 4.3. Zoomed cross section view of finite element model of resonator for anchor loss simulation is shown in Figure 4.4 as the size of resonator is small compared to the PML size.

Anchor loss prediction using FE is sensitive to parameters such as PML thickness and mesh size. Modelling parameters of PML are arrived based on the guidelines in Frangi *et al.* [2013]. It is always a good practice to select PML size (W_{PML}) as a function of wave number (υ) such that $\upsilon W_{PML} > 0.1$ to optimize the global size of the problem and Q_{Anchor} convergence. Larger value of W_{PML} results better Q_{Anchor} convergence. This ensures that the waves entering to the PML are totally absorbed within the PML. In order to avoid spurious reflections and allow for a smooth dissipation of waves, the decay over one single element should be limited by setting an upper bound on the typical dimension of elements. PML should be modelled

with fine mesh size elements. 25 elements are in the radial direction and 32 elements are in the circumferential direction in the PML region.

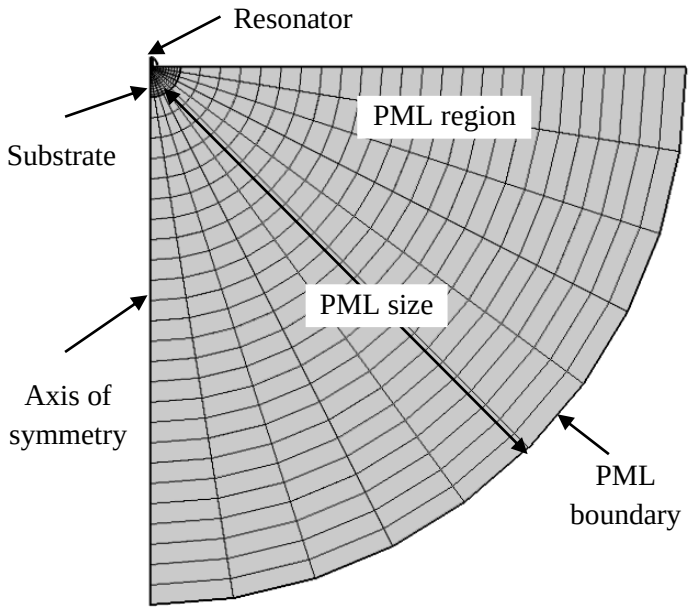

Figure 4.3: Half cross section view of finite element model of resonator with substrate and PML region

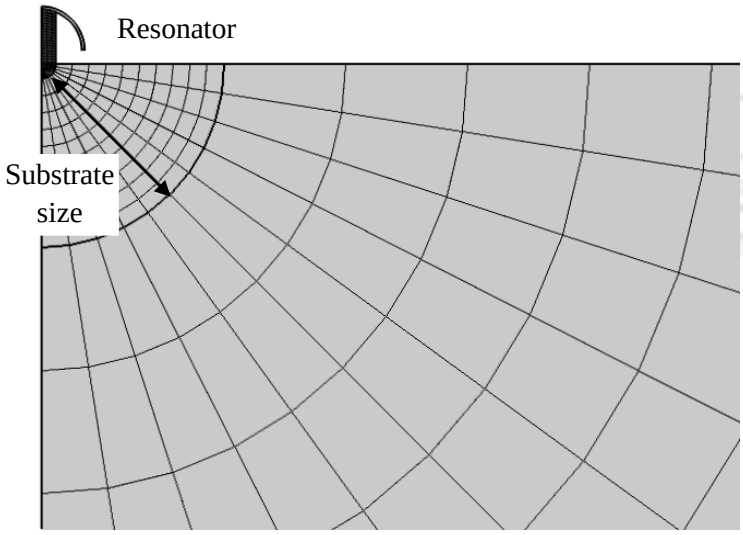

Figure 4.4: Zoomed cross section view of finite element model of resonator for anchor loss simulation

The central stem is mounted to the substrate. The substrate is considered as a hemispherical volume with radius equal to 10×(stem diameter) and the calculated radius is 0.064 m. Spherical volume is suitable for the PML as it effectively absorbs waves from the hemispherical resonator (Darvishian *et al.* [2017]). Fixed boundary condition is applied at the PML outer surface. As explained earlier, Q_{Anchor} is expressed in terms of the ratio of the

imaginary part to the real part of the resonant angular frequency. Thus, this eigen value problem is numerically solved to obtain the Q_{Anchor}. Different PML sizes and the corresponding Q_{Anchor} for present HRG resonator configuration are given in Table 4.2. For PML size equal to or more than one wavelength, Q_{Anchor} converges to 10^{11}. PML size is chosen as equal to the one wavelength based on this Q_{Anchor} convergence study for further simulations. This ensured that the waves entering to the PML is totally absorbed within the PML.

Table 4.2: PML size and Q_{Anchor} of HRG configuration

PML size (m)	Q_{Anchor}
0.87	2.2×10^{10}
0.97	4.5×10^{10}
1.07	4.1×10^{11}
1.17	1.9×10^{11}
1.27	1.3×10^{11}

Now, how the energy is propagated from the resonator to the substrate is shown using the normalized resultant displacement obtained from the eigen value problem. The normalized displacement plot is shown in Figure 4.5 where the maximum displacement is seen at the rim of the hemispherical resonator. Figure 4.5 shows displacement result of a portion of the total numerical simulation domain. Figures (4.6) and (4.7) show normalized displacement plots of stem and a portion of substrate where the normalization is done with respect to hemisphere rim displacement. It can be seen from Figure 4.6 that the normalized resultant displacement at the stem is less compared to the rim displacement because of the symmetrical hemispherical structure which cancels the majority of the displacement from the resonator rim. Also, the stem is interfaced to the nodal point of the $N = 2$ mode of the hemispherical resonator. Since the cross-section displacement plot is taken along one of the $N = 2$ mode axis, the top corners of the stem are showing the maximum displacement in Figure 4.6. Smaller stem radius reduces the anchor loss as the anchoring location is further away from the maximum displacement rim location. Smaller stem radius also reduces $N = 2$ frequency as effective hemispherical radius from the rim to the anchor location increases. The normalized displacement of substrate in Figure 4.7 is very much less compared to that of the resonator and the stem. This shows that there is negligible energy transfer to the substrate when there is lengthy stem which connects the nodal point in the hemisphere to the substrate. The length of the stem helps to cancel out the waves that come from both sides of shell which is under $N = 2$ mode resonance. Hence, very less energy is transferred to the substrate. This is the reason for high Q_{Anchor} for an ideal highly symmetrical hemispherical resonator with inside stem which has sufficient length. It is to be noted that PML concept provides an over

estimate of Q_{Anchor} as it is a full absorbing layer and no reflections goes back to the resonator. Inevitably, some vibration will be reflected back into the resonator in a real gyroscope. However, PML concept is globally used by researchers for anchor loss prediction. PML is used more specifically for studying the effect of geometric dimensions and imperfections on Q_{Anchor}. Now, the sensitivity of geometric dimensions on Q_{Anchor} is studied.

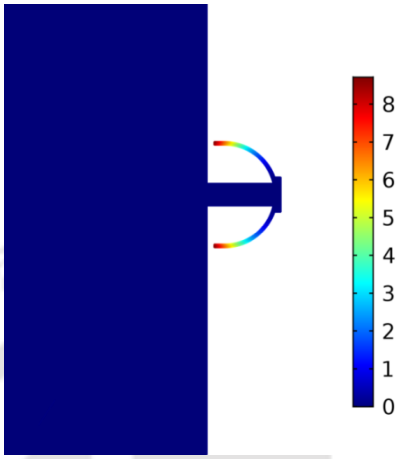

Figure 4.5: Normalized displacement plot of eigen value solution of anchor loss simulation

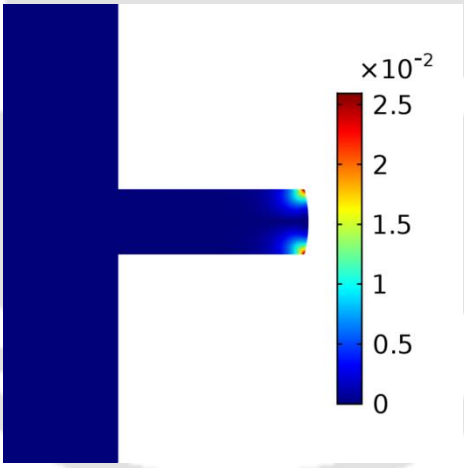

Figure 4.6: Normalized displacement (with respect to hemisphere rim) plot of the stem and portion of the substrate

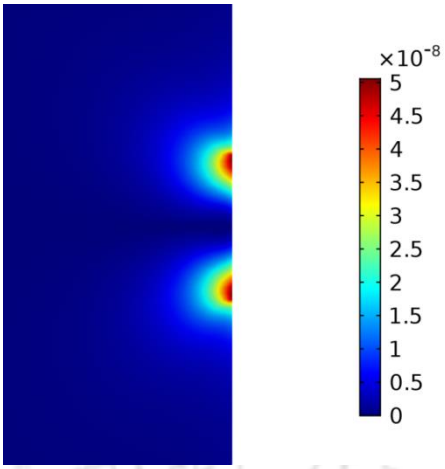

Figure 4.7: Normalized displacement (with respect to hemisphere rim) plot of portion of the substrate

4.2 Effect of resonator geometric parameters

4.2.1 Shell radial thickness

The effect of shell radial thickness is studied by changing the outer radius of the shell keeping the inner radius constant. Shell radial thickness is varied from 0.5 mm to 2 mm. It is found that the frequency is increasing and the Q_{Anchor} is decreasing with increase in shell radial thickness as shown in Figure 4.8. As the shell radial thickness increases, shell becomes stiffer and induces more deformation to the substrate through the stem. Thus, more wave energy propagates to the substrate and reduces the Q_{Anchor} due to the increased substrate deformation. Lesser shell radial thickness is good for higher Q_{Anchor}. This is similar to the observation for cantilever beam where thicker resonator has lesser Q_{Anchor}. Since the frequency is coming down as the radial thickness reduces, it is not suitable for Q_{TED}. The closeness of N = 2 mode with other frequencies also reduces Q_{Anchor}. Hence, radial thickness of 1 mm is optimum from the Q_{TED} and Q_{Anchor} point of view.

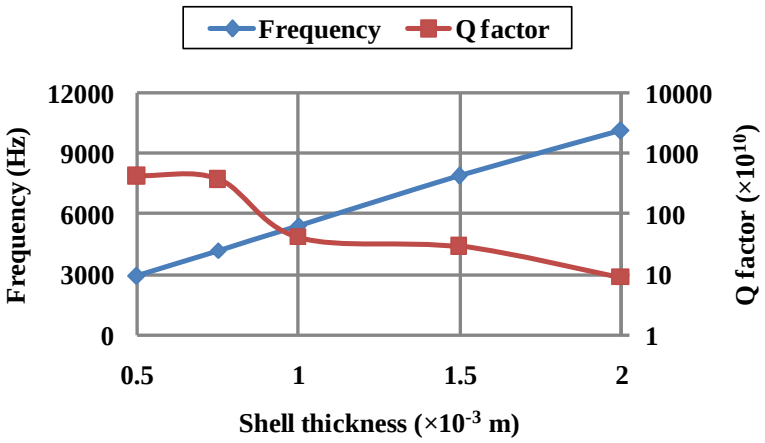

Figure 4.8: Effect of the shell radial thickness on Q_{Anchor}

4.2.2 Shell mean radius

The effect of the shell mean radius on the anchor loss is studied and results are shown in Figure 4.9. As the shell mean radius increases, $N = 2$ frequency decreases. As the shell radius increases, the anchor location is moving away from hemispherical rim region where maximum deformation occurs. Thus, wave energy propagates to the stem is less and increases the Q_{Anchor}. This is similar to the effect of length increase on Q_{Anchor} for the cantilever beam resonator configuration.

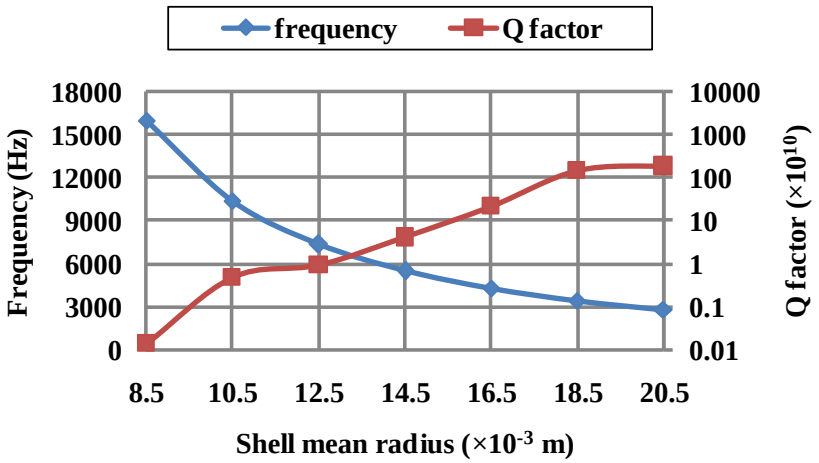

Figure 4.9: Effect of the shell mean radius on Q_{Anchor}

4.3 Effect of mode interactions

Stem is provided as a supporting element for the shell hemispherical resonator to its mounting substrate. As explained earlier, inside stem configuration with sufficient length is considered based on low anchor loss, and better vibration and shock sensitivity. Effect of shell radial thickness and stem length on the frequency and the Q_{Anchor} is now studied based on the interaction of $N = 2$ mode with other vibration modes. Shell radial thickness and stem length are the two critical parameters which decide the frequencies of two nearby modes such as $N = 2$ mode and tilt mode. Table 4.3 shows the effect of shell radial thickness on the mode interaction induced Q_{Anchor} reduction. When the $N = 2$ mode frequency is closer to the stem tilt mode frequency, anchor loss increases due to energy transfer between the modes.

Table 4.3: Effect of shell thickness on closeness of $N = 2$ mode with stem tilt mode

Shell radial thickness (mm)	$N = 2$ mode (Hz)	Tilt mode (Hz)	Frequency separation (Hz)	Q_{Anchor}
0.88	4860.6	4842.6	18	1.6×10^{8}

1.00	5459.0	4681.5	777	4.1×10^{11}
1.20	6440.1	4523.0	1917	6.4×10^{11}

As the shell radial thickness increases, $N = 2$ mode frequency increases because of the increased stiffness effect of the hemispherical region and the stem tilt frequency decreases because of the increased mass effect of the hemispherical region. As the frequency separation increases, Q_{Anchor} increases. When the shell thickness is reduced to 0.88 mm, the separation between the two modes becomes 18 Hz and the Q_{Anchor} reduces to 1.6×10^{8}. It can be seen that the stem length is non-linearly related to the stem tilt mode frequency. Effect of stem length is also studied based on the interaction between the $N = 2$ shell mode and the stem tilting mode. When the frequency separation is less, Q_{Anchor} reduces significantly and the results are shown in Figure 4.10. The central stem should be projecting below the bottom equator plane of the cylindrical region for mounting to the substrate. Hence, the minimum length for the stem is the sum of the hemisphere inner radius and the cylinder length which is 17 mm. Based on the mode interaction study, it is found that a stem length of 19 mm is good choice for sufficient frequency separation to minimize the anchor loss. The dimensional tolerances on the shell and the stem are to be controlled stringently to ensure sufficient frequency separation.

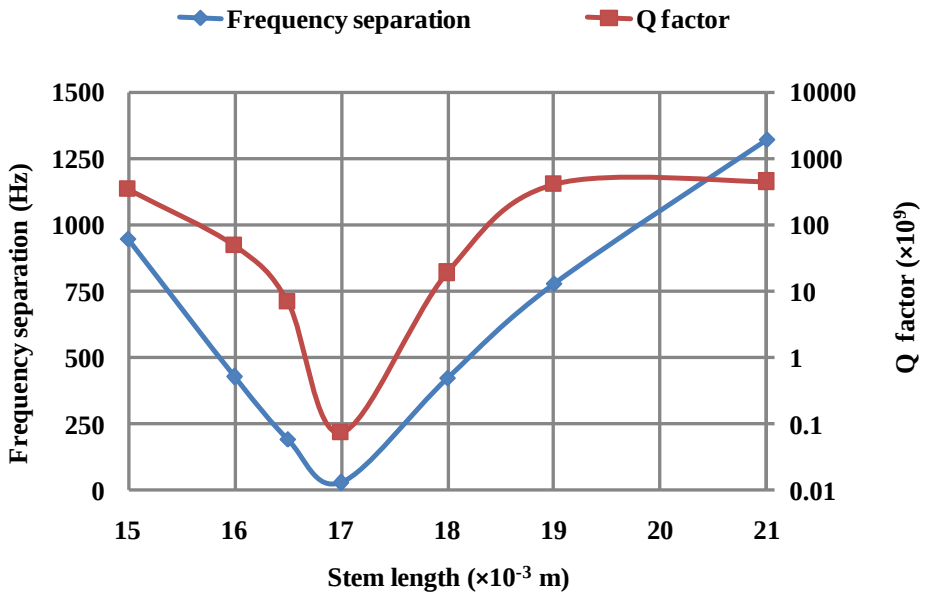

Figure 4.10: Effect of the stem length on frequency separation and Q_{Anchor}

Further the effect of the stem radius on Q_{Anchor} is studied and result is shown in Figure 4.11. When the stem radius increases, its attachment area at the hemispherical region increases and overlaps with the regions of $N = 2$ mode deformation. This results in more energy propagation to the substrate and reduces the Q_{Anchor}. Thus, lower value of stem radius is better for low anchor loss. However, this will also reduce the natural frequency of the stem

tilting mode. A non-linear increase in Q_{Anchor} is seen when the stem radius is less than 3 mm. 3.2 mm stem radius is selected considering the mode interaction and the launch environments. Sufficient strength should be available for withstanding launch induced vibration loads on resonator.

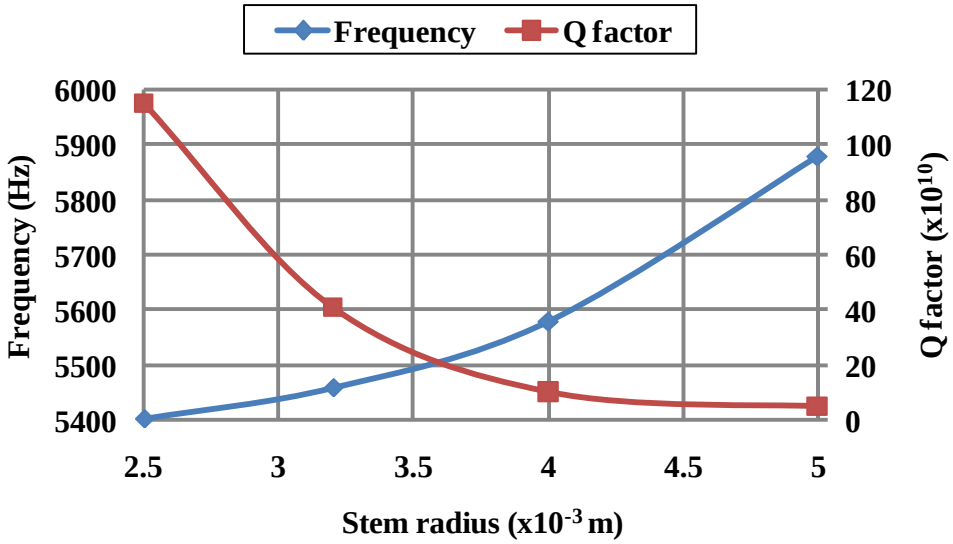

Figure 4.11: Effect of the stem radius on frequency and Q_{Anchor}

4.4 Effect of resonator material properties

Fused silica is a good choice from the low TED point of view. Hence, it is taken as the reference material. The effect of variation of resonator material properties on the anchor loss is studied. One material property is changed at a time keeping other properties constant. Young's modulus and density are varied as multiples of that of fused silica material. Here, E_{FS} and ρ_{FS} are the Young's modulus and density of the fused silica material.

Tables (4.4) and (4.5) show the effect of variation of Young's modulus and density on Q_{Anchor} respectively. It can be seen that the Young's modulus of resonator increases, resonator become stiffer and exerts more deformation to the substrate. This reduces the Q_{Anchor}. However, it can be seen that the density has no significant effect on Q_{Anchor}.

Table 4.4: Effect of resonator Young's modulus on Q_{Anchor}

E value	Frequency (Hz)	Q_{Anchor}
$4E_{FS}$	10592	9.01×10^{10}
$2E_{FS}$	7527	1.04×10^{11}
E_{FS}	5459	4.10×10^{11}

Table 4.5: Effect of resonator density on Q_{Anchor}

ρ value	Frequency (Hz)	Q_{Anchor}
$3\rho_{FS}$	3308	3.76×10^{11}
$2\rho_{FS}$	4051	3.90×10^{11}
ρ_{FS}	5459	4.10×10^{11}

4.5 Effect of support structure

Young's modulus of the resonator does not have a direct relation on the Q_{Anchor}. However, the ratio of Young's modulus of the resonator ($E_{resonator}$) to that of the supporting substrate ($E_{substrate}$) has an effect on the Q_{Anchor}. Hence, a study is done by varying the Young's modulus ratio (E_{RS}) and the results are tabulated in Table 4.6.

Table 4.6: Effect of ratio of E value of the resonator to the substrate on Q_{Anchor}

$E_{RS}=\frac{E_{resonator}}{E_{substrate}}$	Frequency (Hz)	Q_{Anchor}
4.0	10600	9.01×10^{10}
2.0	7532	1.04×10^{11}
1.0	5459	4.10×10^{11}
0.5	3794	2.62×10^{12}

It can be seen that as the value of E_{RS} decreases, support structure becomes stiffer as compared to the resonator and the resonator imparts less deformation to the support structure. Thus, the energy loss from the resonator decreases during vibration and results in less anchor loss.

The resonator is attached to the substrate using bonding method. Then, the effect of resonator bonding material's Young's modulus value on Q_{Anchor} is studied by varying the Young's modulus of the bonding material between the resonator and the mounting substrate. The result is tabulated in Table 4.7. As the bonding material E value reduces, the residual energy transfer to the substrate becomes less and thus Q_{Anchor} increases.

Table 4.7: Effect of ratio of E value of the resonator to the bonding material on Q_{Anchor}

$E_{RB}=\frac{E_{resonator}}{E_{bonding}}$	Q_{Anchor}
1	4.15×10^{10}
10	6.00×10^{10}
100	1.39×10^{11}
1000	2.30×10^{11}

4.6 Effect of resonator structure imperfections

In practice, perfect resonator structures cannot be realized. There will be always some dimensional and geometrical fabrication deviations which will affect the anchor loss. These imperfections make the resonator as unsymmetrical structure. Then, the nodal points of vibrations will not coincide with the stem vertical axis. This increases the stem deformation due to the residual force and moment transfer from the vibrating structure. This increases the energy loss through the anchor. Thus, more energy is dissipated in the mounting structure and results in more anchor loss. A detailed study of the effects of different cases of possible imperfections is done to arrive at the critical fabrication tolerances.

4.6.1 Hemisphere shell axis is offset with respect to the stem axis

There will be concentric error between the hemisphere shell axis and the stem axis. This results in lateral offset between the nodal location of the vibrating hemisphere and the stem axis. Shell axis offset is shown in Figure 4.12. Different shell offset values are considered for study and results are shown in Figure 4.13.

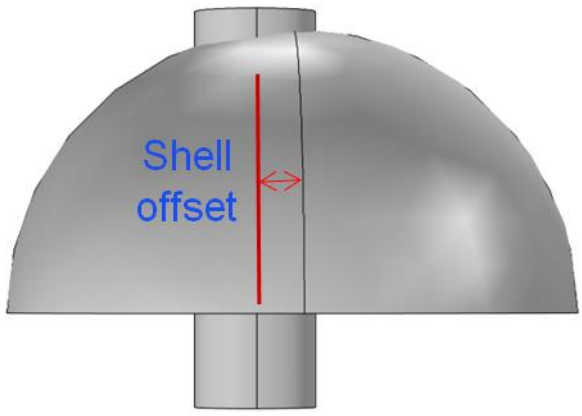

Figure 4.12: Representation of the shell axis offset with respect to the stem axis

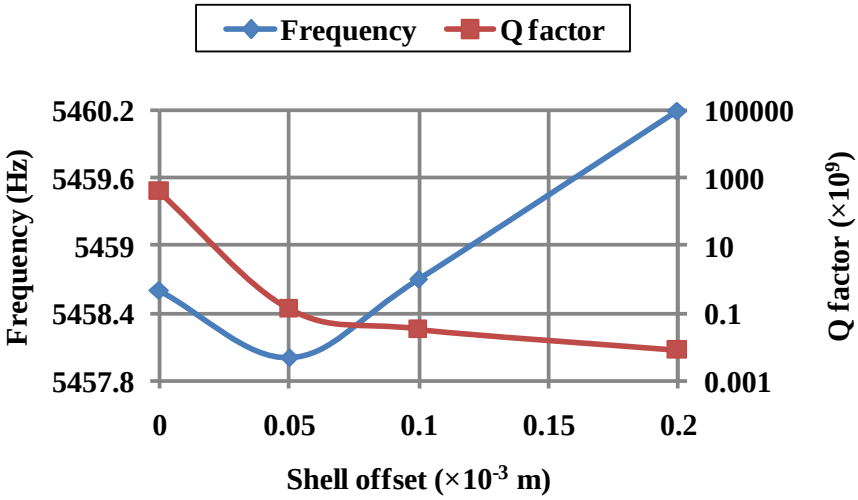

Figure 4.13: Effect of the shell axis offset on Q_{Anchor}

It can be seen that Q_{Anchor} reduces as the geometric offset increases. Reduction of the order of four is seen for the offset value of 0.2 mm. This is because of the transfer of the residual force and the moment to the mounting stem and increased stem displacement due to unsymmetrical structural vibration with respect to stem. This results in more vibration energy loss through stem to the mounting structure. Hence, the offset value of less than 50 microns should be achieved during the fabrication where there is a drastic increase of Q_{Anchor} is seen.

4.6.2 Effect of shell tilt with respect to the stem

There will be cylindricity error between the hemisphere shell and the stem. This causes tilt between the shell axis and the stem axis. Shell axis tilt is shown in Figure 4.14. Different shell tilt values are considered for study and results are shown in Figure 4.15.

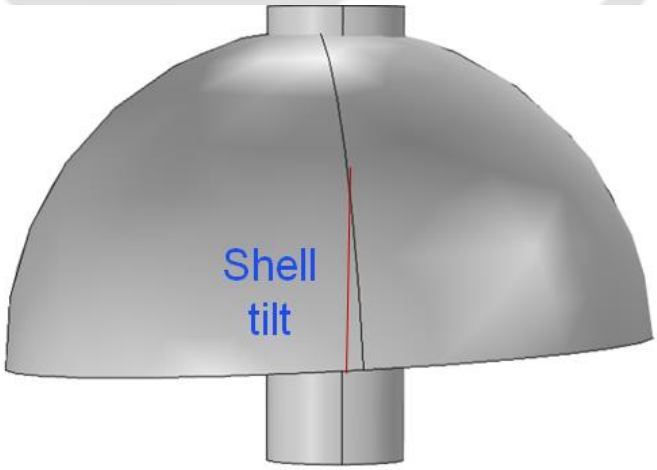

Figure 4.14: Representation of the shell tilt with respect to the stem axis

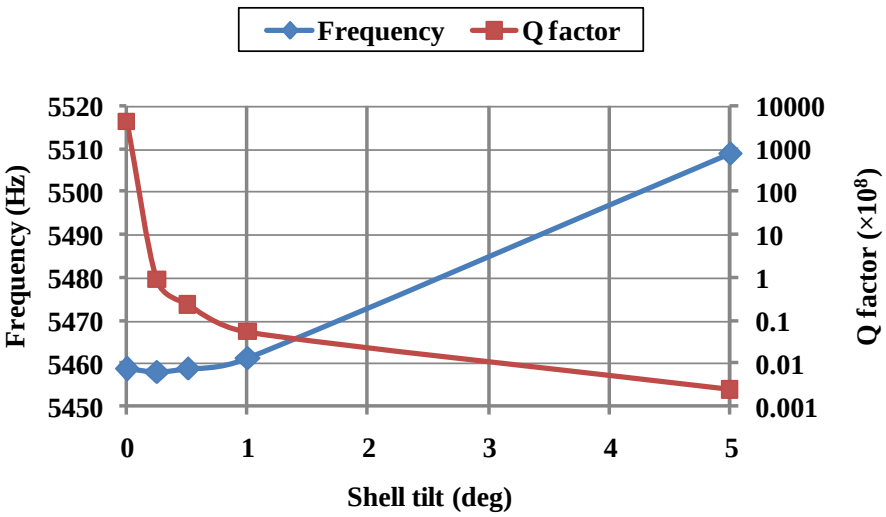

Figure 4.15: Effect of the shell tilt on Q_{Anchor}

It can be seen that the Q_{Anchor} reduces as the shell tilt increases. This is because of the residual force and the moment transfer to the stem which causes vibration energy loss to the mounting substrate similar to the case of shell offset. There is three order of reduction seen even with 0.25 deg tilt value. Same order reduction is reported in Darvishian *et al.* [2017] micromachined birdbath type gyroscope resonator. Hence, the tilt value of less than 0.25 deg should be achieved during the fabrication.

4.6.3 Effect of shell radial thickness variation

This is another probable fabrication deviation. The effect of the shell radial thickness variation around the circumferential direction is studied. Radial thickness is varied up to 10% of nominal thickness. Shell radial thickness on one side is kept at a nominal value of 1 mm and the radial thickness of the opposite side is reduced to 0.9 mm to generate the case of shell radial thickness variation. This also results in change of vibration nodal location away from the stem axis similar to other deviations. It is shown in Figure 4.16. The results are shown in Figure 4.17.

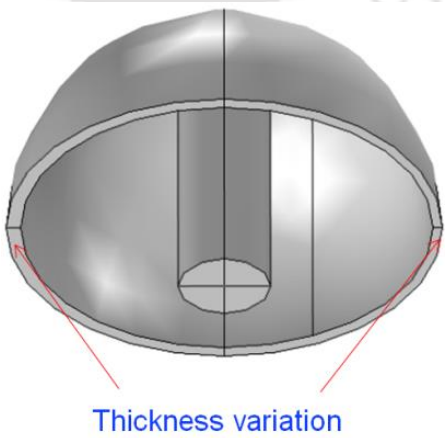

Figure 4.16: Representation of shell radial thickness variation

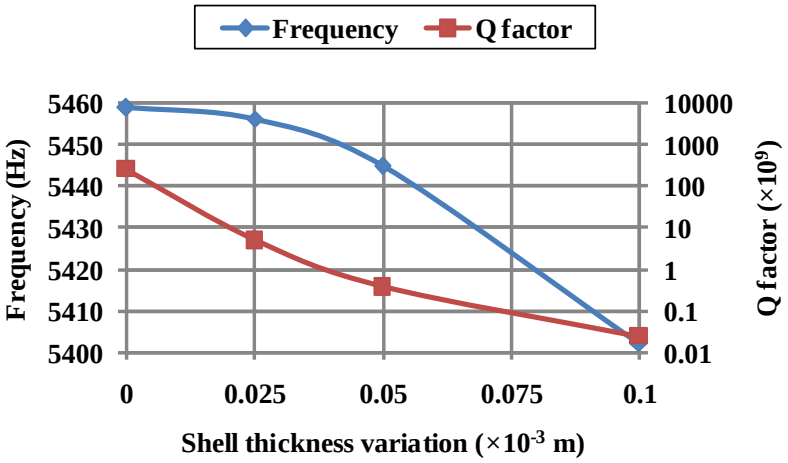

Figure 4.17: Effect of the shell radial thickness variation on Q_{Anchor}

It can be seen that the Q_{Anchor} decreases as the magnitude of the radial thickness variation increases. This is because of the residual force and the moment transfer to the base because of the unbalanced resonator working in $N = 2$ mode. Radial thickness variation affects Q_{Anchor} of the two $N = 2$ modes differently. One of the $N = 2$ mode Q_{Anchor} is affected more and it is reported here. There is an order of four reduction is seen even with 10% radial thickness variation and reasonably matching with the reported value in Darvishian *et al.* [2017] for micromachined gyroscope resonator. The radial thickness variation of the shell should be achieved less than 20 microns during fabrication.

4.6.4 Effect of hemispherical height variation

Study is carried out for the case of non-uniform hemisphere height variation from the equatorial plane. This is modeled by removing the material for different depths and sector angles from the hemispherical equator plane as shown in Figure 4.18. Material is removed to different depths of 0.2 mm, 0.1 mm, and 0.05 mm, and for sector angles of 180 deg, 90 deg and 45 deg. The effect on Q_{Anchor} is tabulated in the Table 4.8. Q_{Anchor} increases as height variation reduces and with lesser sector angle of deviation.

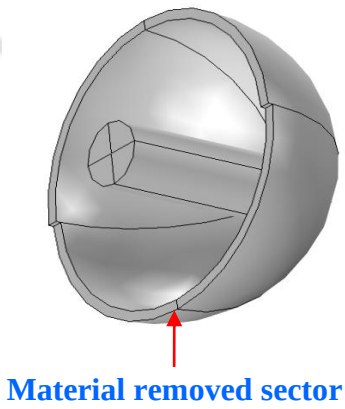

Figure 4.18: Representation of non-uniform hemisphere height variation from the equatorial plane

Table 4.8: Effect of non-uniform hemisphere height variation from the equatorial plane

	0.2×10^{-3} m depth	0.1×10^{-3} m depth	0.05×10^{-3} m depth
180 deg sector angle	1.8×10^{7}	1.1×10^{8}	4.3×10^{8}
90 deg sector angle	3.9×10^{7}	1.4×10^{8}	5.8×10^{8}
45 deg sector angle	2.5×10^{8}	9.8×10^{8}	2.3×10^{9}

Another case of the effect of height variation in discrete sector angles on Q_{Anchor} is studied by material removal from hemispherical equatorial plane to a depth of 0.2 mm as shown in Figure 4.19. The results are tabulated in Table 4.9. There is not much Q_{Anchor} reduction for the case of four numbers of 45 deg sector deviation separated by 90 deg because the deviation pattern is similar to N = 2 elliptical mode shape. There are orders of Q_{Anchor} reduction when the height deviation profile is unsymmetrical with respect to N = 2 mode elliptical shape. Absolute sector angle of deviation also has an effect on Q_{Anchor}. It can be inferred that the effect of deviations on Q_{Anchor} depends on its pattern for a particular mode shape.

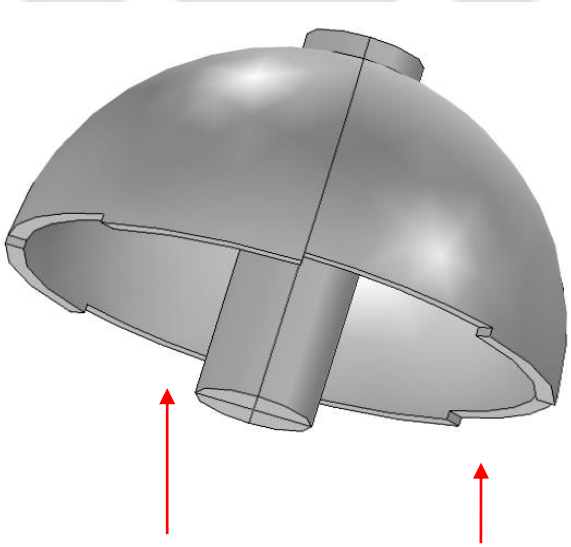

Figure 4.19: Representation of height variation in discrete sector angles from equator plane

Table 4.9: Effect of height variation in discrete sector angles from equatorial plane on Q_{Anchor}

Deviation pattern description	Q_{Anchor}
45 deg sector 4 nos separated by 90 deg	1.1×10^{11}
45 deg 2 sectors separated by 45 deg Such 2 sets 180 deg separated	2.2×10^{9}
45 deg 2 sectors separated by 45 deg Such 2 sets 120 deg separated	4.7×10^{7}
45 deg 2 sectors separated by 45 deg Such 2 sets 90 deg separated	2.5×10^{7}
30 deg 2 sectors separated by 45 deg Such 2 sets 180 deg separated	9.3×10^{9}
30 deg 2 sectors separated by 45 deg Such 2 sets 120 deg separated	4.6×10^{8}
30 deg 2 sectors separated by 45 deg Such 2 sets 90 deg separated	5.6×10^{7}

4.6.5 Single unbalanced mass sensitivity on frequency split and Q_{Anchor}

Ideally eigen values of the two $N = 2$ modes for the hemispherical resonator should be the same. However, ideal resonators cannot be realized. Fabrication imperfections results in different eigen values for the operating $N = 2$ mode which is called the frequency split. Frequency splitting of an axisymmetric shell resonator is a common problem caused mainly by the fabrication defects. Material anisotropy also can cause frequency split. However, this can be minimized by use of a highly isotropic material. Fabrication deviation induced unsymmetry can be represented as unbalanced mass. Consider the case of a single unbalanced mass in the resonator generating the frequency split of the $N = 2$ modes. The frequency split leads to the reduction of gyroscopic effect which in turn affects the resonator performance is affected (Lin *et al.* [2015]). The sensitivity relation is given by Zhbanov and Zhuravlev [1998] and Fox [1990] as:

$$\frac{\Delta f}{f} = \frac{m_u}{3m_{eff}} \tag{4.1}$$

where Δf is the frequency split of $N = 2$ mode, f is the resonant eigen frequency of $N = 2$ mode with no unbalanced mass, m_u is the unbalanced mass, and m_{eff} is the effective mass participating in $N = 2$ mode.

The effective mass, which is participating in $N = 2$ mode, of the present hybrid hemispherical configuration is 0.54×10^{-3} kg. The sensitivity is calculated analytically using equation (4.1) as 0.29×10^{-6} kg/Hz. FE model with highly refined mesh is used for numerical verification of the unbalanced mass sensitivity to minimize the effect of mesh density variation on the frequency split. The configuration of the resonator considered here is the hybrid configuration. Then, the effect of the unbalanced mass resonator on frequency split is simulated by adding a point mass at the equator plane and the result is tabulated in the Table 4.10. The highly refined mesh for the balanced resonator gives only 3 milliHz frequency split which is sufficient for unbalanced mass sensitivity study. As the unbalanced mass increases, frequency split increases. The sensitivity is calculated from the FE results given in Table 4.10 by dividing the unbalance mass with the frequency split. The sensitivity is 0.29×10^{-6} kg/Hz and it exactly matches with the analytical value.

Table 4.10: Effect of single unbalanced mass on frequency split for $N = 2$ mode

Unbalanced mass (kg)	Two $N = 2$ frequencies (Hz)	Frequency split (Hz)
No unbalanced mass (balanced resonator)	5187.1194 5187.1220	0.003
10^{-9}	5187.1148 5187.1211	0.006
10^{-8}	5187.073 5187.111	0.038
10^{-7}	5186.66 5187.01	0.350
10^{-6}	5182.3 5186.0	3.700
10^{-5}	5148.0 5182.7	34.7

Now the effect of the unbalanced mass on Q_{Anchor} is studied. The unbalanced resonator produces undesired resultant forces and moments to the stem which results in higher unsymmetric displacement in the stem. This increases more anchor loss dissipation. The normalized displacement in the stem for an ideal resonator is shown earlier in Figure 4.6

where the maximum normalized value is 0.025 and is symmetrical with respect to the stem axis. Figure 4.20 shows the normalized displacement in the stem with unbalanced resonator. It is clear from Figure 4.20 that the normalized displacement is unsymmetrical with respect to the stem axis and is more compared to that of a balanced resonator. This results in lower Q_{Anchor} as given in Table 4.11. Hence, a very fine balancing of the shell is required to reduce the frequency split and to increase the Q_{Anchor}.

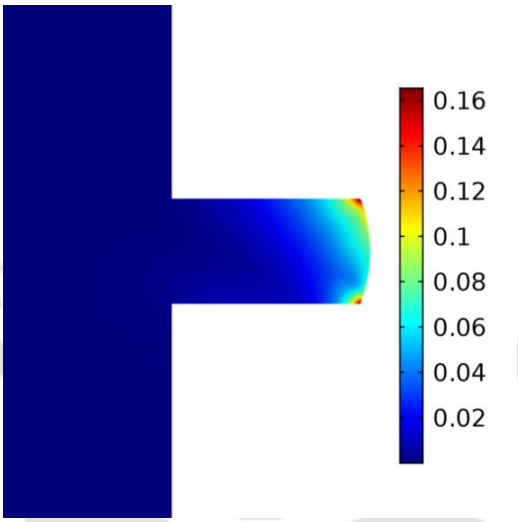

Figure 4.20: Normalized displacement in the stem with unbalanced resonator

Table 4.11: Effect of single unbalanced mass on Q_{Anchor}

Unbalanced mass (kg)	Q_{Anchor}
No unbalanced mass	4.1×10^{11}
10^{-7}	6.9×10^{10}
10^{-6}	6.8×10^{8}
10^{-5}	6.1×10^{6}

4.6.6 Effect of unbalanced mass profile on frequency split and Q_{Anchor} mismatch

Now the effect of unbalanced mass profile over the circumferential direction on the frequency split and Q_{Anchor} is studied. The unbalance profile has got three effects. It can cause frequency split of $N = 2$ mode as discussed earlier. However, it depends on the locations of unbalanced mass. Unbalanced mass also results in overall Q_{Anchor} reduction and mismatch between the Q_{Anchor} corresponds to the two different $N = 2$ frequencies. Q_{LF} is the Q factor corresponds to the lower $N = 2$ frequency and Q_{HF} is the Q factor corresponds to the higher $N = 2$ frequency. Also, the location of mass imperfection influences the orientation of the mode

shape. Total unbalanced mass of 10^{-5} kg is added as a single mass or multiple equal lumped masses in different configurations as shown in Table 4.12 for sensitivity simulation study. Typically, balancing is done using single, two- or four-point correction methods which is explained later in section 6.4. The discrete patterns considered here are based on the balancing schemes. In general, it can be seen that the frequency split increases and Q_{Anchor} reduces as the unbalanced mass increases.

Table 4.12: Effect of unbalanced mass configuration on frequency split and Q_{Anchor} mismatch

Case no.	Unbalance locations	Description	Frequency split (Hz)	Q_{LF} and Q_{HF}
1		Single mass	35	6.1×10^{6} 2.7×10^{7}
2		2 masses 180 deg	35	2.9×10^{10} 8.4×10^{7}
3		3 masses 120 deg	Nil	1.8×10^{8} 1.8×10^{8}
4		4 masses 90 deg apart	35	1.1×10^{11} 3.0×10^{11}
5		2 pairs (1 pair separated by 45 deg) of masses 180 deg apart	Nil	2.2×10^{9} 1.8×10^{8}
6		2 pairs (1 pair separated by 45 deg) of masses 90 deg apart	Nil	2.5×10^{7} 1.8×10^{7}

- Case 1 represents a single unbalanced mass and it causes 35 Hz frequency split, overall Q_{Anchor} reduction and mismatch between Q_{LF} and Q_{HF}. Low frequency axis is along the single unbalanced mass and Q_{LF} is lower compared to Q_{HF}. This is due to the higher axial and radial displacement of the stem which is caused by the resultant force and the moment.
- Case 2 has the same frequency split as case 1 because the total unbalanced mass is the same and are at the two antinodal locations of the low frequency axis. However, the Q_{LF} is increased by more than three orders because of the significant reduction in the radial displacement. But the axial displacement component is still present.

- Unbalanced mass distribution has similar effect on the two $N = 2$ modes for the case 3 and frequency split is not present. There is no Q_{Anchor} mismatch even though there is stem displacement.
- Case 4 represents four unbalanced masses at the antinodal locations of one of the $N = 2$ mode. This causes frequency split. Q_{Anchor} is not affected because the resultant force and the moment get cancelled in the radial and the axial directions.
- Case 5 represents two unbalanced masses at antinodal locations of one of the $N = 2$ mode and the other two unbalanced masses at the antinodal locations of the other $N = 2$ mode. This does not affect frequency split. Q_{Anchor} is affected because there is resultant axial stem displacement.
- Case 6 represents the case where Q_{Anchor} is significantly affected without frequency split. Unbalanced masses are located to one sector and results in more radial and axial displacements.

From these cases, it is inferred that the pattern of unbalanced mass has got significant effect on the frequency split and Q_{Anchor} mismatch. The effect depends on the overlap of $N = 2$ mode shape over the unbalance pattern in circumferential direction. It is desirable that a frequency split in milliHz should be obtained after the fine balancing.

4.7 Wine glass configuration resonator

Typical wine glass hemispherical resonator configuration has outside mounting stem configuration as shown in Figure 4.21. This resonator is mounted to the support structure using the outer stem. This configuration of HRG is also studied for the anchor loss. Hemispherical and stem dimensions are taken same as that of the nominal dimensions of the inside stem configuration. The effect of stem length is studied and results are tabulated in Table 4.13. Shorter stem has high anchor loss and sufficient stem length need to be kept. Hence, overall height of the resonator is more in this configuration for the same Q_{Anchor}. Also, this configuration is inferior in terms of shock sensitivity (Cho and Najafi [2015]. Hence, this configuration is not used further.

Table 4.13: Effect of bottom stem length on Q_{Anchor} of wine glass resonator

Bottom stem length ($\times 10^{-3}$ m)	Q_{Anchor}
0.5	4.8×10^{8}
2.0	3.1×10^{9}
3.5	1.1×10^{10}
5.0	1.7×10^{11}

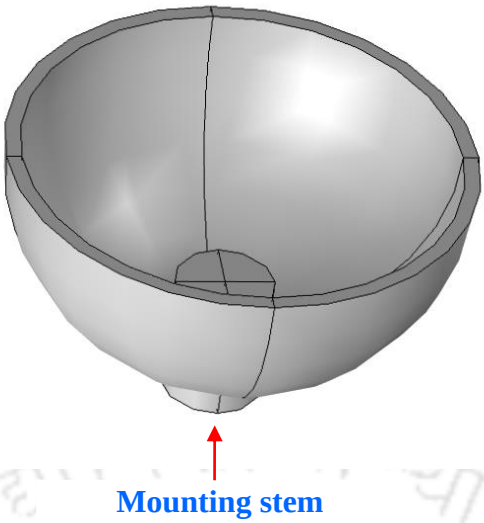

Figure 4.21: Typical wine glass configuration with outside mounting stem

4.8 Summary

Q_{Anchor} is high for an ideal highly symmetrical hemispherical resonator with inside stem of sufficient length. Hence, Q_{Anchor} is not significant for a perfectly designed ideal hemispherical resonator structure. However, it is highly sensitive to minor geometric imperfections in the hardware realisation. The shell-stem offset value of less than 50 microns, the tilt value of less than 0.25 deg and the radial thickness variation of less than 20 microns should be achieved during the fabrication. When the $N = 2$ mode frequency is closer to the stem tilt mode frequency, anchor loss increases by few orders of magnitude. As the unbalanced mass increases, the frequency split increases with a sensitivity of 0.29×10^{-6} kg/Hz. The effect of unbalanced mass profile on the frequency, the overall reduction and the variation of the Q_{Anchor} depends on the overlap of $N = 2$ mode shape over the unbalance pattern in the circumferential direction.

Chapter 5

Resonator fabrication and Metrology

Based on the design and the sensitivity studies related to thermoelastic loss and anchor loss, a high precision hybrid resonator is fabricated using fused silica material. Fused silica material is selected based on minimum TED. High precision fabrication is required to meet minimum anchor loss. Since the designed resonator is macro size with all dimensions are in mm scale, conventional machining techniques can be used. As the material is brittle and demands high precision, appropriate machining methods and machines should be used. Another criticality is that the fabricated structure should act as a high Q_{Eff} resonator where the energy loss should be minimum. Hence, it is also to be ensured that the fabrication induced energy dissipations are also minimal during the functional operation.

This chapter presents fabrication procedure, description of the precision machines used, realisation of fused silica shell resonator and its metrology measurements of dimension and geometrical parameters.

5.1 Fabrication of brittle material

Grinding is the most widely used process for machining hard and brittle materials. Ultra sonic machining (USM) is a popular machining technique for the materials with low ductility and high hardness (Guzzo *et al.* [2004]). A tool with diamond grit is hammered on the work piece surface by the tool vibration (normally greater than 15 kHz). This removes the material by microchipping. The ultrasonic vibration reduces tool wear rate and minimizes brittle fracturing in glass machining. Brittle mode machining of glass causes cracks which results in substantial amount of surface damage. High precision machine tool ensures the suppression of these cracks by using appropriate machining parameters to some extent (Ravindra and Patten [2011], Brinksmeier *et al.* [2010]).

Even brittle material like fused silica has some extent of ductility. In order to avoid crack formation during fabrication, the penetration depth should be controlled within a certain critical value. If the critical value of feed rate and depth of cut for every material is maintained, fabrication can be done in ductile mode regime even for a brittle material. Very low depth of cut is required for ductile mode cutting for brittle material like glass. This mechanism is referred to as ductile regime machining. Ductile mode machining of glass without crack is critical.

5.1.1 Fabrication procedure of fused silica high precision resonator

5.1.1.1 Blank selection

Blank material size selection is done based on the minimum internal residual stress during blank realization. Birefringence, which is the optical property of a material, is used to

measure the mechanical stress. In the present work, birefringence measurements are taken to evaluate the blank internal stress. Isotropic solids do not exhibit birefringence. However, birefringence effect occurs in a solid when they are under mechanical stress. This experimental method for analyzing stress distribution in solids is called photoelasticity.

Blank material in the form of rods of diameters 35 mm and 45 mm are available and considered for fabrication. Figures (5.1) and (5.2) show the birefringence plots of rods of diameters 35 mm and 45 mm respectively.

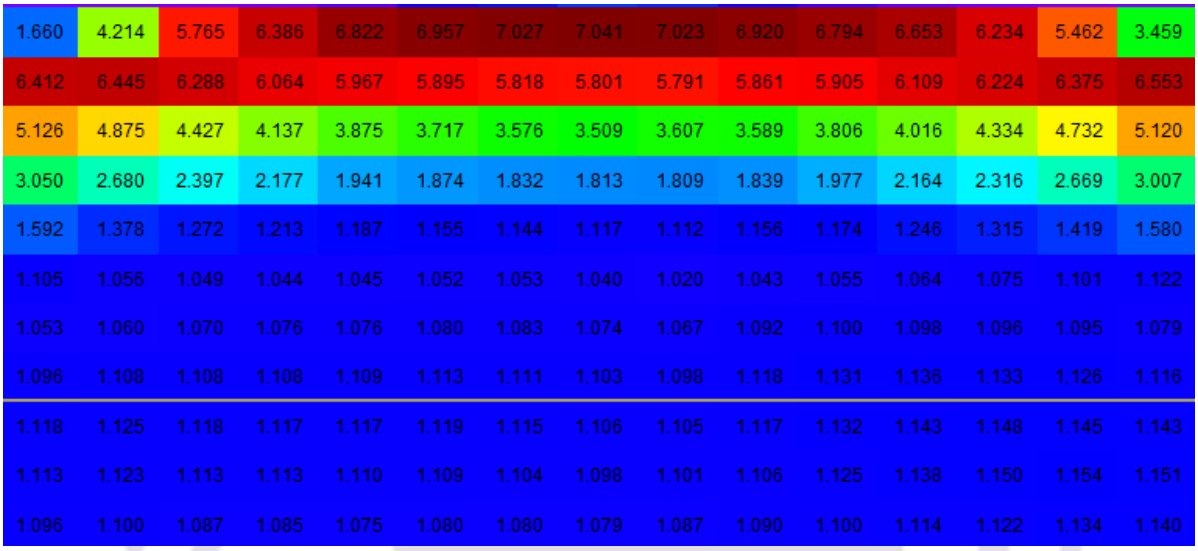

Figure 5.1: Birefringence result of 35 mm diameter rod

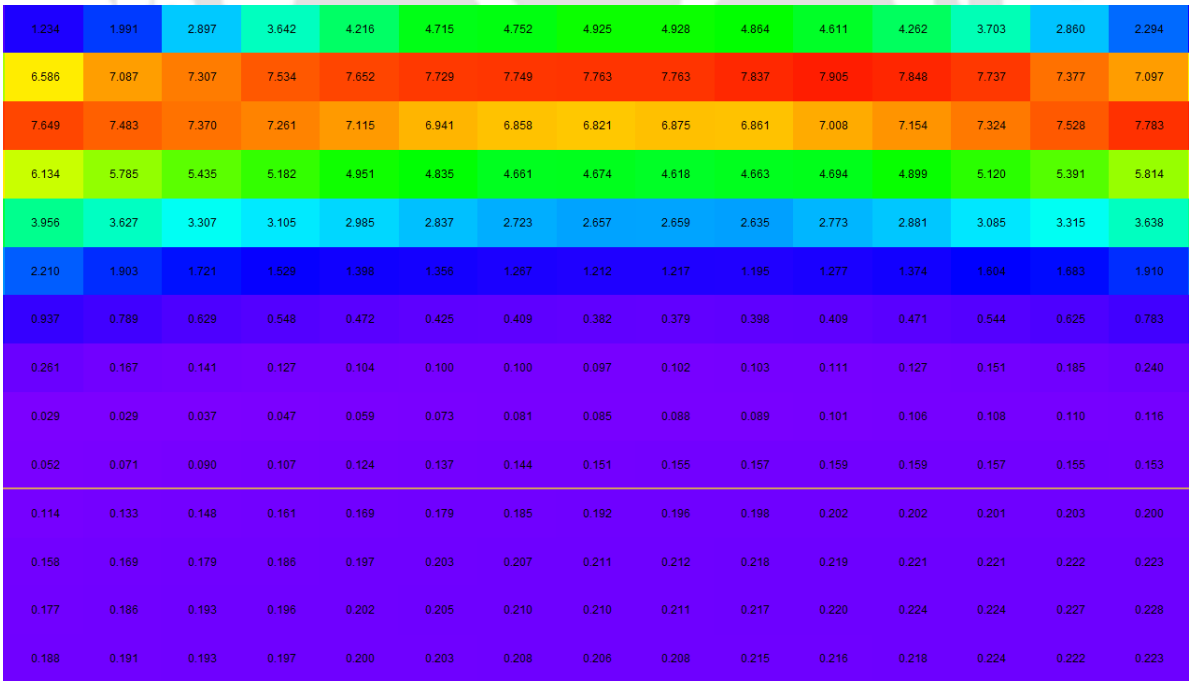

Figure 5.2: Birefringence result of 45 mm diameter rod

The top boundary of the plot represents the outer diameter of the rod. Each vertical segment of the plot is equivalent to 1 mm size of the rod in radial direction. The stress levels in both the rods at 30 mm diameter, which is the diameter of resonator, are compared. The stress is expressed as nm/cm where 4 nm/cm is equivalent to 0.133 MPa. The internal stress level is 1.1 nm/cm to 1.6 nm/cm for 35 mm rod. The internal stress level is 0.19 nm/cm to 0.22 nm/cm for 45 mm rod. It can be inferred from the measurements that there is difference in the internal stress values between the two rod sizes. 45 mm rod has 5 times lesser stress level. Hence, for fabrication a rod of 45 mm diameter is preferred to ensure less internal stress.

5.1.1.2 Fused silica blank preparation

First operation is to slit the rod to the required length of 35 mm. The blank end face is lapped and fine polished to achieve surface finish less than 10 A^o and flatness error within half of wavelength of laser light. Thus, the blanks are prepared for further machining.

5.1.1.3 Bulk machining

The blank is bonded to a special job holder using bonding material with the polished surface facing up. The bulk machining operation is carried out using ultrasonic machining technique. For machining purpose, the lapped top face and outer diameter are taken as the reference. The bulk machining of the resonator has been done using ultrasonic CNC milling machine. Machining operations are completed up to 1.4 mm shell thickness against a final thickness of 1 mm and 6.8 mm stem diameter against a final diameter of 6.4 mm for precision finishing operations.

5.1.1.4 Chemical cleaning

Before the chemical etching process, the shell is subjected to full level chemical cleaning to remove the traces of any impurities such as bonding material, machining coolant traces and oil traces.

5.1.1.5 Bulk etching

The bulk machining of the shell using ultrasonic technique leaves some residual layer of cracked material throughout the surface as the basic material is brittle. By proper optimization of fabrication parameters, this can be minimized to some extent. The cracked and stressed surface layer reduces the $Q_{Surface}$ of the resonator. This damaged layer is removed by bulk chemical etching to some extent. It is to be ensured that uniform etching is done by an agitation mechanism. Generally chemical etching changes the geometry of the precision components. Hence, it is also to be ensured that the geometry is not degraded much due to the etching. Chemical etching may also increase the surface roughness which is another contributor to the $Q_{Surface}$. Surface characterization at each stage of the fabrication process is useful to understand and address this issue.

5.1.1.6 Precision machining

Then, precision grinding of the resonator is carried out up to shell thickness of 1.04 mm where approximately 40 μm additional thickness is kept for any further etching requirement. This precision machining is done using a jig grinding machine. The resonator needs to be chemically cleaned after grinding.

5.1.2 Fabrication of high precision resonator

Bulk machining is done by ultrasonic machining with DMG MORI make 5 axes ultrasonic machining centre which is shown in Figure 5.3. The kinematic overlapping of the tool rotation with an additional oscillation effects a reduction of the process forces in comparison to the conventional machining. The tool rotation is superimposed using an ultrasonic actuator tool holder with an additional oscillation in the axial direction using the piezoelectric effect. Depending on the workpiece requirements, this allows higher feed, longer tool life, and significantly better surface finishes with average roughness less than 0.1 micron. This USM provides fitting accuracy of 5 micron and roundness of 2 micron. Thus, USM enables economical grinding, milling and drilling of hard and brittle as well as hard to machine other advanced materials.

The machine has the following features:

a) Superimposition of ultrasonic axial movement of tool (with amplitude up to 10 micron) with tool rotation.
b) 40% reduction in process forces for better surface finish.
c) Reduced subsurface damage.
d) Feasibility of realizing thin walls with less than 0.5 mm thickness.
e) Ultrasonic frequency in the range of 15-55 kHz.

Figure 5.3: DMG MORI make 5 axes ultrasonic machining centre for bulk machining

A thick base is kept at this stage of machining for holding the job to minimize undesired jittering of the hemispherical region to achieve good precision. The photo of the ultrasonic machined resonator is shown in Figure 5.4. The shell is not transparent because of the damaged surface layer after USM.

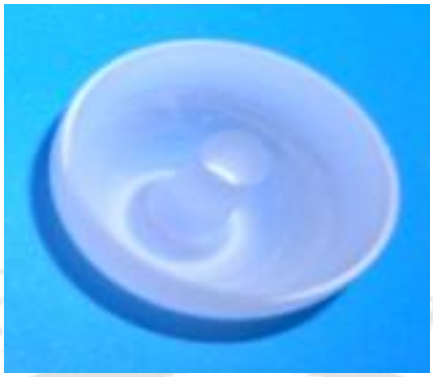

Figure 5.4: Prefinished resonator after ultrasonic machining

After the chemical cleaning and etching, precision jig grinding is done using Hauser make H35 robust machine which is shown in Figure 5.5.

The machine has the following features:

a) Highest accuracy (less than 0.5 μm) and finish.
b) Hydrostatic guided spindle bearing system.

Figure 5.5: Hauser make H35 jig grinding machine for precision machining

The photo of the precision machined shell is shown in Figure 5.6. The shell has become transparent because the majority of the damaged surface layer has got removed in the etching process.

Figure 5.6: High precision fused silica resonator after precision machining

5.2 Metrology

Eight numbers of resonators are realized to establish the fabrication procedure. Metrological inspection has been carried out for all the dimensions and the geometric parameters. The geometrical inspection is carried out using a coordinate measuring machine (CMM) by sensing discrete points on the surface of the resonator with a probe. Talyround machine is used for roundness and cylindricity measurement. The spherical and the cylindrical profiles are measured to assess the concentricity and circularity. The critical dimensions, which decide the resonator frequency, are the shell radial thickness, spherical and cylinder mean radius, and stem diameter. The measurements are done to the resolution of 1 micron level. The measured dimensions are tabulated in Table 5.1.

Table 5.1: Measured dimensions of resonators

Resonator sl. no.	Shell radial thickness ($\times 10^{-3}$ m)	Sphere mean radius ($\times 10^{-3}$ m)	Cylinder mean radius ($\times 10^{-3}$ m)	Stem diameter ($\times 10^{-3}$ m)
1	1.135	14.604	14.600	6.426
2	1.040	14.601	14.597	6.400
3	1.062	14.606	14.601	6.474
4	0.966	14.600	14.600	6.349
5	1.006	14.600	14.600	6.372
6	1.002	14.602	14.596	6.383
7	1.002	14.625	14.622	6.396
8	0.995	14.597	14.593	6.352

The nominal radial thickness is 1 mm, sphere mean radius is 14.6 mm and stem diameter are 6.4 mm. The geometric parameters are tabulated in Table 5.2. From the metrological measurements, it is found that the precision levels achieved during fabrication are different for different resonators. There is variation in different dimensions and geometry parameters of the resonators. Based on the closeness of the dimensional and the geometric measurements with respect to the design values, the lowest precision and the highest precision resonators are identified. Resonator 1 has the lowest precision and resonator 6 is the highest precision resonator. The effect of these geometric deviations on performance parameter is discussed in section 6.3.3.

Table 5.2: Measured geometry of resonators

Geometry parameter	Location	Low precision resonator (resonator 1)	High precision resonator (resonator 6)
Cylinder concentricity ($\times 10^{-3}$ m)	Inner	0.0669	0.0018
	Outer	0.0268	0.0011
Sphere concentricity ($\times 10^{-3}$ m)	Inner	0.0878	0.002
	Outer	0.0244	0.0011
Cylinder circularity ($\times 10^{-3}$ m)	Inner	0.0126	0.0038
	Outer	0.0133	0.0098
Sphere circularity ($\times 10^{-3}$ m)	Inner	0.0099	0.0075
	Outer	0.0111	0.0013

5.3 Summary

High precision machines are used to fabricate fused silica hemispherical resonators. The precision levels achieved during the fabrication are different for different resonators. Shell offset is achieved well within 50 microns and shell tilt is achieved well within 0.25 deg in one high precision resonator (resonator number 6). Thus, a highly symmetrical precision resonator is realized as per the dimensional and the geometric tolerance requirement from the anchor loss sensitivity analysis.

Chapter 6

Resonator characterization

The main characteristics of CVG type HRG gyroscope resonator are its $N = 2$ natural frequency, frequency split (between the two $N = 2$ frequencies of the degenerate pair), Q_{Eff} and Q_{Eff} mismatch. This chapter discusses resonator characterization set-up, equipments used for characterization, measurement procedures, natural frequency measurement and its variation with dimensional deviations in fabrication. The effect of geometric deviations on the frequency split and balancing scheme are also discussed.

6.1 Resonator excitation setup

The characterization needs to be performed under ultra high vacuum conditions to eliminate the fluid damping effects. Thus, the Q_{Fluid} contribution to the overall Q_{Eff} is minimized. An ultra-high vacuum (UHV) chamber is used for this purpose. A rotary pump is used to get the low pressure level up to the order of 10^{-2} millibar. Then, a turbopump is used to get ultra-low pressure of the order of 10^{-5} millibar. The pressure level at which the resonator to be operated in the final sensor configuration is found by a sensitivity test of Q_{Eff} under different ambient pressures.

Resonator needs to be excited for characterization under resonance condition. There should be an excitation mechanism which will induce minimum excitation induced damping. Hence, the resonator is acoustically excited with a very low coupling force which is just sufficient to excite the mode. This will eliminate the contribution of $Q_{Electronics}$ in the overall Q_{Eff} while characterization. Lead zirconate titanate (PZT) based piezo actuators are bonded to the spokes of a wheel. Piezo actuator generates strain to the spoke due to piezoelectric effect when electric field is applied. Actuators are configured in such a way that the torsion mode of the dither wheel actuator is made to resonate when an electric supply is given. An acoustic forcing arm is attached to the dither wheel. The 3D model of the set-up is shown in Figure 6.1.

The realized dither actuator wheel with arm is shown in Figure 6.2. Dither wheel is fabricated with eight spokes. Piezo actuator strips are pasted to both sides of each spoke. These spokes undergo flexing when piezo strips are supplied with electrical excitation sinusoidal voltage. All the spokes are attached through a rim at the outside. The integral rim undergoes a torsional vibration. The arm attached to the rim also undergoes sinusoidal motion which is used to excite the resonator. Proper chemical cleaning of the resonator and the slab needs to be done and allow enough time to get it dried. Contaminations are not permitted on the resonator surface as well as the bonding area. Any micro level contamination on the surface of the resonator causes surface energy loss. Bonding area contamination results in improper bonding. The resonator is bonded to the quartz slab using cyano acrylate locktite 4014 bonder with a small known pressure loading. The load applied during the curing process ensures consistent bonding interface with adequate strength. It is ensured that the resonator is

properly bonded to the quartz slab before taking into the characterization set-up. Stick a circular protractor with fine angle marking around the resonator circumferential direction but not on the resonator. This is required to identify the low and the high frequency axes which corresponds to the two $N = 2$ modes.

The assembled resonator with glass slab is shown in Figure 6.3. Then, the dither wheel actuator and the quartz slab with resonator are assembled to a common mounting base fixture. The end of the arm is kept in close proximity (approximately 1 mm) to the cylindrical portion of the resonator to transfer acoustics energy to the resonator. Thus, the resonator characterization set-up is prepared for testing.

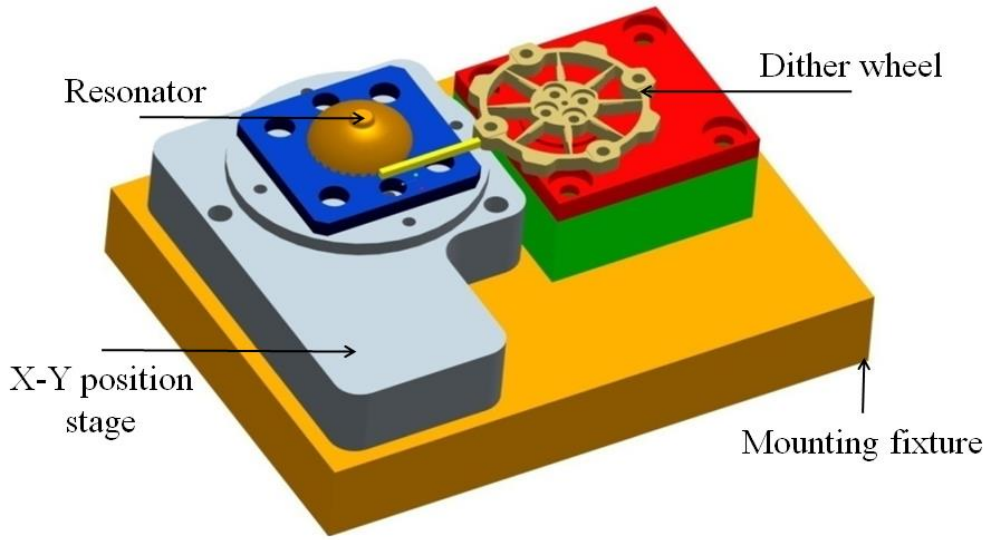

Figure 6.1: 3D model of resonator excitation set-up

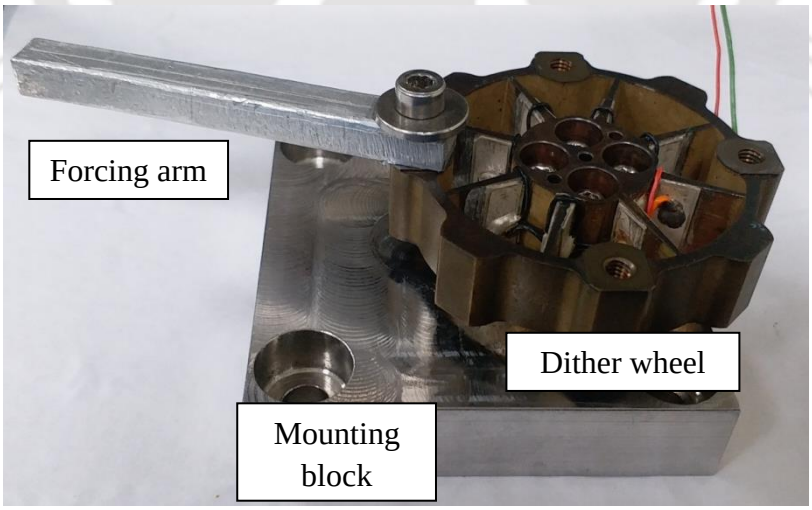

Figure 6.2: Dither actuator wheel with arm

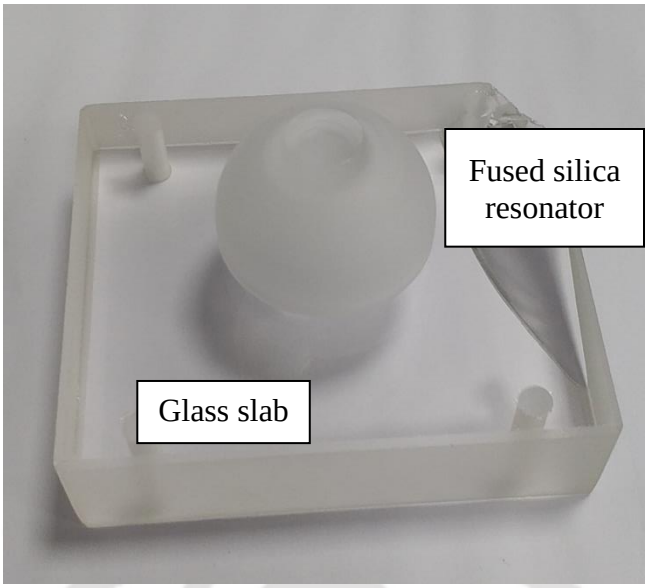

Figure 6.3: Assembled hemispherical resonator with glass slab fixture

6.2 Characterization setup

Vibration displacement is derived from the velocity measurement done using a non-contact Laser doppler vibrometer (LDV). LDV measurement is done using the principle of doppler shift of the reflected laser beam frequency due to vibration of the surface. Laser interferometry is used to get the frequency shift. Output is proportional to target surface velocity component along the laser beam. Polytek GmbH make PSV 500 scanning vibrometer is used for measurement and is shown in Figure 6.4.

The features of the instrument are as follows:

a) Measures on entire surface with high resolution.
b) Measurement done without mass loading effect.
c) Targets can be inside chambers.
d) Frequencies up to 50 kHz, velocities of up to 10 m/s with a resolution of 5 μm/s.

The testing is carried out keeping the resonator characterization setup inside the ultra-high vaccum chamber to eliminate the fluid damping as shown in Figure 6.5. Figure 6.6 shows zoomed view of the resonator setup through the viewing port of vaccum chamber.

Figure 6.4: Polytek GmbH make PSV 500 scanning vibrometer for vibration displacement measurement

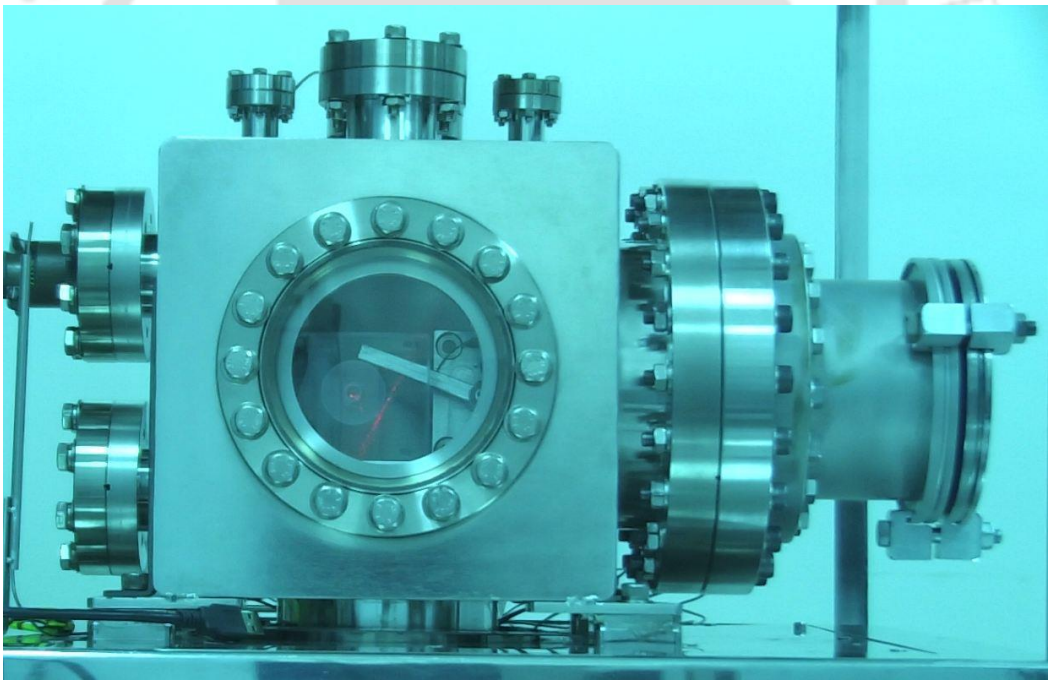

Figure 6.5: Resonator characterization setup in ultra high vaccum chamber

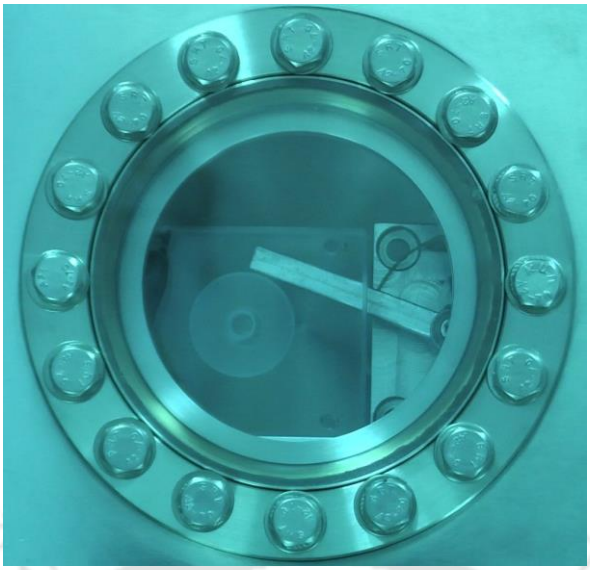

Figure 6.6: Zoomed view of the resonator setup through the viewing port of vaccum chamber

6. 3 Measurement procedure

Dither wheel actuator is driven using a sinusoidal voltage with $N = 2$ frequency of the hybrid resonator for characterization under resonance condition. The pointed laser target (red colour) from the LDV is focussed to the rim of the resonator where the maximum displacement occurs. The points on the rim have in-plane and out-of-plane displacements when the resonator is excited at $N = 2$ mode. LDV measures the velocity of points on the rim which is the product of the $N = 2$ mode frequency and the corresponding displacement. After steady state resonance is reached, natural frequency of the resonator is obtained using FFT of the velocity signal from the LDV. Figure 6.7 shows the resonator under characterization where laser target is focused at the rim of the resonator.

Figure 6.7: Resonator under characterization in ultra high vaccum chamber and LDV measurement

6.3.1 Measurement procedure of frequency

1. A frequency sweep is performed to identify the resonance frequency of the resonator. A preliminary sine sweep (between 4000 Hz and 7000 Hz) is performed to identify the natural frequency of the $N = 2$ mode in 1 atmosphere pressure condition ($f_{ambient}$). This is done keeping the setup inside the vaccum chamber with the chamber door in open condition to test under 1 atmosphere pressure condition.

2. Once the vaccum chamber door is closed, switch on the rotary pump and achieve low pressure of 10^{-2} millibar.

3. Perform a coarse sine sweep in the range of +/- 25 Hz around $f_{ambient}$ to identify the frequency of the $N = 2$ mode. From this result, narrow down the range of the natural frequency to within 5 Hz and then subsequently reduce to fine range of 2 Hz. The mode shape is also captured. 72 points need to be scanned to find the mode shape. Maximum sampling is used (approx. 80 sec up to 7000 Hz) to get the exact resonance frequency. Then, a fine scan is required with 2 degree resolution (180 points). So, the full mode shape can be accurately assessed by two scans. As explained earlier, realisation imperfections result in different eigen values for the operating $N = 2$ mode. $N = 2$ mode is split into high frequency (f_2^H) and low frequency (f_2^L) in actual resonator due to imperfections. Using the scanning provision of the instrument, the two frequencies of the $N = 2$ mode are measured. Then, the locations of the high and the low frequency axes are identified.

4. Then, attain very low pressure of 10^{-5} millibar using turbo pump.

5. Repeat the process in step 3 and find out the frequencies.

6. Identify the low frequency axis and high frequency axis on the circumference of the resonator for balancing of the resonator.

6.3.2 Measurement of frequency

The natural frequencies of the eight resonators are measured based on the above mentioned procedure. The effect of the shell thickness and the stem diameter on $N = 2$ frequency are plotted in Figures (6.8) and (6.9).

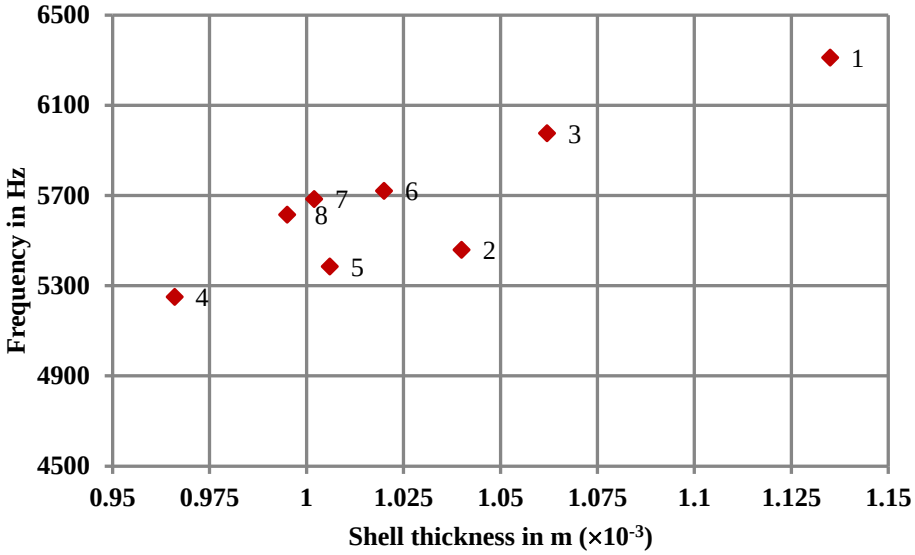

Figure 6.8: Effect of the shell thickness on $N = 2$ mode frequency

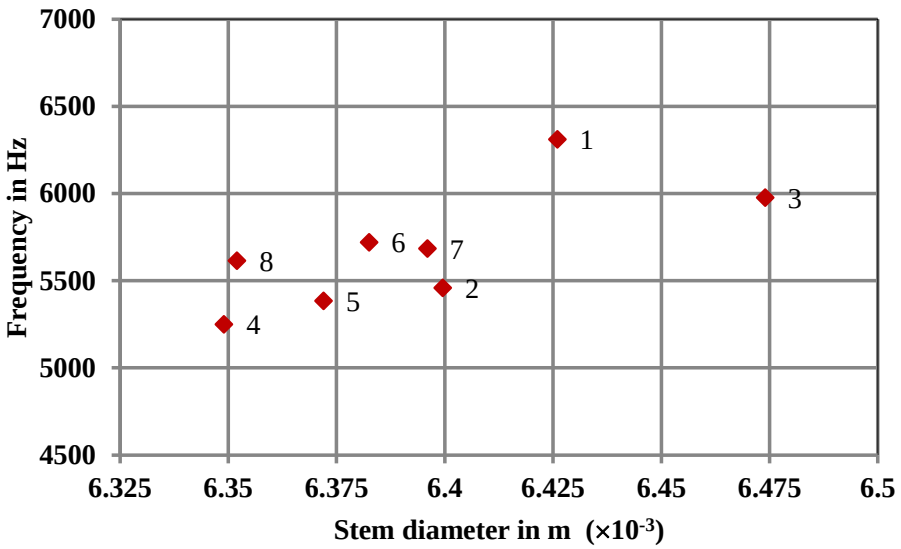

Figure 6.9: Effect of the stem diameter on $N = 2$ mode frequency

It can be seen that there is a variation in the natural frequency which is due to the dimensional deviations during fabrication. The frequency increases as the radial thickness increases. From the Figure 6.8, the test frequency for the nominal 1 mm radial thickness is 5510 Hz. Table 6.1 gives the comparison of the FE and the experimental result, and very good match is seen.

Table 6.1: Comparison of the FE and the experimental test result of $N = 2$ frequency

Mode	FE frequency (Hz)	Test frequency (Hz)	% deviation	Remarks
$N = 2$	5567	5510	1	FE result is for the nominal hemispherical and cylinder mean radius 14.6 mm, stem diameter 6.4 mm and radial thickness 1 mm

6.3.3. Measurement of frequency split

Anomalies in the distribution of mass of a hemispherical resonator substantially influence the performance of the sensor. The unbalanced mass distribution of non-ideal resonator has got two effects i.e., frequency split and reduction in Q_{Anchor} as discussed earlier. Ideally mounting stem is interfaced to the hemispherical region at the nodal location of the $N = 2$ mode. This condition is not satisfied in the mass unbalanced resonator. Then, there is resultant force and the moment transfer through the stem to the mounting substrate and results in substrate displacement. This reduces the Q factor related to anchor loss.

Geometric parameters affect the mass distribution of resonator at a finer level. All realized resonators have geometric errors in varying magnitude which depends on the precision of realization. The axis offset is the concentricity error between the hemispherical or cylindrical axis and the stem axis. The tilt is estimated using the difference (measured dimension – nominal dimension) in equatorial height measurement at the rim from the stem bottom reference plane. Table 6.2 gives the measured and the estimated values of geometric parameters and its effect on the frequency split.

Table 6.2: Effect of geometric parameters on frequency split

Geometry parameter	Location	Low precision resonator (resonator 1)	High precision resonator (resonator 6)
Cylinder concentricity (axis offset in ($\times 10^{-3}$ m))	Inner	0.0669	0.0018
	Outer	0.0268	0.0011
Sphere concentricity (axis offset in ($\times 10^{-3}$ m))	Inner	0.0878	0.002
	Outer	0.0244	0.0011
Cylinder circularity	Inner	0.0126	0.0038

(thickness variation in ($\times 10^{-3}$ m))	Outer	0.0133	0.0098
Sphere circularity (thickness variation in ($\times 10^{-3}$ m))	Inner	0.0099	0.0075
	Outer	0.0111	0.0013
Shell tilt (deg)		0.30	0.003
Frequency split (Hz)		5.95	0.30

It is found that the frequency split increases as the geometric error increases. Out of eight resonators, good precision level is achieved in few resonators. Shell offset is achieved well within 50 microns and shell tilt is achieved well within 0.25 deg in one high precision resonator and achieved $N = 2$ frequency split less than 0.5 Hz. Thus, a highly symmetrical precision resonator is realized as per the dimensional and geometric tolerance requirement from the anchor loss sensitivity analysis. Thus, the contribution of anchor loss in the realized high precision uncoated resonator is minimized in overall Q_{Eff}.

6.4 Balancing methods

Resonator balancing can be done either by mass addition or mass removal technique (Xi *et al.* [2014]). The low stiffness axis, which corresponds to $f_2 - \Delta f_2$ (f_2^L) frequency, is along the line joining the concentrated unbalanced mass location in the rim to the centre of hemisphere. High stiffness axis, where the corresponding frequency is $f_2 + \Delta f_2$ (f_2^H), is at 45 deg with respect to low stiffness axis. The exact locations of these axes are identified using the LDV measurement.

6.4.1 Balancing procedure

A typical response plot from LDV over 45 deg circumferential direction (between two antinodal points) is shown in Figures 6.10 (a), (b), (c) and (d). At antinodal location of one of the $N = 2$ mode axes, there is one response peak. Two responses are seen when the monitoring location is between the antinodal points of the two degenerate modes. Figure 6.11 shows the frequencies and corresponding axes locations around circumferential direction. The anti-nodal location of low frequency mode 1 (f_2^L) is at a reference circumferential location 0 deg and the anti-nodal location of high frequency mode 2 (f_2^H) is at circumferential location 45 deg. Thus, the low and the high frequency axes are found out for balancing purpose.

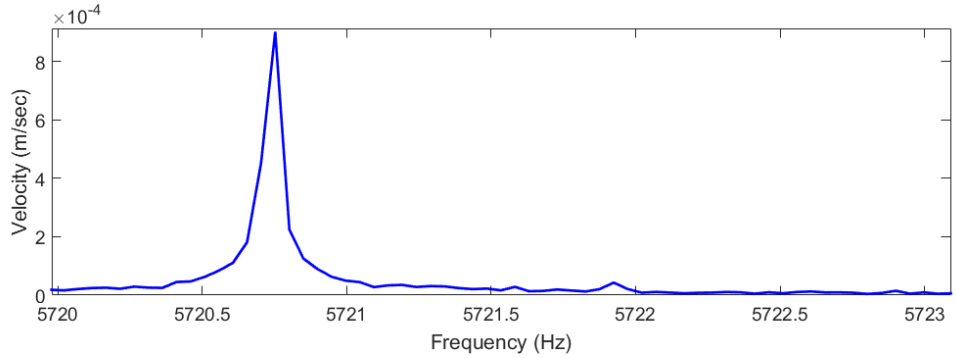

(a) Location 1

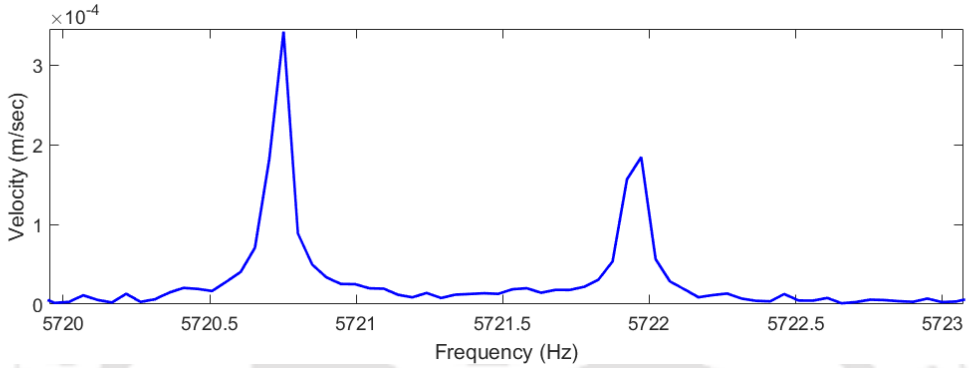

(b) Location 2

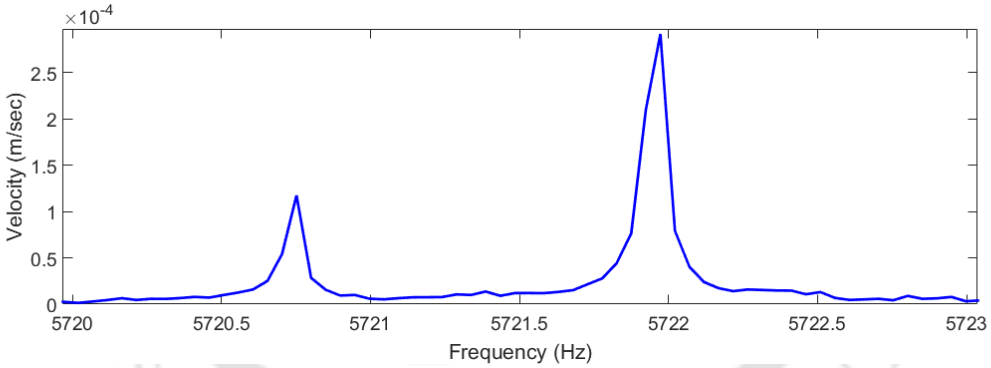

(c) Location 3

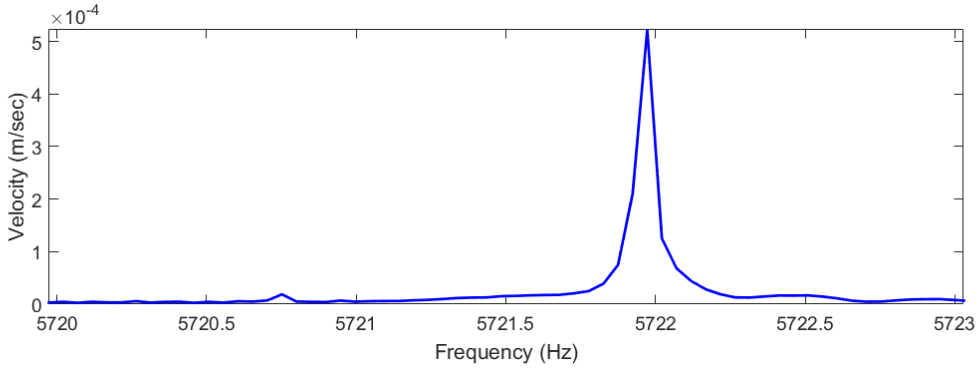

(d) Location 4

Figure 6.10: Typical LDV responses of two $N = 2$ modes between two antinodal points

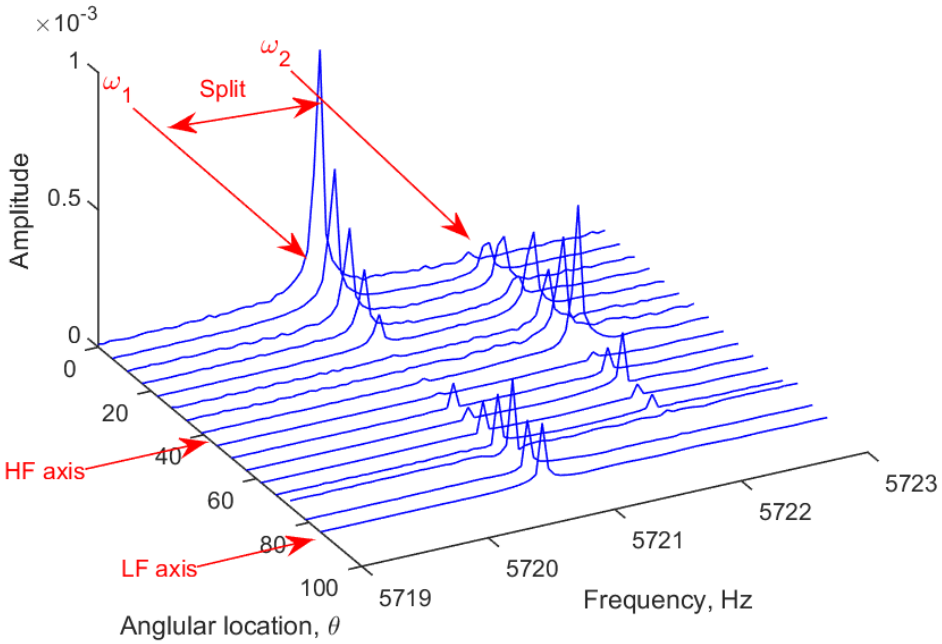

Figure 6.11 Responses of the two $N = 2$ modes (ω_1 and ω_2) showing the frequencies and corresponding axes locations around circumferential direction

6.4.2 Balancing by mass removal method

Mass is removed from the low stiffness axis in this case of balancing by mass removal method. The approach to eliminate the frequency split is to remove one, two or four unbalanced masses from each of the antinode of the low frequency axis of the unbalanced resonator. The total mass to be removed is equal to the mass of the equivalent imperfect single unbalanced mass.

Although frequency splits can be eliminated with some kind of unevenly distributed mass removal, uniformly distributed mass removal will not make the centre of mass deviate from the symmetric axis of the resonator. Therefore, the uniformly distributed mass removal can make the real mode shape closer to the theoretical shape. Hence, balancing should be done by equal mass removal technique at four antinodal points of low frequency mode. This is applicable for balancing by mass addition technique also.

The advantage of uniformly distributed four-point balancing correction is studied using finite element model. The case 10^{-5} kg unbalanced mass is considered and corrected using single, two- and four-point correction methods. The result is provided in Table 6.3.

Table 6.3: Balancing correction scheme comparison

Description	Frequency split (Hz)
Single mass unbalance	35
Single point correction at 45 deg to unbalance axis	1.23
Two-point correction at 45 deg and 225 deg to unbalance axis (180 deg apart)	0.22
Four-point correction at 45 deg, 135 deg, 225 deg and 315 deg to unbalance axis (90 deg apart)	0.19

It is found that four-point mass correction of equal amount at 90 deg apart in circumferential direction results in lower frequency split. Hence, mass removal needs to be done from four antinodal points on the rim, which are 90 deg apart, in equal amount. Remaining areas are masked. The measurements with LDV are repeated after each material removal process. The entire process is repeated till the required frequency split is achieved. There are uncertainties such as mass estimate, etching rate and axis location marking. Low precision resonator (resonator 1) is balanced by mass removal method from frequency split of 5.95 Hz. Four trials are done to achieve frequency split of less than 0.5 Hz. The frequencies of the two degenerate modes and the frequency split are shown in Table 6.4 during the balancing.

Table 6.4: Stage by stage balancing result of low precision resonator by mass removal method

Trial	Low frequency (Hz)	High frequency (Hz)	Split (Hz)
1	6296.63	6298.34	1.71
2	6298.14	6299.39	1.25
3	6298.68	6299.27	0.59
4	6299.41	6299.90	0.49

It can be seen that frequency split reduces to 0.49 Hz. Amount of mass to be removed in each trial is calculated according to the sensitivity study done earlier. Mass is removed from the low frequency axis by chemical etching method. There is 2.78 Hz frequency increase in the low frequency axis and 1.56 Hz frequency increase in the high frequency axis due to mass removal. Since mass is removed from the low frequency axis, more frequency increase is seen in low frequency axis compared to high frequency axis. However, one order

less frequency split is required to meet the resonator specification. This is addressed and achieved as mentioned in section 8.2.

6.5 Summary

The frequency increases as the radial thickness increases and the frequency split increases as the geometric error increases. The frequency split of less than 0.5 Hz is achieved in high precision resonator (resonator number 6) without balancing. It is found from the numerical simulation that four-point mass correction of equal amount of mass at 90 deg apart in the circumferential direction results in lower frequency split. Balancing procedure with mass removal method is established in low precision resonator (resonator number 1). Frequency split is reduced from 5.95 Hz to less than 0.5 Hz by balancing.

Chapter 7

Material internal friction, Surface loss and Fluid damping

In this chapter, significance and studies of other damping mechanisms such as material internal friction, surface loss and operating medium induced fluid damping are discussed. Also, the details of surface characterization equipment, surface characterization using nanoindentation, *Q* factor estimation methods, *Q* factor measurement, effect of etching on *Q* factor and evaluation of fluid damping are discussed. Based on these studies, the limiting *Q* factor is identified.

7.1 Internal friction of resonator material

Various studies have been done in the past to measure the very low material internal friction of fused silica keeping other losses away during evaluation as discussed in Chapter 1. By adopting a nodal support technique, the support loss was effectively eliminated in the previous studies. This technique enabled a systematic comparison of the samples with one another. The material internal friction induced Q_{MIF} were observed to vary between different kinds of fused silica. Fused silica has been mainly classified into four types (Type I, II, III, and IV) according to its production process. Many of the fused silica samples studied earlier were Type III which is synthetic fused silica.

The resonance quality factors of the samples were measured in a vacuum at room temperature with the ring-down method. The resonance mode vibration was excited by a piezoelectric actuator and the decay of the displacement was measured on the lateral surface by a Michelson interferometer. The mode shapes were identified by comparing the calculated resonant frequencies with the measured ones. The quality factors of all of the samples are improved by the annealing process which was done around 950 ^{o}C. The reduction of the loss in silica, caused by a high-temperature treatment, is attributed to a reduction of the surface loss. The improvement of the intrinsic loss by annealing is due to the release of residual strain and neutralizing several imperfections in the SiO_2 network. Long annealing period and cooling period was chosen to decrease internal density fluctuations that could be responsible for additional dissipation. It is to be ensured that the annealing does not degrade the other properties. It is reasonable to say that decreasing losses at decreasing frequencies is the fundamental behavior of fused silica. This behavior is not seen when imperfections are dominant.

The synthetic fused silica is classified into different grades according to homogeneity. The summary of the studies on different grades of Heraeus make Suprasil synthetic fused silica material is tabulated in the Table 7.1.

Table 7.1: Summary of fused silica material internal friction studies

Material	Q_{MIF}	Remarks
Suprasil 311	3.4×10^7	Highest Q_{MIF} reported material Annealing done at 900 ^{0}C Frequency dependency seen at high frequencies
Suprasil 312	3.4×10^7	Highest Q_{MIF} reported material Annealing done at 980 ^{0}C Frequency dependency seen at high frequencies
Suprasil 2	1.3×10^7	Large OH content Frequency dependency is weak
Suprasil 2	1.5×10^7	Flame polishing done to increase Q_{MIF} 3.0×10^7 around 5000 Hz

It is clear that Q_{MIF} of 10^7 or more is possible for an uncoated shell considering material internal friction as the only source of dissipation**.** Heraeus make Suprasil 311, which has low material internal friction, is used for the present resonator realization. It is high purity synthetic fused silica material. It is a 3D isotropic material which has high degree of index homogeneity. Suprasil grades are free from bubbles and inclusions. Hence, internal friction from fused silica will not be the limiting contributor in the effective quality factor of the uncoated resonator for the requirement of few millions.

Now, the effect of temperature on silica internal friction is discussed. Lower operating temperature is preferred for sensor operation from thermoelastic dissipation point of view because TED decreases as the operating temperature decreases. However, the material internal friction of fused silica increases towards the sub-zero temperature by over two orders from 300 K to 50 K which adversely affects the effective quality factor. Further, it reduces to a very low value at 2 K (Joshi *et al.* [2014]). Accordingly, the resonator operating temperature region should be selected.

7.2 Internal friction of coating material

Ceramic micro resonators are coated with a relatively thin metallic film for the functional requirements as sensor. Thin electrically conductive coating is applied in gyroscope resonators for electrostatic forcing and sensing. The metallization invariably degrades the quality factor due to additional TED and coating material internal friction. Studies have been done in the past to measure the internal friction of these thin film coatings as discussed in

Chapter 1. Li and Bellon [2011] developed theoretical model for internal friction in coatings for beam resonators. Based on this, expression for quality factor of metal coating is given by (Li and Bellon [2011]):

$$Q_{MIF\ coating} = \frac{1}{3}\frac{E}{E_c}\frac{d}{d_c}\frac{1}{\delta_c} \tag{7.1}$$

where d is the thickness of beam resonator, E_c is the Young's modulus of the coating material, d_c is the thickness of the coating and δ_c represents intrinsic viscoelasticity of coating material. As the coating thickness reduces, the coating material induced internal friction also reduces. Hence, ultra-thin film coating is the most preferred as TED and material internal dissipation increases as coating thickness increases. Li and Bellon [2011] measured the viscoelastic damping of gold coating for different coating thickness in micro cantilevers.

7.3 Surface loss

Machining of brittle material such as silica results in surface and subsurface damages as discussed earlier. Surface damage indicates to damages on the surface of the material such as surface roughness (SR). Sub surface damage (SSD) indicates to the damaged layer beneath the surface such as subsurface cracks, dislocations, residual stress. Both SR and SSD increases surface loss and reduce $Q_{Surface}$ (Palasantzas [2008]). When brittle failure is the dominant mechanism in material removal process, lateral cracks lead to chips removal and create the surface roughness and medial cracks cause subsurface damages (Lucca *et al.* [1998]).

7.3.1 Nanoindentation

Nanoindentation technique is used to understand surface mechanical properties compared to its bulk material property. This is done by probing of a material surface to nanometer scale depths while simultaneously monitoring high resolution data of load and depth of indentation very precisely. This method is an excellent way to measure very small volumes of materials. The only problem is determining the indentation area. For the indents below 1 mm in size, the resolution of optical microscope is insufficient. The depth sensing indentation method in nanoindentation technique is used to solve this problem. In this method, the load and the displacement of the indenter are recorded during indentation (Kim *et al.* [2003]). Mechanical properties of the indented volume can be determined without seeing the indent. The mechanical properties on surface or subsurface obtained from this nanoindentation test are hardness, reduced modulus, creep, wear resistance, interfacial adhesion and fracture toughness (Sattler [2010]). The indenter is made of diamond with symmetric three-sided high precision Berkovich pyramid shape as shown in Figure 7.1. The geometrical relationship between the contact depth of indentation (h_c) and the projected contact area (A) is known. Hence, the in-situ contact depth sensing is used to calculate the projected contact area. Typical indentation profile is given Figure 7.2 where the contact pressure, the contact depth and the penetration depth are shown. Figure 7.3 shows the indentation profile at full load condition, full unload condition and plastic deformation.

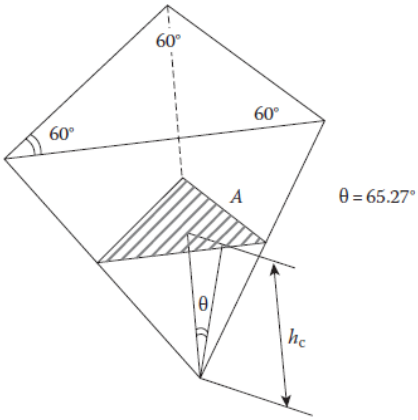

Figure 7.1: Berkocich pyramid indenter used for nanoindentation test (Reproduced with permission from Sattler [2010])

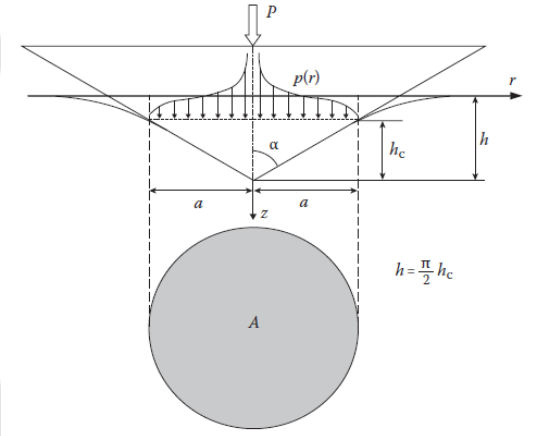

Figure 7.2: Typical indentation profile in nanoindentation test showing the contact depth and the penetration depth (Reproduced with permission from Sattler [2010])

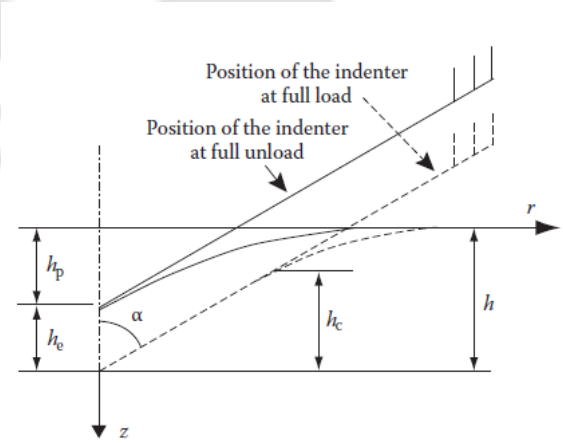

Figure 7.3: Schematic of a typical profile at full load condition, full unload condition and plastic deformation (Reproduced with permission from Sattler [2010])

During the test, the force and the displacement are recorded as the indenter tip is loaded to the specimen with a prescribed loading and unloading profile. A typical load-displacement (P-h) characteristic of the test is as shown in Figure 7.4. The shape of the graph is different for different materials. These are the characteristics of energy absorbing or energy releasing mechanisms during the evaluation.

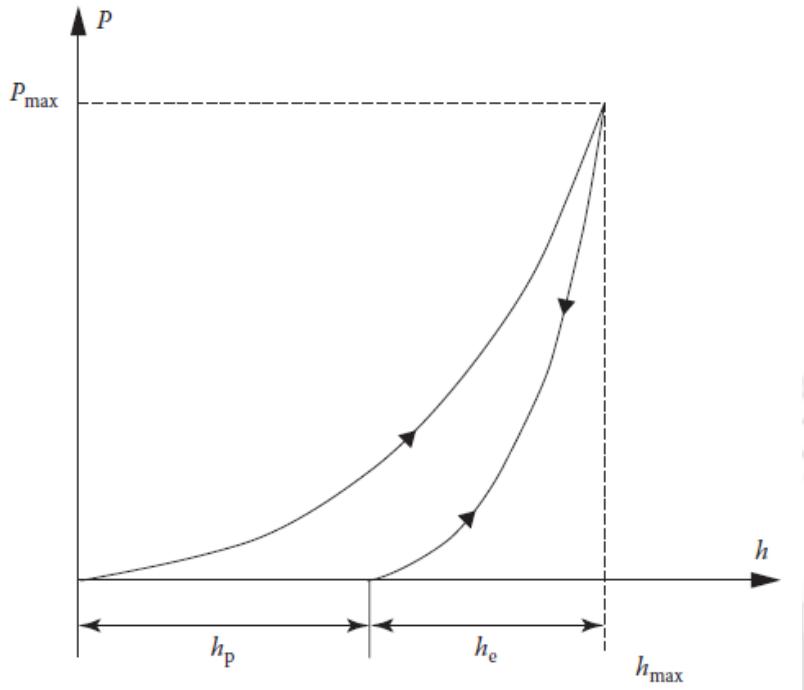

Figure 7.4: Typical P-h curve of nanoindentation test (Reproduced with permission from Sattler [2010])

7.3.2 Theory of nanoindentation

Young's modulus of the material under test is calculated based on the Sneddon equation (Sattler [2010]):

$$\frac{1}{E^*} = \frac{1-\vartheta_s^2}{E_s} + \frac{1-\vartheta_i^2}{E_i} \tag{7.2}$$

where $E^*$is the reduced Young's modulus which is obtained from nanoindentation test, E_s and ϑ_s are Young's modulus and Poisson's ratio of the test sample, E_i and ϑ_i are Young's modulus and Poisson's ratio of the diamond indenter.

The load - penetration depth relationship is given by (Sattler [2010]):

$$P = 2E^* \frac{\tan\alpha}{\pi} h^2 \tag{7.3}$$

where P is the force applied to the indenter, α semi angle of indenter and h is the indenter penetration depth.

Contact stiffness is calculated at the starting of the unloading elastic region of the test and is given by (Sattler [2010]):

$$\frac{dP}{dh} = 4E^* \frac{\tan\alpha}{\pi} h \tag{7.4}$$

Relationship between the penetration depth and the contact depth is given by (Sattler [2010]):

$$h = \frac{\pi}{2} h_c \tag{7.5}$$

where h_c is the contact depth.

Projected contact area A is calculated based on the depth measurement during the test for a given indenter tip and is given by (Sattler [2010]):

$$A = \frac{4}{\pi} h^2 \tan^2\alpha = \pi h_c^2 \tan^2\alpha \tag{7.6}$$

Contact stiffness can also be expressed in terms of the projected area and is given by (Sattler [2010]):

$$\frac{dP}{dh} = 2\mathrm{E}^* \frac{\sqrt{\mathrm{A}}}{\sqrt{\pi}} \tag{7.7}$$

For Berkovich indenter, the projected contact area is given by (Sattler [2010]):

$$A = 9.93\ h^2 \tag{7.8}$$

Hardness H can be obtained from the relationship (Sattler [2010]):

$$H = \frac{P}{24.5\ h_c^2} \tag{7.9}$$

7.3.3 Surface characterization results

Hysitron make Ti Premier series nanoindenter is used for nano-micro mechanical and tribological characterization. The equipment is shown in Figure 7.5.

The following are the features of the nanoindenter:

a) Nanoindentation: Quantitative modulus, hardness, creep, fracture toughness.
b) Dynamic mechanical analysis: Storage modulus and loss modulus as a function of measurement depth, frequency and time.
c) Imaging: In-situ topography imaging with high accuracy and measurement reliability.
d) Normal load range : 75 nanoN to 10 milliN
e) Normal displacement range : 0.2 nm to 5 micron

Figure 7.5: Hysitron make Ti Premier series nanoindenter

Surface characterization of fused silica standard is carried out first to evaluate the mechanical properties and the following is test parameters.

Maximum force	: 998.2 microN
Maximum depth	: 79.8 nm
Contact depth	: 50.1 nm
Contact area	: 94390.5 nm^2
Contact stiffness	: 25.3 microN/nm

It is estimated that the Young's modulus and the hardness are 72.84 GPa and 10.57 GPa respectively. Then, the surface characterization of the fused silica shell is carried out after machining and after chemical treatment. The measurements are done on the cylindrical and the spherical regions of the shell as shown in Figure 7.6. The characterization is carried out on the ultrasonically machined surface and the force - displacement plot is given in Figure 7.7. The red curve gives the loading characteristics and the green curve gives the unloading characteristics. The contact stiffness is calculated at the starting of the unloading elastic region. The maximum force applied is 998.1 microN and the corresponding maximum depth is 107.4 nm.

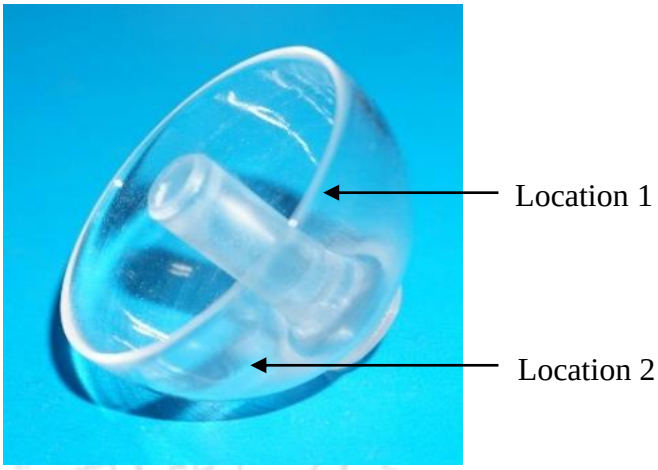

Figure 7.6: Identification of locations on ultrasonically machined resonator surface

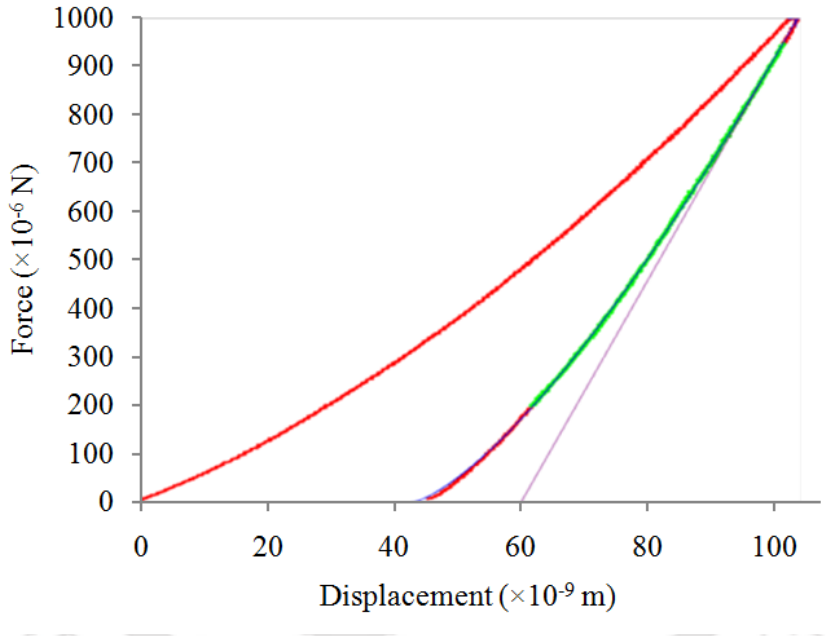

Figure 7.7: Force – displacement result of nanoindentation test

The nanoindentation test results on the ultrasonically machined surface are given below:

Maximum force	: 998.1 microN
Maximum depth	: 107.4 nm
Contact depth	: 73.7 nm
Contact area	: 180171 nm^2
Contact stiffness	: 22 microN/nm

Table 7.2 gives the resonator surface mechanical properties such as hardness and reduced modulus after ultrasonic machining (USM) on two locations.

Table 7.2: Mechanical properties of the resonator surface after USM

Location (no.)	Hardness (GPa)	Reduced Young's modulus (GPa)
Cylindrical region (1)	0.5-0.2	16.1-5.0
Spherical region (2)	1.4-0.7	23.2-12.2

It can be seen that the hardness and reduced Young's modulus is very much less compared to the bulk material nominal hardness of 11 GPa and Young's modulus of 73 GPa because of the formation of damaged surface layer after USM. In order to remove the micro cracks created by USM, an etching process is required. There are wet chemical etching and dry plasma etching methods. In the wet chemical etching, the component is etched 10-12 sec in hydrofluoric acid (HF) solution at a temperature of 20 ºC. Chemical etching is done in two stages and 25 micron material is removed from inside and outside surfaces in each stage of the etching. Dry etching by chemical action is also possible in plasma etching method which is a very slow etching rate process. The improvement of the hardness and the reduced Young's modulus over the resonator surface after wet chemical etching is tabulated in Tables (7.3) and (7.4).

Table 7.3: Effect of chemical etching on the hardness of the resonator surface

Location (no.)	Hardness (GPa) after chemical etching 1 (25 micron)	Hardness (GPa) after chemical etching 2 (25 micron)
Cylindrical region (1)	12.3-4.1	12.5-10.4
Spherical region (2)	11.4-2.3	8.9-8.4

Table 7.4: Effect of chemical etching on Young's modulus of the resonator surface

Location (no.)	E^* (GPa) after etching 1 (25 micron)	E^* (GPa) after etching 2 (25 micron)	E (GPa) after etching 2
Cylindrical region (1)	64.0-32.9	62.6-58.0	64.7-59.7
Spherical region (2)	56.3-21.6	57.6-44.0	59.2-44.7

It can be seen that the reduced Young's modulus and the hardness improves after each stage of chemical etching due to the removal of major part of the damaged surface layer. However, the bulk material hardness of 11 GPa and Young's modulus of 73 GPa is not

reached over the entire surface. The spherical region shows relatively lower mechanical properties compared to the cylindrical region. This shows that there is still presence of surface damage on the spherical region. More chemical etching results in reduction in the nominal dimensions. The reduction in dimensions causes frequency change from the design value which can cause mode interactions and increases anchor loss.

7.3.4 Surface loss estimation

Generally surface loss is modelled by a damaged surface layer with complex Young's modulus (Jinling *et al.* [2002], Imboden and Mohanty [2014], Bernstein *et al.* [2015]). Using the damaged surface layer thickness of δ and dissipative surface complex Young's modulus of E_{ds}, energy loss per cycle due to the damaged surface is found out. Then, the following expression is used for the estimation of $Q_{Surface}$ of beam resonators (Hao *et al*. [2003]):

$$Q_{Surface} = \frac{bd}{3b+d} \frac{E}{2\delta E_{ds}} \tag{7.10}$$

where b is the width of beam resonator, d is the thickness of beam resonator, E is the Young's modulus of the bulk material, δ denotes the characterized thickness of the surface layer, E_{ds} is a constant related to the surface defects and stress which is a surface layer property. It is very difficult to estimate the values of δ and E_{ds}. For thin structures with $d \ll b$, $Q_{Surface}$ increases as the thickness increases. This is because of the lesser surface loss due to smaller surface area to volume ratio. Hao *et al*. [2003] used best-fit values of δE_{ds} to minimize the error between the model and the experimental data. The range of δE_{ds} used by them is from 1.38 to 0.81 for different beam resonator configurations and surface conditions.

7.4 Limiting *Q* factor estimation

Now, the Q factor corresponds to the major damping mechanisms such as TED, anchor loss, surface loss and material internal friction are estimated. This is to understand the limiting damping mechanism at different stages from the design to the realization of the resonator with respect to the design requirement of few millions of effective quality factor.

The major TED simulation results, which are obtained in Chapter 3, are reproduced here for the uncoated and the coated final functional hybrid resonators. Q_{TED} for the hybrid configuration without coating is 2.9×10^9 (result from section 3.5.1). Q_{TED} with 1000 A^o coating on all faces of functional hybrid configuration is 4×10^6 (result from section 3.5.3). Next, Q_{Anchor} estimate is made.

The precision dimension and tolerance requirements, which are derived from the anchor loss sensitivity studies, are met during the fabrication of the resonator. Discrete dimensions and geometries are measured during the metrology. However, the exact 3D surface profiles could not be measured due to the non-availability of the appropriate measuring instruments. Hence, the exact 3D geometry of the realized resonator could not be simulated. Hence, only an approximate estimate of the anchor loss can be made. Based on the

metrological measurements, the Q_{Anchor} for the fine precision resonator would be more than 10^7.

By using equation (7.10), an approximate estimate of $Q_{Surface}$ of the present silica resonator can be made. However, the actual value of δE_{ds} might be different from those reported by Hao *et al*. [2003]. This should be arrived for a given realized resonator with respect to the experimental results as discussed in (Hao *et al*. [2003], Imboden and Mohanty [2014]). For δE_{ds} value of 1.38, $Q_{Surface}$ is 8.8×10^6 for 1 mm thick present silica resonator.

Since Suprasil 312 high purity fused silica material is used for the fabrication of the present resonator, Q_{MIF} should be more than 10^7. Now, the material internal friction from gold coating material is estimated using the measured internal damping due to viscoelasticity by Li and Bellon [2011]. For the resonator with 1000 A^o gold coating and operating in few kHz, the viscoelastic damping value is 0.002. Even though equation (7.1) is developed for estimating coating internal friction for beam structure, it is used here for the hemisphere configuration by considering the beam thickness same as the hemisphere radial thickness. Also, the actual viscoelastic damping of gold in the present resonator coating might be different from the measured viscoelastic damping by Li and Bellon [2011]. Using the equation (7.1), an approximate estimation of $Q_{IF\ coating}$ can be made. $Q_{IF\ coating}$ for 1000 A^o gold coating with viscoelastic damping value of 0.002 is 1.74×10^6.

Q_{Fluid} is not significant as the resonator is characterized under ultra high vacuum. The test results at different vaccum levels are discussed later in this chapter. $Q_{Electronics}$ is not significant as the resonator is excited using acoustics and the excitation forces are very minimal. By operating the resonator at appropriate low pressure environment and with the selection of suitable electrical parameters, the contributions of Q_{Fluid} and $Q_{Electronics}$ in the effective quality factor can be minimized.

Based on the estimation of different damping mechanisms, the limiting damping mechanism is arrived for the Q_{Eff} requirement of few millions. It can be inferred that the Q_{Eff} of uncoated high precision fused silica material resonator of millimetre size can be limited by the surface loss. Q_{Eff} of gold coated fused silica material resonator can be limited by Q_{TED} (with coating), $Q_{IF\ coating}$ and $Q_{Surface}$ as these losses are in the same order (10^6).

7.5 Q_{Eff} measurement without thin layer coating

Q_{Eff} is evaluated at each stage as per the procedure explained below.

7.5.1 Measurement of the frequency and Q_{Eff} (for Q_{Eff} less than 10^5)

The step-by-step procedure for the measurement of the frequency and the quality factor is discussed below. Rotary pump is used for obtaining a medium vaccum level.

1. Perform sine sweep (between 4000 and 7000 Hz) to identify the frequency of the N = 2 mode ($f_{Ambient}$) using LDV. After steady state resonance is reached, natural frequency of the resonator is obtained using FFT of the velocity signal from the LDV.

Q factor in ambient condition ($Q_{Ambient}$) is measured keeping the chamber in open condition. Here, the measurement is done at 1 atmospheric pressure condition. Q factor is calculated using the following relationship (Pan *et al.* [2016], Bernstein *et al.* [2015]):

$$Q = \frac{f}{f_{\mathrm{BW}}} \tag{7.11}$$

where the f is the resonant eigen frequency at which the response reaches its maximum, f_{BW} is the frequency bandwidth at half power point.

2. Once the vaccum chamber door is closed, switch on the rotary pump and achieve a pressure of 10^{-2} millibar to start the measurements in vaccum condition.

3. Perform a coarse sine sweep in the range of +/- 25 Hz around $f_{ambient}$ to identify the frequency of the N = 2 mode. From this result, narrow down the range of the natural frequency to within 5 Hz and then subsequently reduce to fine range of 2 Hz. The mode shape is also captured. 72 points need to be scanned to find the mode shape. Maximum sampling is used (approximately 80 sec up to 7 kiloHz) to get the exact resonance frequency. Then, a fine scan is required with 2 degree resolution (180 points). So, the full mode shape can be accurately assessed by two scans. N = 2 mode is split into high frequency (f_2^H) and low frequency (f_2^L) modes in actual resonator due to imperfections. Then, the locations of the high and the low frequency axes are identified. Then, Q factor estimation is done using equation (7.11).

7.5.2 Measurement of the frequency and Q_{Eff} (for Q_{Eff} more than 10^5)

High vaccum level is required to minimize the fluid induced damping in order to achieve high quality factor. Turbo pump should be used for obtaining a high vaccum level. The step-by-step procedure for the measurement of the frequency and the quality factor are mentioned below.

1. Attain a pressure of 10^{-5} millibar using turbo pump to start the measurements.

2. After steady state resonance is reached, the dither drive is switched off to remove forced excitation to the resonator. Then, natural run down happens and the amplitude of vibration decays. Natural frequency of the resonator is obtained using FFT of the velocity signal from the LDV. The resonance N = 2 frequency is around 5500 Hz. The sampling rate used is 20,000 Hz. Thus, measurement sampling frequency is more than twice of N = 2 frequency and it meets Nyquist criterion.

3. Now, the Q factor estimation can be made in the natural run down. The better estimate of damping for high Q resonators is by ‘ring-down’ method. The ring-down time, which is the time taken for the vibration amplitude to reach $(1/e)^{th}$ of the original amplitude, is measured in this method. Ring-down measurements are done on the rim of the cylindrical region. Q factor is calculated using the following relation (Jeanroy *et al.* [2014]):

$$Q = \pi \tau_r f \tag{7.12}$$

where τ_r is decay time constant obtained from the ring-down test.

A typical run-down measurement of velocity using the LDV is shown in Figure 7.8 for the high precision resonator. Figure 7.9 shows the corresponding FFT of the velocity measurement to obtain $N = 2$ natural frequency. Since it is natural rundown after removal of excitation, $N = 2$ frequency is very predominant and is noise free.

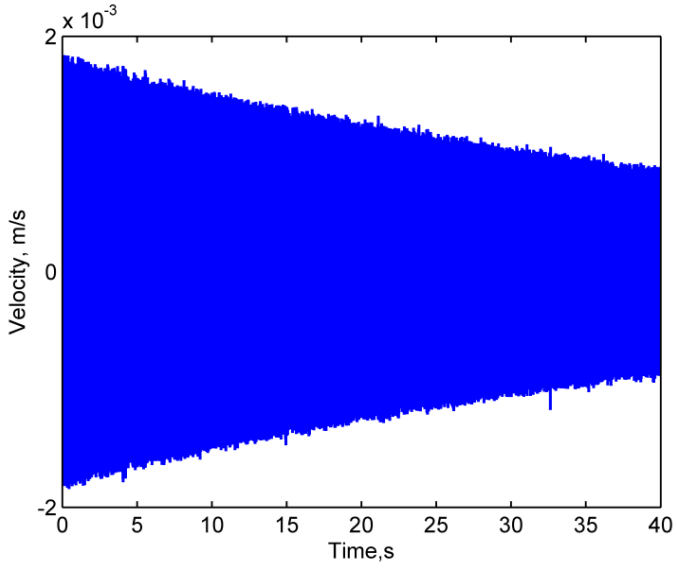

Figure 7.8: A typical run-down measurement of velocity at resonator rim using the LDV

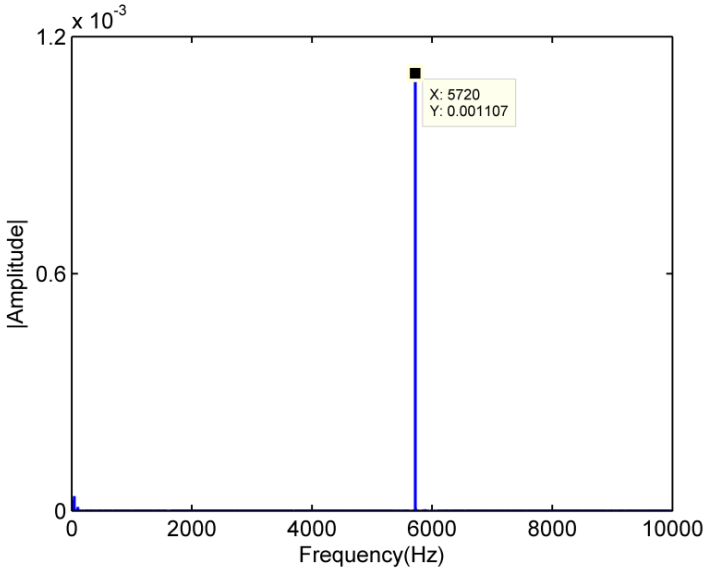

Figure 7.9: A typical FFT of the velocity measurement showing $N = 2$ natural frequency

The Q_{Eff} measurements are carried out after USM and at each stage of etching till Q_{Eff} of more than two million is achieved. More etching will result in more reduction in basic

dimensions. This increases the capacitive gaps and will affect the drive voltage requirements and the sensitivity. Also, more chemical etching results in significant reduction in nominal dimensions and can increase anchor loss due to mode interactions as mentioned in section 7.3.3.

The results of Q_{Eff} for six resonators are tabulated in Table 7.5. Low precision resonator (resonator 1) was used for dry etching trials using plasma and could reach a Q_{Eff} of 1.5×10^5 only. There is very low material removal rate for plasma etching and is not sufficient for removal of the damaged surface layer in the present maturity of the process. Q_{Eff} improvement by plasma etching is one order less that that by chemical wet etching. Other resonators are etched chemically. Resonator 7 got damaged during handling.

Table 7.5: Effect of chemical wet etching on Q_{Eff}

Resonator sl. no.	After USM	After etching 1	After etching 2	After etching 3
2	15×10^3	2.5×10^6		
3	50×10^3	1.2×10^6	4.0×10^6	4.5×10^6
4	25×10^3	2.2×10^6		
5	20×10^3	1.0×10^6	2.0×10^6	
6 (high precision resonator)	70×10^3	5.0×10^6		
8	6×10^3	4.0×10^6		

It can be seen that the very low Q_{Eff} is obtained after ultrasonic machining. This is because of the surface damage caused by the machining. There is a variation in Q_{Eff} after USM which means that the fabrication parameters are to be optimized further from the surface damage point of view and process should be consistent.

It can also be seen that the chemical etching removes major part of the damaged surface layer which is the main contributor of the surface loss. The Q_{Eff} is improved by order of three to the range of millions after etching. Some resonators needed more etching trials because wet chemical etching method is not a precisely controlled process.

7.6 Q_{Eff} circumferential variation

Two resonators (resonator no 3 and 6) are characterized for the Q_{Eff} variation in circumferential direction and the result is as shown in Figure 7.10. The Q_{Eff} evaluation is carried out every 45 deg in circumferential direction and 15% variation is found from mean value. The variation is mainly due to the variation in the surface loss around circumferential direction and mass unbalance pattern.

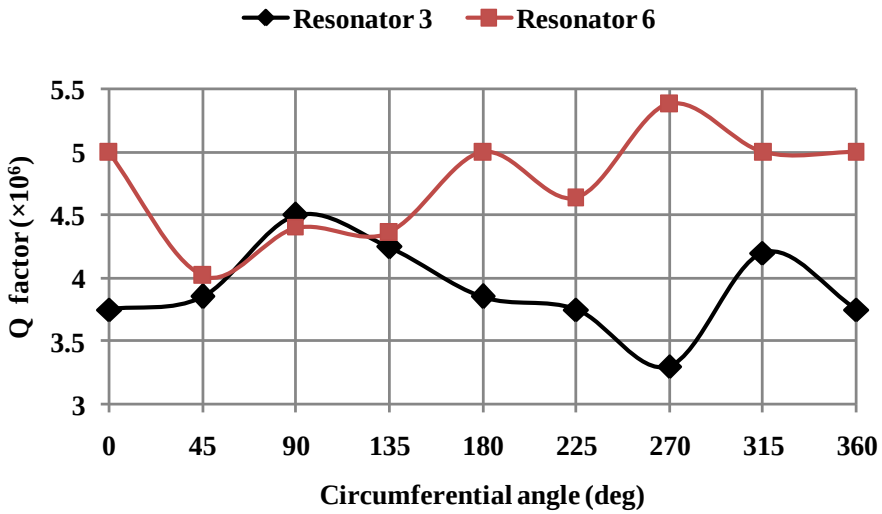

Figure 7.10: Q_{Eff} variation in the circumferential direction

7.7 Fluid damping

As discussed in Chapter 1, there is a critical pressure below which the Q_{Fluid} is independent of the operating ambient pressure. This pressure depends mainly on factors such as resonator size and configuration. This is very difficult to estimate by simulation for complex hybrid configurations. Hence, an experimental evaluation is done to obtain this critical operating pressure for the present hybrid resonator configuration. One resonator (resonator 4) is characterized in the vaccum chamber for different ambient pressures to arrive at the sensor operating pressure as shown in Figure 7.11.

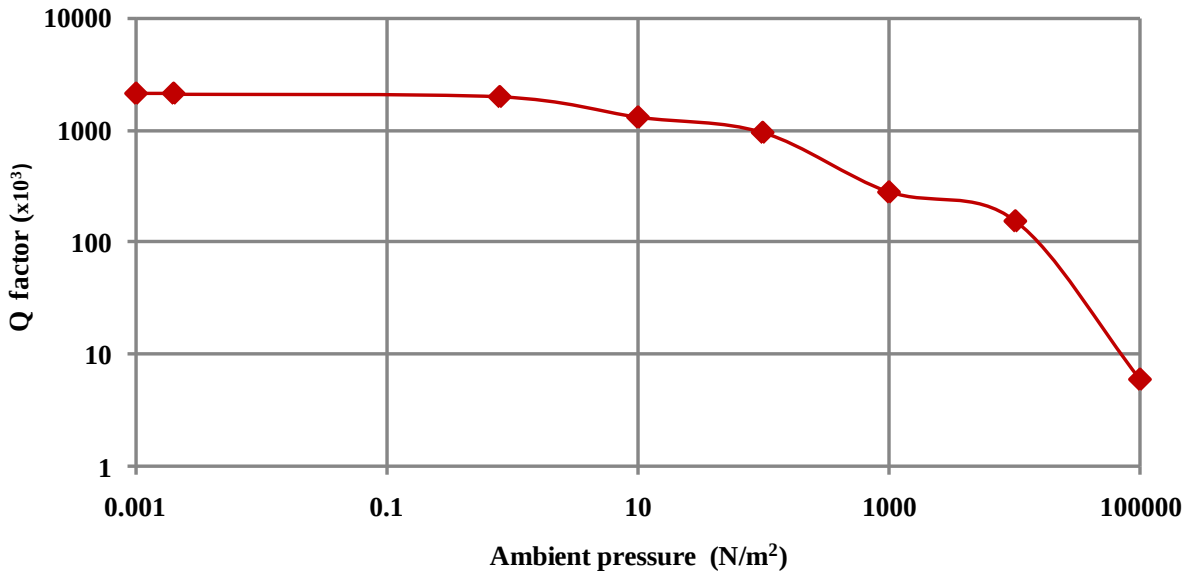

Figure 7.11: Effect of ambient pressure on Q_{Eff}

It is found that there is no significant Q_{Eff} improvement for pressure less than 1 N/m^2 (10^{-2} millibar). Similar observation is also seen in Candler *et al.* [2003] and Svitelskiy *et al.* [2009]. Since the characterisation and sensor operation is done at 10^{-3} N/m^2, Q_{Fluid} is not significant in Q_{Eff}. Since the resonator is excited using acoustics, the contribution of $Q_{Electronics}$ in Q_{Eff} is also not significant.

The maximum Q_{Eff} measured for the hybrid resonator is 5.5 million as shown in Figure 7.10. This Q_{Eff} is less than the reported value of 10 million for the space proven hemispherical alone resonating structure configuration in Rozelle [2009]. The hybrid configuration resonator presented in this work has more angular gain and effective mass (approximately 35 %) which also improve the MNER similar to Q_{Eff} contribution. Also, further optimizations of the fabrication parameters, etching and chemical cleaning process parameters are proposed to minimize the surface loss contribution as mentioned in scope for the future work under section 9.3. This will improve Q_{Eff} to more than 10 million. Then, the sensor level performance is expected to be better than that reported in Rozelle [2009].

7.8 Summary

Internal friction from fused silica is not the limiting contributor in the effective quality factor of the uncoated resonator. Ultra-thin film coating is the most preferred as the thermoelastic dissipation and the coating material internal dissipation increases as the coating thickness increases. Increase of hardness and Young's modulus is seen after each stage of the chemical etching due to the removal of the major part of the fabrication induced damaged surface layer. Q_{Eff} is improved by order of three to the range of few millions after chemical etching. No significant Q_{Eff} improvement is found for pressure less than 1 N/m^2 (10^{-2} millibar). The sensor operation is proposed to be done much lower than 1 N/m^2 to eliminate

contribution of Q_{Fluid} in Q_{Eff}. Thus, Q_{Eff} of uncoated high precision fused silica material resonator of millimetre size is limited by the fabrication induced surface loss. Also, Q_{Eff} of gold coated fused silica material resonator is limited by the thermoelastic damping from the coating material, the coating material internal friction and the fabrication induced surface loss as these losses are in the same order (10^6).

Chapter 8

Demonstration of effective *Q* factor in functional form resonator

The resonator material is fused silica which has low coefficient of thermal expansion and very low material internal friction. These factors are good from thermoelastic damping and material intrinsic damping point of view. However, it is an electrical insulator. Hence, the resonators need to be made electrically conductive for electrostatic excitation of its $N = 2$ functional mode and sensing of its precession for using the structure as a gyroscope resonator. Gold is the most preferred material for this electrical application. But gold has large value of α and low TED. Based on the studies of the effect of thin layer coating thickness, it is preferred to have coating with minimum thickness which simultaneously meets the contradictory requirement of lower electrical resistance. Hence, thin film gold coating, its characterization and Q_{Eff} evaluation of coated resonator are critical. This chapter deals with details of coating machine, thin film coating procedures, surface profile measurements, coating characterization, and evaluation of Q_{Eff} in the coated resonator.

8.1 Thin film coating

There are different deposition techniques such as plating, evaporation, and sputtering (Martin [1986]). The advantage of sputter coating process is that it is a high energy process and it produces high density, improved adhesion, hardness and roughness, and high stability coatings compared to evaporation. Sputter deposition is a physical vapour deposition process for depositing thin films. Sputtering means ejecting material from a target and depositing it on a substrate. The target is the source coating material. Substrates are placed in a vacuum chamber and the chamber is pumped down to a prescribed process pressure. Sputtering starts when a negative charge is applied to the source material causing plasma or glow discharge. Positive charge gas ions, generated in the plasma region, are attracted to the negatively biased source plate at a very high speed. This collision creates a momentum transfer and ejects atomic size particles from the source. These particles are deposited as a thin film onto the surface of the substrate.

There are two types of sputter coating methods such as magnetron sputtering and ion beam sputtering. Magnetron sputtering is preferred where a relatively thicker coating thickness is needed. Magnetron sputtering can be done either in DC or RF modes. DC magnetron sputtering is done with conducting materials. If the source is a non-conducting material, the positive charge will build up on the material and it will stop sputtering. RF magnetron sputtering can be done on both the conducting and the non-conducting materials. Here, magnets are used to increase the percentage of electrons that take part in ionization of events and it increases the ionization efficiency significantly. However, ion beam sputtering technique can do ultra-thin, precise and complex configuration coating. Quartz crystal gives

feedback on deposition rate and physical thickness of the coating. The coating is carried out in high vacuum environment. In-situ sputter cleaning of the substrate is preferred for good adhesion.

Ion beam sputtering is used for shell coating as it requires ultra-thin film coating of the order of 1000 A^{o}. Shell resonator is the substrate to be coated from a gold target in the coating unit. The available general ion beam coating machine cannot be used for coating of 3D spherical surfaces. The existing machine is augmented with a glancing mechanism to ensure coating of the resonator spherical surfaces. The 3D model of the glancing mechanism is shown in Figure 8.1. Figure 8.2 shows the components of the glancing mechanism. It consists of small bearings, universal joints and other structural connecting elements. The coating unit interface of the glancing mechanism has got rotating and non-rotating part assemblies. The stator part of the glancing mechanism is attached to the static body of coating unit and the rotating part of the glancing mechanism is attached to the rotating shaft of the coating unit. Initially, the substrate to be coated is assembled to appropriate substrate holding fixture. Then, it is interfaced to the substrate interface of the glancing mechanism which is a rotating part. The resonator substrate needs to be rotated during coating for getting exposure to the entire coating surface. The areas, where coating is not required, are to be masked during coating. The stem base needs to be masked as it is resonator mounting interface. Before thin film coating, resonator should be chemically cleaned about 10 minutes.

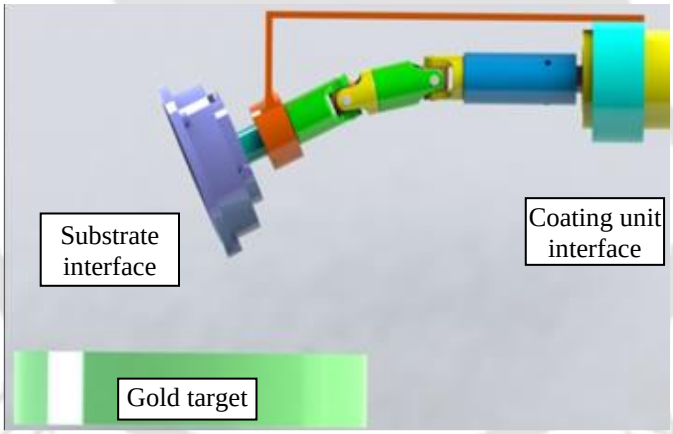

Figure 8.1: 3D model of glancing mechanism in coating machine for 3D coating

Figure 8.2: Realized components and subassemblies of glancing mechanism

Resonator 3 is assembled to the substrate holder. This resonator has frequency split of 0.39 Hz and Q_{Eff} of 4.5×10^6 before coating. Then, this is assembled to the substrate interface of the glancing mechanism. The glancing mechanism is assembled to the coating machine. Figure 8.3 shows the setup for the inside surface coating of the resonator in ion beam sputter coating machine. Coated resonator with substrate holding fixture is shown in Figure 8.4. The stem base was masked to avoid coating at the mounting interface. After ultra-thin film coating, coated component is subjected to thermal cycling to relieve stress. The resonator 3 is fully gold coated as shown in Figure 8.5.

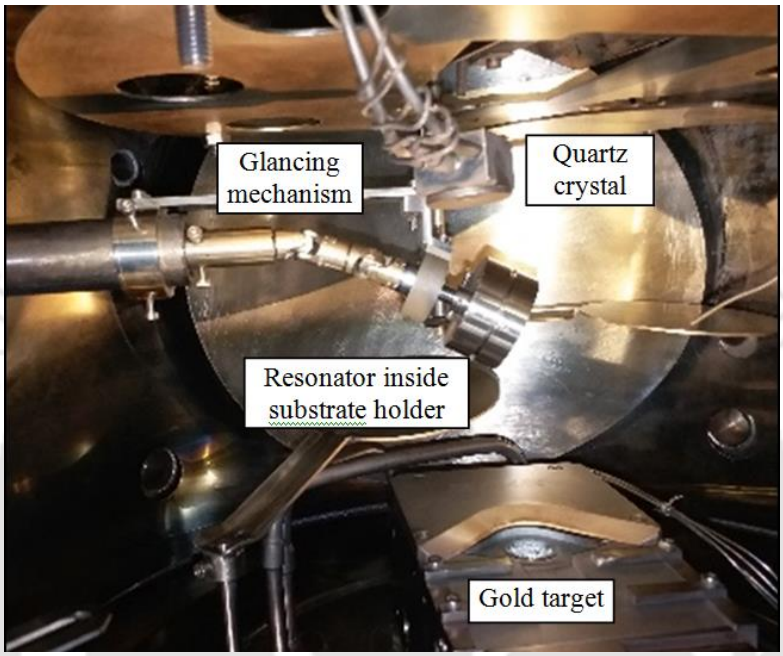

Figure 8.3: Resonator inside surface coating setup in ion beam sputter coating machine

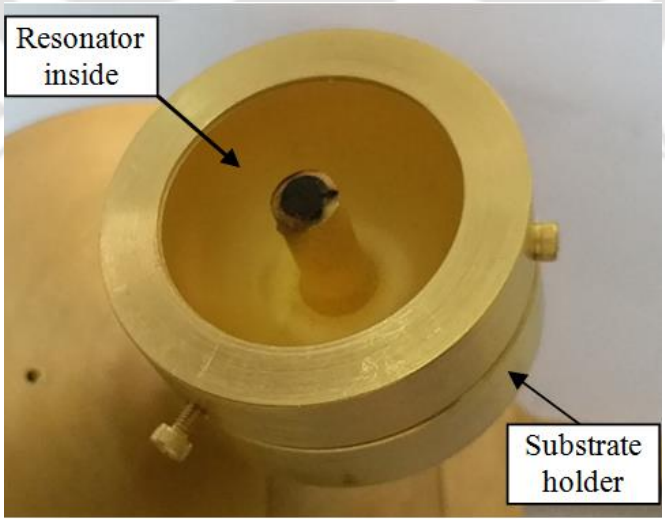

Figure 8.4: Gold coated resonator with substrate holder

Figure 8.5: Fully gold coated fused silica resonator

8.2 Balancing and Q_{Eff} of coated resonator

As discussed earlier, balancing can also be done by mass addition technique. Also, the finer level of balancing can be done after gold coating. Chemical etching, which is used for balancing by mass removal method, is not a precise process and involves more process parameters. Hence, more trials are required and also difficult to achieve ultra-low frequency split. Mass addition technique is more precise because of the lesser process parameters. Uniformly distributed balancing masses can be added to imperfect resonator to eliminate frequency split (Lin *et al.* [2015]). Hence, balancing should be done by equal mass addition at four anti-nodal points of high frequency axis.

Magnetron sputter deposition technique is used for mass addition at the required locations of the resonator. Gold is used as mass addition material for the gold coated resonator. The quantity requirement is calculated using the unbalanced mass - frequency split sensitivity relationship as discussed earlier. It is estimated that thickness of up to few microns is required depending on the milliHz unbalance value. Hence, magnetron sputtering is preferred as the mass addition thickness is relatively higher for balancing.

Gold is deposited as four equal masses of the required quantity at four anti-nodal locations of high frequency axis on the rim using magnetron sputter coating machine. Table 8.1 gives stage by stage result of balancing trials of coated resonator by mass addition method.

Table 8.1: Stage by stage result of balancing trials of coated resonator by mass addition method

Description	Low frequency (Hz)	High frequency (Hz)	Frequency split (Hz)
Before balancing	5975.88	5976.27	0.39
Trial 1	5975.98	5976.12	0.14
Trail 2	5975.46	5975.51	0.05

It can be seen that the higher frequency has come down by 0.76 Hz while the lower frequency has come down by 0.42 Hz as the mass addition is done at higher frequency axis. One order improvement in the frequency split is achieved by this precise mass addition technique. The achieved frequency split is 50 milliHz which meets the fine balancing specification. The achieved Q_{Eff} after coating is 2.4×10^6 which also meets the specification of more than one million. The Q_{Eff} and frequency split meets the specification requirement for the final functional hybrid resonator as discussed in Chapters 3 and 4.

8.3 Coating characterization

The surface characterization of thin film gold conductive coating mainly involves coating thickness measurement and coating adhesion to its parent material as functional requirements. Since the characterization using nanoindentation technique is a destructive method, it cannot be done on the actual high precision resonator. Hence, it is done at coupon level. The surface integrity of the lapped and fine polished surface is very good (Guzzo and Mello [2000]) and it is required for good adhesion of coating on base structure. Hence, polished silica coupons are used and they are coated using the magnetron sputter thin film coating method and ion beam sputter ultra-thin film coating method. These coupons are coated along with the actual resonator coating. Coating characterization is done for coupons coated using both the coating methods.

8.3.1 Atomic force microscopy (AFM)

AFM is a high resolution scanning probe type microscopy with demonstrated resolution of the order of fractions of a nanometer which is 1000 times better than the optical diffraction limit. It is an imaging technique based on mechanical interactions between a very sharp microfabricated probe and sample surface. Probe scans the surface line by line and across the surface to trace its topography. Different AFM modes such as contact mode and non-contact mode are available. The probe drags in contact with the surface at a constant force in the contact mode while the probe oscillates at its resonance in the non-contact mode. Park make XE7 series instrument, which is shown in Figure 8.6, is used to make sample

images and its characteristics. It measures surface profile and roughness in nanometer resolution. It has got decoupled XY and Z flexure based scanners. Its non-contact mode provides less tip wear and prolonged high resolution scan with minimum sample modification. The non-contact mode is used in the present measurement to get prolonged high resolution data and immunity from parameter dependent results. The roughness of the surface needs to be measured before the thin film coating to ensure that the roughness values are much less than the planned coating thickness. Figures 8.7 (a) and (b) show the images of the rough and the smooth surfaces. Polishing is done to achieve very low surface roughness. The surface roughness value is measured at 12 locations on coupon before the coating and is tabulated in Table 8.2.

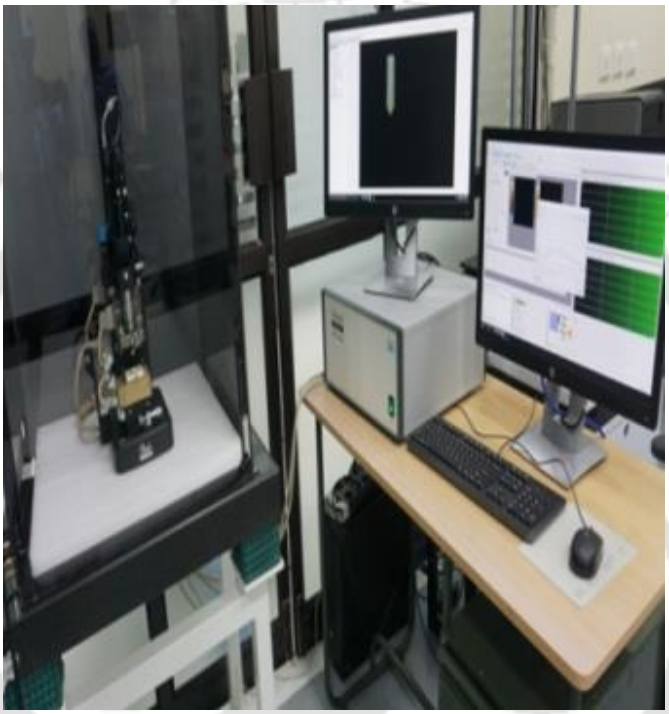

Figure 8.6: Park make XE7 series AFM for surface roughness measurement

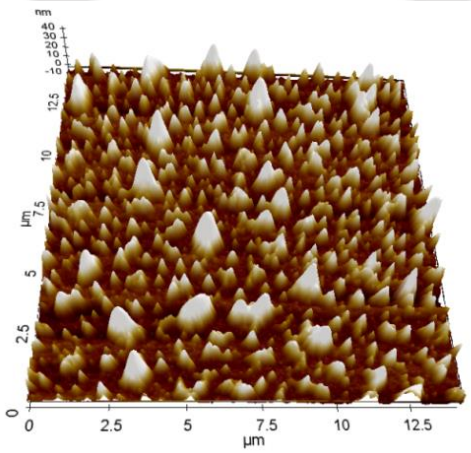

(a) Image of rough surface

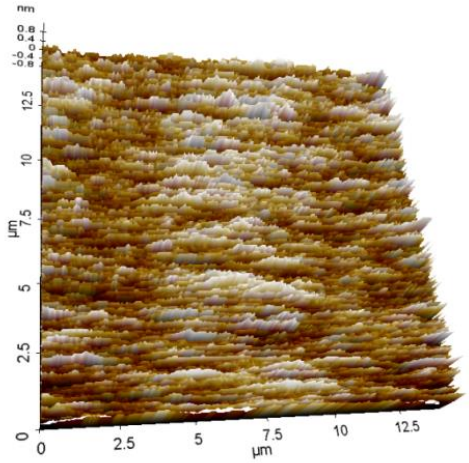

(b) Image of smooth surface

Figure 8.7: Typical AFM images of a rough and a smooth surface

Table 8.2: Surface roughness (R_a) values on silica coupon before coating

Location on coupon	Roughness R_a ($\times 10^{-9}$ m)
1	0.204
2	0.199
3	0.214
4	0.221
5	0.211
6	0.212
7	0.392
8	0.395
9	0.369
10	0.376
11	0.223
12	0.225

It can be seen that the range of roughness values is 2 A^o - 4 A^o which is much lesser than the thin film coating thickness range of bulk surface coating (few thousands of A^o) and local coating for balancing (few microns). Thus, it is ensured that the surface profile meets the thin film coating requirement.

8.3.2 Characterization of magnetron coated thin film

The magnetron sputtering based thin film coated coupon is shown in Figure 8.8. An area is not coated to measure the coating thickness because the coating thickness is measured as a step height measurement between the coated and the uncoated area. The height difference is measured using optical profiler equipment.

Figure 8.8: Magnetron sputtering based thin film gold coated coupon shows coated and uncoated area

8.3.2.1 Coating thickness measurement

Bruker make Contour GTX 3D optical profiler, which is shown in Figure 8.9, is used for measuring thin film coating thickness.

Figure 8.9: Bruker make 3D optical profiler for coating film thickness

Figure 8.10 shows the optical profiler image of the coated coupon. Coated and uncoated areas are created in the coupon for coating thickness measurement. Adhesive tape is used to mask some area of the coupon where coating is not required. Adhesive tape is removed after the coating. Then, the height difference between the uncoated and the coated regions gives the coating thickness. Since the adhesive tape is removed after coating, coating at the boundary between the uncoated region and the coated region gets disturbed during the tape removal. The boundary region measurement should not be taken for estimation of coating thickness. Figure 8.11 shows the measured coating thickness in the coupon which comes to 4.5 μm including chromium undercoat in the range of 400 A^o - 500 A^o.

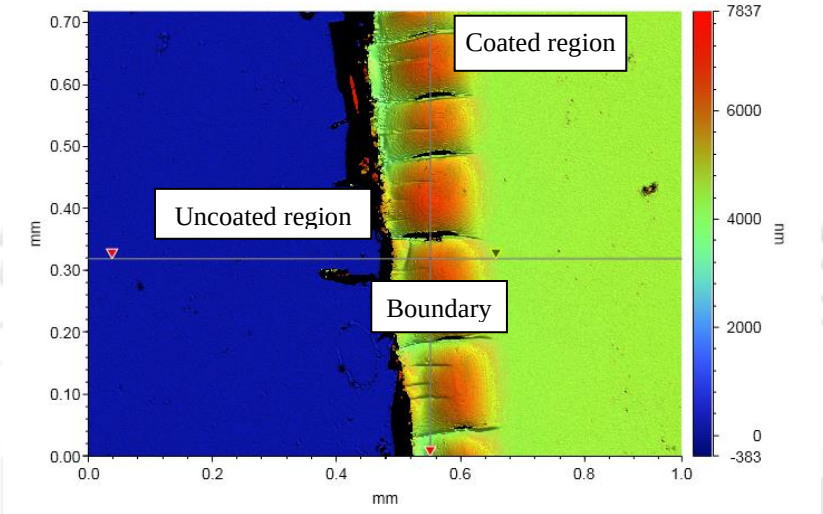

Figure 8.10: Optical profiler image of magnetron sputtering based gold coated coupon

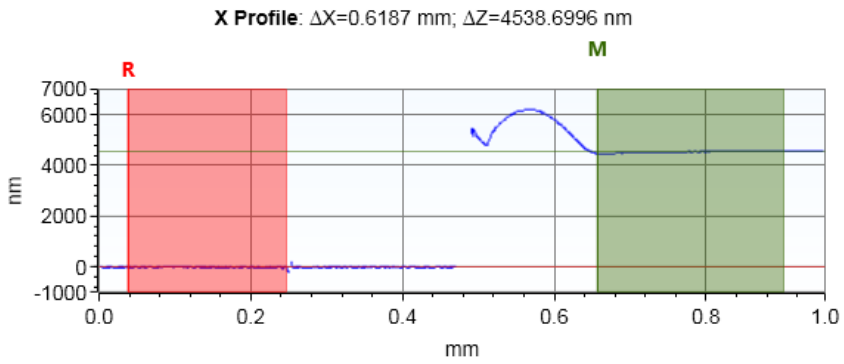

Figure 8.11 Measured magnetron sputtering based gold coating thickness

8.3.2.2 Nanoscratch testing

Nanoindentation is reliable for determining mechanical properties of the thin film coatings (Nazemian and Chamani [2019]). But there are limitations to meet the criteria of indentation depth considering the film thickness and surface roughness on shallow rough thin films. The general criteria are that the indentation depth should be 10% of the film thickness

and 20 times of roughness value. Nanoscratch testing along with nanoindentation is the highly reliable method for evaluating a variety of thin film properties. Nanoscratch test also evaluates the film friction coefficient. The sudden change of friction coefficient during the scratch test shows the poor adhesion and coating peel off. This experiment is performed in Hysitron make Ti Premier series instrument which is shown in Figure 8.12.

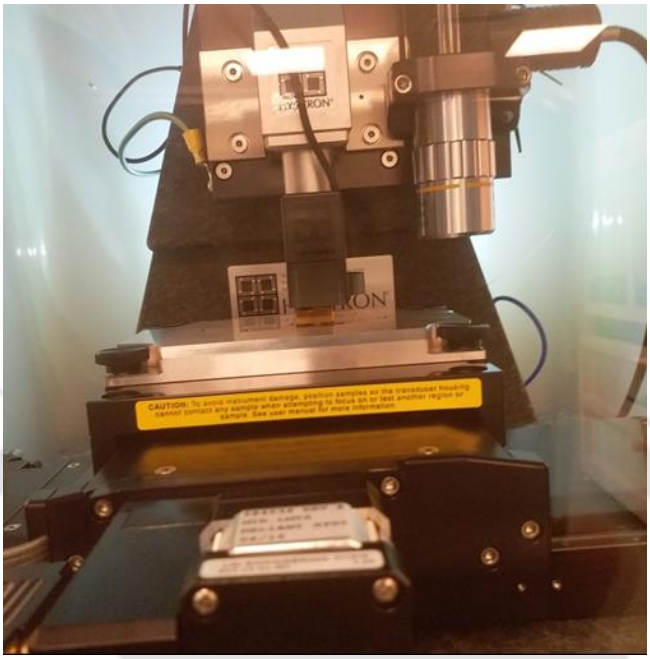

Figure 8.12: Hysitron make Ti Premier series equipment for scratch test

The stylus chosen for the scratch test is Berkovich indenter (McAdams *et al.* [1995]). Scratches can be made with an edge of the pyramid indenter and with a face of the pyramid indenter facing the direction of scratching. These are called edge forward and face forward scratch methods respectively. Scratches with face forward are more damaging to the film. Face forward friction is also higher than the other case. In order to make effective use of the displacement data, the slope and the curvature of the specimen are to be accounted and compensated during sample placing. Many parameters are involved in scratch test such as methods of scratch test, loading profiles, indenter properties, thin film surface properties and base substrate properties (Bhattacharyyaa *et al.* [2017]).

Load control is used for the scratch test of metallic film coating. The scratch tests are done for different normal loads from 1000 microN to 7000 microN in steps of 1000 microN. The input normal load profile for the case of 7000 microN is shown in Figure 8.13. The input lateral displacement profile of the thin film coated coupon is shown in Figure 8.14. The scratch test steps are as given in Table 8.3. Micro scratch hardness test using a diamond stylus is done as per ASTM G171-03 (modified for thin coatings). It is done in 9 steps with scratch length of 10 micron. Settling time is provided to minimize the creep effect.

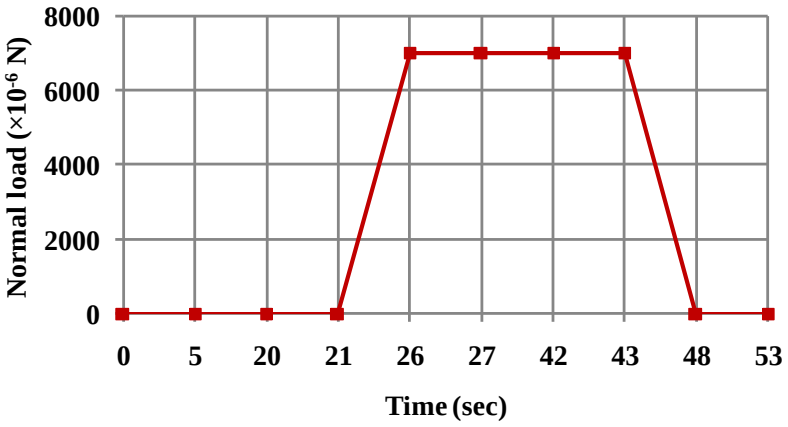

Figure 8.13: Input normal load profile for scratch test of thin film coating

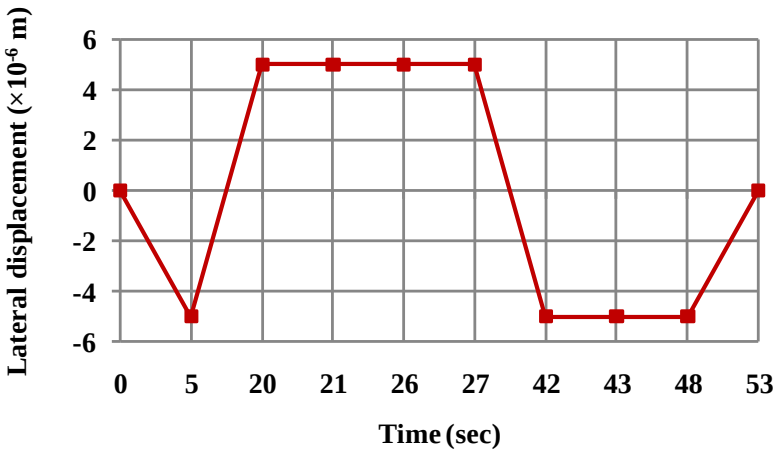

Figure 8.14: Input lateral displacement profile for scratch test of thin film coating

Actual coupon under scratch testing is shown in Figure 8.15. Figure 8.16 shows the nanoindenter mark on the gold coating after step 4 in Table 8.3. The scratch made on the coating is shown in Figure 8.17. The normal load obtained during the test is shown in Figure 8.18 and the lateral force obtained during test is shown in Figure 8.19. The indentation depth and width profile are shown in Figure 8.20. It is known that the friction coefficient is the ratio of lateral load to the normal load. Figure 8.21 shows the obtained friction coefficient plot during the entire period of scratch test. However, the realistic friction coefficient value is only during the scratch time segment from 27 to 42 sec. The friction coefficient is measured to be 0.129. There is no lateral force in other time segments and hence the friction coefficient is not realistic. The results of the scratch tests for different normal loads are tabulated in Table 8.4.

Table 8.3: Scratch test steps

Step no.	Time segment (sec)	Lateral displacement ($\times 10^{-6}$ m)	Normal load ($\times 10^{-6}$ N)	Remarks
1	0-5	5 (0 to -5)	0	Coupon moves to one extreme end from centre
2	5-20	10 (-5 to +5)	0	Coupon moves to another extreme end by 10 micron movement
3	20-21	0	0	Settling time
4	21-26	0	0-7000	Normal load increases, Normal indentation happens
5	26-27	0	7000	Settling time, Held under constant load
6	27-42	10 (+5 to -5)	7000	Scratching at constant normal load for 10 micron length
7	42-43	0	7000	Settling time, Held under constant load
8	43-48	0	7000-0	Normal load decreases, Unloading happens
9	48-53	5 (-5 to 0)	0	Coupon moves to centre from one extreme end

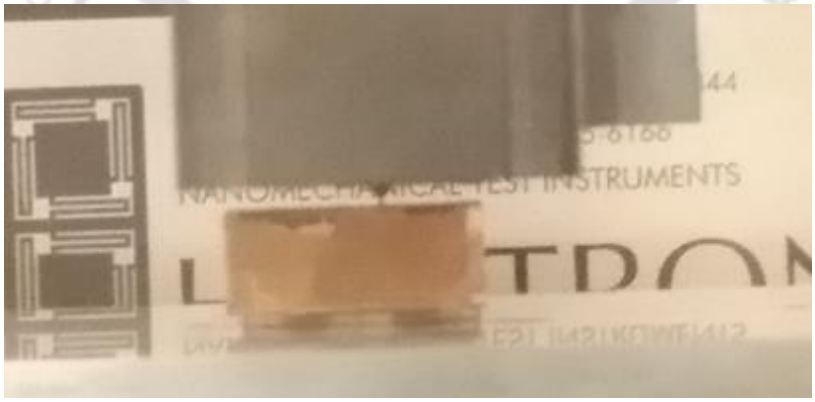

Figure 8.15: Actual coupon under scratch testing

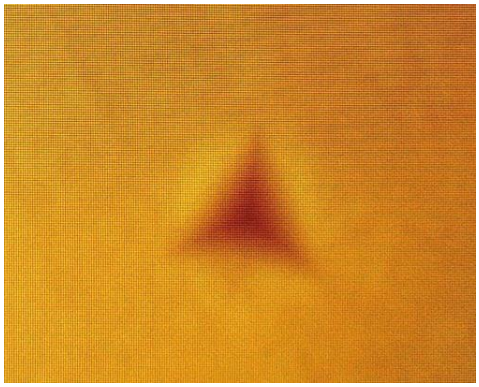

Figure 8.16: Nanoindenter mark on magnetron sputtering based gold coating

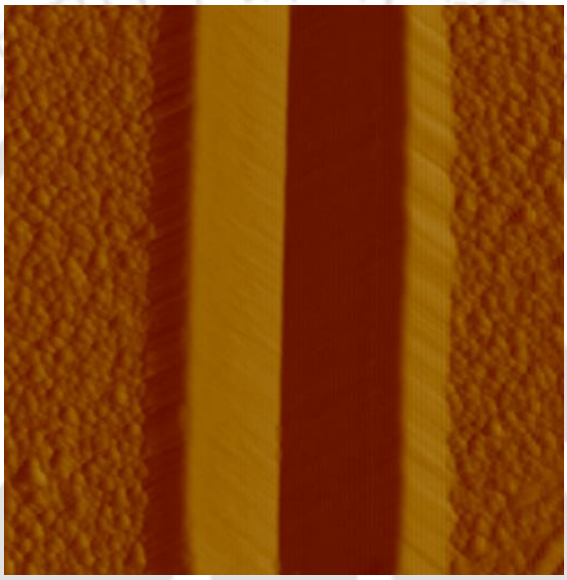

Figure 8.17: Scratch made on magnetron sputtering based gold coating

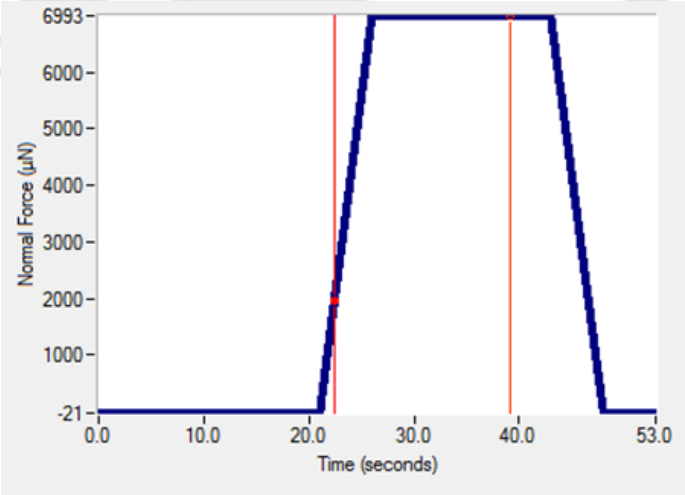

Figure 8.18: Normal force during scratch test

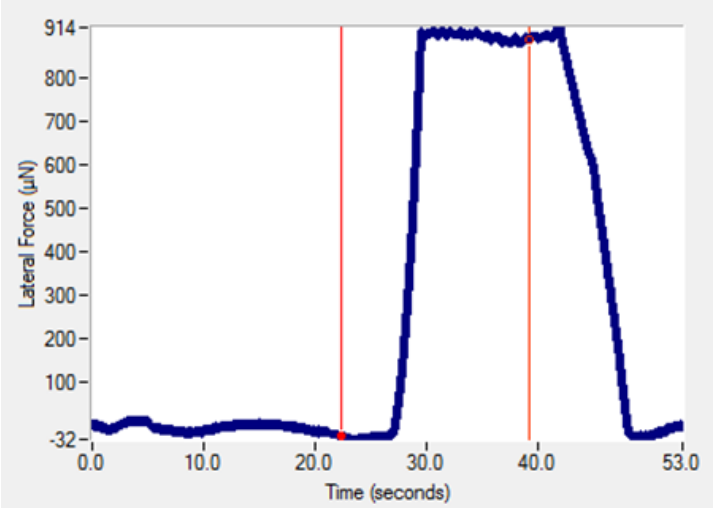

Figure 8.19: Lateral force during scratch test

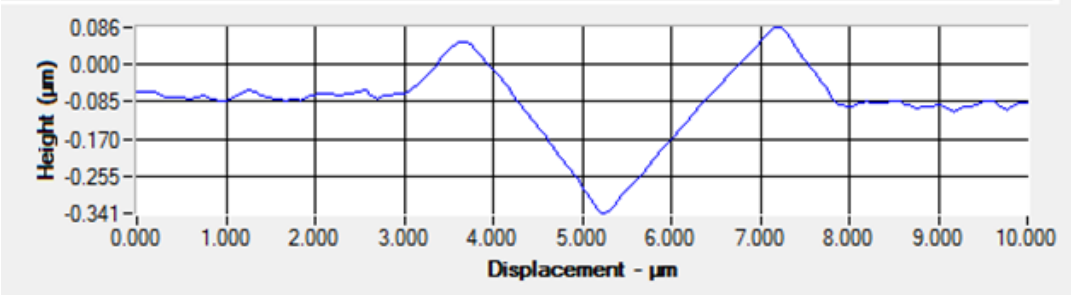

Figure 8.20: Indentation depth and width profile during scratch test

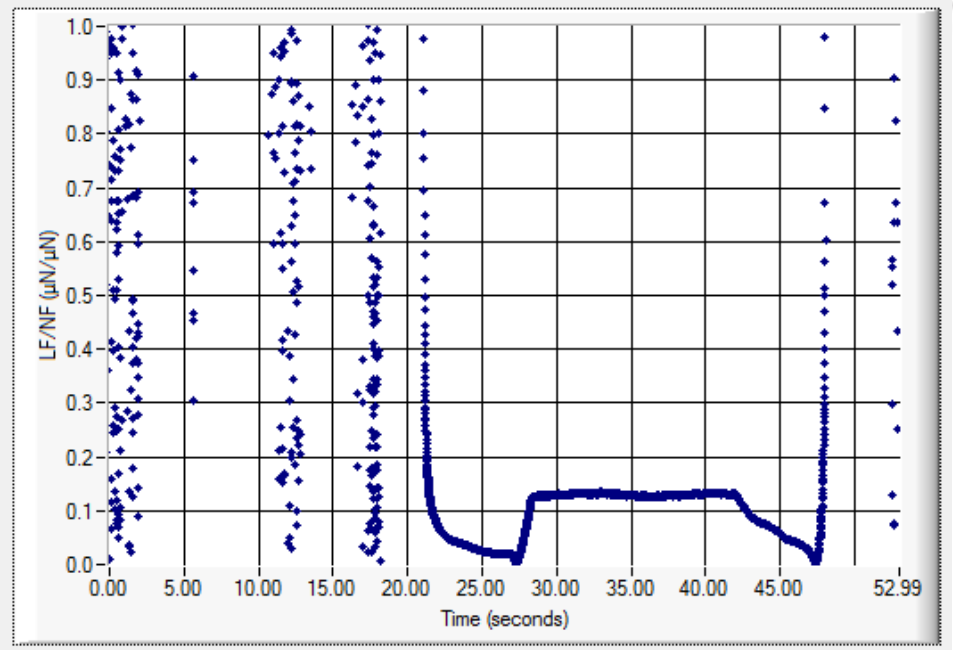

Figure 8.21: Friction coefficient during entire period of scratch test

Table 8.4: Scratch test results for different normal loads on magnetron sputter coated thin film

Sl. No.	Normal load (input) ($\times 10^{-6}$ N)	Lateral force (measured) ($\times 10^{-6}$ N)	Friction	Indentation depth ($\times 10^{-6}$ m)	Indentation width ($\times 10^{-6}$ m)
1	1000	120	0.120	0.093	1.20
2	2000	260	0.130	0.140	1.75
3	3000	375	0.125	0.225	1.95
4	4000	520	0.130	0.265	2.40
5	5000	630	0.126	0.312	2.70
6	6000	775	0.129	0.322	2.95
7	7000	900	0.129	0.370	3.40

It can be seen that there is no sudden change in friction coefficient during the scratch period. Hence, there is no coating adhesion failure even at 7000 microN normal load. Friction coefficient variation is less than 10% under different normal load tests. Scratch depth and width increases as the normal load increases. The scratch test results show that the magnetron sputtering based thin film gold coating integrity with the base silica material.

8.3.3 Characterization of ion beam coated ultra-thin film

Ion beam sputtering based ultra-thin film coating is done on the bulk surfaces of the resonator as explained earlier. Hence, coating characterization is also done for ion beam coated ultra-thin film. The ion beam ultra-thin film coated coupon is shown in Figure 8.22. Partial coating is done to measure the coating thickness because the coating thickness is measured as a step height measurement between the coated and the uncoated area. In order to address the issues related to the masking using tape and subsequent measurement errors, a metal mask with sharp edges is realized for the coating. This ensures that the boundary between the coated and the uncoated regions is sharp, and the coating thickness measurement is more accurate. Since the ion beam coating thickness is less compared to the magnetron sputtering coating thickness, the measurement errors will be critical. Three gold coated strips are realized. The height difference is measured using the optical profiler equipment.

Figure 8.22: Ion beam sputtering based ultra-thin film gold coated coupon shows coated and uncoated area

8.3.3.1 Coating thickness and roughness measurement

The roughness values of the surface of coupon are measured using Park make XE7 series atomic force microscopy (AFM) instrument before coating. The range measured is 2 A^o - 4 A^o which is much less than the planned thin film coating thickness in the range of 1000 A^o - 2000 A^o. Thus, it is ensured that the surface profile meets the thin film coating requirement. Post coating surface roughness values are in the range of 15 A^o - 22 A^o as shown in Table 8.5. The coating thickness is measured using Bruker make Contour GTX 3D optical profiler equipment and result is shown in Figure 8.23. The total coating thickness is 1545 A^o which includes chromium undercoat in the range of 400 A^o - 500 A^o. Hence, gold coating thickness is approximately 1000 A^o.

Table 8.5: Surface roughness (R_a) values on ion beam gold coated surface

Location on coupon	Roughness R_a ($\times 10^{-9}$ m)
1	1.564
2	1.594
3	2.003
4	2.007
5	1.906
6	1.943
7	2.121
8	2.225
9	2.121
10	2.229
11	2.108
12	2.097

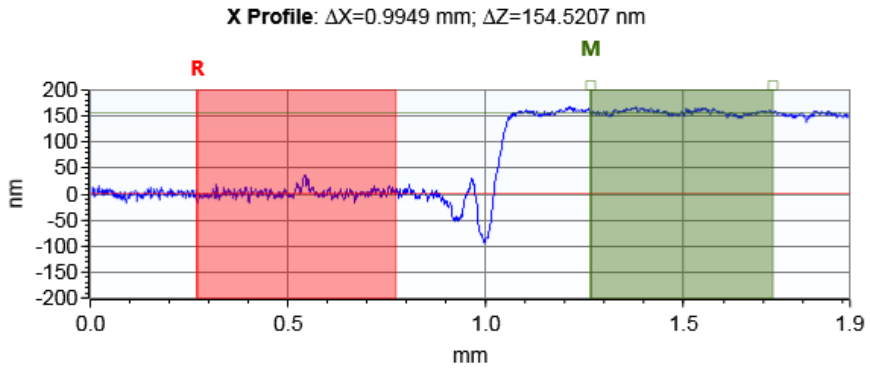

Figure 8.23: Measured ion beam sputtering based coating thickness using optical profiler

8.3.3.2 Nanoindentation and nano scratch testing

Since the ion beam coating method is used for the bulk surface ultra-thin film coating of resonator, it is functionally required to evaluate the properties of gold coating. Nanoindentation is done on the coated surface for determining the mechanical properties using Hysitron make Ti Premier series instrument with different normal loads. The loads are selected in such a way that it meets the criteria of indentation depth considering the film thickness and the surface roughness on thin films. The result is tabulated in Table 8.6.

Table 8.6: Nanoindentation test results on ion beam coated ultra-thin film for different normal loads

Normal load ($\times 10^{-6}$ N)	Indentation depth ($\times 10^{-6}$ m)	Young's modulus (GPa)	Hardness (GPa)
100	0.028	43.5	1.91
200	0.042	48.7	2.83
500	0.070	52.6	3.01

It can be seen that modulus and hardness increases and reaches closer to the bulk properties of gold as the indentation depth increases. The effect of surface roughness dominates at lower indentation depths. The effect of base material dominates at higher indentation depths which is closer to the coating thickness. Nanoscratch test is used for assessing the adhesion of thin film using friction coefficient measurement. Load control is used for the scratch test. The nanoindentation and scratch made on the coating are shown in Figures (8.24) and (8.25). Figure 8.26 shows the obtained friction coefficient plot during the scratch time segment. The results of the scratch tests of different normal loads are tabulated in Table 8.7.

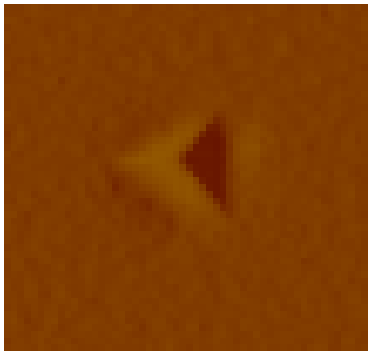

Figure 8.24: Nanoindentation made on the ion beam sputtering based ultra-thin film gold coating

Figure 8.25: Scratch made on the ion beam sputtering based ultra-thin film gold coating

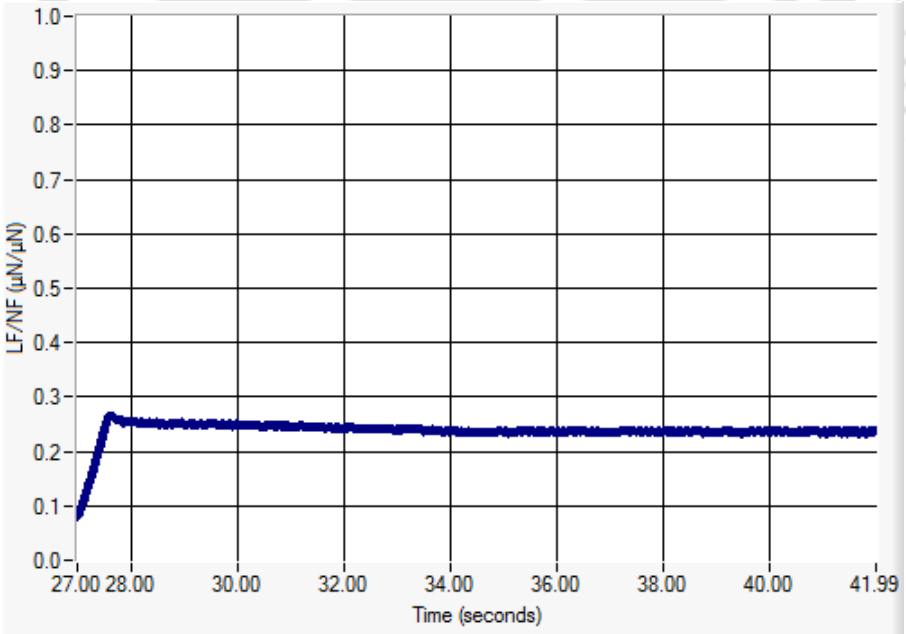

Figure 8.26: Friction coefficient during scratch time segment

Table 8.7: Scratch test results for different normal loads on ion beam coated ultra-thin film

Normal load (input) ($\times 10^{-6}$ N)	Lateral force (measured) ($\times 10^{-6}$ N)	Friction	Indentation depth ($\times 10^{-6}$ m)	Indentation width ($\times 10^{-6}$ m)
100	26	0.26	0.020	0.16
200	50	0.25	0.026	0.25
500	126	0.25	0.060	0.60
1000	263	0.26	0.090	0.85
2000	504	0.25	0.137	1.20
5000	1148	0.23	0.180	1.60

It can be seen that there is no sudden change in friction coefficient during the scratch period. Hence, there is no coating adhesion failure even at 5000 microN normal load. Friction coefficient variation is 10% only under different normal load tests. Indentation depth and scratch width increases as the normal load increases. The scratch test results show good adhesion of the ion beam based ultra-thin film gold coating on the base silica material.

8.4 Summary

Thin film gold coating is done on complex 3D surfaces of the hybrid resonator using customized coating machine. The AFM measurement ensured the surface profile requirement for thin film coating. The scratch test results showed good adhesion of the thin film gold coating on the base material. The resonator, which has a frequency split of 0.39 Hz, is balanced using the precise mass addition technique. The frequency split is reduced to 50 milliHz. The Q_{Eff} of the gold coated hybrid resonator is 2.4×10^6 which meets the specification of more than one million Q factor in the final functional form of the resonator.

Chapter 9

Conclusions and Scope for future work

9.1 Summary

Hemispherical Resonator Gyroscope (HRG) is a state-of-the-art inertial navigation sensor proposed for the future high valued long duration interplanetary satellite missions. HRG is a kind of Coriolis Vibratory Gyroscope (CVG). Mechanical resonator is a very critical functional part of the HRG. The performance of the HRG sensor is decided by the resonating structures Quality factor (*Q* factor) which is a measure of damping. High *Q* factor means low energy loss from the resonator. Ultra high *Q* factor is a mandatory requirement for very fine resolution and accurate resonant frequency reference based sensors like HRG.

In the present work, the quantitative requirement of Quality factor is arrived for the mechanical resonator of HRG. The *Q* factor requirement is estimated based on TNER (total noise equivalent rate) for the very fine resolution. Specification of resonator is arrived based on other different functional requirements and design constraints. Different damping mechanisms such as thermoelastic damping, anchor loss, surface loss, material internal friction, fluid damping and electronics damping are addressed. Study of various damping mechanisms is done using finite element simulations. Hemispherical geometry is considered for the design of the resonator. The basic size of the resonator is arrived based on achieving high Q_{TED}. Effect of different resonator dimensions on Q_{TED} is simulated. The sensor operating frequency is decided by this sensitivity study. The specific advantages of hybrid resonator configuration are brought out in terms of improved effective mass and angular gain for lower TNER and this hybrid configuration is used for further simulations. The selection of the $N = 2$ mode as the functional mode is also justified considering the performance parameter. Then, a detailed study of TED with thin film electrically conductive coating, effect of coating variations and configurations on TED is carried out. A sensitivity study of the effect of different dimensional parameters such as shell mean radius, shell thickness, stem radius, stem height on the Q_{Anchor} is carried out. Effect of geometric imperfections due to fabrication such as shell offset, shell tilt, shell thickness variation, mass unbalance is studied in detail and arrived at the fabrication tolerances.

Fused silica material is chosen for the hemispherical resonator. The fabrication procedure of fused silica brittle material and its effect on $Q_{Surface}$ is discussed. Hemispherical resonator is realized using high precision machines. Characterization facilities for frequency, *Q* factor and surface defects have been established. Then, detailed metrology measurements of realized resonators are done for assessing the precision of the fabricated resonators. Surface characterization has been carried out after machining and after chemical etching using nanoindentation technique. $N = 2$ mode resonance frequency measurement is carried out for resonators and compared with the simulation results. The effect of the measured dimensional and geometric deviations on the frequency and frequency split is analyzed.

Coarse and fine methods of balancing are arrived. These balancing procedures have been established for correcting the frequency split of realized resonators. *Q* factor estimation from internal friction and surface loss is also discussed. *Q* factor measurement is carried out using Laser Doppler Vibrometry (LDV) for uncoated resonator. Experiment is carried out to estimate the effect of fluid damping and arrived at the sensor operating pressure level for the present resonator design. *Q* factor measurement of the thin film coated resonator is also carried out. *Q* factor of few millions and other functional specifications are achieved in the final functional hybrid configuration of the resonator.

The conclusions, based on the above studies, are presented in next section.

9.2 Conclusions

The primary choice to improve MNER is to maximise the effective *Q* factor (Q_{Eff}) of the resonator followed by improving the effective mass and the angular gain. Minimum Q_{Eff} of 10^6 (one million) is required to achieve MNER of 10^{-3} deg/hr. Hence, it is proposed to design a macro scale resonator as it is very difficult to establish the required Q_{Eff} in micron scale resonators in its final functional form with all dissipative mechanisms. Based on the results presented in Chapters 2, 3, 4, 5, 6, 7 and 8, the following conclusions can be drawn.

9.2.1 Thermoelastic damping based design and simulations

- Q_{TED} of fused silica ring resonator of mm scale is 10^8 without any conductive coating. Since the mechanical frequency is larger compared to the relaxation rate i.e., $\omega_{mech}\tau_{th} >> 1$, the oscillations are adiabatic in nature. As this range of size is sufficiently away from the Debye peak of highest dissipation, the thermoelastic dissipation is very less. Thus, the design of the resonator is done to achieve ultra high *Q* factor.

- It is found that there is only 7 milliHz increase in eigen frequency with the presence of TED for fused silica material ring resonator. As the operating frequency is in the range of few kiloHz in the present macro size resonators, the frequency dependent Young's modulus change is very small and it is very close to the isothermal relaxed Young's modulus.

- The functional $N = 2$ elliptical mode eigen frequency of HRG resonator, which operates nearly in the adiabatic region, could be kept well above 2000 Hz. Hence, launch induced resonance vibration loading on the resonator is eliminated. The energy loss due to the mode interactions is minimized by keeping the functional mode frequency sufficiently away from the other nearby modes.

- As the τ_{th} becomes smaller, the resonator works away from the adiabatic region and results in more dissipation. Also the radial thickness direction temperature gradient contributes more to the thermoelastic dissipation. The polar and the circumferential thermal time constant have less influence on the Q_{TED} of this resonator size.

- A decrease in k causes a longer thermal transport time and increases the Q_{TED}. E and α do not have the same effect. An increase in E causes more thermo-mechanical coupling and reduces the Q_{TED}. Also, an increase in E increases the frequency and shifts the operating region towards adiabatic conditions and hence improves the Q_{TED}. But, a more predominant effect is to reduce the Q_{TED} with increase of E. When T increases, the coupling between the structural and the thermal domains increases and reduces Q_{TED}.

- When the shell mean radius reduces, the frequency increases and the behaviour becomes more adiabatic which results in higher Q_{TED}. The influence of the shell thickness increase on Q_{TED} increase is more compared to that of the shell mean radius.

- Q_{TED} decreases significantly (order of three) even with thin film coating of 1000 A^o (coating thickness is 0.01% of 1 mm shell thickness). As the coating thickness increases, the thermoelastic damping increases due to higher entropy generation. However, the initial reduction in Q_{TED} is more. This is due to high strain rate at the boundary between the bulk material and the coating.

- The natural frequency comes down only by 3 Hz with 1000 A^o thin film coating due to the mass effect of the gold film compared to the stiffness effect. Hence, the change of natural frequency is not significant as compared to the quality factor reduction with coating. It is found that the eigen frequency increases by 40 milliHz in 1000 A^o coated resonator from the isothermal Young's modulus based eigen value. It is inferred that the change (increase) of frequency dependent Young's modulus increases as the dissipation increases.

- The most significant coating material properties are E and α with respect to Q_{TED}. The effect of coating thickness variations depends on the overlap between the circumferential direction thickness variation and the $N = 2$ elliptical mode shape. Q_{TED} increases as the coating area reduces with reduced latitude angle of coating. Q_{TED} reduction is more for the outside coating case compared to the inside coating case.

- The effective mass and the angular gain of hybrid resonator configuration is 15% more than that of a hemispherical alone configuration. $N = 2$ mode is considered for functional mode as it gives 75% more angular gain compared to $N = 3$ mode.

9.2.2 Anchor loss simulations and fabrication requirements

- Q_{Anchor} is high for an ideal highly symmetrical hemispherical resonator with inside stem of sufficient length. Q_{Anchor} is found to decrease with increase in the shell radial thickness and decrease in the shell radius. When the $N = 2$ mode frequency is closer to the stem tilt mode frequency, anchor loss increases by few orders of magnitude. The ratio of E value of the resonator to that of the supporting substrate has an effect on the Q_{Anchor}.

- Q_{Anchor} is not significant for a designed perfect resonator structure and approach Q_{TED} even with minor geometric imperfections in the hardware realisation. The shell-stem offset value of less than 50 microns, the tilt value of less than 0.25 deg and radial thickness variation of less than 20 microns should be achieved during the fabrication.
- As the unbalanced mass increases, frequency split increases with the sensitivity of 0.29×10^{-6} kg/Hz. The effect of unbalanced mass profile on frequency, overall reduction and variation of the Q_{Anchor} depends on the overlap of $N = 2$ mode shape over the unbalance pattern in circumferential direction.

9.2.3 Realization of precision resonator

- The birefringence measurement shows that higher diameter blank material has $(1/5)^{th}$ internal stress compared to lower blank diameter. Hence, the higher diameter blank material is preferred for the resonator fabrication.
- The precision levels achieved during fabrication are different for different resonators. The frequency increases as the radial thickness increases and the frequency split increases as the geometric error increases.
- Shell offset is achieved well within 50 microns and shell tilt is achieved well within 0.25 deg in one high precision resonator. Frequency split is also achieved within 0.5 Hz. Thus, a highly symmetrical precision resonator is realized as per the dimensional and geometric tolerance requirement from the anchor loss sensitivity analysis.

9.2.4 Characterization of precision resonator

- It is found from the numerical simulation that four-point mass correction of equal amount at 90 deg apart in circumferential direction results in lower frequency split. Low precision resonator (resonator 1) is balanced by mass removal method from frequency split of 5.95 Hz to less than 0.5 Hz.
- It is seen from the nanoindentation test that the hardness and reduced Young's modulus is very much less compared to the bulk material nominal hardness of 11 GPa and Young's modulus of 73 GPa because of the formation of damaged surface layer after USM. These values improved after each stage of the chemical etching process due to the removal of major part of the damaged surface layer.
- Very low Q_{Eff} is obtained after ultrasonic machining. Q_{Eff} improvement by plasma etching is one order less that that by chemical wet etching. The Q_{Eff} is improved by order of three to the range of millions after chemical etching. Some resonators needed more etching trials because wet chemical etching method is not a precisely controlled process.
- 15% variation of Q_{Eff} is found in the circumferential direction. No significant Q_{Eff} improvement is found for pressure less than 1 N/m^2 (10^{-2} millibar). The sensor

operation is proposed to be done much lower than 1 N/m^2 to eliminate contribution of Q_{Fluid} in Q_{Eff}.

- Q_{Eff} of uncoated high precision fused silica material resonator of millimetre size is limited by the fabrication induced surface loss. Q_{Eff} of gold coated fused silica material resonator is limited by the thermoelastic damping from the coating material, the coating material internal friction and the fabrication induced surface loss as these losses are in the same order (10^6).
- The resonator, which has frequency split of 0.39 Hz and Q_{Eff} of 4.5×10^6 before coating, is balanced using the precise mass addition technique and one order reduction is achieved in the frequency split. The achieved frequency split is 50 milliHz which meets the fine balancing specification.
- The AFM measurement ensures the surface profile requirement for thin film coating. The scratch test results show the thin film gold coating integrity with the base silica material. Scratch depth and width increases as the normal load increases. Friction coefficient variation is less than 10% under different normal load tests.

The achieved Q_{Eff} after coating is 2.4×10^6 which meets the specification of more than one million Q factor. The frequency split and the other functional parameters meet the specification requirement for the final functional hybrid resonator. Thus, the demonstration of high Q factor in the final functional high precision macro scale resonator configuration is done.

In view of the above, the objectives of the present thesis work such as study of different vibration energy loss mechanisms, design and demonstration of ultra high quality factor precision macro scale gyroscope resonator for high end inertial applications in space sector are met.

9.3 Scope of the future work

Further work can be carried out in the following aspects:

- In the present work, sensitivity analysis of dimensions of resonator is carried out. Measurement of actual 3D surface profile of resonator hemispherical region and cylindrical region can be done using profile and form metrology instrument. Further, the FE model can be modified with actual measured surface profile and detailed anchor loss simulations can be done. Then, the actual unbalance profile and the locations on the hardware can be found from this model. This will result in further improvement of balancing with minimum number of trials.
- The bulk material hardness of 11 GPa and Young's modulus of 73 GPa is not reached over the entire surface even after chemical etching in the resonators realized at present. The spherical region shows relatively lower mechanical properties compared to the cylindrical region. There is still presence of surface damage in the spherical

region. Also, there is a wide variation in the *Q* factors of different resonators after USM. This show that the machining parameters need to be optimized further to minimize the surface damage and fabrication process should be consistent.

- In the present work, the chemical etching requirement after machining is more and this can result in reduction in the nominal dimensions. The reduction in dimensions causes frequency change from the design value which can cause mode interactions and increases the anchor loss. Hence, the etching requirement should be minimized by optimized fabrication process. As the chemical etching process is not precise, non-uniform etching can result in more geometric errors. Hence, plasma etching process should be explored further for this type of precise application.
- There is a variation of the Q_{Eff} in circumferential direction in the realized resonators. The most probable causes are the variation in the surface loss due to varying surface damage around circumferential direction, actual mass unbalance pattern, and thin film coating variations. More elaborate and sophisticated measurements and characterizations should be done to understand the exact root cause and address this variation as this is also a functional parameter.
- Variations in the thin film coating over the 3D surface should be characterized further and its impact on resonator electro-mechanical performance should be assessed. The adhesion characteristics in dynamic vibrating condition should be demonstrated for the functional application.
- Q_{Eff} of fused silica HRG resonator can be increased to 10^7 which is the limit with respect to the silica material internal friction. Hence, the surface loss, the additional thermoelastic damping due to the coating, and the internal dissipation from coating material should be further reduced. This can be addressed by further optimization of the fabrication parameters, the etching and the chemical cleaning process, and the thin film coating parameters.

References

A. Bose, K. N. Bhat, and T. Kurian. *Fundamentals of Navigation and Inertial Sensors.* PHI Learning Pvt. Ltd., 2002.

V. Apostolyuk. *Coriolis Vibratory Gyroscopes: Theory and Design.* Springer International Publishing, 2016.

V. M. N. Passaro, A. Cuccovillo, L. Vaiani, M. D. Carlo, and C. E. Campanella. Gyroscope technology and applications: A review in the industrial perspective. *MDPI Sensors 2017*, 17(10), 2017.

R. R. Ragan. Inertial technology for the future. *IEEE Transactions on Aerospace and Electronic Systems, 20(4);414-444, 1984.*

A. Jeanroy, A. Bouvet, and G. Remillieux. HRG and marine applications. *Gyroscopy and Navigation*, 5(2);67-74, 2014.

A. M. Shkel. Type I and Type II micromachined vibratory gyroscopes. *Proceedings of IEEE/ION, PLANS*, 586-593, Sandiego, U.S.A., 2006.

R. L. Greenspan. Inertial navigation technology from 1970-1995. *Navigation: Journal of The Institute of Navigation*, 42(1);165-185, 1995.

L. Rosellini, O. Girard, and J. Caron. REGYS20 a HRG IMU for space applications. *Symposium gyro technology*, Karlsruhe, Germany, 2007.

W. Xu, W. Wenqi, L. Bing, and L. Yun. The modelling of hemispherical gyro and its space applications. *Proceedings of 7th International Symposium on Precision Engineering Measurements and Instrumentation,* 8321(1);4-9, 2011.

G. H. Bryan. On the beats in the vibrations of a revolving cylinder or bell. *Proceedings of the Cambridge Philosophical Society*, 7(1);101-111, 1890.

D. Lynch. Hemispherical resonator gyro. *IEEE Transactions on Aerospace and Electronics Systems*, 20(4), 1984.

Y. Pan, D. Y. Wang, Y. Y. Wang, J. P. Liu, S. Y. Wu, T. L. Qu, K. Y. Yang, and H. Luo. Monolithic cylindrical fused silica resonators with high Q factors. *MDPI Sensors*, 16(8);1185_1-14, 2016.

C. H. J. Fox. Vibrating cylinder rate gyro: Theory of operation and error analysis. *Proceedings of Symposium on Gyro Technology*, 5;1-23, Stuttgart, Germany, 1988.

J. Y. Cho and K. Najafi. A high Q all fused silica solid stem wineglass hemispherical resonator formed using micro blow torching and welding. *28thIEEE International Conference on MEMS*, 821-824, Estoril, Portugal, 2015.

S. Fan, G. Liu, and Z. Wang. Theory and experiment on operating principle of hemispherical resonator gyro. *Proceedings of 18th ICAS Congress*, 1;632-636, Beijing, 1992.

H. A. C. Tilmans. M. Elwebspoek, and J. H. J. Fluitman. Micro resonant force gauges. *Sensors and Actuators A: Physical*, 30(1-2);35-53, 1992.

T. B. Gabrielson. Mechanical thermal noise in micromachined acoustic and vibration sensors. *IEEE Transactions on Electron Devices*, 40(5);903-909, 1993.

X. Zhou, D. Xiao, Z. Hou, Q. Li, Y. Wu, and X. Wu. Influences of the structure parameters on sensitivity and Brownian noise of the disk resonator gyroscope. *Journal of Microelectromechanical Systems*, 26(3);519-527, 2017.

F. Ayazi and K. Najafi. A HARPSS polysilicon vibrating ring gyroscope. *Journal of Microelectromechanical Systems*, 10(2);169-179, 2001.

V. Choudhary and K. Iniewski. *MEMS: Fundamental technology and applications*. CRC Press, 2013.

Z. H. Wang, J. Lee, and P. X. L. Feng. Spatial mapping of multimode brownian motions in high-frequency silicon carbide micro disk resonators. *Nature Communications*, 5(1);5158-5168, 2014.

E. A. Izmailov, M. M. Kolesnik, A. M. Osipov, and A. V. Akimov. Hemispherical resonator gyro technology: Problems and possible ways of their solutions. *International Conference on Integrated Navigation Systems*, 24-26, St. Petersburg, Russia, 1999.

D. M. Rozelle. The hemispherical resonator gyroscope: From wine glass to the planets, *Proceedings of 19th AAS/AIAA Space Flight Mechanics Meeting*, Georgia, U.S.A., 2009.

S. Joshi, S. Hung, and S. Vengallatore. Design strategies for controlling damping in micromechanical and nanomechanical resonators. *EPJ Techniques and Instrumentation*, 1(5);1-14, 2014.

M. Imboden and P. Mohanty. Dissipation in nanoelectromechanical systems. *Physics Reports*, 534(3);89-146, 2014.

W. Thomson, On the dynamical theory of heat. *Earth and Environmental Science: Transactions of the Royal Society of Edinburgh*, 20(2);261-288, 1853.

J. E. Bishop and V. K. Kinra. Elastothermodynamic damping in laminated composites. *International Journal of Solids and Structures*, 34(9);1075-1092, 1997.

C. Zener. Internal friction in solids. I. Theory of internal friction in reeds. *Physical Review*, 52(3);230-235, 1937.

C. Zener, A. P. Wills, D. P. Mitchell, and H. W. Farwell. Internal friction in solids: II. General theory of thermoelastic internal friction. *Physical Review*, 53(1); 90-99, 1938.

B. S. Berry. Precise investigation of the theory of damping by transverse thermal currents. *Journal of Applied Physics*, 26(10);1221-1224, 1955.

T. V. Roszhart. The effect of thermoelastic internal friction on the Q of micromachined silicon resonators. *IEEE 4th Technical Digest on Solid-State Sensor and Actuator Conference*, 13-16, S.C., U.S.A., 1990.

K. Y. Yasumura, T. D. Stowe, E. M. Chow, T. Pfafman, T. W. Kenny, B. C. Stipe, and D. Rugar. Quality factor in micron and submicron thick cantilevers. *Journal of Microelectromechanical Systems*, 9(1);117-125, 2000.

R. Lifshitz and M. L. Roukes. Thermoelastic damping in micro and nano mechanical systems. *Physical Review B*, 61(8);5600-5609, 2000.

S. K. De and N. R. Aluru. Theory of thermoelastic damping in electrostatically actuated microstructures. *Physical review B*, 74(14);144305_1-13, 2006.

Y. Sun, D. Fang, and A. K. Soh. Thermoelastic Damping in micro-beam resonators. International Journal of Solids and Structures. 43(10);3213-3229, 2006.

F. L. Guo and G. A. Rogerson. Thermoelastic coupling effect on a micro-machined beam machined beam resonator. *Mechanics Research Communications*, 30(6);513-518, 2003.

B. H. Houston, D. M. Photiadis, J. F. Vignola, M. H. Marcus, Xiao, Liu, D. Czaplewski, L. Sekaric, J. Butler, P. Pehrsson, and J. A. Bucaro. Loss due to transverse thermoelastic currents in microscale resonators. *Material Science and Engineering A*, 370(1);407-411, 2004.

R. N. Candler, H. Li, M. Lutz, W. Park, A. Partridge, G. Yama, and T. W. Kenny. Investigation of energy loss mechanisms in micromechanical resonators. *Proceedings of 12th International Conference on Solid state Sensors, Actuators and Microsystems*, 2A3.3;332-335, MA, USA, 2003.

Y. Yi and M. A. Matin. Eigenvalue solution of thermoelastic damping in beam resonators using a finite element analysis. *Journal of Vibration and Acoustics - Transactions of the ASME*, 129(4);478-483, 2007.

J. Rajagopalan and M. T. A. Saif. Single degree of freedom model for thermoelastic damping. *Journal of Applied Mechanics - Transactions of the ASME*, 74(3);461-468, 2007.

S. Prabhakar and S. Vengallatore. Theory of thermoelastic damping in micromechanical resonators with two-dimensional heat conduction. *Journal of Microelectromechanical Systems*, 17(2);494-502, 2008.

S. Prabhakar, M. P. Paidoussis, and S. Vengallatore. Analysis of frequency shifts due to thermoelastic coupling in flexural-mode micromechanical and nanomechanical resonators. *Journal of Sound and Vibration*, 323(1):385-396, 2009.

V. K. Kinra and K. B. Milligan. A second-law analysis of thermoelastic damping. *Journal of Appled Mechanics-Transactions of the ASME*, 61(1);71–76, 1994.

S. A. Chandorkar, R. N. Candler, A. Duwel, R. Melamud, M. Agarwal, K. E. Goodson, and T. W. Kenny. Multimode thermoelastic dissipation. *Journal of Applied Physics*, 105(4);043505_1-13, 2009.

S. Ghaffari and T. W. Kenny. Thermoelastic dissipation in composite silicon MEMS resonators with thin film silicon dioxide coating. *Symposium A: Amorphous and Polycrystalline Thin film Silicon Science and Technology*, 1426;193-198, 2012.

A. Duwel, R. N. Candler, T. W. Kenny, and M. Varghese. Engineering MEMS resonators with low thermoelastic damping. *Journal of Microelectromechanical Systems*, 15(6);1437-1445, 2006.

COMSOL Multiphysics ver 5.2, COMSOL Inc., Massachusetts, U.S.A.

R. N. Candler, A. Duwel, M. Varghese, S. A. Chandorkar, M. A. Hopcroft, W. T. Park, B. Kim, G. Yama, A. Partridge, M. Lutz, and T. W. Kenny. Impact of geometry on thermoelastic dissipation in micromechanical resonant beams. *Journal of Microelectromechanical Systems*, 15(4);927-934, 2006.

A. Darvishian, T. Nagourney, J. Y. Cho, B. Shiari, and K. Najafi. Thermoelastic dissipation in micromachined birdbath shell resonators. *Journal of Microelectromechanical Systems*, 26(4);758-772, 2017.

A. H. Nayfeh and M. I. Younis. Modelling and simulations of thermoelastic damping in microplates. *Journal of Micromechanics and Microengineering*, 14(12);1711-1717, 2004.

S. J. Wong, C. H. J. Fox, S. McWilliam, C. P. Fell, and R. Eley. A preliminary investigation of thermo-elastic damping in silicon rings. *Journal of Micromechanics and Microengineering*, 14(9);S108-S113, 2004.

S. J. Wong, C. H. J. Fox, and S. McWilliam. Thermo elastic damping of the in-plane vibration of thin silicon rings. *Journal of Sound and Vibration*, 293(1-2);266-285, 2006.

S. Prabhakar and S. Vengallatore. Thermoelastic damping in bilayered micromechanical beam resonators. *Journal of Micromechanics and Microengineering*, 17(3);532-538, 2007.

R. Sandberg, K. Molhave, A. Boisen, and W. Svendsen. Effect of gold coating on the Q factor of a resonant cantilever. *Journal of Micromechanics and Microengineering*, 15(12); 2249-2253, 2005.

Y. Sun, J. Yang, and Y. Jiang. A theoretical analysis of thermoelastic damping model in laminated trilayered circular plate resonators. *World Journal of Mechanics*, 4;102-111, 2014.

A. Duwel, J. Gorman, M. Weinstein, J. Borenstein, and P. Ward. Experimental study of thermoelastic damping in MEMS gyros. *Sensors and Actuators A: Physical*, 103(1-2);70-75, 2003.

C. Hwang. Some experiment on the vibration of a hemispherical shell. *Journal of Applied Mechanics*, 33(4);817-824, 1966.

S. Fan, G. Liu, and Z. Wang. On vibration of hemispherical shell using finite element method. *Applied Mathematics and Mechanics*, 12(12);1169-1175, 1991.

S. Y. Choi, Y. H. Na, and J. H. Kim. Thermoelastic damping of inextensional hemispherical shell. *Proceedings of World Academy of Science, Engineering and Technology*, 56;198-203, 2009.

M. L. Chan, J. Xie, P. Fonda, H. Najar, K. Yamazaki, L. Lin, and D. A. Horsley. Micromachined polycrystalline diamond hemispherical shell resonators. *International Conference Proceedings of Solid state sensors, Actuators and Microsystems*, Beijing, China, 2011.

A. Darvishian, B. Shiari, J. Y. Cho, T. Nagourney, and K. Najafi. Investigation of thermoelastic loss mechanism in shell resonators. *Proceedings of ASME International Mechanical Engineering Congress and Exposition*, 39331-39336, Montreal, Canada, 2014.

L. Sorenson, P. Shao, and F. Ayazi. Bulk and surface thermoelastic dissipation in micro hemispherical shell resonators. *Journal of Microelectromechanical Systems*, 24(2);486-502, 2015.

Y. Jimbo and K. Itao. Energy loss of a cantilever vibrator. *Journal of Horological Institute of Japan*, 47;1-15, 1968.

Z. Hao, A. Erbil, and F. Ayazi. An analytical model for support loss in micromachined beam resonators with in plane flexural vibrations. *Sensors and Actuators A: Physical*, 109(1);156-164, 2003.

J. Yang, T. Ono, and M. Esashi. Mechanical behavior of ultrathin microcantilever. *Sensors and Actuators A: Physical*, 82(1);102-107, 2000.

M. C. Cross and R. Lifshitz. Elastic wave transmission at an abrupt junction in a thin plate with application to heat transport and vibration in mesoscopic systems. *Physical Review B*, 64(8);085324_1-22, 2001.

D. M. Photiadis and J. A. Judge. Attachment losses of high Q oscillators. *Applied Physics Letters*, 85(3);482-484, 2004.

Z. Hao and F. Ayazi. Support loss in micromechanical disk resonators, *18th IEEE International Conference on Micro Electro Mechanical Systems (MEMS 2005)*, 137-141, Miami, USA, 2005.

Z. Hao and F. Ayazi. Support loss in the radial bulk-mode vibrations of center-supported micromechanical disk resonators. *Sensors and Actuators A: Physical*, 134(2);582-593, 2007.

D. Rabinovich, D. Givoli, and E. Becache. Comparison of high order absorbing boundary conditions and perfectly matched layers in the frequency domain. *International Journal for Numerical Methods in Biomedical Engineering*, 26(10);1351-1369, 2010.

D. S. Bindel, E. Quevy, T. Koyama, S. Govindjee, J. W. Demmel, and R. T. Howe. Anchor Loss simulation in Resonators. *18thIEEE International Conference on Microelectromechanical Systems*, 133-136, Miami, USA, 2005.

U. Basu and A. K. Chopra. Perfectly matched layers for time-harmonic elastodynamics of unbounded domains: theory and finite-element implementation. *Computer Methods in Applied Mechanics and Engineering*, 192(11-12);1337-1375, 2003.

A. Frangi, A. Bugada, M. Martello, P. T. Savadkoohi. Validation of PML based models for the evaluation of anchor dissipation in MEMS resonators. *European Journal of Mechanics A / Solids*, 37;256-265, 2013.

V. Thakar and M. Rais-Zadeh. Optimization of tether geometry to achieve low anchor loss in Lame mode resonators. *Joint Europian Frequency and Time forum and International Frequency Control Symposium*, Prague, Czech Republic, 129-132, 2013.

J. E.Y. Lee, J. Yan, and A. A. Seshia. Quality factor enhancement of bulk acoustic resonators through anchor geometry design. *22nd International Conference proceedings of Solid state Sensors, Actuators and Microsystems*, 536-539, Dresden, Germany, 2008.

J. E. Y. Lee, J. Yan, and A. A. Seshia. Study of lateral mode SOI-MEMS resonators for reduced anchor loss. *Journal of Micromechanics and Microengineering*, 21(4);045010_1-10, 2011.

K. Wang, A. C. Wong, and C. T. C. Nguyen. VHF free-free beam high Q micromechanical resonators. *Journal of Microelectromechanical Systems*, 9(3):347-360, 2000.

A. Darvishian, B. Shiari, H. Guohong, and K. Najafi. Effect of substrate thickness on quality factor of mechanical resonators. *Proceedings of IEEE International Symposium on Inertial Sensors and Systems*, 1-4, Hapuna, U.S.A., 2015.

P. G. Steeneken, J. J. M. Ruigrok, S. Kang, J. T. M. van Beek, J. Bontemps, and J. J. Koning. Parameter extraction and support loss in MEMS resonators. *Proceedings of COMSOL Conference*, 725-730, Grenoble, France, 2007.

S. A. Zotov, B. R. Simon, I. P. Prakhobko, A. A. Trusov, and A. M. Shkel. Quality factor maximization through dynamic balancing of tuning fork resonators. *IEEE Sensors Journal*, 14(8);2706-2714, 2014.

D. S. Bindel and S. Govindjee. Elastic PMLs for resonator anchor loss simulation. *International Journal for Numerical Methods in Engineering*, 64(6);789-818, 2005.

A. Heidari, M. L. Chan, H. A. Yang, G. Jaramillo, P. T. Tehrani, P. Fonda, H. Najar, K. Yamazaki, L. Lin, and D. A. Horsley. Micromachined polycrystalline diamond hemispherical shell resonators. *17th International Conference proceedings of Solid state Sensors, Actuators and Microsystems*, W4A005;2415-2418, Barcelona, Spain, 2013.

R. S. Hwang, C. H. J. Fox, and S. McWilliam. Free vibrations of elliptical rings with circumferentially variable thickness. *Journal of Sound and Vibration*, 228(3);683-699, 1999.

S. Y. Choi and J. H. Kim. Natural frequency split estimation for inextensional vibration of imperfect hemispherical shell. *Journal of Sound and Vibration*, 330(9);2094-2106, 2011.

L. Sorenson and F. Ayazi. Effect of structural anisotropy on anchor loss mismatch and predicted case drift in future micro-hemispherical resonator gyros. *IEEE/ION Position, Location and Navigation Symposium*, 493-498, Monterey, U.S.A., 2014.

A. Darvishian, B. Shiari, J. Y. Cho, T. Nagourney, and K. Najafi. Anchor loss in hemispherical shell resonators. *Journal of Microelectromechanical Systems*, 26(1);51-66, 2017.

Y. Pan, T. Qu, D. Wang, S. Wu, J. Liu, Z. Tan, K. Yang, and H. Luo. Observation and analysis of the quality factor variation behaviour in a monolithic fused silica cylindrical resonator. *Sensors and Actuators A: Physical*, 260;81-89, 2017.

A. M. Gretarsson and G. M. Harry. Dissipation of mechanical energy in fused silica fibers. *Review of Scientific Instruments*, 70(10);4081-4087, 1999.

A. Picard, P. Barat, M. Borys, M. Firlus, and S. Mizushima. State of the art mass determination of ^{28}Si spheres for the Avogadro project. *Metrologia*, 48(2);S112-S119, 2011.

R. H. Doremus. Diffusion of water in silica glass. *Journal of Materials Research*, 10(9);2379-2389, 1995.

B. S. Lunin, S. N. Torbin, M. N. Danachevskaya, and I. V. Batov. On the mechanism of acoustic losses in the hydroxylated surface layer of silica glass. Moscow University Chemistry Bulletin, 56;19-22, 2001.

B. Kim, M. A. Hopcroft, R. N. Candler, C. M. Jha, M. Agarwal, R. Melamud, S. A. Chandorkar, G. Yama, and T. W. Kenny. Temperature dependence of quality factor in MEMS resonators. *Journal of Microelectromechanical Systems*, 17(3);755-766, 2008.

R. E. Mihailovich and N. C. MacDonald. Dissipation measurements in vacuum operated single crystal silicon micro resonators. *Sensors and Actuators A: Physical*, 50(3);199-207, 1995.

P. L. Guzzo, A. H. Shinohara, and A. A. Raslan. A comparative study on ultrasonic machining of hard and brittle materials. *Journal of Brazilian Society of Mechanical Science and Engineering*, 26(1);56-61, 2004.

G. Palasantzas. Surface roughness influence on the quality factor of high frequency nano resonators. *Journal of Applied Physics*, 103(4);046106_1-3, 2008.

D. A. Lucca, E. Brinksmeier, and G. Goch. Progress in assessing surface and subsurface integrity, *CIRP Annals: Manufacturing Technology*, 47(2);669-693, 1998.

P. E. Miller, T. I. Suratwala, L. L. Wong, M. D. Feit, J. A. Menapace, P. J. Davis, and R. A. Steele. The distribution of subsurface damage in fused silica. *Proceedings of SPIE*, 5991(1); 599101_1-25, 2005.

D. Ravindra and J. Patten. Ductile regime single point diamond turning of quartz resulting in an improved and damage free surface. *Machining Science and Technology*, 15(4);357-375, 2011.

E. Brinksmeier, Y. Mutlugunes, F. Klocke, J. C. Aurich, P. Shore, and H. Ohmori. Ultra precision grinding. *CIRP Annals: Manufacturing Technology*, 59(2);652-671, 2010.

V. A. Matveev, B. S. Lunin, and M. A. Basarb. Solid state gyroscope navigation system, *Harbin Institute of Technology Press: Harbin*, China, 89-96, 2013.

L. Wong, T. Suratwala, M. D. Feit, P. E. Miller, and R. Steele. The effect of HF/NH4F etching on the morphology of surface fractures on fused silica. *Journal of Non-Crystalline Solids*, 355(13);797-810, 2009.

Y. Gogots, C. Back, and F. Kirscht, Raman microspectroscopy study of processing induced phase transformations and residual stress in silicon. *Semiconductor Science and Technology*, 14(10);936-944, 1999.

A. Esmaeilzare, A. Rahimi, and S. M. Rezaei. Investigation of subsurface damages and surface roughness in grinding process of Zerodur glass ceramic. *Applied Surface Science*, 313;67-75, 2014.

S. T. Chen and Z. H. Jiang. A force controlled grinding-milling technique for quartz glass micromachining. *Journal of Materials Processing Technology*, 216;206-215, 2015.

B. Shiari and K. Najafi. Surface effect influence on the quality factor of microresonators. *17th International Conference on Solid state Sensors, Actuators and Microsystems*, 1715-1718, Barcelona, Spain, 2013.

M. J. Ahamed, D. Senkal, and A. M. Shkel. Effect of annealing on mechanical quality factor of fused quartz hemispherical resonator. *Proceedings of IEEE International Symposium on Inertial Sensors and Systems*, 1-4, Laguna, U.S.A., 2014.

T. Nagourney, J. Y. Cho, A. Darvishian, B. Shiari, and K. Najafi. Effect of metal annealing on the Q factor of metal coated fused silica micro shell resonators. *Proceedings of IEEE International Symposium on Inertial Sensors and Systems*, 1-5, Hapuna, U.S.A., 2015.

D. Saito, C. Yang, A. Heidari, H. Najar, L. Lin, and D. A. Horsley. Microcrystalline diamond cylindrical resonators with quality factor up to 0.5 million. *Applied Physics Letters,* 108(5);051904_1-5, 2016.

J. J. Bernstein, M. G. Bancu, J. M. Bauer, E. H. Cook, P. Kumar, E. Newton, T. Nyinjee, G. E. Perlin, J. A. Ricker, W. A. Teynor, and M. S. Weinberg. High Q diamond hemispherical resonators: fabrication and energy loss mechanisms. *Journal of Micromechanics and Microengineering,* 25(8);085006 _1-12, 2015.

W. J. Startin, M. A. Beilby, and P. R. Saulson. Mechanical quality factors of fused silica resonators. *Review of Scientific Instruments,* 69(10);3681-3689, 1998.

S. D. Penn, G. M. Harry, A. M. Gretarsson, S. E. Kittelberger, P. R. Saulson, J. J. Schiller, J. R. Smith, and S. O. Swords. High quality factor measured in fused silica. *Review of Scientific Instruments,* 72(9);3670-3673, 2001.

K. Numata, K. Yamamoto, H. Ishimoto, S. Otsuka, K. Kawabe, M. Ando, and K. Tsubono. Systematic measurement of the intrinsic losses in various kinds of bulk fused silica. *Physical Letters: A*, 327(4);263-271, 2004.

A. Ageev, B. C. Palmer, A. D. Felice, S. D. Penn, and P. R. Saulson. Very high quality factor measured in annealed fused silica. *Classical and Quantum Gravity,* 21(16);3887-3892, 2004.

D. Senkal, M. J. Ahamed, M. A. Ardakani, S. Askari, and A. M. Shkel. Demonstration of 1 million Q factor on microglassblown wineglass resonators with out-of-plane electrostatic transduction. *Journal of Microelectromechanical Systems,* 24(1);29-37,2015.

J. Cho, T. Nagourney, A. Darvishian, B. Shiari, J. Woo, and K. Najafi. Fused silica micro birdbath shell resonators with 1.2 million Q and 43 second decay time constant. *Proceedings of Solid state Sensors, Actuators and Microsystems Conference*, 103-104, Carolina, U.S.A., 2014.

K. Michael, B. Punnathat, K. Dennis, S. Nate, D. Amish, M. C. Robert, and S. Jan. Metallic glass hemispherical shell resonators. *Journal of Microelectromechanical Systems,* 24(1);19-28, 2015.

N. Mehanathan, V. Tavassoli, P. Shao, L. Sorenson, and F. Ayazi. Invar-36 Micro Hemispherical shell resonators. *Proceedings of IEEE 27th International Conference on Microelectromechanical Systems*, San Francisco, U.S.A., 2014.

V. V. Chikovani, Y. A. Yatsenko, A. S. Barabashov, P. I. Marusyk, E. O. Umakhanov, and V. N. Taturin. Improved accuracy metallic resonator CVG. *IEEE Aerospace Electronic Systems Magazine,* 24;40-43, 2009.

X. Xi, X. Wu, Y. Zhang, X. Zhou, X. Wu, and Y. Wu. A study on Q factor of the trimmed resonator for vibratory cupped gyroscopes. *Sensors and Actuators A: Physical,* 218;23-32, 2014.

B. E. White and R. O. Pohl. Internal friction of subnanometer α-SiO films. *Physical Review Letters*, 75(24);4437-4439, 1995.

T. J. Li, and L. Bellon. Dissipation of micro-cantilevers as a function of air pressure and metallic coating. *Europhysics Letters*, 98(1);14004_1-4, 2011.

H. Walther. Internal friction in solids. The Scientific Monthly, 41(3);275-277, 1935.

G. Sosale, S. Prabhakar, L. Frechette, and S. Vengallatore. A microcantilever platform for measuring internal friction in thin films using thermoelastic damping for calibration. *Journal of Microelectromechanical Systems*, 20(3);764-773, 2011.

G. Sosale, K. Das, L. Frechette, and S. Vengallatore. Controlling damping and quality factors of silicon microcantilevers by selective metallization. *Journal of Micromechanics and Microengineering*, 21(10);105010_1-7, 2011.

E. Serra, F. S. Cataliotti, F. Marin, F. Marino, A. Pontin, G. A. Prodi, and M. Bonaldi. Inhomogeneous mechanical losses in micro-oscillators with high reflectivity coating. *Journal of Applied Physics*, 111(11);113109_1-10, 2012.

W. E. Newell. Miniaturization of tuning forks. Science: New Series, 161(3848);1320-1326, 1968.

A. K. Pandey, R. Pratap, and F. S. Chau. Effect of pressure on fluid damping in MEMS torsional resonators with flow ranging from continuum to molecular regime. *Experimental Mechanics*, 48(1);91-106, 2007.

C. Zhang, G. Xu, and Q. Jiang. Analysis of the air damping effect on a micromachined beam resonator. *Mathematics and Mechanics of Solids*, 8(3);315-325, 2003.

F. R. Blom, S. Bouwstra, M. Elwenspoek, and J. H. J. Fluitman. Dependence of the quality factor of micromachined silicon beam resonators on pressure and geometry. *Journal of Vacuum Science and Technology B,* 10(1);19-26, 1992.

L. Khine and M. Palaniapan. High Q bulk mode SOI square resonators with straight beam anchors. *Journal of Micromechanics and Microengineering,* 19(1);015017_1-10, 2009.

S. Ghaffari, C. H. Ahn, E. J. Ng, S. Wang, and T.W. Kenny. Crystallographic effects in modeling fundamental behavior of MEMS silicon resonators. *Microelectronics Journal* 44(7);586-591, 2013.

S. A. Zotov, B. R. Simon, G. Sharma, J. Han, I. P. Prikhodko, A. A. Trusov, and A. M. Shkel. Investigation of energy dissipation in low frequency vibratory MEMS demonstrating a

resonator with 25 minutes time constant, *Proceedings of Solid state Sensors, Actuators and Microsystems Conference*, South Carolina, U.S.A., 2014.

R. Abdolvand, H. Johari, G. K. Ho, A. Erbil, and F. Ayazi. Quality factor in trench-refilled polysilicon beam resonators. *Journal of Microelectromechanical Systems*, 15(3);471-478, 2006.

P. M. Morse. *Vibration and Sound*. McGraw-Hill, New York, 1936.

L. D. Landau and E. M. Lifshitz. *Theory of Elasticity*. Pergamon Press, Oxford, 1959.

X. Zeyuan, Y. Guoxing, Q. Ziyang, H. Chao, and F. Haibin. Structural optimization research on hemispherical resonator gyro based on finite element analysis. *Proceedings of 35th Chinese Control Conference*, 5737-5742, Chengdu, China, 2016.

L. Guzman, A. Miotello, R. Checchetto, and M. Adami. Ion beam induced enhanced adhesion of gold films deposited on glass. *Surface and Coatings Technology*, 158;558-562, 2002.

E. Darque-Ceretti, D. Helary, and M. Aucouturier. An investigation of gold/ceramic and gold/glass interfaces. *Gold bulletin*, 35(4);118-129, 2002.

A. Darvishian. Design and analysis of extremely low noise MEMS gyroscope for navigation. PhD thesis, Electrical and Computer Engineering, The University of Michigan, 2018.

J. Y. Cho. High performance micromachined vibratory rate and rate integrating gyroscopes. PhD thesis, Electrical Engineering, The University of Michigan, 2012.

J. J. Hwang, C. S. Chou, and C. Chang. Precession of vibrational modes of a rotating hemispherical shell. *ASME Journal of Vibration and Acoustics*, 119(4);612-617, 1997.

Z. Lin, M. Y. Fu, Z. H. Deng, N. Liu, and H. Liu. Frequency split elimination method for a solid-state vibratory angular rate gyro with an imperfect axisymmetric shell resonator. *MDPI AG Sensors*, 15(2);3204-3223, 2015.

Y. K. Zhbanova and V. F. Zhuravlev. On the balancing of a hemispaherical resonator gyro. *Mechanics of Solids*, 33(4);2-13, 1998.

C. H. J. Fox. A simple theory for the analysis and correction of frequency splitting in slightly imperfect rings. *Journal of Sound and Vibration*, 142(2);227-243, 1990.

J. H. Kim, T. Tabaru, and H. Hirai. Evaluation technique of the hardness and elastic modulus of materials with fine microstructures, *Materials Transactions*, 44(4);673-676, 2003.

K. Sattler. *Handbook of Nanophysics*. CRC Press, Taylor and Francis, Florida, U.S.A., 2010.

Y. Jinling, T. Ono, and M. Esashi. Energy Dissipation in submicrometer thick single crystal silicon cantilevers. *Journal of Microelectromechanical Systems*, 11(6);775-783, 2002.

O. Svitelskiy, V. Sauer, N. Liu, K. M. Cheng, E. Finley, M. R. Freeman, and W. K. Hiebert. Pressurized fluid damping of nanoelectromechanical systems. *Physical Review Letters*, 103(24);244501_1-4, 2009.

P. J. Martin. Ion enhanced adhesion of thin gold films. *Gold bulletin*, 19(4);102-116, 1986.

P. L. Guzzo and J. D. B. De Mello. Effect of crystal orientation on lapping and polishing processes of natural quartz. *IEEE Transactions on Ultrasonics, Ferroelectrics, and Frequency Control*, 47(5);1217-1227, 2000.

M. Nazemian and M. Chamani. Experimental investigation and finite element simulation of the effect of surface roughness on nanoscratch testing. *Journal of Mechanical Science and Technology*, 33(5);2331-2338, 2019.

S. D. McAdams, T. Y. Tsui, G. M. Pharr, and W. C. Oliver. Effects of inter layers on the scratch adhesion performance of ultra-thin films of copper and gold on silicon substrates. *Material Research Society Symposium*, 356;809-814, P.A., U.S.A., 1994.

A. S. Bhattacharyyaa, R. P. Kumara, G. Acharyaa, and V. Ranjan. Nanoindentation and scratch test on thin film energy materials. *Current Smart Materials*, 2;39-43, 2017.